LABORATORY LOAD-BASED TESTING, PERFORMANCE MAPPING AND RATING OF RESIDENTIAL COOLING EQUIPMENT

A Dissertation

Submitted to the Faculty

of

Purdue University

by

Li Cheng

In Partial Fulfillment of the

Requirements for the Degree

of

Doctor of Philosophy

December 2020

Purdue University

West Lafayette, Indiana

THE PURDUE UNIVERSITY GRADUATE SCHOOL
STATEMENT OF DISSERTATION APPROVAL

Dr. James E. Braun, Chair

School of Mechanical Engineering

Dr. W. Travis Horton, Chair

School of Civil Engineering

Dr. Eckhard A. Groll

School of Mechanical Engineering

Dr. Neera Jain

School of Mechanical Engineering

Approved by:

Dr. Nicole L. Key

Head of the School Graduate Program

To my beloved parents, Yaping and Yuping, for always being there for me.

ACKNOWLEDGMENTS

I'm very grateful to Professor James E. Braun and Professor W. Travis Horton for their advice, inspiration and support throughout my master and PhD career. Prof. Braun is always ready to share his knowledge, resources to me through our face-to-face weekly meetings, email exchanges and report revisions. I'm significantly impressed by his attention to details and academic insight through the beginning of a job till the very end of it. Prof. Horton is a great person and advisor who can always remind me of positive sides, especially when I encountered setbacks and difficulties. My PhD research benefited a lot from his intuition for experiments and his suggestion on technical details. Moreover, I gained a significant amount of research interests in building and HVAC area since he introduced topics of sustainable buildings to my master degree research. I would also like to appreciate advice from Prof. Groll and Prof. Jain as members of my research committee. I will never be able to achieve this advanced degree without their help and contributions.

In addition, I would like to thank you, to my Herrick folks and colleagues. I have collaborated with Parveen Dhillon, Jie Ma, Akash Patil, Andy Hjortland, Donghun Kim and Jie Cai in my PhD career. I won't be able to explain how helpful they are within this limited page. I'm really grateful to our shop technician Frank Lee for his magic hands that are able to bring things on blueprint to reality. Thank you, Frank.

To friends that I met in Purdue and West Lafayette, thank you. Ruoyi, Rui, Keyou, Kairui, Haotian, Xinye and all the lovely people that I met have left so many happy moments in my memory that I will cherish for a life time. I'm sure we will be able share these memories in future when we join each other someday.

TABLE OF CONTENTS

Page

LIST OF TABLES viii

LIST OF FIGURES x

SYMBOLS xvii

ABBREVIATIONS xx

ABSTRACT xxi

1 INTRODUCTION 1

1.1 Background and motivation 2

1.2 Previous load-based testing development 4

1.3 Thermostat environment emulators 5

1.4 Residential cooling equipment performance mapping 9

1.5 Research objectives and approaches 15

1.6 Thesis organization 17

2 LOAD-BASED TESTING METHODOLOGY AND EXPERIMENTAL EVALUATION 18

2.1 Virtual building model 19

2.2 Automated load-based testing procedures 25

2.3 Seasonal performance rating 32

2.4 Experimental evaluation of load-based testing 33

2.4.1 Test setup 33

2.4.2 Load-based testing and rating results 38

2.4.3 Evaluation of sensitivity to building load parameters 45

2.4.4 Evaluation of repeatability 49

2.4.5 Impact of residual capacity in cycling tests 50

2.5 Interim conclusions 56

Page

3 ALTERNATIVE VIRTUAL BUILDING MODEL 58
3.1 Overview of two-node virtual building model 58
3.1.1 Mathematical description 59
3.2 Estimates of virtual building parameters 60
3.2.1 Regression using detailed building model simulations 61
3.2.2 Scaling and tuning of parameters for the two-node model 65
3.3 Load-based testing using sensible two-node model 70
3.4 Interim conclusion 73
4 THERMOSTAT ENVIRONMENT EMULATOR 74
4.1 Impact of thermostat location on load-based testing 77
4.1.1 Thermostat locations in test chamber 77
4.1.2 Dry-coil test results 79
4.2 Air sampling apparatus 86
4.3 Independently conditioned apparatus 92
4.3.1 Design and controls of the TEC heat exchanger 95
4.3.2 Dynamic model of a thermoelectric heat exchanger 100
4.3.3 Load-based testing results 109
4.4 Interim conclusion 115
5 EXTENDING LOAD-BASED TESTING FOR EQUIPMENT PERFORMANCE MAPPING 117
5.1 Input and output variables in performance mapping 119
5.2 A load-based quasi-steady-state model for a variable-speed air conditioner 121
5.3 Model training and validation based on a simulation database 127
5.3.1 Model training 130
5.3.2 Acquisition of the optimal training dataset 132
5.3.3 Prediction results obtained using the optimal training dataset 135
5.4 Performance mapping experimental design 138
5.4.1 Clustering of test points in a 2-dimensional experimental design space 141

Page

5.4.2 Clustering of test points in a 4-dimensional experimental design space . . . 144
5.5 Load-based test results and an optimal performance map . . . 146
5.5.1 Dehumidifying mode test results . . . 147
5.5.2 Acquisition of the optimal training dataset . . . 152
5.5.3 The optimal performance map . . . 157
5.6 Next-generation performance rating using equipment performance map 164
5.6.1 Co-simulation results . . . 167
5.6.2 Comparison of simulation-based $SCOP_c$ against temperature-bin-based $SCOP_c$ . . . 173
5.7 Interim conclusion . . . 180
6 CONCLUSIONS AND FUTURE WORK . . . 183
6.1 Conclusions . . . 183
6.2 Future work . . . 187
REFERENCES . . . 190

LIST OF TABLES

Table Page

2.1 Summary of Virtual Building Model Parameters for Load-Based Testing . 26

2.2 Outdoor dry-bulb temperature $T_{OD,j}$ of the j^{th} cooling test interval 27

2.3 Load-based tests used for climate zones in seasonal performance ratings for cooling 32

2.4 Test equipment rating characteristics 33

2.5 Sensor accuracy 37

2.6 AHRI 210/240 A2 steady-state test 38

2.7 Results for dry-coil test 41

2.8 Results for wet-coil test 44

2.9 Seasonal coefficients of performance for cooling 45

2.10 $SCOP_c$ for dry climate zones with different F values 47

2.11 $SCOP_c$ for humid climate zones with different SHR 48

2.12 Results for three dry-coil tests 50

2.13 $SCOP_c$ for three dry-coil tests 51

2.14 COPs for dry-coil test intervals with and without damper 55

2.15 $SCOP_c$ for dry climate zones with and without damper 55

3.1 Building geometry information 61

3.2 Parameters in sensible virtual building model 64

4.1 Characteristics of three locations 79

4.2 Results for three dry-coil tests 83

4.3 $SCOP_c$ for three dry-coil tests 84

4.4 TEC manufacturer's data 101

4.5 TEC steady-state results for different applied voltages 108

5.1 Rated information for a four-ton variable-speed air conditioner 128

Table Page

5.2 Applicable range of Nyika's model 128

5.3 Optimal training dataset with respect to the simulation database 134

5.4 Test matrix obtained using heuristic experimental design 139

5.5 Test matrix obtained using clustering experimental design 145

5.6 Test results for five dehumidifying mode tests 148

5.7 Test results of the optimal training dataset 155

5.8 Test input matrix of the optimal training dataset 156

5.9 Model coefficients of the optimal performance mapping model for the test equipment 157

5.10 Impact of reproduction of COPs on temperature-bin-based $SCOP_c$ . . . 164

5.11 Building geometry information 165

5.12 Temperature bin hour fractions 174

5.13 Simulation-based $SCOP_c$ compared against a range of temperature-bin-based $SCOP_c$ 179

1 Performance mapping load-based test results obtained according to heuristic experimental design test matrix 194

2 Performance mapping load-based test results obtained according to clustering experimental design test matrix 195

3 EXP-07 cooling load-based test results 196

LIST OF FIGURES

Figure Page

1.1 NEMA thermostat testing apparatus 7

1.2 Air sampling tree in the AHRI 550/590 8

1.3 Clustering result of a compressor operating envelope 14

1.4 Objectives and proposed approach of this work 16

2.1 Load-based test apparatus and emulated virtual building 19

2.2 Sensible building cooling load line 21

2.3 Flow chart of cooling test procedure 29

2.4 Refrierant-side measurement locations 34

2.5 Air-side measurement locations: Indoor unit 35

2.6 Air-side measurement locations: Outdoor unit 37

2.7 Sensible cooling rate, sensible load, and power measured in dry-coil load-based testing 39

2.8 Temperatures in dry-coil load-based test testing 40

2.9 Sensible cooling rate, sensible load, and power measured in wet-coil load-based testing 41

2.10 Temperatures in wet-coil load-based testing 42

2.11 Latent results in wet-coil load-based testing 43

2.12 COPs for cooling test intervals 44

2.13 COPs for dry-coil test intervals with different sizing factor F 46

2.14 COPs for wet-coil intervals with different building SHR when F=1.3 48

2.15 Residual capacity in load-based test 52

2.16 Diagram of supply air damper 52

2.17 Pseudo damper logic based on threshold of indoor power 54

2.18 77 $^{\circ}F$ test interval performance with supply duct pseudo damper 54

Figure Page

3.1 Diagram of one-node model for sensible building loads 59
3.2 Diagram of sensible two-node model 60
3.3 Prototype building geometry 61
3.4 Dynamic building response and the associated inputs 62
3.5 Zone air temperature prediction by sensible two-node model 64
3.6 Sample cycling behaviors for two virtual building models 67
3.7 Cycling rate domes for both building models compared to the NEMA dome 68
3.8 Frequency response of virtual building models 69
3.9 Energy rates in load-based testing using two-node model for sensible loads 71
3.10 Temperatures in load-based testing using two-node model for sensible loads 72
4.1 Thermostat environment emulator in load-based testing 75
4.2 Three thermostat locations in test chamber 78
4.3 Three thermostat locations in closer looks 78
4.4 Dry-coil test results with thermostat mounted at location A 80
4.5 Dry-coil test results with thermostat mounted at location B 80
4.6 Dry-coil test results with thermostat mounted at location C 81
4.7 Equipment Return air temperatures in three tests 82
4.8 Air sampling apparatus 87
4.9 Drawing of air sampling plenum 88
4.10 Sensible cooling rate, sensible load, and power measured in dry-coil load-based testing using air sampling apparatus 90
4.11 Temperatures in dry-coil load-based test testing using air sampling apparatus91
4.12 Independently conditioned apparatus 93
4.13 3D drawings of TECHX assembly 95
4.14 TECHX assembly 96
4.15 (a) Schematic of airflow pattern (b) 3D drawing of TECHX (c) Arrangement of TEC layer 97
4.16 Schematic of the TECHX control 99

Figure Page

4.17 Comparison of TEC predicted (solid lines) and manufacturer's (dashed lines) performance for cooling 102

4.18 Problem setup for dynamic TECHX model 103

4.19 TECHX temperature distribution responding to 20V power after 50 seconds 105

4.20 Air-side response of TECHX to 20V power 106

4.21 TECHX responses to different supplied voltages 107

4.22 Sensible cooling rate, sensible load, and power measured in dry-coil load-based testing using independently conditioned apparatus 109

4.23 Temperatures in dry-coil load-based testing using independently conditioned apparatus 110

4.24 Thermostat inlet temperature control 111

4.25 Sensible cooling rate, sensible load, and power measured in wet-coil load-based testing using independently conditioned apparatus 112

4.26 Temperatures in wet-coil load-based testing using independently conditioned apparatus 113

4.27 Latent results in wet-coil load-based testing using independently conditioned apparatus 114

5.1 Conceptual comparison between temperature-bin-based and simulation-based performance rating approaches 117

5.2 Input and output variables in performance mapping of this study 121

5.3 Implementation procedure for the load-based quasi-steady-state model . 126

5.4 Histogram of unique training datasets 133

5.5 Parity plot for equipment total cooling rate prediction 135

5.6 Parity plot for equipment latent cooling rate prediction 136

5.7 Parity plot for equipment sensible heat ratio prediction 136

5.8 Parity plot for equipment COP prediction 137

5.9 Parity plot for equipment power prediction 137

5.10 Uniform sampling of candidate test points 141

5.11 Hierarchical clustering tree 142

5.12 6 clusters of 20 candidate test points 142

Figure Page

5.13 6 cluster centroids 143

5.14 Sensible results of dehumidifying mode test 4 in table 5.6 148

5.15 Latent results of dehumidifying mode test 4 in table 5.6 149

5.16 Representation of 39 points including 5 dehumidifying mode points . . . 151

5.17 Representation of 34 points excluding 5 dehumidifying mode points . . . 151

5.18 Cost function evaluated over generations 154

5.19 Parity plot for equipment total cooling rate prediction 158

5.20 Parity plot for equipment latent cooling rate prediction 158

5.21 Parity plot for equipment sensible heat ratio prediction 159

5.22 Parity plot for equipment COP prediction 159

5.23 Parity plot for equipment power prediction 160

5.24 Parametric study of the optimal performance map: Impact of T_{OD} and BL on COP 161

5.25 Parametric study of the optimal performance map: Impact of B_{ID} and BL on COP 162

5.26 Parametric study of the optimal performance map: Impact of B_{ID} and BL on SHR 162

5.27 Flowchart of EnergyPlus and performance map co-simulation 166

5.28 Co-simulation results: annual building responses 168

5.29 Co-simulation results: building responses for three days in August 169

5.30 Co-simulation results: equipment responses for three days in August . . . 169

5.31 Co-simulation results: building responses for three days in July 170

5.32 Co-simulation results: equipment responses for three days in July 171

5.33 Co-simulation results: annual equipment responses 172

5.34 Daily averaged outdoor temperature and cooling degree days for Albuquerque 175

5.35 Sensible building load line for the simulated single-family building in Albuquerque 177

1 Sensible results of performance mapping test 1 197

2 Latent results of performance mapping test 1 197

Figure		Page
3	Sensible results of performance mapping test 2	198
4	Latent results of performance mapping test 2	198
5	Sensible results of performance mapping test 3	199
6	Latent results of performance mapping test 3	199
7	Sensible results of performance mapping test 4	200
8	Latent results of performance mapping test 4	200
9	Sensible results of performance mapping test 5	201
10	Latent results of performance mapping test 5	201
11	Sensible results of performance mapping test 6	202
12	Latent results of performance mapping test 6	202
13	Sensible results of performance mapping test 7	203
14	Latent results of performance mapping test 7	203
15	Sensible results of performance mapping test 8	204
16	Latent results of performance mapping test 8	204
17	Sensible results of performance mapping test 9	205
18	Latent results of performance mapping test 9	205
19	Sensible results of performance mapping test 10	206
20	Latent results of performance mapping test 10	206
21	Sensible results of performance mapping test 11	207
22	Latent results of performance mapping test 11	207
23	Sensible results of performance mapping test 12	208
24	Latent results of performance mapping test 12	208
25	Sensible results of performance mapping test 13	209
26	Latent results of performance mapping test 13	209
27	Sensible results of performance mapping test 14	210
28	Latent results of performance mapping test 14	210
29	Sensible results of performance mapping test 15	211
30	Latent results of performance mapping test 15	211

Figure Page

31 Sensible results of performance mapping test 16 212
32 Latent results of performance mapping test 16 212
33 Sensible results of performance mapping test 17 213
34 Latent results of performance mapping test 17 213
35 Sensible results of performance mapping test 18 214
36 Latent results of performance mapping test 18 214
37 Sensible results of performance mapping test 19 215
38 Latent results of performance mapping test 19 215
39 Sensible results of performance mapping test 20 216
40 Latent results of performance mapping test 20 216
41 Sensible results of performance mapping test 21 217
42 Latent results of performance mapping test 21 217
43 Sensible results of performance mapping test 22 218
44 Latent results of performance mapping test 22 218
45 Sensible results of performance mapping test 23 219
46 Latent results of performance mapping test 23 219
47 Sensible results of performance mapping test 24 220
48 Latent results of performance mapping test 24 220
49 Sensible results of performance mapping test 25 221
50 Latent results of performance mapping test 25 221
51 Sensible results of performance mapping test 26 222
52 Latent results of performance mapping test 26 222
53 Sensible results of performance mapping test 27 223
54 Latent results of performance mapping test 27 223
55 Sensible results of performance mapping test 28 224
56 Latent results of performance mapping test 28 224
57 Sensible results of performance mapping test 29 225
58 Latent results of performance mapping test 29 225

Figure Page

59 Sensible results of performance mapping test 30 226

60 Latent results of performance mapping test 30 226

SYMBOLS

A	area
a	model coefficient
B	wetbulb temperature
b	model coefficient
BF	bypass factor
BL	building load
c	model coefficient
C	capacitance or specific heat
CDD	cooling degree day
COP	coefficient of performance
Cp	specific heat at constant pressure
d	model coefficient
DCR	demand cooling rate
F	sizing factor
f	correction factor
G	transfer function
h	enthalpy or heat transfer coefficient
I	current
j	index of test interval
J	cost function
k	scaling factor for thermal capacitance or thermal conductivity
N	equipment cycling rate or number of datapoints
NTU	number of transfer unit
nk	number of hours in k^{th} temperature bin

PLR	part load ratio
R	resistance
R^2	coefficient of determination
RH	relative humidity
S	Seeback coefficient or set
$SCOP$	seasonal coefficient of performance
SHR	sensible heat ratio
T	temperature
t	time
TF	tuning factor
$\dot{Q}$	heat transfer rate
UA	building envelope conductance
V	voltage
$\dot{V}$	volumetric flow rate
w	absolute humidity
$\dot{W}$	power
X	equipment cycling duty or input vector
ΔA	differential area
Δq	differential heat transfer rate
ΔV	differentaial volume
α	model coefficient
δ	differential distance
ε	heat exchanger effectiveness
θ	parameter vector or thermal resistance (used only in chapter4)
ρ	density
	Subscript:
ADP	apparatus dew point
Bal	balance point

c	cooling (mode) or convective
D	design condition
DA	daily average
$dband$	dead band
eff	effective
fg	vaporization of water
fl	full load
G	transfer function
h	heating
ID	indoor
i	i^{th} datapoint or index of row or index of datapoint
in	inlet
int	internal
k	index of a temperature bin
l	latent
m	number of temperature bin or internal mass node
max	maximum
OD	outdoor
out	outlet
rat	rated
ref	refrigerant
s	sensible or sheet metal
SA	supply air
sp	setpoint
t	total
vr	virtual room
z	zone air node

ABBREVIATIONS

AHRI	Air-conditioning, Heating, and Refrigeration Institute
ASHRAE	American Society of Heating, Refrigeration and Air-conditioning Engineers
CSA	Canadian Standards Association
DX	Direct Expansion
EIR	Energy Input Ratio
HSPF	Heating Seasonal Performance Factor
MAPE	Mean Absolute Percentage Error
NEMA	National Electrical Manufacturers Association
RMSE	Root Mean Square Error
TEC	Thermal Electric Cooler
TMY	Typical Meteorological Year

ABSTRACT

Cheng, Li PhD, Purdue University, December 2020. Laboratory Load-Based Testing, Performance Mapping and Rating of Residential Cooling Equipment. Major Professors: Jim Braun and Travis Horton.

In the U.S., unitary residential air conditioners are rated using standard AHRI 210/240 that is inadequate to credit equipment with advanced controls and variable-speed components since the ratings are based on results of steady-state laboratory tests. Contrarily, a load-based testing and rating approach is presented in this work that can capture equipment performance with its integrated controls and thermostat responses that is more representative of the field. In this approach, representative building sensible and latent loads are emulated in a psychrometric test facility at different indoor and outdoor test conditions utilizing a virtual building model. The indoor test room conditions are continuously adjusted to emulate the dynamic response of the virtual building to the test equipment sensible and latent cooling rates and the equipment dynamic response is measured. Meanwhile, the inlet temperatures to the test equipment thermostat are independently controlled to track the same virtual building response using a thermostat environment emulator that encloses the test thermostat, that provides typical flow conditions and of which the design and control are presented in this work. Climate-specific cooling seasonal performance ratings can be determined by propagating load-based test results through a temperature-bin method to estimate a seasonal coefficient of performance (SCOP). In addition, a next-generation rating approach is developed that extends load-based testing for performance mapping, such that the SCOP can be obtained using building simulations that incorporate specific building types, climates and an equipment-specific performance map.

In this work, the proposed approaches were implemented to test and rate a variable-speed residential heat pump operating in cooling mode. Trained with results from only 12 load-based test intervals carried out using the test equipment, a quasi-steady-state mapping model was able to map the equipment performance across almost the entire operating envelope within $\pm 10\%$ errors and the R^2 values were very close to 1. Using the identified performance map, the next-generation SCOP was obtained based on an annual simulation deployed in EnergyPlus, where the map was coupled to a typical single-family building in Albuquerque,NM. Compared to the temperature-bin-based rating, this simulation-based rating is able to comprehensively and appropriately reflect equipment annual field performance associated with a specific building type and climate, as the rating is extended from automated laboratory load-based testing and performance mapping.

1. INTRODUCTION

The seasonal energy efficiency ratio is a primary performance indicator for residential air conditioners and heat pumps reported by each manufacturer. To determine equipment seasonal performance, current rating standards utilize a steady-state testing approach where the equipment native controls are overridden. However, as these standards were originally developed for equipment with simple on/off controls, they are deficient in estimating the seasonal performance characteristics of equipment with advanced technologies that employ variable-speed drives with sophisticated control algorithms. To better capture these behaviors, a load-based testing methodology and associated rating approaches are presented and demonstrated in this work, where the equipment is tested together with its integrated controls in an automated, repeatable and reproducible fashion.

The target systems for this methodology are electrically powered direct expansion vapor compression cycle residential air conditioners. A load-based testing approach is particularly appropriate for variable-speed equipment but is also applicable to single-stage and discrete multi-stage equipment. In this work, the methodology was applied to a state-of-the-art high efficiency, variable-speed, 2-ton ducted split system. The approach can be also extended to ductless or packaged equipment. Definitions and categories of equipment can be found in a book by Mitchell and Braun [1]. A pair of psychrometric test chambers with reconditioning equipment and controls is the major testing apparatus employed for testing equipment performance in this work. In addition, a thermostat environment emulator is the other required testing apparatus that will be introduced in chapter 4.

1.1 Background and motivation

AHRI 210/240 [2] forms the basis for rating unitary residential air conditioners and heat pumps in the U.S. This standard applies steady-state testing that requires overriding of the integrated controls to achieve specified part-load conditions and therefore does not include dynamic control interactions that occur in the field. Proctor and Cohn [3] studied field performance of four dual-stage air conditioners and found that their actual seasonal energy efficiency ratios (SEERs) were between 59% and 84% of their rated SEERs. Hart et al. [4] noted that the benefits of a number of potential energy-saving measures in addition to base efficiency were not captured with the current steady-state testing procedure (e.g. AHRI 210/240), such as equipment control configuration and cycling effects.

Unlike single-stage and multi-stage equipment, variable-speed air conditioners are equipped with electronically commutated motors (ECM) for fans and inverter-driven compressors. Variable-speed equipment can be controlled more intelligently for part-load conditions by modulating both the air-side and refrigerant-side mass flow rates without cycling off the compressor and fan, except at very low capacity conditions. As a result, variable-speed equipment in the field can have significantly better seasonal energy efficiency than single-stage equipment. However, AHRI 210/240 has shortcomings in characterizing equipment part-load performance in a manner that is representative of the field. For on/off cycling behavior, the standard prescribes a specific cycling pattern in order to estimate a cycling degradation effect for the equipment. This "prescribed" test configuration does not account for differences in the cycling behavior of various equipment due to different controller designs, thermostat responses, and thermostat temperature deadbands. Also, the actual cycling pattern and its effect on equipment performance changes directly with the load so that a single cyclic pattern and test result is not representative. For variable-speed behavior, the steady-state tests in the AHRI 210/240 specify that manufacturers provide overrides to the equipment controller using a proprietary test mode to run

the equipment at minimum, intermediate, and maximum speed. This can lead to behavior that does not represent in-situ performance.

Furthermore, the seasonal energy performance of a system can have a strong dependence on building type and climate zone. Although AHRI 210/240 specifies different climate zones for evaluating heating seasonal performance factor (HSPF), the SEER determination is not climate specific. As a result, an air conditioner that has significantly different seasonal performance in marine and hot climates due to very different part-load distributions and latent loads would have the same performance rating. This shortcoming was noted by Fairey et al. [5] in their simulation study of the climatic impacts on SEER and HSPF. In addition, variable-speed systems may better handle building latent and sensible loads across different building types and climate zones since the on-board controller is able to independently adjust evaporator air flowrate and evaporating temperature. Therefore, the building and climate impacts on seasonal energy performance for variable-speed equipment could be even more significant, which needs to be captured in the testing methodology.

To address these shortcomings, the motivation for this work was the investigation of a new load-based testing methodology and associated rating approaches. An improved methodology should reflect the combined effects of the system and its integrated controls in evaluating performance under representative field operating conditions. The testing should be automated to reduce time and resource requirements and the results should be useful in generating climate-specific performance ratings. The ratings and the test equipment behaviors should be repeatable within a testing facility and reproducible across different test facilities. In addition to performance ratings, load-based testing should be useful as a tool for engineers in the early development and validation of improved feedback and supervisory control algorithms.

1.2 Previous load-based testing development

Cremaschi and Perez Paez [6] investigated a load-based testing approach for light commercial rooftop units (RTUs) with economizers where the environmental chambers are controlled to provide specified sensible and latent gains and the equipment attempts to maintain a thermostat setpoint temperature. The loads that they employed in their testing were based on simulation results for a representative commercial building that were generated prior to testing. In this way, the indoor test room served as a proxy for an actual building in which the space temperature and humidity responded dynamically per the energy balance between the equipment capacity and prescribed loads. However, Cremaschi and Perez Paez had difficulty in achieving repeatable test results within their test rooms due to variations in implemented sensible and latent loads because of hardware control limitations. In general, this approach has the disadvantage that environmental test chambers have unique dynamic responses, making it difficult to achieve reproducible results across different facilities. Furthermore, the temperature and moisture response dynamics of a test facility will not be representative of an actual building.

To address this issue, Hjortland and Braun [7] recently presented an alternative load-based testing approach for unitary equipment, that utilizes the indoor environmental chamber controls to regulate the temperature and humidity of the equipment return air inlet in a manner that emulates the response of a representative building. This approach requires the use of a virtual building model with inputs that include real-time equipment sensible and latent cooling rates along with indoor and outdoor room temperatures. The outputs from the virtual building model are indoor environmental temperature and humidity setpoints for environmental chamber controls that mimic the response of an actual building.

Using this approach, Hjortland and Braun compared the performance characteristics of an RTU in three different control modes: single-stage, two-stage and variable-speed. The test unit operating under variable-speed mode showed a higher

part-load efficiency compared to single-stage and two-stage mode. Patil et al. [8] provided a limited description of the methodology and presented some sample results. Dhillon et al. [9] presented some initial comparisons of seasonal performance estimates based on the load-based testing approach with results obtained using the AHRI 210/240 steady-state testing approach for two different variable-speed heat pumps. They found that the steady-state testing approach estimates higher seasonal efficiency than the load-based testing approach for cooling as well as heating. These developments were carried out in collaboration with the development of a new Canadian testing standard (CSA EXP-07 [10]) that is focused on residential heat pumps and air conditioners.

1.3 Thermostat environment emulators

In load-based testing, since the temperature of the indoor environmental chamber that simulates indoor conditions continuously tracks virtual room temperature setpoints that are adjusted based on outputs from the virtual building model, the test equipment thermostat senses the floating air temperature and communicates with the test equipment as if it were installed in the field. In order to achieve realistic dynamic behavior, it is important to guarantee that the thermostat inlet airflow conditions and inlet temperature dynamics be representative of field conditions and be reproducible across different test facilities. The current CSA EXP-07 [10] specifies that the thermostat be located in the return to the indoor test unit. This ensures that both the thermostat and equipment see the same conditions and was thought to have the best chance of achieving reproducible results across different facilities.

Cheng et al. [11] studied the impact of thermostat location in load-based testing and found that a test thermostat installed at three different locations led to significantly different load-based testing behaviors and performance. The dynamics of the thermostat varied significantly with location due to non-uniform air velocity and temperature distribution within the indoor chamber. Locating the thermostat in the

return air stream led to the fastest thermostat dynamics, but it is far from being representative of typical conditions that a thermostat would experience in the field. In the interest of achieving representative and reproducible results for load-based testing, it is important to ensure that the test equipment thermostat has an inlet temperature that is the same as (or has a fixed offset with respect to) the test unit return air temperature, but with an air flow that is representative of convection experienced in a room. This requires that the thermostat have its own emulated environment that tracks virtual building setpoints.

The development of a thermostat environment emulator that can provide realistic and reproducible inlet conditions to the test thermostat in load-based testing was another goal of the work embedded in the overall load-based testing methodology. The environment emulator should include a plenum or a small chamber that encloses the test thermostat, air velocity controls that provide representative flow conditions and air temperature controls that emulate the virtual building dynamics to the test thermostat. The design and operation of the thermostat environment emulator should be reproducible across different test facilities in order to be standardized as a universal solution to the test equipment thermostat configuration in load-based testing.

Since 1943, the residential controls section of the National Electrical Manufacturers Association (NEMA) has maintained a standard for room thermostats [12] that describes a testing apparatus to emulate a test environment for thermostats. The original NEMA thermostat testing apparatus incorporated an internal heater, while the cooling function was obtained by installing the chamber in an ambient of approximately 40°F. However, working in and maintaining a 40°F ambient was found to be very inconvenient and therefore Boldt [12] developed the second version of the testing apparatus for NEMA that integrates both heating and cooling as described in the most recent standard [13]. The primary purpose of the NEMA testing apparatus is to test cycling behaviors of a thermostat. As illustrated in figure 1.1, the dimension is 28.5"x40"x84.5". Air is circulated through a cooling coil, a heating coil and the thermostat using a blower in the apparatus. The thermostat is connected to

the apparatus controller for the purpose of determining whether the thermostat inlet temperature should ramp up or down (cycling) with prescribed rates of change.

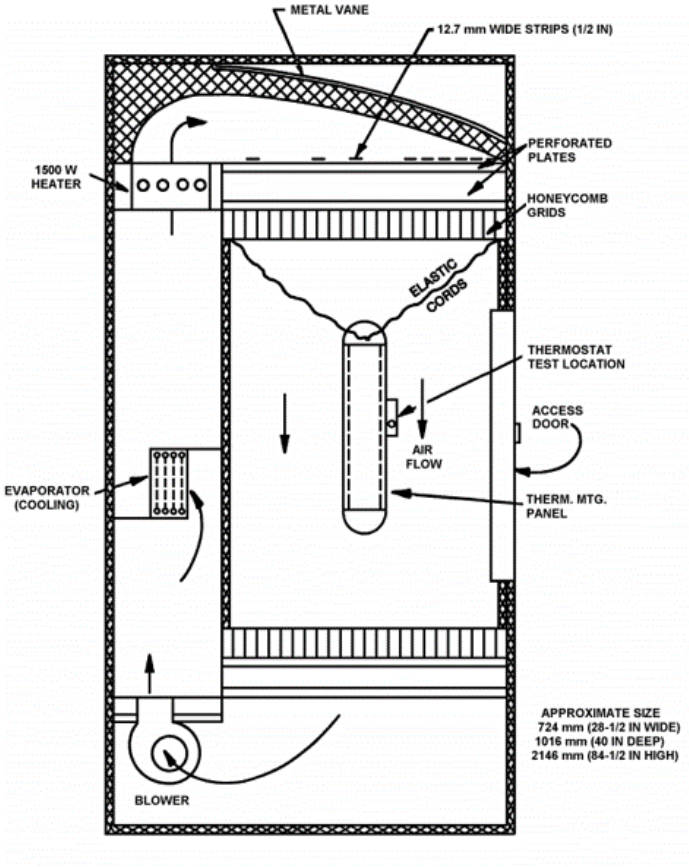

Fig. 1.1. NEMA thermostat testing apparatus

In terms of providing typical flow conditions to the test thermostat, the NEMA standard specifies that air should flow across the thermostat vertically and uniformly with a nominal velocity of 30 ft/min. This is thought to be representative of a wall-mounted thermostat and is the basis for the air velocity specification in the current work. However, the overall NEMA testing apparatus was thought to be too bulky for integration with a test unit in the indoor environmental chamber and have too slow a response for load-based testing. The inlet temperature to a test thermostat needs

to closely track (be controlled to) the virtual building temperature dynamics during load-based testing.

In terms of the test thermostat inlet air temperature control, lower-cost, smaller and faster responding cooling/heating devices or alternative approaches are preferred for integration within a thermostat environment emulator as compared with the evaporator coil and electric heater utilized in the NEMA testing apparatus. One approach considered in this work is to sample the indoor test equipment return air and draw it to the inlet of the test thermostat inside an emulator, with the goal of having consistent inlet conditions for both the thermostat and the test equipment in load-based testing. The emulator developed using this approach is called an "air sampling apparatus". Figure 1.2 shows a sampling device described in the standard AHRI 550/590 [14] that can be adapted and used in an air sampling apparatus to draw air from the indoor test equipment return air inlet.

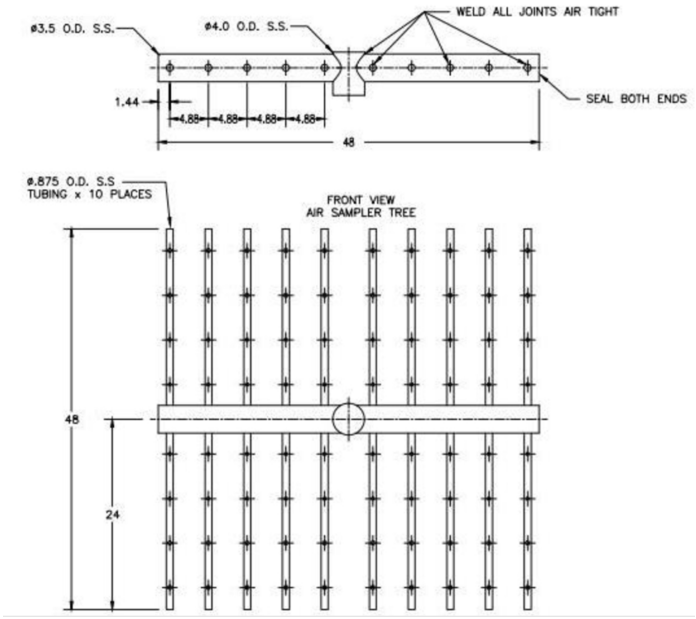

Fig. 1.2. Air sampling tree in the AHRI 550/590

Another approach considered in this work involved building a smaller version of the NEMA testing apparatus using fast responding thermoelectric devices. The use

of separate cooling/heating devices instead of the air sampling device requires that the thermostat inlet temperature "mirror" the response of the return air temperature with both independently controlled to temperature setpoints dictated by the virtual building model. This thermostat environment emulator is referred to as the "independently conditioned apparatus." Bustamante et al. [15] demonstrated the concept of utilizing thermoelectric coolers in combination with a thermal blanket within a miniature thermostat test chamber. Although this small chamber could not provide typical flow conditions or realistic building dynamics for a test thermostat, it inspired the use of thermoelectric coolers (TECs) for our thermostat environment emulator. TECs can be readily scaled to a small thermostat emulator, can provide a fast response, and can provide either heating or cooling when their power polarity is reversed.

1.4 Residential cooling equipment performance mapping

The seasonal performance of unitary residential equipment for various climate zones can be rated by directly propagating test results for COP at different ambient temperatures into estimates of seasonal performance ratings based on temperature bins and weight for each bin (e.g. calculation of HSPF and SEER in AHRI 210/240 [2]). However, a "holy grail" for load-based testing and performance rating is to be able to map equipment performance from automated testing results measured over a relatively short period of time. This performance map can then be implemented as a "model" in building simulations to generate seasonal energy efficiency ratings that are specific to various building types and climates.

Previously, performance mapping of unitary air conditioners has been well studied. A significant number of modeling approaches have been investigated for mapping equipment capacity and power under different operating conditions. It is important to adopt approaches that can be employed to extend load-based testing results to generate a performance map. For example, since load-based testing results are harvested after the equipment reaches a quasi-steady or steady-period condition as a response to

fixed building loads (Patil et al. [8]), dynamic equipment models are not necessary for the intended purpose. In addition, this work focuses on mapping of variable-speed equipment, since this is the more general case and a load-based testing approach is particularly important for the next generation of equipment with variable-speed drives and advanced on-board controls.

Component-based forward modeling approaches capture equipment performance accurately. For example, Shen [16] estimated the evaporator heat transfer rate with an average deviation of 2.0% when using detailed models with finite segment heat exchanger models that use detailed geometry descriptions. Bell [17] developed ACHP that is a detailed model for direct expansion residential heat pumps and air conditioners. However, forward modeling approaches incorporate numerous geometrical and other parameters that would be time consuming to collect and implement in a model. Also, construction, tuning and simulation of such a model requires significant expertise and computational time. This approach is not suitable for mapping load-based test performance results.

Component-based inverse modeling approaches use simplified semi-physical (semi-empirical) models with key model parameters trained from experimental data. Cheung [18] successfully generated a simulation database for different equipment operating scenarios under both faulted and non-faulted conditions where the models were generated using an inverse modeling approach. Cai and Braun [19] employed a gray-box model structure for the vapor compression cycle. However, these component-based models only represent the equipment performance at steady-state without consideration of their integrated controllers. Also, the model training required a significant number of different measurements over a wide range of operating conditions. The typically data available from current equipment rating procedures would not be useful in developing equipment-specific models using this approach.

The controls for single-stage equipment are relatively straight-forward and typically involve cycling the compressor and condenser fan on and off in response to a call for heating or cooling from the thermostat. The equipment operates at full capacity

when it is on and turns off in cooling when thermostat temperature falls below its setpoint by a dead-band built into the thermostat logic. Under dead-band control, the equipment cycles with a cycle duty that depends on the part-load conditions. Full-load performance is usually recorded in equipment catalogs as a result of manufacturers steady-state rating tests and this data can be used to map the equipment full-load performance.

Yang and Li [20] proposed a generic rating-data-based DX coil model that predicts both wet-coil and dry-coil conditions of an air conditioner. Brandemuehl et al. [21] presented a polynomial estimation approach to predict single-stage equipment total cooling capacity and energy input ratio (EIR) in the ASHRAE secondary toolkit. Rated total capacity and EIR are corrected using factors that capture the effects of inlet air wet bulb temperature to the evaporator, inlet air dry bulb temperature to the condenser and airflow rate. Air conditioner sensible heat ratio is calculated using a bypass factor (BF) method. This overall approach is based on the approach used in the DOE-2 [22] building simulation program. Henderson et al. [23] further developed part-load curves for use in the DOE-2 model to predict performance degradation of single-stage equipment at part-load conditions.

Based on the ASHRAE toolkit approach, Cai and Braun [24] proposed a modification to enable mapping of multistage equipment by adding a factor that corrects equipment total capacity and energy input ratio to performance at different stages. Hjortland [25] further applied this model to variable-speed equipment using a compressor speed correction factor to replace Cai's compressor stage factor. However, this particular approach employs indoor fan airflow rate and compressor speed (stage) as model inputs which are essentially control signals or outputs of variable-speed equipment on-board controls. Therefore, the equipment controller is not characterized in these approaches.

Variable-speed embedded control decisions are difficult to quantify even with the help of a load-based testing approach which outputs the overall behavior of equipment with its controller. Different equipment manufacturers use different control logic. The

variable-speed equipment tested by Hjortland and Braun [7] used two PI controllers that maintained equipment discharge air temperature and indoor room temperature separately. This logic is an example but cannot represent a generic variable-speed equipment controller design. The variable-speed equipment model [26] in EnergyPlus utilizes four discrete cooling coil speed levels each of which is represented by a DOE-2 performance polynomial. Selection of the speed level is a result of comparison between the capacity of each speed level to the building load requirement. This approach lumps fan speed and compressor speed into cooling coil speed, but still cannot represent a generic control logic.

Nyika et al. [27] proposed a generalized performance map for variable-speed heat pumps that employed equipment total load and indoor fan airflow rate as model inputs along with indoor and outdoor temperatures. This model is essentially still a vapor compression cycle model, but Nyika proposed an empirical algebraic controller model to be coupled with the equipment model that correlated equipment part-load ratio to indoor fan speed. Therefore, indoor fan speed becomes an intermediate variable in this model. Nyika's model can be used to generate data that can be employed to identify and validate future model forms that map the complete equipment and controller performance. In addition, future quasi-steady-state equipment mapping should consider the idea of using an empirical approach to model on-board control logic, due to its limited known physics.

It is possible to decouple a variable-speed equipment model into controller and vapor compression cycle sub-models. However, this could significantly increase model complexity and requirements for training data. The approach proposed in this work starts with a model that maps the lumped performance of equipment and its integrated controls. Nyika's model and Cai's model are the basis for the performance mapping model form of this work.

After the identification of a performance mapping model form, a critical future step is to consider optimal experimental design that specifies the testing requirements for mapping equipment performance using the proposed model form. The goal is to

determine an acceptably small number of test conditions required to determine the model that can accurately represent equipment quasi-steady-state performance over its operating envelope.

Alternatively, a more general experimental design approach can be obtained that focuses more on uniform, complete and unbiased coverage of the operating envelope for any variable-speed air conditioners. In particular, an acceptably small number of the test points sampled from the experiment design space should be able to well represent the whole space. In this work, both the optimal experiment design approach and the unbiased sampling experiment design approach were investigated.

There are various approaches to achieve uniform and unbiased sampling from a design space, when probability distributions are not considered. Uniform sampling is the most commonly used approach. In this case, a fixed number of alterations are uniformly sampled for each dimension (design variable) in the space, and the full combinations of these alterations from each dimension compose the whole set of sampled points. This approach is very useful when the design space is one-dimensional or two-dimensional. However, too many points will be required when sampling from a 3-dimensional space or hyperspace. Nevertheless, some advanced sampling approaches start from a candidate set that is obtained using the uniform sampling approach. Random sampling is another commonly used approach, but the sampled points are not ensured to be uniform and be repeatable.

Hierarchical clustering is an algorithm that groups objects over a variety of scales by creating a hierarchical clustering tree. The tree is not a single set of clusters, but rather a multilevel hierarchy, where clusters at a lower level are joined as clusters at a higher level of the hierarchical tree. Objects in a cluster are similar to each other, while objects from different clusters are dissimilar. Therefore, the similarities/dissimilarities of objects in each level are used as criteria for partitioning/grouping. There are various choices of similarity metrics, and the Euclidean distance between two objectives in their space is a popular measurement that will also be used in this work. Every object at the lowest level of the hierarchical tree is a cluster itself. In an upper level, two

clusters from the lower level that are in the closest proximity to each other are grouped into a new cluster. In this way, the complete set of all the objects form the last and final cluster at the very top level of the hierarchical tree. A user of the algorithm can decide which level of clustering/partitioning is needed in different applications. Chopping off the hierarchical tree at the lower level results in more clusters while a higher level cut off results in less clusters.

The goal of applying hierarchical clustering in experimental design is to group similar test points in one cluster and partition the design space into dissimilar clusters. Therefore, the test points sampled from these clusters (e.g. cluster centroids) can represent the entire experimental design space well. Compared to random sampling from the design space, test points sampled after clustering should better span across the space and be more repeatable.

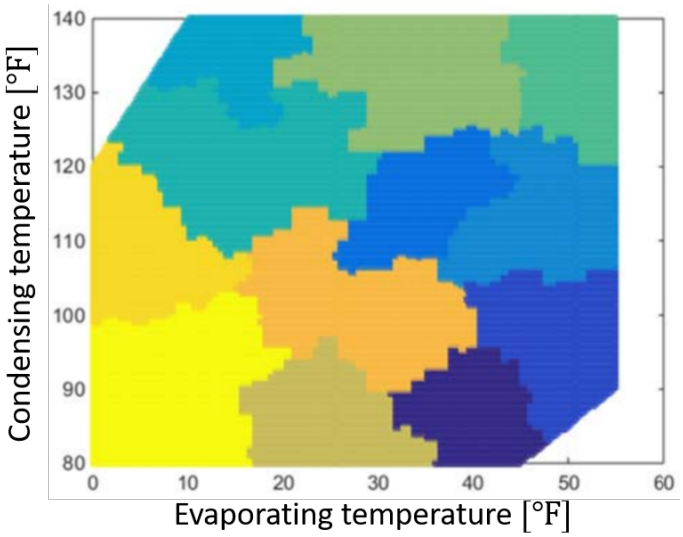

Fig. 1.3. Clustering result of a compressor operating envelope

As an example, Aute et al. [28] utilized the clustering approach to group candidate test points within a compressor operating envelope (a two-dimensional space) into different clusters, with different colors in figure 1.3. As each cluster can be represented

by its geometric centroid, these centroids combine into a set that well represents the whole domain.

1.5 Research objectives and approaches

The objectives of this work were to: 1) develop an updated, more complete, and archival description of the laboratory load-based testing methodology that includes the basis for development, necessary steps for automation and convergence criteria; 2) design and validate a thermostat environment emulator that can provide realistic and reproducible inlet conditions to a test thermostat for the purpose of load-based equipment testing; 3) demonstrate and validate the complete load-based testing methodology using residential equipment within a laboratory setup; 4) develop a methodology that employs load-based testing for performance mapping that captures both the equipment performance and its integrated controllers under quasi-steady-state operation; 5) compare both a traditional approach and a next-generation approach for determining the seasonal coefficient of performance index for rating of residential unitary cooling equipment.

A flow chart of the associated approaches are shown in figure 1.4. For the first objective, a single-node-structure virtual building model was specified for load-based testing that incorporates prescribed sensible/latent building loads, and that dynamically responds to the test equipment and its native controls in a realistic fashion. Alternative building models were also considered in terms of the impact on testing and implementation requirements. Moreover, automated testing procedures along with convergence criteria were developed to measure equipment steady-periodic performance during load-based testing. This is crucial to minimize the test time, and to improve repeatability and reproducibility across different test facilities.

To further improve test reproducibility, another important task is to configure the test thermostat in a realistic and reproducible fashion. Therefore, for the second task, the thermostat environment emulator was developed that is able to emulate the

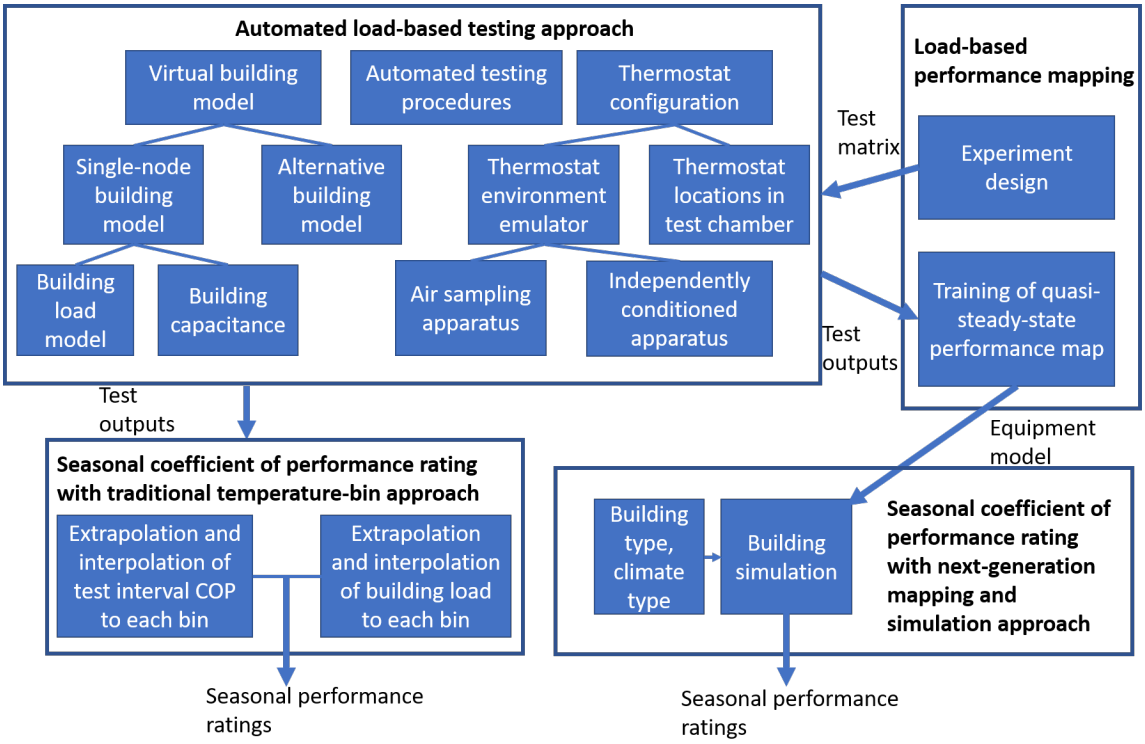

Fig. 1.4. Objectives and proposed approach of this work

virtual building dynamics to the test thermostat and provide airflow that is representative of a typical indoor environment. The design and operation of this thermostat environment emulator are reproducible across different test facilities in order to be standardized as a universal solution to the test thermostat configuration in load-based testing. Two types of thermostat environment emulators were developed and evaluated in this work: 1) an air sampling apparatus, and 2) an independently conditioned apparatus.

For the third objective, the proposed overall methodology was implemented to test and rate a state-of-the-art high efficiency, variable-speed, 2-ton ducted split system, that was installed in a pair of psychrometric test chambers. Furthermore, the sensitivity of load-based testing results to virtual building parameters was investigated. Finally, repeatability results from the load-based testing approach are presented.

For the fourth objective, the investigation of applying load-based testing for performance mapping started with the identification of an appropriate model form for variable-speed air conditioners. Input and output variables were established as extended from the load-based test inputs and outputs but modified for mapping purposes. Both a heuristically optimal experimental design approach and a clustering approach were considered for generating an overall test matrix for performance mapping. A comprehensive evaluation of the mapping model form and the experiment design approaches is presented after analysis of the test results.

For the last objective, the traditional seasonal equipment performance rating approach is presented that uses a temperature-bin method for generating climate-specific ratings. Then a next-generation rating approach is developed and evaluated that incorporates equipment performance map into building simulation to generate seasonal energy performance ratings that are both building-type and climate-zone specific.

1.6 Thesis organization

In chapter 2 of this dissertation, the automated load-based testing methodology is introduced along with the traditional temperature-bin-based seasonal coefficient of performance rating approach, followed by the experimental evaluation and demonstration using a residential 2-ton split cooling system. In chapter 3, a two-node building sensible load model is developed and evaluated as an alternative virtual building structure for utilization in load-based testing. In chapter 4, the effect of thermostat configuration on load-based testing results is investigated followed by the presentation and evaluation of two thermostat environment emulators. In chapter 5, the residential cooling equipment performance mapping methodology is developed and presented along with the next-generation seasonal performance rating approach that utilizes the performance map. Chapter 6 concludes this work and proposes future steps.

2. LOAD-BASED TESTING METHODOLOGY AND EXPERIMENTAL EVALUATION

In this chapter, the automated load-based testing methodology is introduced along with the temperature-bin-based seasonal coefficient of performance rating approach, followed by the experimental evaluation and demonstration for a 2-ton split system. The virtual building model for load-based testing is explained in section 2.1. The automated testing procedures are described in section 2.2. Section 2.3 describes the temperature-bin-based seasonal performance rating approach. The experimental evaluation of the load-based testing methodology and the associated rating approach is discussed in section 2.4.

Figure 2.1 shows a schematic of the load-based methodology test setup and testing approach. In load-based testing, the virtual building model determines the magnitude of the thermal and moisture loads based on an outdoor temperature associated with a test interval and parameters that are chosen to be typical of a residential building and that are scaled to the test equipment design capacity. For each test interval, the outdoor test room conditions are kept constant, while the indoor test room conditions are continuously adjusted to emulate the dynamic response of the virtual building to the test equipment sensible and latent cooling rates that are adjusted using the test equipment thermostat and integrated controls. As a result, the test unit cooling rates must be determined from real-time measurements and provided as inputs to the virtual building model. Then, based on the difference between the test unit cooling rates and building loads, the virtual building temperature and humidity conditions are updated and provided as setpoints to the indoor test room reconditioning system. In this way, the indoor psychrometric test room behaves as a proxy for the response of an actual building. The test unit thermostat, installed in the indoor test room, senses this dynamic temperature and humidity variation, and the test equipment responds

accordingly. In this manner, the test equipment dynamic performance is similar to what would be expected in the field at each outdoor test condition.

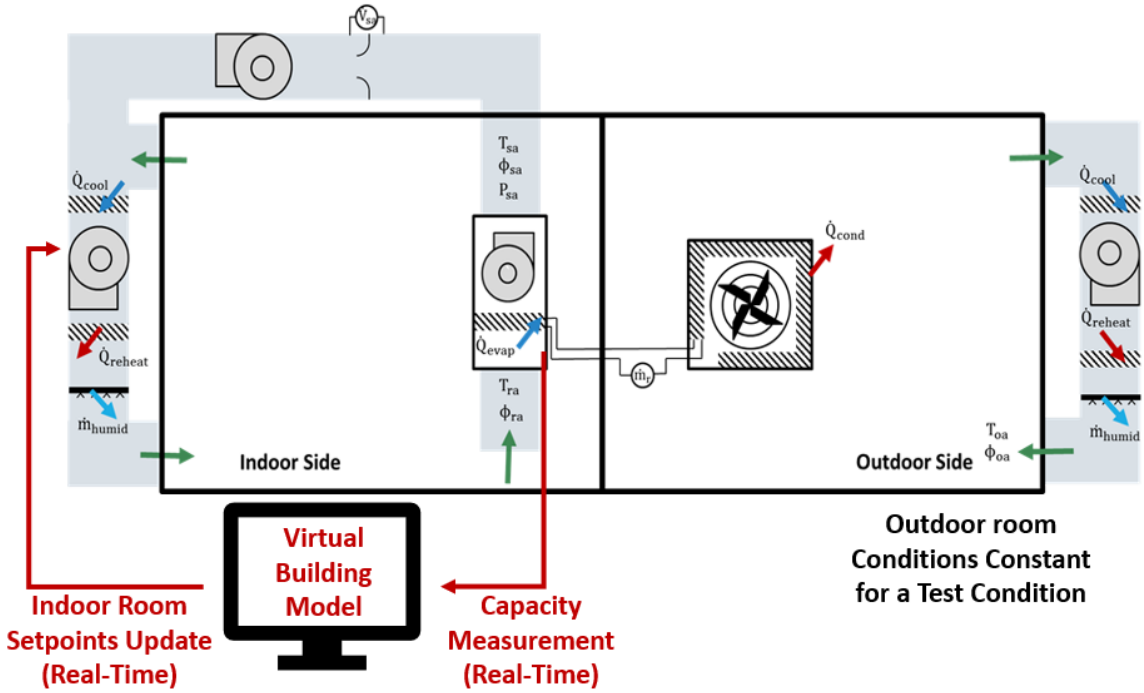

Fig. 2.1. Load-based test apparatus and emulated virtual building

2.1 Virtual building model

A virtual building model for load-based testing needs to reasonably capture dynamic interactions between the test equipment, zone air, and building thermal mass, be relatively easy to implement and scale for different size equipment, and should enable convergence to steady-periodic conditions within a reasonable time frame. High-order models that require many parameters to specify could be difficult to implement and scale and require very long testing times to achieve steady-periodic results that would be reproducible across different test facilities, as can be seen in chapter 3. The approach presented in this chapter is easy to apply and provides representative

dynamic responses for testing equipment with their integrated controls. In addition, the model is specified with parameters that are automatically scaled with rated capacity of the test equipment and that have been tuned to provide dynamic response representative of measurements obtained in the field.

The virtual model assumes simple single-node representations for the internal temperature and humidity responses as originally presented by Patil et al. [8] and Hjortland and Braun [7]. In this model, the dynamics of the internal temperature (T_{ID}) are expressed using a simple sensible energy balance as

$$C_s \frac{dT_{ID}}{dt} = \dot{Q}_{int,s} + UA(T_{OD} - T_{ID}) - \dot{Q}_{c,s} \tag{2.1}$$

where C_s is an effective sensible thermal capacitance that captures the combined effects of the "near surface" building thermal mass, internal air, and thermostat, $\dot{Q}_{int,s}$ represents sensible heat gains associated with any internal (people, lights, equipment) and solar sources, UA is an effective steady-state conductance for heat gain between the outdoor (T_{OD}) and indoor (T_{ID}) temperatures that accounts for envelope conduction and infiltration, and $\dot{Q}_{c,s}$ is the test equipment sensible cooling rate determined from measurements.

The idea behind the simple model of equation (2.1) is that it captures both the steady-state effects of ambient temperature on heat gains and the short-term dynamics associated with equipment and building interactions with feedback control. For a set of building parameters and outdoor temperature, this differential equation can be numerically integrated over a fixed time step to provide updated setpoints to the indoor room conditioning system in response to measured equipment cooling rates. However, in order to scale the steady-state heat gains with equipment size, the model is further simplified by defining an overall building sensible cooling load as

$$BL_{c,s} = \dot{Q}_{int,s} + UA(T_{OD} - T_{ID}) \tag{2.2}$$

For a design indoor temperature and heat gain, the virtual building sensible cooling load is a linear function of outdoor temperature as shown in figure 2.2 and has

a zero-load intercept at an outdoor temperature that is equal to a design balance point temperature ($T_{Bal,D}$). In the load-based testing procedure, the design balance temperature is specified along with the design outdoor temperature ($T_{OD,D}$). The design sensible building cooling load ($BL_{c,s,D}$) associated with ($T_{OD,D}$) is scaled according to the test equipment design sensible cooling capacity ($\dot{Q}_{D,s}$). At the design point outdoor temperature, the sensible building load is assumed to be equal to the equipment design sensible cooling divided by a sizing factor ($BL_{c,s,D} = \dot{Q}_{D,s}/F$). The CSA EXP-07 draft standard assumes a sizing factor (F) of 1.2, meaning that the equipment rated sensible cooling capacity is 20% greater than the sensible building load at the design condition.

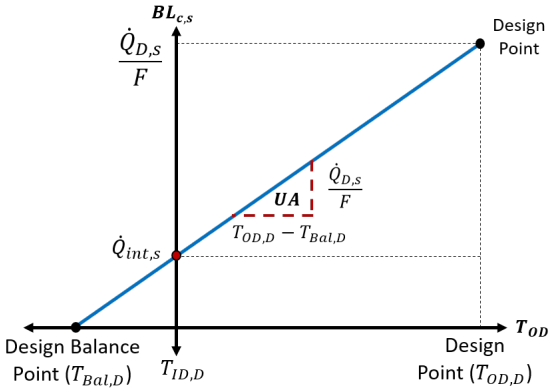

Fig. 2.2. Sensible building cooling load line

In implementing load-based testing, the outdoor room temperature is specified and held constant for each test interval and the indoor room temperature varies near the test unit thermostat setpoint based on dynamic interaction between the test unit controls and the virtual building. The building sensible load at any given time is determined as

$$BL_{c,s} = \frac{1}{F}\frac{\dot{Q}_{D,s}}{T_{OD,D} - T_{Bal,D}}(T_{OD} - T_{Bal}) \tag{2.3}$$

where, T_{Bal} is the balance point temperature corresponding to the current indoor room temperature (T_{ID}) and is determined as

$$T_{Bal} = T_{Bal,D} + (T_{ID} - T_{ID,D}) \tag{2.4}$$

where $T_{ID,D}$ is the indoor temperature setpoint for the test unit thermostat (design value for T_{ID}).

The test equipment design sensible cooling rate that is used to scale the virtual building load is determined from the rated overall cooling capacity ($\dot{Q}_{D,s}$) and an estimate of the sensible heat ratio (SHR) of the equipment as

$$\dot{Q}_{D,s} = SHR \times \dot{Q}_{D,t} \tag{2.5}$$

The rated overall cooling capacity is determined from a full-load equipment test, while the sensible heat ratio is controlled in load-based testing to values that depend on the climate type. The CSA EXP-07 draft standard considers wet-climate testing with $SHR = 0.8$ and dry-climate testing with $SHR = 1.0$.

It is also necessary to determine an appropriate effective building thermal capacitance that provides representative dynamics for residential buildings and that is scaled with the test equipment size. In an actual building, the thermal mass is highly distributed in different building materials and furnishings. Zone air and near-surface thermal mass respond faster to heat transfer inputs compared to the slow responding deep thermal mass of a building. For load-based testing at a given outdoor condition, we are only interested in the "shallow" mass, which is closely coupled to the zone air, in capturing the short-term dynamics associated with equipment and building interactions for feedback control.

In terms of the short-term dynamics, for single-stage or multi-stage residential equipment at part-load condition, integrated controls tend to cycle equipment between different stages to maintain a room indoor condition within the thermostat dead band. Therefore, in order to provide a representative response that is fast enough to realize equipment cycling behavior that is observed in field applications, the virtual building model should have a sensible capacitance that primarily characterizes a combination of the zone air and shallow thermal mass.

Henderson (1989) [29] simulated combined thermostat, air conditioner and building performance in a house and found the maximum cycling rate to be 3.4 cycles per hour. In addition, Henderson (1991) [30] collected field data for 30 air conditioners and their thermostats in Florida and found the maximum cycling rate was 2.5 cycles per hour. Both of these cycling frequencies were based on a thermostat dead band ΔT_{dband} of 1 $^{\circ}F$ which is defined as difference between upper limit and lower limit of room temperature fluctuation. For the purposes of this study, 3 cycles per hour was assumed as a maximum cycling rate to derive capacitance for virtual building model that can be scaled with equipment cooling capacity.

The cycling performance of a single-stage AC/thermostat/building system can be described by equation (2.6). This equation is known as the NEMA thermostat cycling rate curve [31]. N is defined as cycling frequency in units of $1/hr$. X is the cycle duty which is the fraction of on time for each complete on and off cycle. N_{max} is the peak of the curve(maximum cycling rate), which occurs when the cycle duty is 0.5.

$$N = 4N_{max}X(1 - X) \tag{2.6}$$

The maximum cycling rate can also be related to the equipment design sensible capacity, thermostat deadband, and the sensible capacitance for the virtual building model according to equation (2.7).

$$N_{max} = \frac{\dot{Q}_{D,s}}{8C_s * \Delta T_{dband}} \tag{2.7}$$

The maximum cycling rate occurs at a cycle duty of 0.5, which is approximated as a 0.5 part-load ratio. Therefore, a 0.5 cycle duty means that, in half of a complete on and off cycle, the equipment is cooling down the indoor temperature from the upper limit to the lower limit of the dead band by a net cooling rate that is half of equipment sensible capacity. It is also assumed that $N_{max} = 3/hr$, $\Delta T_{dband} = 1^{\circ}F$ and $\dot{Q}_{D,s} = 0.8\dot{Q}_{D,t}$ in determining a sensible capacitance to be used in load-based testing. After plugging in all these assumptions, equation (2.7) can then be reformatted as

equation (2.8) to determine a sensible capacitance that scales with rated total cooling capacity.

$$C_s = k_1 \times \dot{Q}_{D,t} \tag{2.8}$$

where $k_1 = 120 s/^\circ F$ with $\dot{Q}_{D,t}$ having units of Btu/s. The field data for equipment cycling frequency from Henderson [30] included the short-term dynamic interactions of the thermostat, equipment, and building mass in a manner that is consistent with the goal for the virtual building model.

The dynamics of the internal humidity ratio (w_{ID}) are expressed using a simple single-node latent energy balance as

$$C_w h_{fg} \frac{dw_{ID}}{dt} = BL_{c,l} - \dot{Q}_{c,l} \tag{2.9}$$

where C_w is an effective moisture capacitance that is meant to capture the short-term dynamic interactions between the equipment and "shallow" moisture storage within the air and building (carpet, furnishings and other "soft" materials), h_{fg} is the heat of vaporization of water, $BL_{c,l}$ is the virtual building latent load, and $\dot{Q}_{c,l}$ is the test equipment measured latent cooling rate. In this simple model, the moisture capacitance is actually an effective mass of air associated with moisture absorption and desorption and is greater than the mass of air within the conditioned space due to carpet, furnishings, etc.

No representative data could be found for an effective moisture capacitance in residential buildings that characterizes short-term dynamic interactions. Moisture dynamics can be highly variable, depending strongly on the type of interior furnishings and whether carpeting is present. Therefore, a simple approach was taken where the moisture capacitance is estimated as 1.5 times the mass of dry air associated with a typical volume that would be conditioned by the test equipment. A typical equipment sizing rule of thumb of 1 ton of rated total cooling capacity per $700 ft^2$ of floor space was assumed in order to scale the capacitance with the test equipment capacity. For

this scaling, the interior ceiling height is assumed to be 7.5 ft and the density of dry air at standard conditions is used to obtain the relation for moisture capacitance.

$$C_w = k_2 \times \dot{Q}_{D,t} \tag{2.10}$$

where $k_2 = 180 lbm - s/Btu$ with $\dot{Q}_{D,t}$ having units of Btu/s.

2.2 Automated load-based testing procedures

To test and rate residential cooling equipment using the proposed load-based testing methodology, CSA EXP-07 defines a set of dry-coil and wet-coil cooling tests at different conditions that generate data used in evaluating seasonal performance. This section presents testing procedures that can be fully automated to generate the necessary data, whereas the next section presents the seasonal performance determination.

Implementation of the virtual building model for load-based testing requires specification of 6 parameters to define the building sensible and latent load lines ($T_{OD,D}$, $T_{ID,D}$, $T_{Bal,D}$, $\dot{Q}_{D,t}$, F, SHR) and 2 parameters that define the dynamics of the internal temperature and humidity (C_s, C_w). Table 2.1 summarizes the values or approaches used to determine the values of these 8 parameters. CSA EXP-07 specifies test intervals for dry-coil and wet-coil tests in terms of the outdoor dry-bulb temperatures shown in table 2.2. The outdoor conditions are the same, except the dry-coil sequence includes a $113°F$ desert condition.

The automated testing sequence begins at the lowest outdoor temperature. At each test interval, the outdoor temperature is used as a setpoint for the outdoor chamber conditioning system and as an input to the building load model. The temperature of the indoor room is indirectly controlled by the test equipment thermostat with its setpoint adjusted to the indoor design temperature ($T_{ID,D}$) specified in table 2.1. The indoor room reacts as if it were controlled by test equipment thermostat. This is accomplished by updating the room temperature setpoint for the indoor test

Table 2.1.
Summary of Virtual Building Model Parameters for Load-Based Testing

Parameter	Value or Approach	Comments
$T_{OD,D}$	Dry-coil tests: $105°F$ Wet-coil test: $95°F$	The higher design outdoor air temperature for the dry coil tests is meant to handle hot-dry climates.
$T_{ID,D}$	Dry-coil tests: $79°F$ Wet-coil test: $74°F$	The design indoor temperature is also used as the setpoint for the test equipment thermostat. A higher setpoint is assumed for a drier climate.
$T_{Bal,D}$	Dry-coil tests: $72°F$ Wet-coil test: $67°F$	The design balance point is $7°F$ lower than the design indoor temperature due to typical internal and solar gains.
$\dot{Q}_{D,t}$	Determined from AHRI 210/240 A2 test	This is a one-time test determined prior to load-based testing. Units of Btu/s are consistent with units for C_s and C_w.
F	1.2	This denotes that the sensible capacity of the equipment is 20% greater than the sensible building load at the design outdoor temperature.
SHR	Dry-coil tests: 1.0 Wet-coil tests: 0.8	For dry-coil tests, this forces the latent load to be zero and the equipment design sensible cooling capacity to match the total rated cooling capacity.
C_s	$C_s = k_1 \dot{Q}_{D,t}$	$k_1 = 120 s/°F$
C_w	$C_s = k_2 \dot{Q}_{D,t}$	$k_2 = 180 lbm - s/Btu$

Table 2.2.
Outdoor dry-bulb temperature $T_{OD,j}$ of the j^{th} cooling test interval

	j=1	j=2	j=3	j=4	j=5
Wet-coil test	$77°F$	$86°F$	$95°F$	$104°F$	N/A
Dry-coil test	$77°F$	$86°F$	$95°F$	$104°F$	$113°F$

room reconditioning system at short time intervals according to a discretized version of the dynamic sensible virtual building model.

$$T_{ID,sp}(t + \Delta t) = T_{ID,sp}(t) + \Delta t \frac{BL_{c,s}(T_{OD,j}) - \dot{Q}_{c,s}(t)}{C_s} \tag{2.11}$$

where Δt is the time step for updating the setpoints during the load-based tests. The test equipment sensible cooling rate, $\dot{Q}_{c,s}$, is determined from real-time measurements of air flow rate and temperature differences across the cooling coil as documented in CSA EXP-07. Both the data sampling and setpoint updating timesteps should be no greater than 5 seconds to avoid large changes in the room setpoints that could result in poor psychrometric chamber control. The building sensible cooling load $BL_{c,s}(T_{OD,j})$ is updated in real-time based on the current indoor room temperature setpoint $T_{ID,sp}(t)$, using the following equation.

$$BL_{c,s}(T_{OD,j}) = \frac{1}{F} \times \frac{SHR * \dot{Q}_{D,t}}{T_{OD,D} - T_{Bal,D}}(T_{OD,j} - T_{Bal}(t)) \tag{2.12}$$

where

$$T_{Bal}(t) = T_{Bal,D} + (T_{ID,sp}(t) - T_{ID,D}) \tag{2.13}$$

The design total cooling capacity $\dot{Q}_{D,t}$, is the measured capacity determined using the AHRI 210/240 A2 test condition, as reported by the equipment manufacturer.

For wet-coil tests, it is also necessary to control the indoor humidity in a manner that emulates the virtual building and its interactions with the test equipment. At

each updating interval, a setpoint for the indoor humidity ratio is updated using a discretized version of the dynamic latent energy balance.

$$w_{ID,sp}(t+\Delta t) = w_{ID,sp}(t) + \Delta t \frac{BL_{c,s}(T_{OD,j})(\frac{1}{SHR}-1) - \dot{Q}_{c,l}(t)}{h_{fg}C_w} \tag{2.14}$$

The test equipment latent cooling rate, $\dot{Q}_{c,l}$, is determined from real-time measurements of air flow rate, inlet humidity, and outlet humidity as described in CSA EXP-07. For dry-coil tests, SHR=1 and there is no latent load. This can be implemented by setting an indoor room humidity setpoint with a dewpoint that is below the expected lowest surface temperature of the test equipment evaporator. Alternatively, application of Equation (2.14) will converge to an indoor humidity where the indoor coil is dry for SHR=1.

According to CSA EXP-07, the temperature and humidity sensors for feedback control of the indoor room and the test equipment thermostat should be located in the inlet to the return air for the test unit. This is meant to ensure reproducible dynamic interactions and performance across different test facilities. The downside is that the thermostat dynamics are faster than what would be expected in the field. To address this issue, a separate thermostat environment emulator was developed and presented in chapter 4 in this work that provides conditions that are representative of residential installations. For the following sample load-based tests, the test thermostat was enclosed within the thermostat emulator and the thermostat inlet temperature was almost perfectly controlled to the virtual room temperature setpoints. The humidity sensor for feedback control of the indoor humidity ratio was located at the inlet duct to the test equipment.

The goal of load-based testing is to determine average equipment coefficient of performance for each outdoor temperature ($COP(T_{OD,j})$), as a ratio of average equipment air-side total capacity over average power consumption) that can be used as input for the seasonal performance rating described in the next section. The auto-

mated load-based cooling test procedure for both the dry-coil and the wet-coil tests is detailed in the following steps and in the flow chart of figure 2.3.

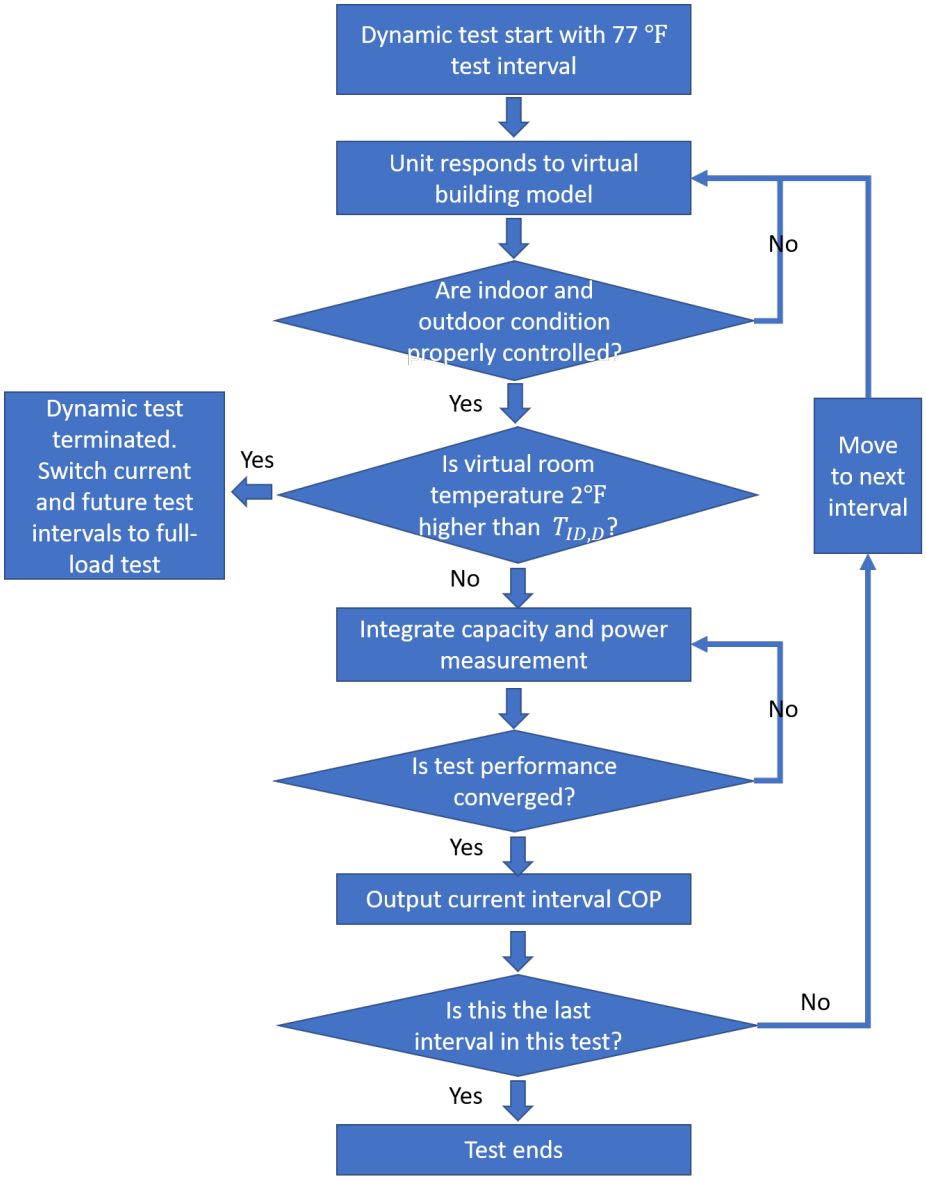

Fig. 2.3. Flow chart of cooling test procedure

1. Initializations: The initial setpoint temperatures for the environmental chambers are set as $77°F$ for the outdoor room and the test equipment target setpoint for dry or wet-coil testing as specified in table 2.1. After the rooms are close to the desired

temperatures, the test unit is turned on with a test thermostat setpoint corresponding to the target value for dry or wet-coil testing (table 2.1). The virtual building sensible model is initialized with $T_{ID,sp}(0)$ set equal to the test unit thermostat setpoint. For dry-coil tests, the virtual building latent model can be initialized with a value of $w_{ID,sp}(0)$ corresponding to a low relative humidity (e.g., 20%) at the thermostat setpoint temperature. For wet-coil tests, $w_{ID,sp}(0)$ should be initialized to a value associated with a representative relative humidity (e.g., 45%) at the thermostat setpoint temperature.

2. Dynamic Updating for Load-Based Testing: The indoor temperature and humidity setpoints for the environmental reconditioning system are updated at regular short intervals using Equations (2.11) and (2.14). Both indoor and outdoor room measurements must track (be controlled to) the setpoints ($T_{OD,j}$, $T_{ID,sp}$ and $w_{ID,sp}$) within specified tolerances in order to initiate data processing of test equipment performance.

3. Full-Load Testing Evaluation and Execution: If the test equipment maximum sensible cooling capacity is not sufficient to meet the sensible building load, then the indoor room temperature setpoint will rise above the test unit thermostat setpoint. In order to evaluate this condition, the average virtual building temperature setpoint ($T_{ID,sp}$) for a moving sampling window of 20 min is compared with the test unit thermostat setpoint ($T_{ID,D}$) and if the difference is greater than $2°F$, then it is assumed that the unit does not have sufficient capacity for the current test interval. At this point, load-based testing is abandoned and full-load testing is implemented for the current and subsequent test intervals at higher outdoor temperatures. For full-load testing, the sensible virtual building model is deactivated, the test equipment return air temperature is controlled to the indoor design temperature ($T_{ID,D}$), and the equipment thermostat setpoint is set to its lowest possible value to ensure that the equipment will be fully loaded. The latent building model is still utilized for updating the indoor humidity according to the prescribed SHR value. However, the measured

sensible capacity of the equipment is used in place of the sensible building load in equation (2.14). At each test interval under full-load testing, test convergence and COP determination are carried out as described in step 4 for variable-speed operation.

4. Load-Based Testing Convergence Evaluation: Data processing for convergence evaluation at a given load-based test interval involves evaluating an overall COP determined from integration over a moving window. If the test equipment is cycling on and off in a test interval, an integrated COP for each on/off cycle is determined as the ratio of the total cooling delivered to the total unit electrical consumption over the on/off cycle. Convergence is achieved when the difference between the COP for successive on/off cycles is less than a specified convergence tolerance (e.g. 1%). If the test equipment is running continuously in variable-speed mode, then the integrated COPs for two neighboring moving 20-minute sampling windows are compared until the difference is less than the convergence tolerance (1%). For both cycling and variable-speed modes, there should be a testing time limit for each test interval to handle situations where convergence criteria cannot be achieved. For an unconverged test interval, the integrated COP should be based on all of the measurement samples obtained after the criteria for the virtual room setpoint control errors are satisfied and data processing begins.

5. Test Termination and Outputs: For load-based testing, steps 2 to 4 are repeated until all of the test intervals for outdoor temperature in table 2.2 are considered. If the test unit doesn't have sufficient capacity to maintain the indoor temperature at the thermostat setpoint, then the full-load testing procedure under step 3 is applied for the remainder of the test intervals The primary outputs from the testing are converged COP values for each of the test intervals.

2.3 Seasonal performance rating

The converged values of COP for the test intervals are used in calculating a seasonal coefficient of performance using a temperature-bin-based approach as outlined in CSA EXP-07 and given by

$$SCOP_c = \frac{\sum_{k=1}^{m}(DCR(T_k) \times n_k)}{\sum_{k=1}^{m}(\frac{DCR(T_k)}{COP(T_k)} \times n_k)} \tag{2.15}$$

where m is the number of temperature bins for the cooling climate zone, $DCR(T_k)$ is a sensible building load for the k^{th} temperature bin, n_k is the number of hours in the k^{th} temperature bin during the cooling season and $COP(T_k)$ is the COP for the k^{th} temperature bin estimated by interpolation using the test outputs ($COP(T_{OD,j})$). Thus, the seasonal cooling coefficient of performance ($SCOP_c$) is the ratio of a total cooling load to a total electrical usage over the cooling season. This performance index does not include stand-by power associated with times that the cooling equipment is not operating. However, the CSA EXP-07 also presents an approach for calculating SCOP that includes non-active-mode power consumption, which is useful in climate zones where equipment has a lot of standby hours.

Table 2.3.
Load-based tests used for climate zones in seasonal performance ratings for cooling

	Very cold	Cold/dry	Cold/humid	Marine
Cooling test	Wet-coil test	Dry-coil test	Wet-coil test	Dry-coil test
	Mixed	Hot/humid	Hot/dry	
Cooling test	Wet-coil test	Wet-coil test	Dry-coil test	

The sensible load line of equation (2.12) evaluated at the design indoor temperature is used along with bin data for outdoor temperature to determine $DCR(T_k)$. Temperature bin data for each climate zone can be found in CSA EXP-07 [10]. The climate zones and load-based test results used for cooling performance ratings in

North America are summarized in table 2.3. For example, ratings of cooling performance for very cold, cold/dry, and hot/dry climates use results from dry-coil cooling tests.

2.4 Experimental evaluation of load-based testing

This section presents results from applying the load-based testing and rating methodology to a state-of-the-art high-efficiency residential heat pump. In addition, the sensitivity of the results to building load sizing parameters is evaluated. Repeatability results associated with testing on three different days are presented. Last but not the least, impact of uncontrolled residual capacity of the test equipment when it cycles off is discussed along with a possible solution.

2.4.1 Test setup

An experiment was set up to test a 2-ton variable-speed ducted split direct-expansion heat pump operating in cooling mode. The manufacturer's rated characteristics are tabulated in table 2.4. Indoor and outdoor units for this equipment were installed in adjacent psychrometric chambers to simulate indoor and outdoor conditions. The system was charged with 13 lb 12 oz of refrigerant R410A with 35 ft of piping separating the indoor and outdoor units.

Table 2.4.
Test equipment rating characteristics

Cooling capacity @95 $^{\circ}F$	25200 Btu/hr
EER cooling Rating	16
SEER Rating	20.5
Heating capacity @47 $^{\circ}F$	23600 Btu/hr
Region IV HSPF Rating	13
Heating capacity @17 $^{\circ}F$	24800 Btu/hr

Refrigerant-side measurements

Refrigerant-side measurement locations are shown in figure 2.4. T represents a T-type immersion thermocouple and P represents a pressure transducer. In the refrigerant circuit of the test heat pump, temperatures and pressures at six locations are measured, including indoor unit inlet and outlet, outdoor unit inlet and outlet, compressor suction and discharge. Refrigerant pressure is measured using 500 psi full scale range Honeywell PX2 sensors.

Refrigerant flow rate is measured using a Micro-Motion R025 Coriolis mass flow meter. The configuration with subcooled liquid flow maintains the accuracy of the measurement and reduces the pressure drop and its impact on system performance.

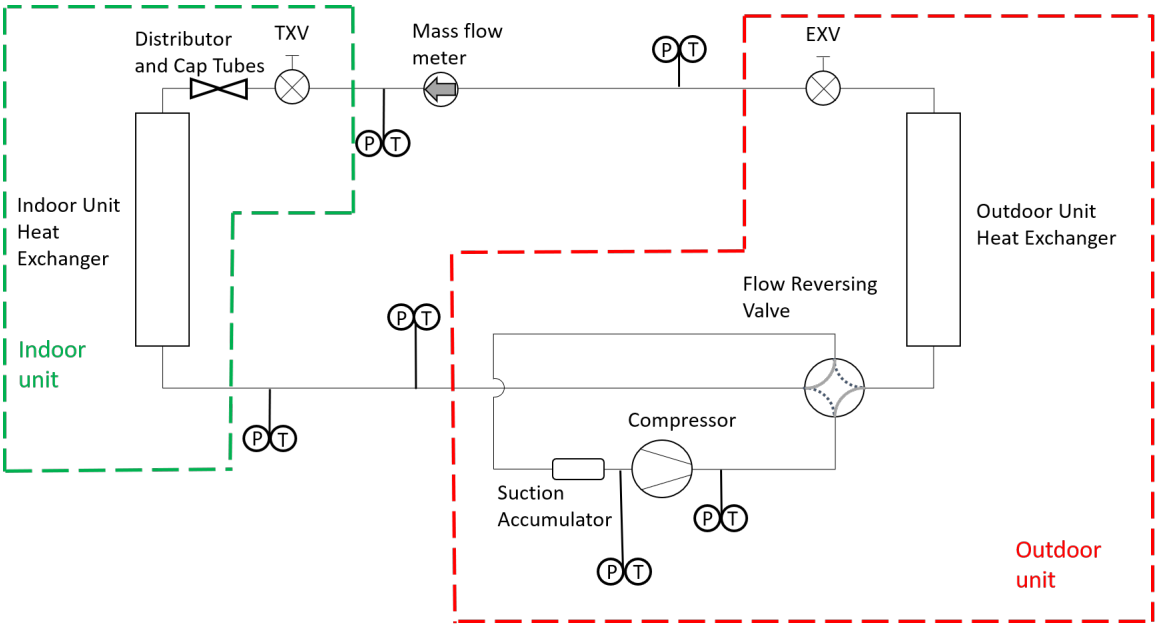

Fig. 2.4. Refrierant-side measurement locations

Equipment refrigerant-side capacity is calculated as the product of refrigerant mass flow rate and enthalpy difference between indoor unit inlet and outlet. Capacity measurement is accurate when single-phase refrigerant mass flow is measured, and the enthalpy calculation is valid. When the indoor unit inlet or outlet has its refrigerant in

a two-phase region, enthalpy cannot be characterized by measurement of temperature and pressure only. For example, in cooling mode, when outdoor ambient and building load are is low, two-phase refrigerant will often flow through the mass flow meter. Determination of refrigerant-side capacity in cooling mode is shown in equation (2.16).

$$\dot{Q}_{ref} = \dot{m}_{ref}(h_{ref,out} - h_{ref,in}) \tag{2.16}$$

Outdoor unit consumed power is measured by a OSI PC5-059C AC watt transducer and indoor unit power is measured by a OSI PC5-002C transducer. The sum of the indoor and outdoor unit real-time measurements of consumed power is the total equipment power that is used in evaluating performance.

Air-side measurements

In order to acquire air-side capacity, indoor unit return air and supply air enthalpies are needed along with air flow rate. In order to determine air enthalpy, drybulb temperature, dewpoint temperature and air pressure are measured.

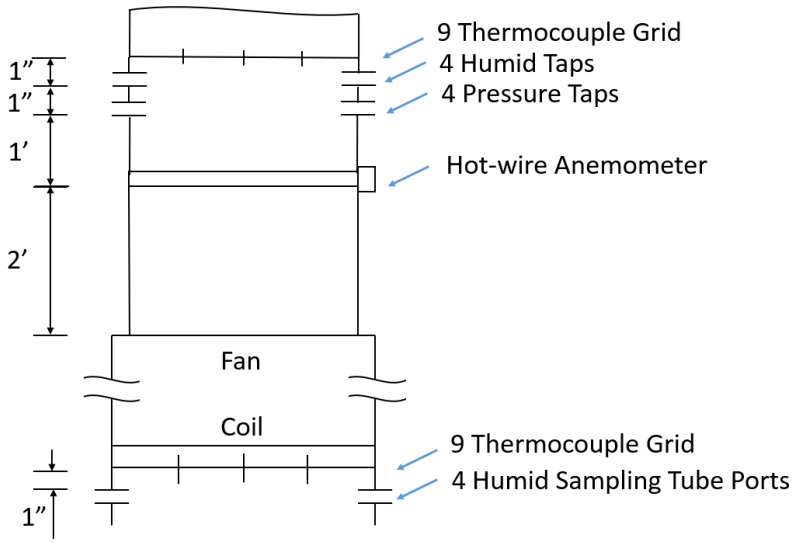

Fig. 2.5. Air-side measurement locations: Indoor unit

The average value of a 9 T-type thermocouples grid is used to represent indoor unit inlet air dry-bulb temperature. Both indoor unit and outdoor unit air inlet pressure is considered as atmospheric pressure and are measured using a barometer. Four ports with plastic tubes sample humid air at the indoor unit inlets and outlets. These tubes are connected to General Eastern (GE) D-2 chilled mirror sensors that measure dew point temperature. Measurements for supply air are taken 3-ft above the discharge of indoor fan in the duct and so are the grid of 9 thermocouples, 4 pressure tabs and 4 humid air tabs. Gauge pressure of the supply air is measured using a SETRA 260 sensor (0.5 inH2O full scale range). An array of Ebtron GP1 Type-A hot wire anemometer (2 probes with a total of 4 velocity sampling holes) are used to measure the air flow rate 2' above the discharge of the indoor fan in the supply air duct.

Air-side total capacity is calculated as the product of air flow rate and enthalpy difference between indoor unit return air and supply air, shown by equation (2.17). Air-side sensible capacity is calculated as the product of air flow rate, constant pressure specific heat and temperature difference between indoor unit return air and supply air, shown by equation (2.18). The constant pressure specific heat is represented as an average value for the return air and supply air. Latent capacity is shown in equation (2.19).

$$\dot{Q}_{c,t} = \dot{m}_{air}(h_{air,in} - h_{air,out}) \tag{2.17}$$

$$\dot{Q}_{c,s} = \dot{m}_{air}\frac{Cp_{in} + Cp_{out}}{2}(T_{air,in} - T_{air,out}) \tag{2.18}$$

$$\dot{Q}_{c,l} = \dot{Q}_{c,t} - \dot{Q}_{c,s} \tag{2.19}$$

In load-based testing, the measured indoor unit return air dry-bulb temperature and humidity level were used as inputs to controller the psychrometric chamber reconditioning system. The controller attempts to control these conditions to track

variable setpoints that are outputs from the virtual building model. In figure 2.6, the inlet air dry-bulb temperature of the outdoor unit is also measured and controlled to the setpoints specified in each test interval. The specified accuracy of each sensor and a description of its use are summarized in table 2.5.

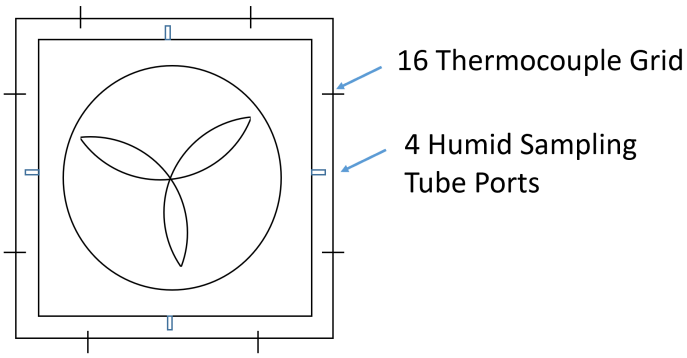

Fig. 2.6. Air-side measurement locations: Outdoor unit

Table 2.5.
Sensor accuracy

Sensor	Accuracy
T-type thermocouple	0.9F
Chilled mirror dewpoint sensor	0.5F
Hot-wire anemometer	3%
Air pressure sensor	1% F.S.
Refrigerant pressure sensor	0.25%
Coriolis mass flow meter	0.50%
Outdoor unit power meter	0.5% F.S.
Indoor unit power meter	5W

As a first step for application of load-based testing, an AHRI 210/240 [2] A2 steady-state test was conducted and the test results are presented in table 2.6. The air-side total capacity only differs from the refrigerant-side capacity by 2%, which is

smaller than the 6% maximum discrepancy allowed by AHRI 210/240. Therefore, $\dot{Q}_{D,t} = 9639W$ was utilized for load-based testing in determining the load line.

Table 2.6.
AHRI 210/240 A2 steady-state test

Indoor dry-bulb temperature	Indoor wet-bulb temperature	Outdoor dry-bulb temperature	
$80°F$	$67°F$	$95°F$	
Air-side total capacity	Refrigerant -side capacity	Total Power	Air flowrate
9639W	9487W	1576W	1010 cfm

2.4.2 Load-based testing and rating results

Results of a dry-coil cooling automated test sequence for all of the outdoor conditions are shown in figure 2.7, including the sensible cooling rate of the equipment (green line), sensible building load (red line), and total unit power (blue line). This test, consisting of a sweep of 5 test intervals, was a fully automated implementation of the load-based testing procedures. The test equipment cycled on/off at the 1^{st} and 2nd test intervals where the sensible building load was smaller than the minimum sensible cooling rate of the test equipment, while at the 3^{rd} and 4^{th} test intervals, the equipment tried to modulate its compressor and indoor fan speed to match its cooling rate to the building load. Unlike steady-state tests, dynamic behaviors of the equipment, such as cycling and speed modulations can be observed here, as the equipment and its integrated controls respond in a realistic way to the imposed building loads.

Temperatures in the dry-coil test are shown in figure 2.8, where the red line indicates outdoor temperature, the green line indicates indoor temperature (indoor unit return air temperature) and the blue line indicates the virtual room temperature setpoints that are updated using the virtual building model. The different outdoor

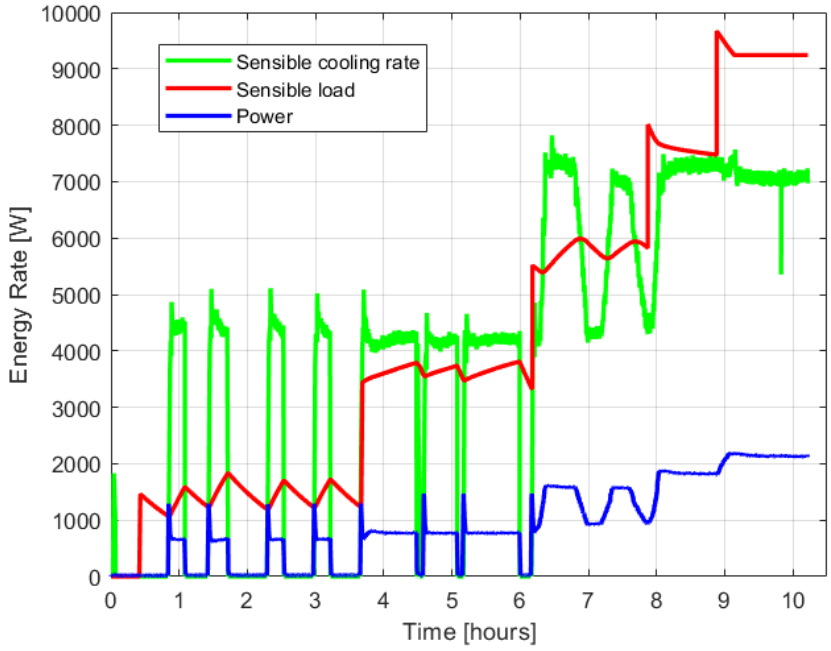

Fig. 2.7. Sensible cooling rate, sensible load, and power measured in dry-coil load-based testing

temperatures in the figure echo the 5 test intervals that correspond to the building loads of figure 2.7. The temperature of the indoor psychrometric chamber tracks the virtual room temperature setpoints well. The fluctuation in the virtual room temperature is due to the test unit controller's behavior, and was maintained between roughly $77°F$ to $80°F$ during the first four test intervals, as the test equipment thermostat setpoint was $79°F$. When the outdoor temperature shifted to $113°F$ in the 5^{th} test interval, the moving averaged virtual room temperature became higher than $81°F$, which marked the termination of the dynamic tests, and the activation of a full-load test for the 5^{th} test interval, since the test equipment did not have enough capacity to meet the virtual building load. For the full-load test, the return air temperature was controlled to a constant setpoint of $79°F$ instead of a dynamic virtual room temperature, since the sensible virtual building model was deactivated.

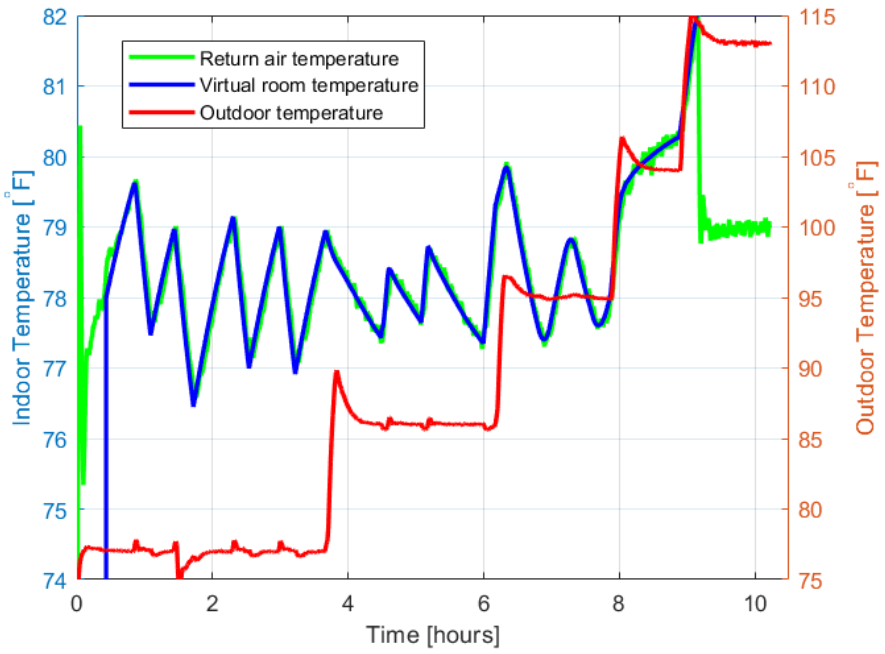

Fig. 2.8. Temperatures in dry-coil load-based test testing

Summary results for each test interval of this dry-coil test are presented in table 2.7. COP decreases with increased outdoor temperature and larger building load. The 1^{st} test interval converged as the last two cycling patterns were identical to each other in figure 2.7. In the 2^{nd} test interval, the test equipment cycled on/off with a larger duty cycle compared to the 1^{st} interval, due to the increased sensible load. The difference of the COPs between the last two cycles in the 2^{nd} test interval was less than 1%. Although the equipment sensible cooling rate fluctuated significantly during the 3^{rd} test interval and did not closely track the sensible building load, the moving averaged COP converged. In the 4^{th} test interval, the equipment was able to track the load and the test converged to a nearly steady state condition.

Figure 2.9 presents sensible cooling rate, sensible building load and power results for a wet-coil test using the same legend as employed for figure 2.7. Four test intervals can be observed. In the 1^{st} interval, the test equipment cycled on/off while in the 2^{nd} and 3^{rd} intervals, the equipment was able to operate in variable-speed mode. Figure

Table 2.7.
Results for dry-coil test

T_j	$77°F$	$86°F$	$95°F$	$104°F$	$113°F$
Behavior	Cycling	Cycling	Variable -speed	Variable -speed	Out of capacity
$COP(T_j)$	5.593	5.334	4.563	4.015	3.328
Uncertainty	± 0.398	± 0.364	± 0.286	± 0.265	± 0.227
Test duration	3.6hrs	2.6 hrs	1.6 hrs	1.0 hrs	1.4 hrs
Cycle period	0.7 hrs	0.9 hrs	-	-	-

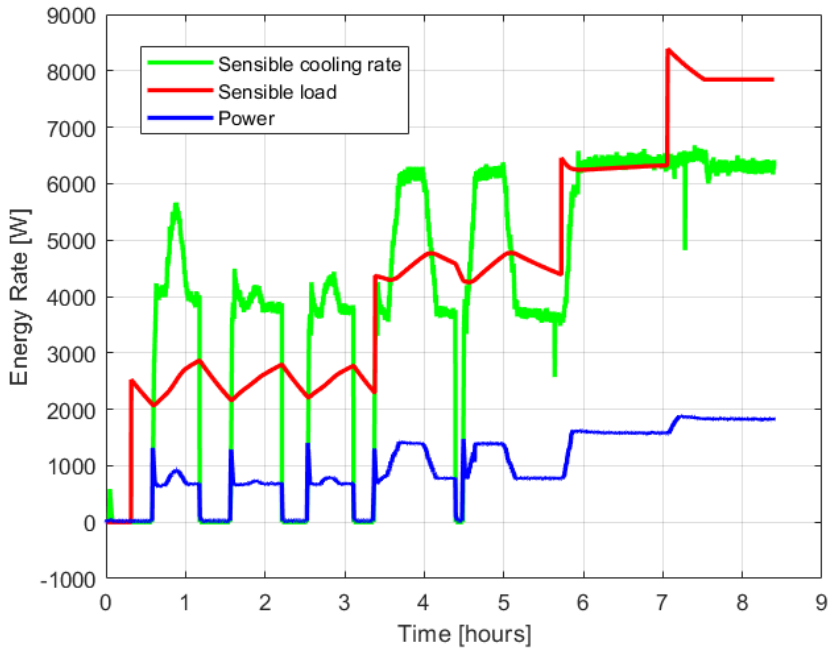

Fig. 2.9. Sensible cooling rate, sensible load, and power measured in wet-coil load-based testing

2.10 shows temperature variations during the wet-coil test using the same legend as figure 2.8. The indoor return temperature was maintained by the test equipment roughly between $72°F$ and $75°F$ during the first three test intervals. In the 4^{th} test

interval, the equipment could not maintain the indoor temperature and a full-load test was performed.

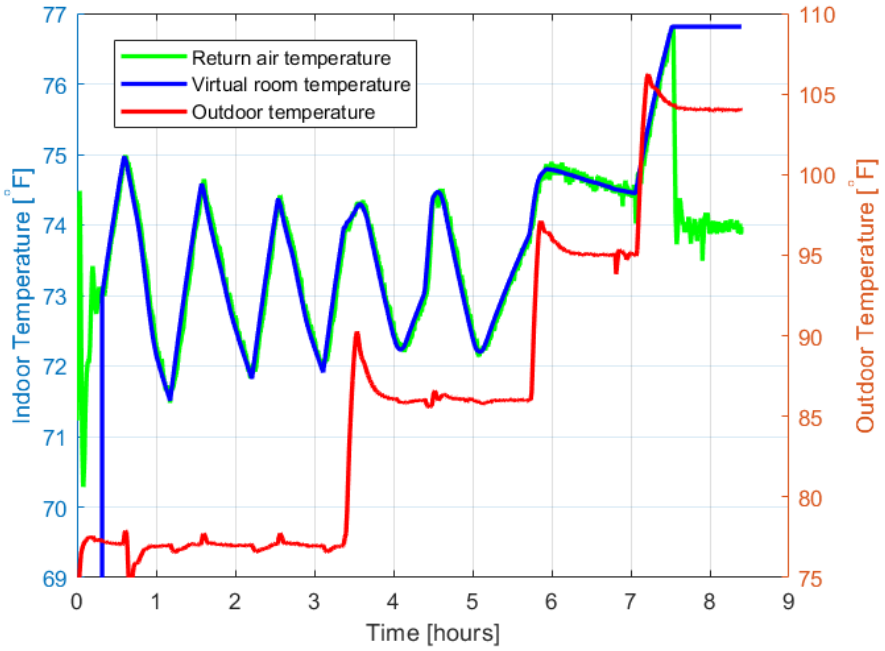

Fig. 2.10. Temperatures in wet-coil load-based testing

Figure 2.11 presents additional results for this wet-coil test including real-time measurements of the test equipment latent capacity (green line), indoor return air relative humidity (magenta line), and total power consumption (blue line) along with virtual building model dynamic outputs of latent building load (red line) and virtual room relative humidity setpoints (cyan line). The latent building load was calculated using the real-time sensible building load associated with a prescribed sensible heat ratio of 0.8 in the wet-coil test. In the 1^{st} test interval, as the equipment turned on its indoor fan in each cycle, negative latent capacity was observed, since the condensate on the indoor coil re-evaporated to add moisture to the room. Indoor relative humidity was maintained between 47% and 52% during this test, and its return air relative humidity was well controlled to the virtual building relative humidity setpoints adjusted based on the virtual building model outputs. In the 4^{th} test interval,

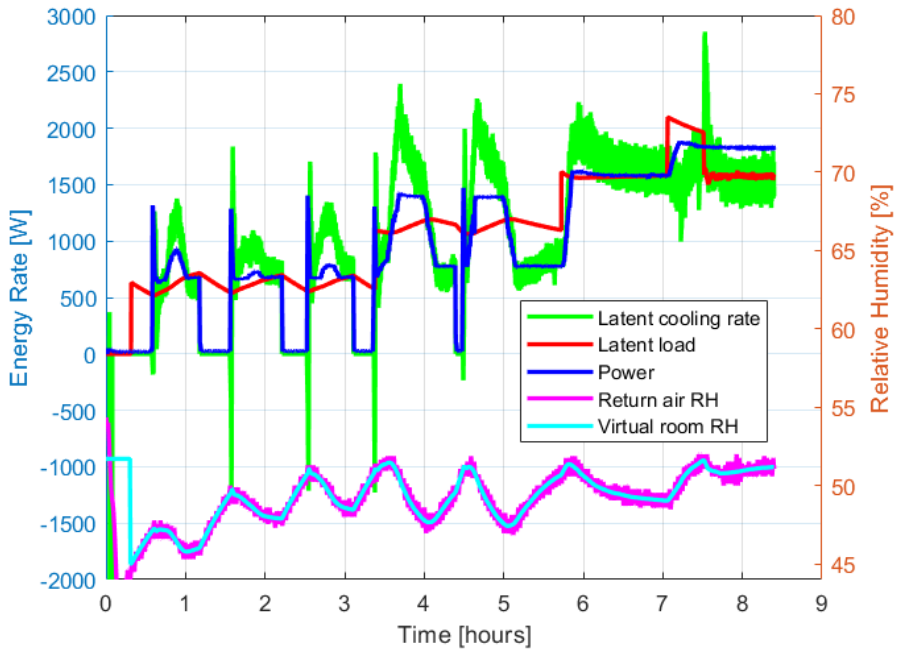

Fig. 2.11. Latent results in wet-coil load-based testing

although the equipment did not have sufficient sensible capacity to meet the sensible load and a full-load test was activated, the latent virtual building was still active. In dynamically updating the return air humidity setpoint using Equation (2.14), the latent load was updated according to a real-time measurement of equipment sensible cooling rate and a sensible heat ratio of 0.8. Summary results for each test interval of this wet-coil test are presented in table 2.8. All four test intervals converged successfully. The 3^{rd} interval converged with variable-speed behavior of the equipment after one on/off cycle.

Overall COP test results for both the dry-coil and wet-coil test intervals are shown in figure 2.12. The green line represents the dry-coil test, while the blue line represents the wet-coil test. For each test interval, the wet-coil COP is observed to be higher than the dry-coil COP with the same outdoor temperature, due to a higher evaporating temperature and the additional latent cooling associated with the wet-coil test. A 0.5K thermocouple uncertainty in return and supply air measurement is the most

Table 2.8.
Results for wet-coil test

T_j	$77°F$	$86°F$	$95°F$	$104°F$
Behavior	Cycling	Variable -speed	Variable -speed	Out of capacity
$COP(T_j)$	6.420	5.745	5.069	4.294
Uncertainty	±0.465	±0.424	±0.349	±0.308
Test duration	3.3 hrs	2.3 hrs	1.4 hrs	1.3 hrs
Cycle period	0.9 hrs	-	-	-

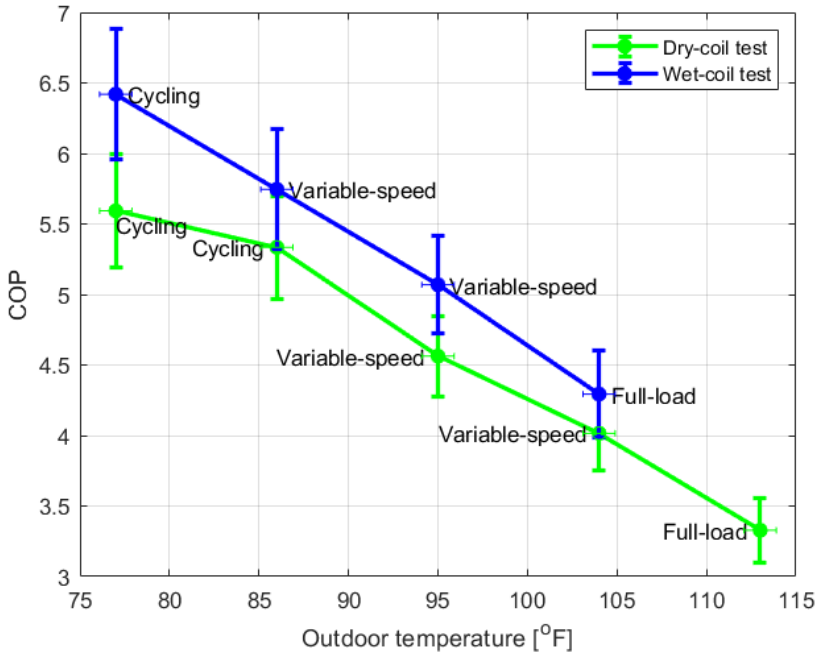

Fig. 2.12. COPs for cooling test intervals

significant source of measurement uncertainty, especially for low-load test intervals. For test intervals with higher loads, air-side enthalpy difference across the indoor unit becomes larger, and therefore the measurement errors of the moist air contribute less to the overall COP uncertainty. For each test interval, the wet-coil test has a larger

COP uncertainty compared to the dry-coil test, due to additional measurement errors of the moist air dewpoints.

The dry and wet-coil test results for COP at different outdoor temperatures were used to calculate seasonal coefficients of performance for the 7 climate zones listed in table 2.3. The results are presented in table 2.9. Not surprisingly, seasonal COPs are lower in the climate zones where the dry-coil test results were employed. The hot/dry climate has the lowest performance. For the same outdoor temperature, this test unit performs significantly better when removing moisture. For the climate zones where wet-coil tests were utilized, the differences in seasonal performance are small. Compared to dry climates, wet climates have larger uncertainties in their seasonal coefficients of performance since these coefficients were obtained using wet-coil test COPs that have larger uncertainties. CSA EXP07 [10] requires that $SCOP_c$ be reported with resolution of 0.05 that is smaller than the measurement uncertainties calculated here, and therefore sensors need to be carefully selected and instrumented in order to obtain accurate seasonal performance ratings of test equipment.

Table 2.9.
Seasonal coefficients of performance for cooling

Climate zone	Very cold	Cold/dry	Cold/humid	Marine
$SCOP_c$	5.83	5.02	5.81	4.92
Uncertainty	±0.25	±0.18	±0.24	±0.17
Climate zone	Mixed	Hot/humid	Hot/dry	
$SCOP_c$	5.77	5.86	4.78	
Uncertainty	±0.23	±0.25	±0.15	

2.4.3 Evaluation of sensitivity to building load parameters

The part-load performance of the equipment depends on its cooling capacity in relation to the load. In load-based testing, this is controlled by a sensible load sizing

factor, F. As F increases, the equipment will operate more of the time at lower speeds and off cycles. In evaluating new control strategies or equipment designs, it useful to understand how changes in the sizing factor affect overall performance.

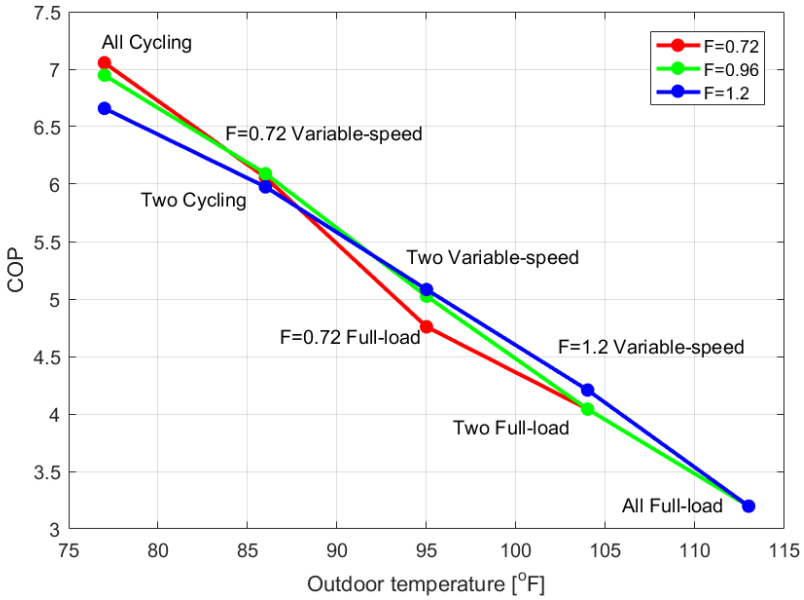

Fig. 2.13. COPs for dry-coil test intervals with different sizing factor F

Figure 2.13 shows dry-coil load-based test results for sizing factors (F) of 0.72, 0.96, and 1.2 where COP is plotted as a function of outdoor temperature. The goal was to demonstrate how load-based testing captures the effects of sizing on performance. At the lowest outdoor temperature of $77°F$, the building load is low and all three of the sizing factors led to on/off cycling behavior. However, the performance associated with the largest sizing factor is considerably lower. As the part-load ratio decreases with increasing sizing factor, the equipment is off more of the time (low duty cycle) and there is greater relative performance penalty associated with cycling the equipment on. For the outdoor temperature of $86°F$, the equipment operated in variable-speed mode for the smallest sizing factor of 0.72 and in on/off cycling mode for the other 2 cases. However, all three cases had a similar efficiency since the duty cycle was relatively high for the cycling behaviors with a relatively low cyclic

degradation. At the outdoor temperature of $95°F$, the equipment ran out of cooling capacity for the F=0.72 test and therefore full-load testing was performed, while the larger sizing factors resulted in variable-speed operation under load-based testing. At this condition, variable-speed performance was considerably better than full-load performance. At the outdoor temperature of $104°F$, the equipment operated at full load for the two smaller sizing factors and both cases had the same performance that was lower than that for the largest sizing factor. All 3 sizing factors resulted in full-load operation at $113°F$ yielding the same overall performance. Uncertainty for each COP is not shown in figure 2.13, but these variations will be used to generate uncertainties for seasonal coefficient of performance in table 2.10.

Table 2.10 summarizes the seasonal coefficient of performance ($SCOP_c$) for three dry climate zones with the three different sizing factors. For the range of sizing factors considered, $SCOP_c$ decreases significantly with decreasing sizing factor (i.e. undersized equipment) for all climate zones due to performance degradation associated with greater full-load operation. Increasing the sizing factor above 1.2 should also ultimately decrease performance due to increasing on/cycling losses.

Table 2.10.
$SCOP_c$ for dry climate zones with different F values

F	Cold/dry	Marine	Hot/dry
0.72	5.44±0.20	5.30±0.19	5.12±0.17
0.96	5.76±0.23	5.60±0.21	5.34±0.19
1.2	5.95±0.24	5.78±0.22	5.52±0.19

Equipment performance also depends on the latent load in relation to the total load. In load-based testing, this is controlled by the building sensible heat ratio, SHR. As SHR decreases for a given outdoor temperature (i.e., fixed sensible load), increasing moisture condensation on the evaporator coil leads to both a higher total cooling rate and higher evaporating temperature. This generally leads to an increase

in COP of the equipment. This effect is seen in the results of figure 2.14 for wet-coil load-based tests performed for two different values of SHR with F=1.3. In addition to the significantly higher COP for the lower SHR of 0.75, the test equipment runs out of capacity at a lower outdoor temperature than for SHR=0.95 ($95°F$ versus $104°F$). Table 2.11 shows the effect of SHR on $SCOP_c$ for four humid climate zones. As expected, the performance increases significantly with decreasing SHR.

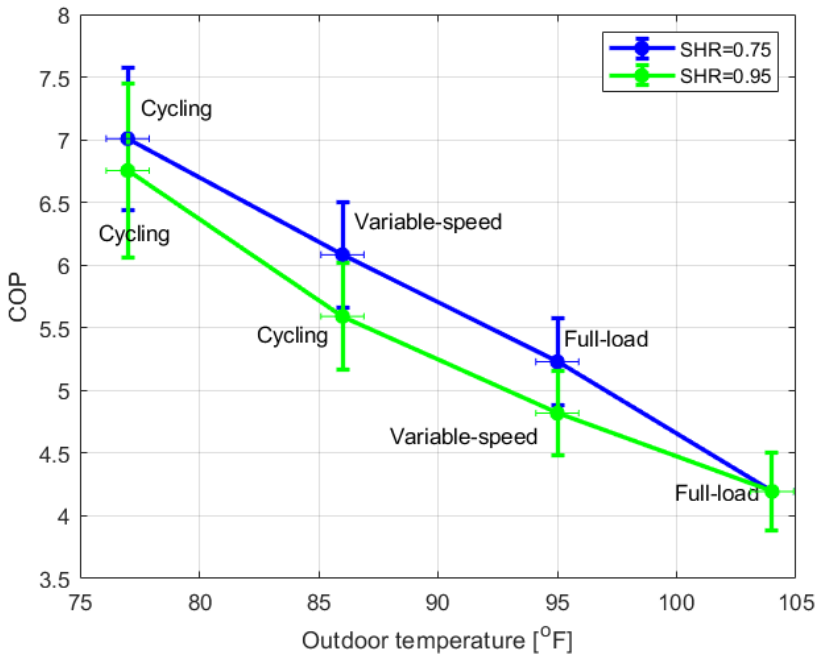

Fig. 2.14. COPs for wet-coil intervals with different building SHR when F=1.3

Table 2.11.
$SCOP_c$ for humid climate zones with different SHR

SHR	F	Very cold	Cold/humid	Mixed	Hot/humid
0.95	1.3	5.91±0.29	5.89±0.28	5.83±0.27	5.92±0.30
0.75	1.3	6.39±0.26	6.36±0.26	6.29±0.25	6.39±0.27

These parametric studies illustrate the ability of load-based testing to capture the impacts of different building-load interactions. These types of studies could be useful to an engineer in the process of developing improved equipment and controller technology. For developing a performance rating approach, it is important to have representative and repeatable test conditions for fair comparisons of different equipment. Any rating scheme, including AHRI 210/240, has a strong dependence on the specific conditions assumed for the tests and therefore it is important that these conditions be representative. The value of F=1.2 specified for CSA EXP-07 was chosen based on typical sizing approaches and experience in applying the load-based testing procedure in the laboratory. In addition, it was found that SHR=0.8 leads to indoor humidity conditions that are within the comfort zone and is representative of more humid climates.

2.4.4 Evaluation of repeatability

Repeatability of load-based testing is essential in ensuring a reliable testing and rating procedure. Repeatability across different facilities depends on many factors, including specification of standard measurement approaches and enforcement of strict criteria for tracking virtual building temperature setpoints and achieving convergence. These issues are addressed by specifications in the CSA EXP-07 and are beyond the scope of this work. However, repeatability of testing and rating results for a given installation can be an issue if the control algorithms within the test equipment are adaptive or their response is sensitive to a time history of behavior. The test equipment considered in this study is considered to be on the cutting edge in terms of performance and sophisticated control. Therefore, repeatability of load-based test results was a potential issue that was addressed by performing three sets of dry-coil load-based tests on 3 different days using the same experimental setup.

Results for the three test sequences are tabulated in table 2.12. For each test interval, the results include whether a test interval converged according the specified

Table 2.12.
Results for three dry-coil tests

T_j		77°F	86°F	95°F	104°F	113°F
Test 1	Convergence	Yes	No	Yes	No	Yes
	Behavior	Cycling	Cycling	Variable	Cycling	Variable
	$COP(T_j)$	6.952	6.023	5.214	4.401	3.613
	Uncertainty	±0.756	±0.467	±0.361	±0.298	±0.263
Test 2	Convergence	Yes	Yes	Yes	Yes	Yes
	Behavior	Cycling	Cycling	Variable	Variable	Variable
	$COP(T_j)$	6.982	6.204	5.278	4.412	3.658
	Uncertainty	±0.725	±0.480	±0.353	±0.289	±0.248
Test 3	Convergence	No	Yes	Yes	Yes	Yes
	Behavior	Cycling	Cycling	Variable	Variable	Variable
	$COP(T_j)$	6.986	6.179	5.305	4.446	3.626
	Uncertainty	±0.739	±0.469	±0.344	±0.279	±0.238

criteria, whether the equipment was cycling or operating in variable-speed mode, and the resulting COP. The COPs of the equipment for test 1 are somewhat lower than for tests 2 and 3, primarily because the equipment cycled more frequently and less stably for test 1, especially at the outdoor temperature of 86°F when the test did not converge. The results for tests 2 and 3 are relatively close. $SCOP_c$ values are tabulated in table 2.13 for three dry climates. Due to faster cycling behavior, test 1 leads to ratings that are between 1.6% and 1.7% less than test 3. Test 2 and test 3 lead to ratings that are consistent with each other within a 0.2% relative difference.

2.4.5 Impact of residual capacity in cycling tests

Uncontrolled air-side residual capacity in load-based tests is seen when equipment compressor and indoor fan cycle off at low load conditions, but the psychrometric

Table 2.13.
$SCOP_c$ for three dry-coil tests

Climate zone		Cold/dry	Marine	Hot/dry
Test 1	$SCOP_c$	5.82	5.68	5.47
	Uncertainty	±0.25	±0.23	±0.20
Test 2	$SCOP_c$	5.91	5.76	5.55
	Uncertainty	±0.25	±0.23	±0.20
Test 3	$SCOP_c$	5.92	5.77	5.56
	Uncertainty	±0.24	±0.22	±0.20
$SCOP_c$ difference	$\frac{SCOP_{c,3}-SCOP_{c,1}}{SCOP_{c,1}}$	1.7%	1.6%	1.6%
	$\frac{SCOP_{c,3}-SCOP_{c,2}}{SCOP_{c,2}}$	0.2%	0.2%	0.2%

chamber fan keeps circulating some air through the indoor coil. For a residential unitary air conditioner operating in the field, the airflow through the indoor coil is only the result of operation of the indoor fan and this is typically cycled off with the compressor. Therefore, test performance and behavior with residual capacity does not correctly represent field results. In addition, this uncontrolled residual capacity could be significantly different in different test facilities having different air distribution methods. This residual capacity could bias the results for load-based testing performance ratings to different degrees depending on the test equipment and test facility. Figure 2.15 indicates residual capacity during one cycle in a red dashed box. As can be seen, it took 15 minutes for residual capacity to attenuate to zero after the compressor and indoor unit fan cycled off.

In order to eliminate uncontrolled capacity when the unit is off in load-based testing, it is suggested that a damper be installed downstream of the indoor equipment in the supply air duct. This damper should completely block airflow when the indoor unit fan is off and not restrict airflow when the indoor fan is on. Therefore, measurement of airflow using a nozzle box or similar instruments will only reflect airflow

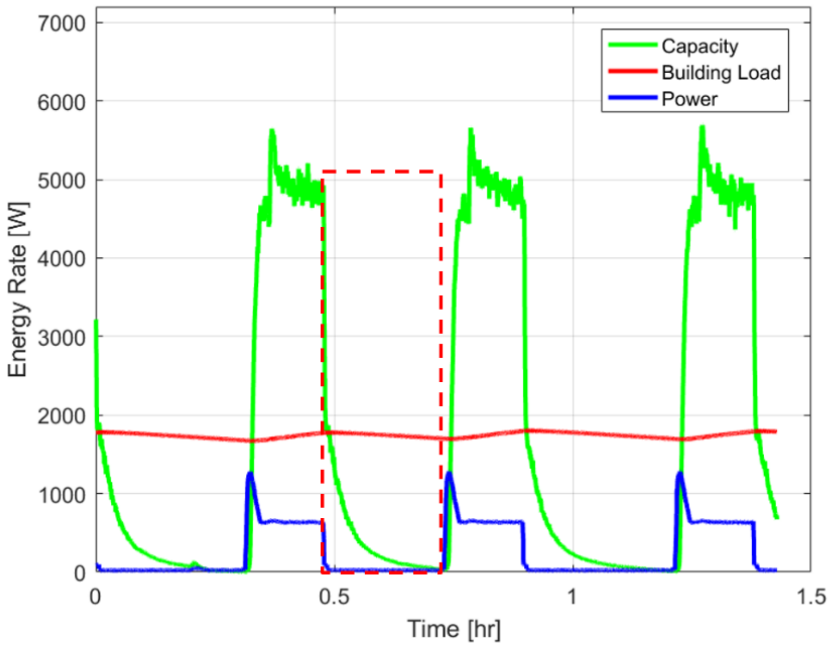

Fig. 2.15. Residual capacity in load-based test

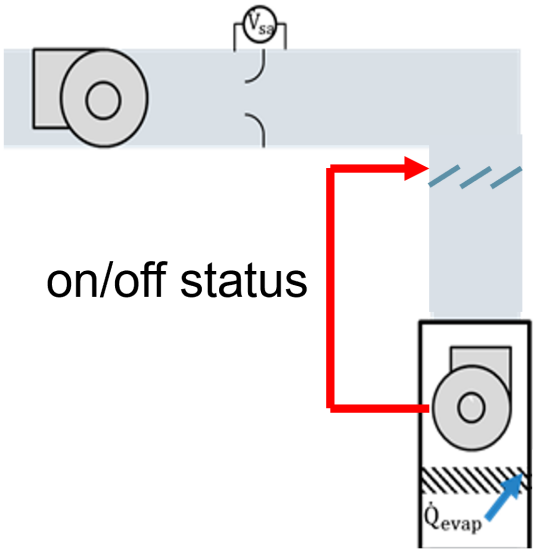

Fig. 2.16. Diagram of supply air damper

circulated by the indoor unit fan. A schematic is shown in figure 2.16. The actuator of the damper needs a control signal for the indoor unit fan on/off status to properly operate the damper. There are various choices regarding criterion for evaluating the indoor unit fan on/off status, such as a threshold on differential static pressure across the indoor unit ductwork for a ducted system, or a threshold on indoor unit power. In this work, a pseudo damper is introduced in load-based testing to serve this purpose equivalently with a threshold on indoor unit power.

Figure 2.17 illustrates the logic of the pseudo damper for airflow in the load-based tests. The pseudo damper algorithm is convenient when given a measurement of indoor unit power. A threshold is prescribed to compare to real-time indoor unit power. If power is smaller than the threshold, which means the indoor unit fan is not running, measured airflow will be overridden to zero. It is important to select the appropriate threshold on either indoor unit power or differential static pressure. For example, a higher threshold on indoor unit power will filter out fan operation with low speed, while a lower threshold on power will falsely regard equipment operation in standby mode as active operation of the indoor fan. A 20W threshold was implemented for indoor unit power measurement for the test equipment, which is slightly larger than the standby power of 18W. The logic of using a threshold on indoor power can be directly transferred to control of an actual damper in load-based tests and then it would not be necessary to override the airflow measurement.

The proposed pseudo damper logic was implemented on the previously collected load-based cooling data and modified test results are shown along with the original results for a $77°F$ dry-coil test interval in figure 2.18. The green solid line indicates equipment capacity with the pseudo damper while the green dashed line indicates capacity without the pseudo damper. The residual capacity is filtered out by the damper and the on/off pattern of capacity is more consistent with that of equipment power and what would be expected in the field. In addition, it is observed that the equipment cycling dynamics in load-based testing are slightly faster with the damper implemented. Both virtual room temperature dead band and cycle period shrink

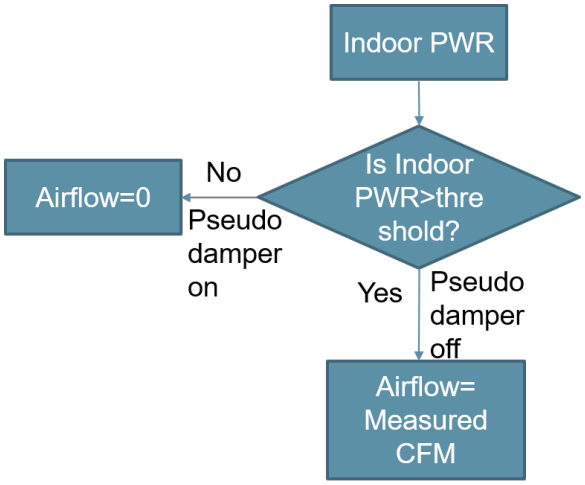

Fig. 2.17. Pseudo damper logic based on threshold of indoor power

slightly since the virtual room temperature rises faster without residual capacity when the equipment is cycled off.

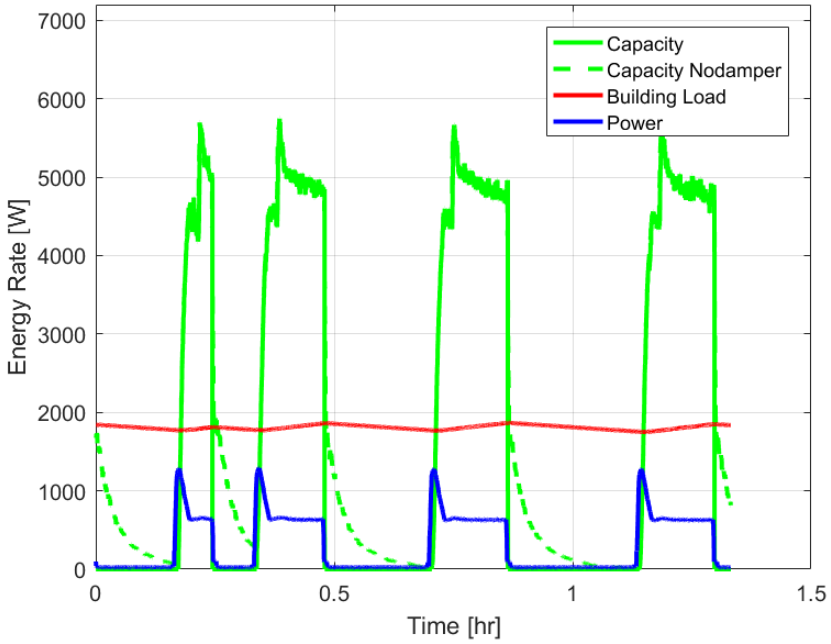

Fig. 2.18. 77 $^{\circ}F$ test interval performance with supply duct pseudo damper

In order to compare the impact of the damper on performance ratings, two complete dry-coil load-based tests were conducted with and without the supply duct damper. As can be seen in table 2.14, with the implementation of the damper, the COP for the 77 $^{\circ}F$ test interval decreased significantly since residual capacity was not integrated into performance calculation. For the 86 $^{\circ}F$ test interval, the equipment ran with a higher cycle duty and residual capacity was less involved in a cycle, but COP still decreased with the damper. For the 95 and 104 $^{\circ}F$ test intervals, the equipment ran in variable-speed mode with the indoor fan running continuously, such that the COP was not affected. In addition, the damper should not affect the full-load 113 $^{\circ}F$ test interval at all.

Table 2.14.
COPs for dry-coil test intervals with and without damper

$COP(T_j)$	$77^{\circ}F$	$86^{\circ}F$	$95^{\circ}F$	$104^{\circ}F$	$113^{\circ}F$
Without damper	6.794	5.801	4.925	3.825	2.646
With damper	6.032	5.728	5.054	3.753	2.646

Comparisons of seasonal performance are given in table 2.15. With the implementation of the damper, $SCOP_c$ for each climate zone dropped. The Hot/Dry climate has less reduction in seasonal performance with the damper since the equipment had larger loads and ran more in variable-speed mode compared to the other two zones.

Table 2.15.
$SCOP_c$ for dry climate zones with and without damper

Climate zones	Cold/dry	Marine	Hot/dry
Without damper	5.54	5.36	5.09
With damper	5.41	5.24	5.01

With implementation of an automated damper in the supply air duct, load-based tests can better represent equipment behavior in the field due to elimination of un-

controlled capacity, which has a significant impact on the test results. Test reproducibility is enhanced across different test facilities since air-side capacity will not be significantly affected by the characteristics of the test facility air distribution system. Overall, performance ratings will be more realistic and repeatable.

2.5 Interim conclusions

Currently, performance ratings for unitary residential air conditioners and heat pumps in the U.S. marketplace are based on results of steady-state laboratory tests according to the procedures and methodology established by standard AHRI 210/240 [2]. However, this current methodology fails to appropriately rate and credit equipment that has improved part-load performance due to the employment of variable-speed components and advanced controls. The automated load-based testing methodology presented in this chapter better reflect the field performance of test equipment with its native controls. This methodology is already implemented within the Canadian Standards Association (CSA) EXP-07 draft standard and is likely to be a basis for future testing and rating standards within the United States and elsewhere. The key element of the methodology is that the dynamic response of a virtual building is emulated using the psychrometric chamber controls to interact with the test equipment in real-time, such that the equipment behaves as if it were installed in the field.

This chapter is an extension of the CSA EXP-07 standard in that it includes background on the development of the virtual building modeling approach and its parameters and also provides example dynamic testing results for a state-of-the-art high efficiency, variable-speed heat pump operating in cooling mode. The paper presented and demonstrated standardized procedures that automatically test different dynamic load-based test intervals as a whole sweep using convergence criteria applied to individual test intervals. In demonstrating the approach for the variable-speed heat pump, typical dynamic behaviors of the equipment were observed such as on/off

cycling, continuous capacity modulation due to feedback control of compressor speed, indoor humidity variation with operating conditions and controller fluctuations, and capacity limits that lead to loss of indoor temperature conditions. The type of information obtained during these dynamic tests can be extremely useful in evaluating advanced controllers during the development process and provide appropriate incentives for improving performance within rating procedures.

This chapter also presented and demonstrated the temperature-bin-based method for propagating load-based test results through a seasonal coefficient of performance as a means of rating equipment. It was found that seasonal ratings were significantly higher in humid climates for the equipment considered in this study because of better test performance for wet-coil than dry-coil conditions. The highest rating occurred for a hot/humid climate, whereas the worst performance was for a hot/dry climate. The effect of building parameters on performance was also investigated and illustrated the ability of load-based testing to capture the impacts of different building-load interactions. This capability for load-based testing could be very useful in the development process for improved equipment and controller technology.

In addition, repeatability of results for the test equipment and installation was addressed by performing three sets of dry-coil load-based tests on 3 different days. Repeatability is a potential issue for high efficiency equipment that has sophisticated control algorithms that are adaptive or have overall responses that are sensitive to a time history of behavior. Although some differences in control behavior were observed for the repeatability tests applied to the high efficiency equipment considered in this study, the overall seasonable efficiency differences were less than 1.7%. Last but not the least, this chapter introduced the automated supply air damper that will close to eliminate uncontrolled residual capacity when the test equipment cycles off. Test repeatability and performance rating results will benefit from implementation of this damper.

3. ALTERNATIVE VIRTUAL BUILDING MODEL

In this chapter, a virtual building model with two nodes is studied as an alternative model form to understand the effect of using a more complicated virtual building structure on load-based testing. The structure of the two-node virtual building model is introduced in section 3.1. Subsection 3.2.1 discusses how two-node model parameters for sensible loads are identified from a detailed model of a prototypical building. Furthermore, in subsection 3.2.2, model parameters are scaled and tuned to have equivalent high frequency dynamics that match equipment cycling behavior observed in the field. Finally, results of load-based testing using a two-node virtual model for sensible loads are presented in section 3.3.

3.1 Overview of two-node virtual building model

A single-node virtual building model with lumped capacitance was introduced in section 2.1, where the single node characterizes a combination of zone air and its nearby shallow mass. For conciseness, this node is denoted as the zone node in this chapter. An electrical analog circuit of the one-node virtual building model for sensible loads with energy flows is illustrated by figure 3.1. The primary concern of employing this simple model form is whether it realistically and comprehensively characterizes the dynamics of a building interacting with test equipment under feedback control in load-based tests.

A good approach to address this concern is to investigate the effect of using a more detailed model in load-based testing. Cai and Braun [32] developed a thermal network model which captured dynamics of a single zone building with inputs of internal gains, ambient temperature, and solar radiation. Bacher and Madsen [33] proposed several gray-box RC network building models with significant reduction of complexity with

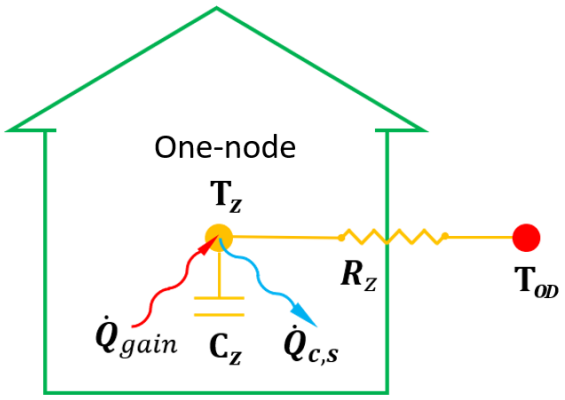

Fig. 3.1. Diagram of one-node model for sensible building loads

lumped thermal nodes for the envelope mass and internal mass. Touretzky [34] used a building model with a structure of a zone air node and an external wall mass node to study control of energy recovery. In spite of these various higher-order model forms, one step further from the single-node model is a good starting point. Therefore, a two-node model for cooling load-based tests is investigated.

3.1.1 Mathematical description

In addition to a zone shallow mass node, a deeper internal mass node is introduced within the two-node model in this chapter for use in load-based testing. Compared to the zone node that represents zone air and nearby shallow mass, the internal mass node represents indoor furniture and deeper internal mass (e.g. partition/demising wall). The model structure is described by equations (3.1) and (3.2) and illustrated with the diagram in figure 3.2. The zone node is coupled to the outdoor air temperature T_{OD} and the internal mass node through thermal resistances, and directly excited by internal heat gains $\dot{Q}_{int,s}$ and the cooling associated with the test equipment $\dot{Q}_{c,s}$, while the temperature of the internal mass node T_m is only excited by the heat transfer from zone air node in return. Within the overall building dynamics, the zone node is supposed to have relatively fast dynamics, whereas the internal deeper

mass tends to slow down the overall dynamic response. The zone node capacitance C_z, external resistance R_z, internal mass capacitance C_m and internal resistance R_m are four parameters that need to be estimated for the model's implementation in load-based testing.

$$C_z \frac{dT_z}{dt} = \dot{Q}_{int,s} + \frac{T_{OD} - T_z}{R_z} + \frac{T_m - T_z}{R_m} - \dot{Q}_{c,s} \tag{3.1}$$

$$C_m \frac{dT_m}{dt} = \frac{T_z - T_m}{R_m} \tag{3.2}$$

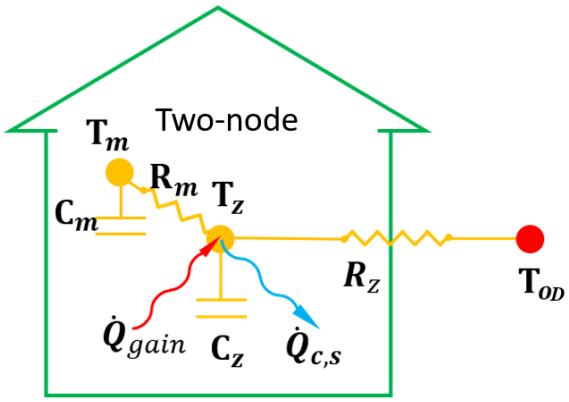

Fig. 3.2. Diagram of sensible two-node model

3.2 Estimates of virtual building parameters

In order to identify/estimate representative values of the four virtual building parameters for the sensible two-node model, dynamic responses of a detailed building simulation model were employed to generate training data used in regression/estimation. After the parameters were obtained, they were fine tuned/scaled when coupled with an equipment model in order to match typical cycling patterns of equipment observed in the field. A residential prototype building model [35] in EnergyPlus [36] was utilized as the detailed building simulation model for the purpose of two-node building model identification.

3.2.1 Regression using detailed building model simulations

The simulated single-family prototype building located in suburban Indianapolis has building geometry shown in figure 3.3 and table 3.1. For the purpose of two-node building model identification, a few modifications were made to the original EnergyPlus prototypical building model.

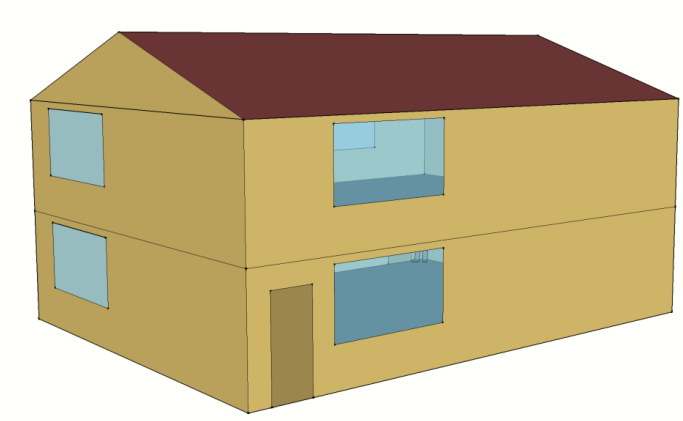

Fig. 3.3. Prototype building geometry

Table 3.1.
Building geometry information

Zones:	2 zones: living zone and attic zone	Floor area:	40ft x 30ft for each floor
Floors:	2 floors in living zone and an attic	Location:	Indianapolis international airport

1. The simulation time step was changed from 15min to 1min in order to obtain the short-term responses of the building dynamics.

2. Vertical heat transfer from the ground was not considered as an input to the two-node mode, and therefore the ground floor was modified to be adiabatic. Also,

the ceiling that separates the living and attic zones was treated as adiabatic, since dynamics of the attic zone are not included in the two-node model.

3. HVAC equipment was removed since only the dynamic building responses were needed for the purpose of two-node building model identification.

4. Solar radiation was removed from the weather data since this was not considered as a dynamic input in the sensible two-node model.

5. The internal sensible heat gain $\dot{Q}_{int,s}$ was configured as a fast-changing random signal peaking at 1000W, in order to generate a rich set of dynamic data for regression.

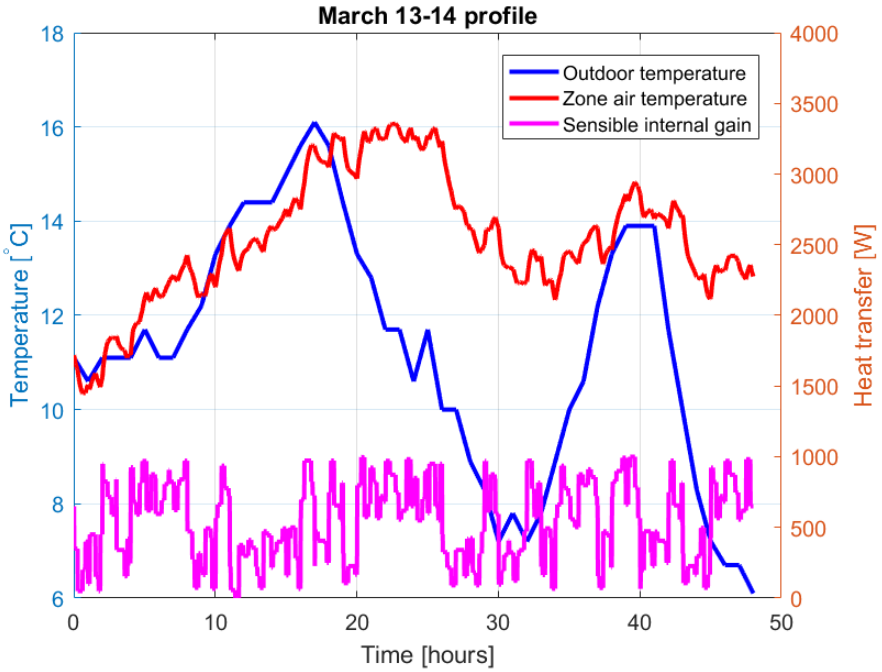

Fig. 3.4. Dynamic building response and the associated inputs

Dynamic building responses were generated over a whole year using EnergyPlus for the subsequent usage of regression. Sample data from March 13 to 14 are shown in figure 3.4. The zone air temperature as the major building response, trended upwards

or downwards in response to the variations in outdoor temperature, but had faster dynamics resulting from fast-changing internal gains.

$X_{T,i} = [T_{OD,i}, \dot{Q}_{int,s,i}]$ represents an input training data vector at timestep i, while θ_T represents a sensible two-node model parameter vector. For the regression of the two-node model, the optimization cost $J_T(\theta_T)$ associated with the usage of parameter vector θ_T is shown in equation (3.4) as a root mean of square error between the zone air temperature T_z simulated in EnergyPlus and the predicted zone air temperature $T_{air}(X_T|\theta_T)$ using the two-node model. After using 20 days of training data in February within the regression process, the optimal $\hat{\theta}_T$ was obtained that best predicts the building responses according to equation (3.5).

$$\theta_T = [R_z, C_z, R_m, C_m] \tag{3.3}$$

$$J_T(\theta_T) = \sqrt{\frac{1}{N_{20days}} \sum_{i=1}^{N_{20days}} (T_{z,i} - T_{air}(X_{T,i}|\theta_T))^2} \tag{3.4}$$

$$\hat{\theta}_T = argmin(J_T(\theta_T)) \tag{3.5}$$

The optimal estimates of parameters are listed as the third column in table 3.2. The optimal cost associated with the set of parameters was 0.2784K, as the building dynamic response was predicted well. The sensible two-node model identified from the prototype building simulation was used to predict outside of the training period as a validation that includes 24 hours of prediction plotted in figure 3.5. In the upper plot, the original zone air temperature is represented by the red line and the predicted zone air temperature using the two-model and the associated optimal parameters is shown by the green line. The predicted internal mass node temperature is represented by the cyan line, which is smoother than the zone air temperature since the internal mass node is trained to have a larger capacitance compared to the zone node.

Table 3.2 also compares the building external resistances R_z and zone capacitances C_z between the one-node and two-node models. The one-node capacitance was de-

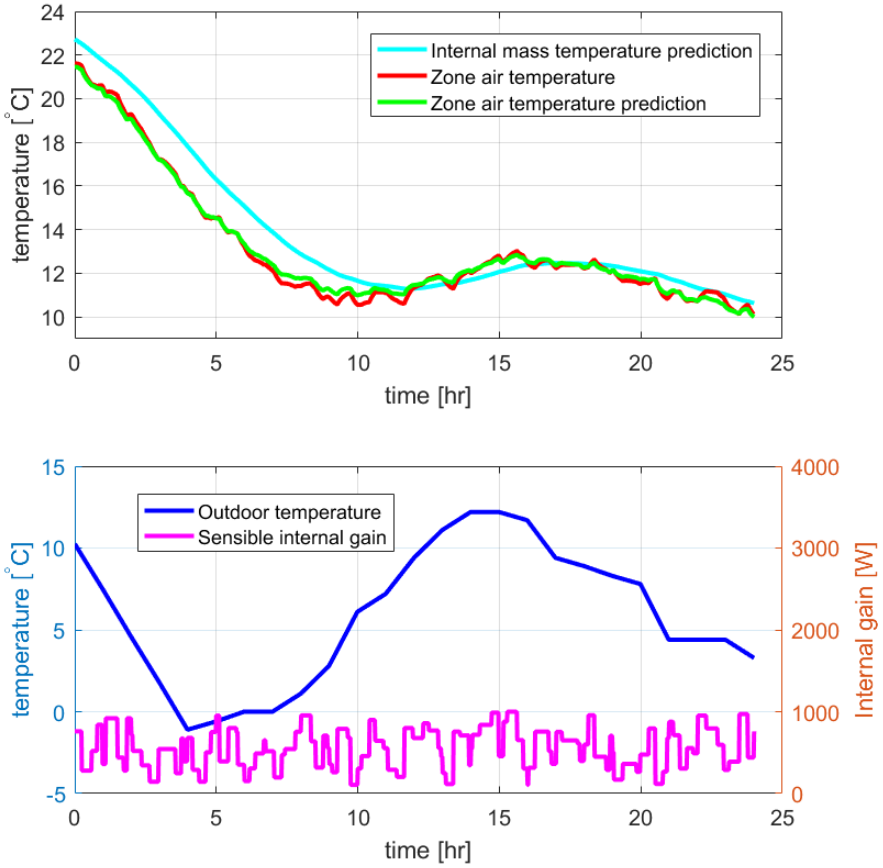

Fig. 3.5. Zone air temperature prediction by sensible two-node model

Table 3.2.
Parameters in sensible virtual building model

Model parameters	One-node model	Two-node model
R_z	$4.60 \times 10^{-3} K/W$	$4.60 \times 10^{-3} K/W$
C_z	$1.35 \times 10^{6} J/K$	$7.27 \times 10^{5} J/K$
R_m	N/A	$7.60 \times 10^{-4} K/W$
C_m	N/A	$6.60 \times 10^{6} J/K$

termined using equation (2.8) in terms of the required equipment cooling capacity. An external resistance for the one-node model was determined using equations (2.12) and (2.13). The expression for the external resistance building R_z is given in equation (3.6) in terms of the equipment capacity and other inputs defined in section 2.2. The equipment total capacity used in determining the one-node building parameters was estimated to be 1.78 tons sized by EnergyPlus for the prototypical building.

$$R_z = \frac{1.2(T_{OD,D} - T_{Bal,D})}{SHR\ \dot{Q}_{D,t}} \tag{3.6}$$

According to table 3.2, the external thermal resistances R_z for the two model forms are identical. However, the zone node thermal capacitance (C_z) values differ by about a factor of two with a smaller C_z for the sensible two-node model. This makes sense because the C_z in the single-node model represents both the zone air and shallow mass, while the C_z in the two-node model is supposed to be more decoupled from the internal mass.

3.2.2 Scaling and tuning of parameters for the two-node model

Similar to the single-node model, it is important to have an approach to scale the parameters of the two-node model for different test equipment in load-based testing. Equation (3.6) can be directly used to determine R_z in the two-node model in terms of test equipment capacity. However, it is still necessary to be able to determine C_z, R_m and C_m using an scaling approach.The next subsection presents an approach to scale C_z. In terms of R_m and C_m, it is assumed that the internal mass capacitance C_m is proportional to the zone capacitance C_z and that the internal thermal resistance R_m is proportional to the external thermal resistance R_z. For the purpose of performing load-based testing using the two-node model, these proportionality constants were determined using table 3.2 results in the following fashions.

$$\frac{C_m}{C_z} = \frac{6.60 \times 10^6}{7.27 \times 10^5} \approx 9 \tag{3.7}$$

$$\frac{R_m}{R_z} = \frac{7.60 \times 10^{-4}}{4.60 \times 10^{-3}} \approx 1/6 \tag{3.8}$$

Tuning of zone node capacitance

It is importance to properly choose a value for zone node capacitance C_z in the two-node building model for use in load-based testing, since equipment dynamic behaviors are very sensitive to the virtual building dynamic response (virtual room air temperature) that will be strongly affected by C_z. As can be seen from table 3.2, the values of C_z for the two models differ by about a factor of two. Therefore, the scaling approach to obtain the value of C_z for the two-node model is based on tuning the value determined for the one-node model from Equation (2.8) that is repeated in Equation (3.9). The scaling/tuning is achieved using a tuning factor TF as expressed in equation (3.10).

$$C_{z,1node} = k_1 \times \dot{Q}_{D,t} \tag{3.9}$$

where $k_1 = 120 s/^\circ F$.

$$C_z = TF \times C_{z,1node} \tag{3.10}$$

In order to determine an appropriate tuning factor, simulation was performed to study cycling rates of equipment when coupled with the one-node and two-node building models. In this approach, the equipment was simply modeled as a single-stage air conditioner with a constant sensible capacity and on/off control to maintain the indoor temperature within a $1^\circ F$ dead band up and down the equipment (thermostat) setpoint. The goal was to determine a tuning factor for zone capacitance of the two-node model that provides a thermostat cycling rate curve that matches the NEMA thermostat cycling rate curve [31].

Figure 3.6 illustrates sample cycling behaviors (patterns) for the two models after the two-node mode was properly tuned. The outdoor temperatures for both simu-

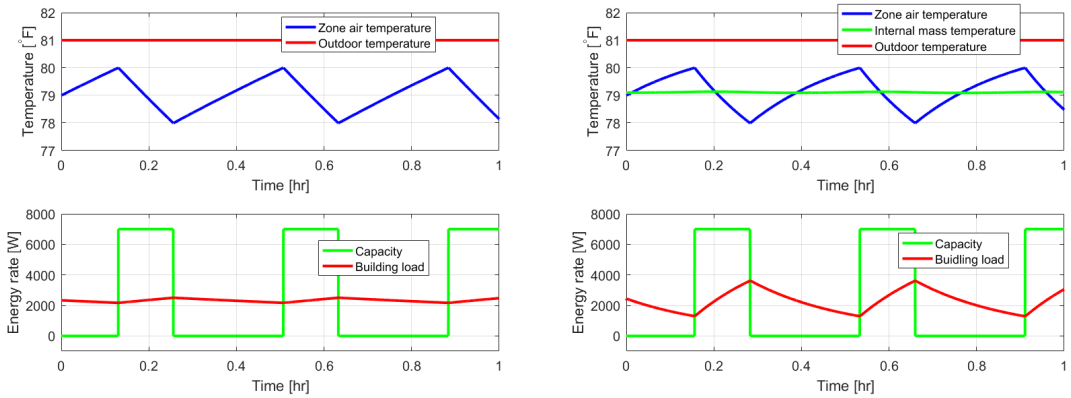

(a) One-node model (b) Two-node model

Fig. 3.6. Sample cycling behaviors for two virtual building models

lations were fixed at 81 $^{\circ}F$. The simulated single-stage equipment cycled on with a 7000W capacity that was also used to scale the virtual buildings for both models. The equipment thermostat setpoint was 79 $^{\circ}F$ and the thermostat dead band was 1 $^{\circ}F$ up and down, such that the temperature varied between 78 to 80 $^{\circ}F$ in response to the equipment cycling behaviors. The cycling rates of the two models are identical, although the zone air node building loads fluctuate differently since heat transfer from the internal mass node is included in the dynamic zone air node building load for the two-node model. However, the average loads over the cycles for both models are the same, because the net heat transfer from the internal mass node to the zone air node in a cycle must be zero at steady state.

The cycling rates for various part-load conditions or cycle duties of the single-stage equipment were acquired by changing the outdoor temperature in the simulations. Simulated cycling rates as a function of cycle duty are compared to NEMA cycling rate dome [31] in figure 3.7. The NEMA cycling rate equation (3.11) is a mathematical description of the single-stage equipment cycling rate N with respect to cycle duty X. Based on field data for residential buildings, N_{max} was prescribed to be 3 times/hr at a cycle duty of 0.5 for determining the one-node model sensible capacitance in section 2.1.

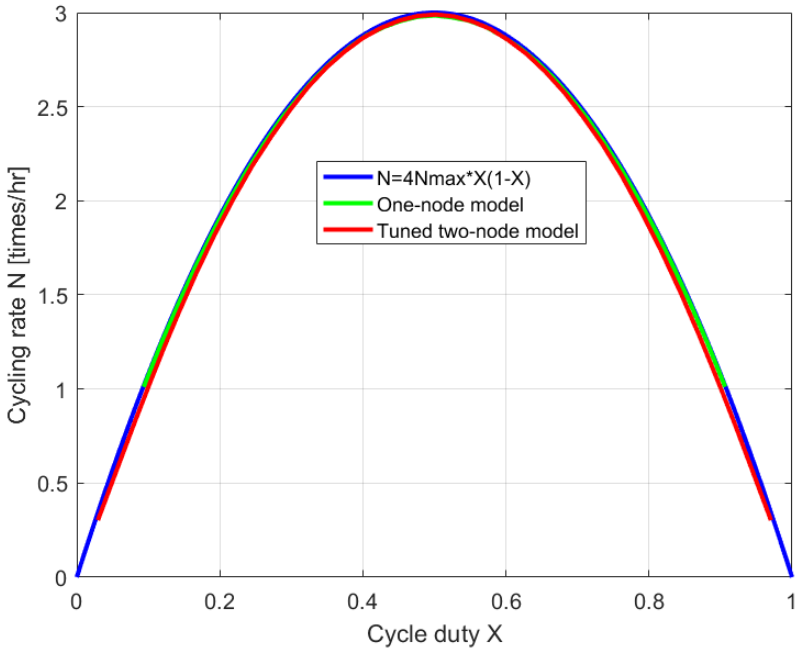

Fig. 3.7. Cycling rate domes for both building models compared to the NEMA dome

$$N = 4N_{max}X(1 - X) \tag{3.11}$$

The cycling rate dome of the one-node model matches the NEMA cycling dome, which is of no surprise since the one-node model capacitance was chosen to reflect this cycling behavior. The two-node model was tuned with $TF = 0.96$ such that its dynamic simulation behavior had a maximum cycling rate of 3 times per hour. Therefore, the cycling rate dome of the two-node model shown in figure 3.7 also matches the one-node model and NEMA cycling domes.

Frequency responses of zone air temperature to indoor convective heat transfer rate (e.g. sensible building loads, equipment cooling rate) can introduce a different perspective to the comparison of the two model forms. To implement frequency analysis, transfer functions for both building models were first acquired using Laplace

transforms, indicated by equations (3.12) and (3.13). Bode diagrams are presented in figure 3.8.

$$G_{1node}(s) = \frac{1/C_{z,1node}}{s + 1/(R_z C_{z,1node})} \tag{3.12}$$

$$G_{2nodes}(s) = \frac{\frac{s}{C_z} + \frac{1}{C_z R_m C_m}}{s^2 + (\frac{1}{R_z C_z} + \frac{1}{R_m C_m} + \frac{1}{R_m C_z})s + \frac{1}{R_z C_z R_m C_m}} \tag{3.13}$$

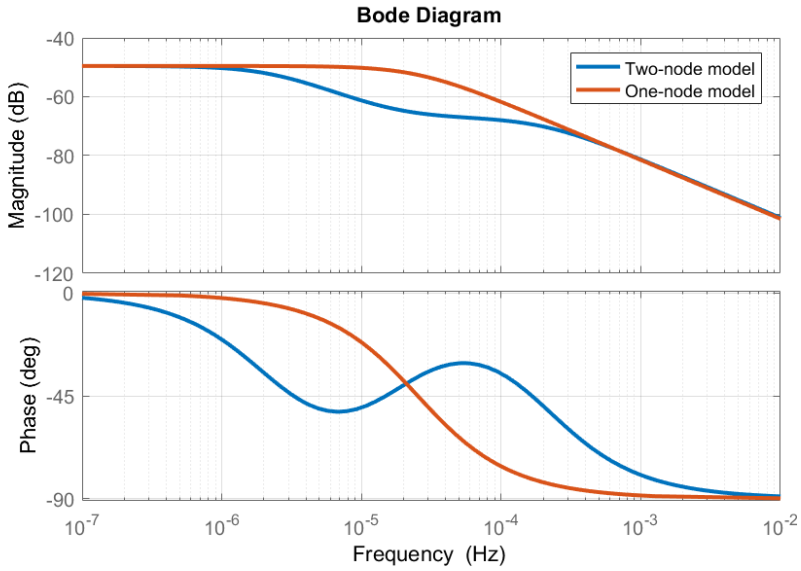

Fig. 3.8. Frequency response of virtual building models

The high-frequency and low-frequency responses of the two models agree well with each other. However, the two-node model response is much slower within mid-range frequencies from 10^{-6} to $10^{-3}Hz$, since its internal mass node stabilizes the indoor air temperature. The consistency between the cycling rate domes echoes the similar system responses for input frequencies higher than $10^{-3}Hz$.

3.3 Load-based testing using sensible two-node model

In order to apply this model for load-based testing, two differential equations (one for the virtual room air temperature dynamics and the other for internal mass temperature dynamics) were discretized using a finite time step Δt.

$$T_{ID,sp}(t+\Delta t) = T_{ID,sp}(t) + \frac{\Delta t(BL_{2nodes} - \dot{Q}_(c,s))}{C_z} \tag{3.14}$$

$$BL_{2nodes} = BL + \frac{T_m(t) - T_{ID,sp}(t)}{R_m} \tag{3.15}$$

$$T_m(t+\Delta t) = T_m(t) + \frac{\Delta t}{R_m C_m}(T_{ID,sp}(t) - T_m(t)) \tag{3.16}$$

$T_{ID,sp}$ is the virtual room air temperature that will be sent as the setpoint to the indoor psychrometric chamber reconditioning system at each timestep. T_m is the internal mass temperature updated at each timestep. BL is the sensible building load used for the one-node model introduced in section 2.1 per Equation (2.12). However, the real-time zone node building load for the two-node model, BL_{2nodes} includes another term that reflects real-time heat transfer from the internal mass node, as indicated in equation (3.15). In load-based testing using the two-node virtual building model, if the test equipment successfully reaches steady-state in variable-speed mode, the internal mass temperature will be equal to the zone air temperature, and therefore BL_{2nodes} will be equal to BL.

When implementing the method, model parameters for the two-node model were determined using equations (3.17) through (3.20). Constants and parameters in equations (3.17) and (3.19) can be found in section 2.1.

$$C_z = 0.96 \times k_1 \times \dot{Q}_{D,t} \tag{3.17}$$

$$C_m = 9 \times C_z \tag{3.18}$$

$$R_z = \frac{1.2(T_{OD,D} - T_{Bal,D})}{SHR\ \dot{Q}_{D,t}} \tag{3.19}$$

$$R_m = \frac{1}{6} \times R_z \tag{3.20}$$

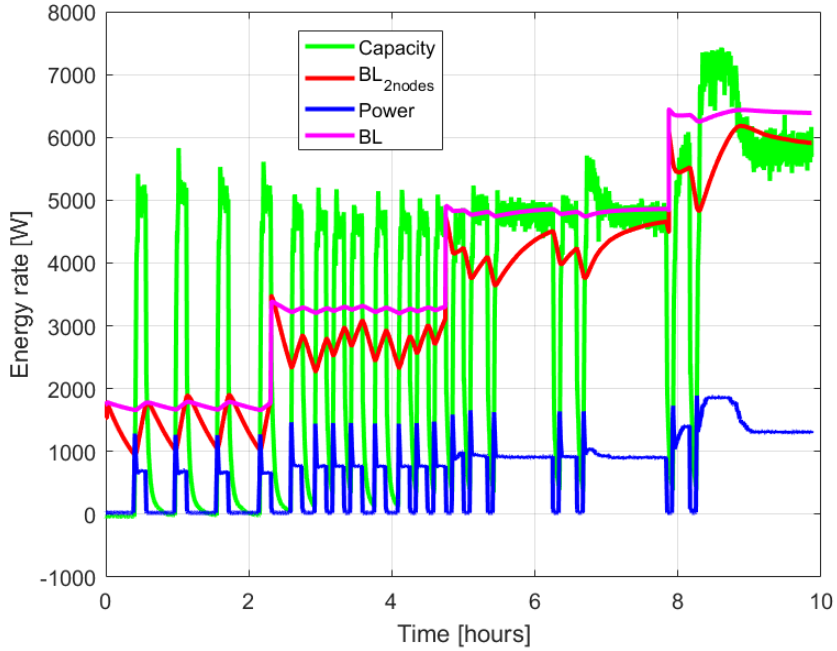

Fig. 3.9. Energy rates in load-based testing using two-node model for sensible loads

A complete sweep of dry-coil load-based testing using the two-node model was conducted using the same experimental setup introduced in section 2.4. In figure 3.9, the blue line represents equipment power, the green line is equipment capacity, the red line represents BL_{2nodes} and the magenta line is BL. BL_{2nodes} is the building load that the equipment needs to handle to maintain the virtual room air temperature (i.e. zone node temperature), whereas BL is the building load excluding heat transfer from the internal mass node.

For the $77°F$, $86°F$ and $95°F$ test intervals, the test equipment cycled on and off since BL_{2nodes} was smaller than the minimum capacity of the test equipment. The

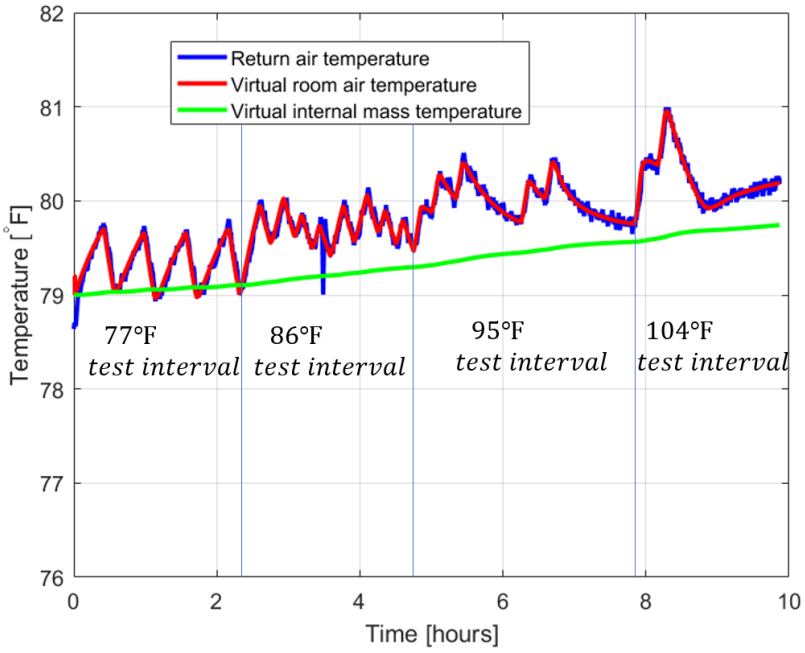

Fig. 3.10. Temperatures in load-based testing using two-node model for sensible loads

$86^{\circ}F$ interval had the highest cycling rate of approximately 3 times per hour since its cycle duty was close to 0.5. For the $104^{\circ}F$ test interval, the test equipment was working in variable-speed mode.

Temperatures are shown in figure 3.10 for the load-based test using the two-node model. The return air temperature (in blue) to the test unit was controlled to the virtual room air temperature setpoint (in red). The virtual internal mass temperature is represented by the green line and its initial value at the beginning of the test was $79^{\circ}F$. Throughout the four test intervals, the internal mass temperature increased continuously and slowly . It is obvious that the testing time was insufficient for this internal mass node temperature to converge to the mean value of the zone air temperature either during each test interval or during the whole sweep of the test, because of the large internal mass node capacitance. Moreover, since the virtual internal mass was cooler than the virtual room air for the most of the time during the

test, the virtual mass served as an additional heat sink that helped the test equipment cool the zone air and that is why BL_{2nodes} was generally smaller than BL during the test, as can be seen in figure 3.9. Therefore, a quasi-steady state/convergence for internal mass node was never achieved in this test.

3.4 Interim conclusion

In this chapter, a two-node model for sensible building loads was developed and evaluated for use in load-based testing. In addition to the zone node that represents zone air and nearby shallow mass, an internal mass node was introduced that represents indoor furniture, deeper and heavier internal mass. Compared to the one-node virtual building model proposed in chapter 2, the two-node model has similar building dynamics when responding to thermal inputs that have higher frequencies associated with feedback control of the equipment. However, the two-node model showed much slower building dynamics when responding to thermal inputs with intermediate frequencies between 10^{-6} to 10^{-3} Hz that are associated with, for example, diurnal changes of outdoor temperature. Compared to the one-node model, these intermediate frequency responses can be captured by the two-node model due to its higher-order model structure, where a heavy internal mass node was introduced.

When implemented in load-based testing, the additional internal mass node starts to show some deficiencies, as it responds very slowly in a test due to its heavy thermal capacitance. Therefore, quasi-steady states/convergence for the internal mass node cannot be achieved in a reasonable time scale. As a result, the use of the two-node model or other more complicated higher-order models is not recommended compared to the lumped capacitance one-node virtual building for load-based testing. The single-node model has the advantages of fast response and a simple model structure, which significantly benefit load-based testing test time and repeatability.

4. THERMOSTAT ENVIRONMENT EMULATOR

To properly rate and credit unitary residential air conditioners that have improved part-load performance and advanced controls, a load-based testing methodology has been enhanced in this work and explained in chapter 2. In load-based testing, a virtual building model is used along with real-time measurements of the test equipment cooling rates to emulate building-equipment interactions at different conditions. The air temperature of an environmental chamber that simulates indoor conditions is continuously controlled to virtual room temperature setpoints that are adjusted based on outputs from the virtual building model. The test equipment thermostat senses the floating zone air temperature and communicates with the test equipment as if it were installed in the field. Therefore, it is important to properly configure the test thermostat such that the associated load-based testing outputs reflect the field behaviors of the test equipment.

A natural starting point for the test thermostat configuration in load-based testing is to find a realistic and representative installation location in the indoor psychrometric chamber. In this chapter, three thermostat installation locations were studied in section 4.1, but the results demonstrate that the dynamics of the test thermostat can vary significantly with location due to non-uniform air velocity and temperature within the indoor test room. The inconsistency could be more significant when reproducing load-based tests in different test facilities due to their different air distribution methods and reconditioning systems.

In order to address this reproducibility issue, the current CSA EXP-07 draft standard [10] specifies that the thermostat be located in the return to the test unit. This ensures that both the thermostat and the equipment see the same conditions and was thought to have the best chance of achieving reproducible results across different facilities. However, locating the thermostat in the return air stream leads to signifi-

cantly fast thermostat dynamics according to the results in section 4.1, and it is far from being representative of typical conditions that a thermostat would experience in the field. Therefore, it is very challenging to directly define a thermostat installation location within a indoor test room that is both representative and reproducible across different testing facilities.

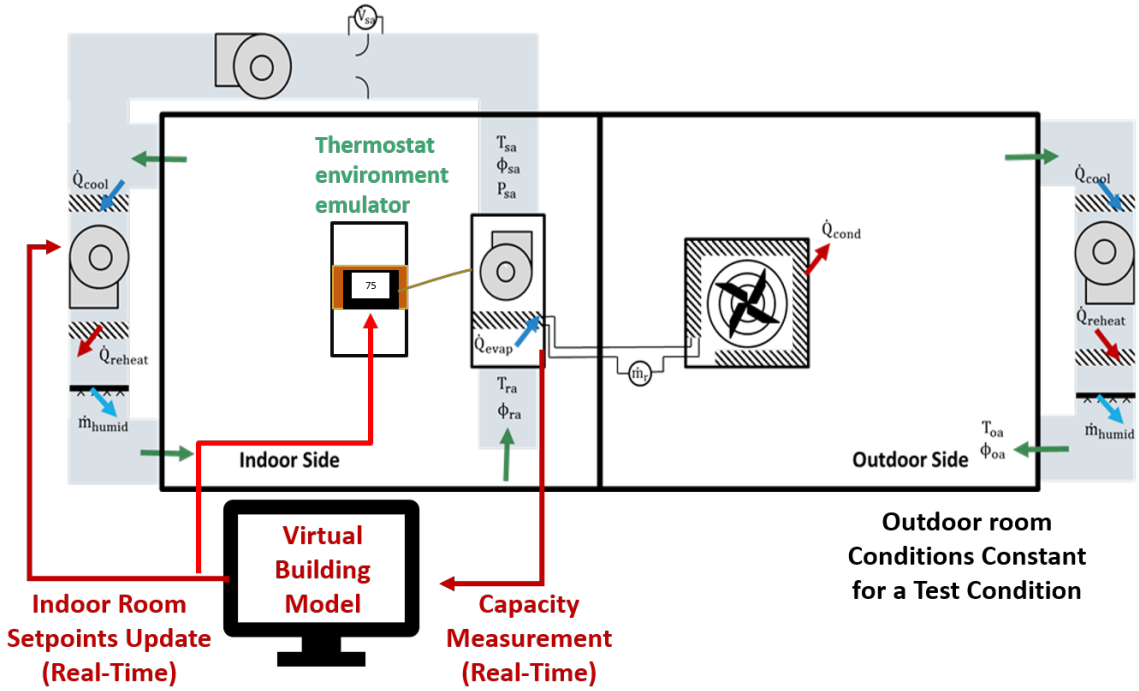

Fig. 4.1. Thermostat environment emulator in load-based testing

In the interest of achieving representative and reproducible results for load-based testing, a thermostat environment emulator approach is introduced in this chapter that can provide to the test thermostat air inlet, both typical airflow conditions and appropriate virtual building dynamics associated with varying inlet temperatures. The overall setup of load-based testing using thermostat environment emulator can be seen in figure 4.1. The test equipment is installed across a pair of psychrometric chambers, where the equipment thermostat is installed inside the environment emulator within the indoor test room. In load-based testing, the temperature and

humidity setpoints for the indoor chamber are determined according to the virtual building dynamics. In addition, the thermostat environment emulator must track the virtual building temperature setpoints with airflow that is representative of a typical indoor environment.

Two different apparatuses were developed and compared that represent two different designs of thermostat environment emulator. The first apparatus is introduced in section 4.2 that continuously samples air from the indoor test equipment return air inlet with the goal of providing consistent inlet temperature variations for both the thermostat and the test equipment. Hence, this emulator is called an "air sampling apparatus". However, the air sampling apparatus was found to be not adequate since there were non-negligible temperature differences between the two inlet conditions during testing and therefore it would be difficult to achieve reproducible conditions in different facilities.

In section 4.3, the second apparatus that was developed and tested is found to be able to independently and dynamically control the thermostat inlet air temperature to the virtual room temperature setpoints using thermoelectric devices, while the indoor test equipment return air temperature is controlled to the same setpoints by the psychrometric chamber. This thermostat environment emulator is referred to as an "independently conditioned apparatus".

Using the independently conditioned apparatus, sample load-based testing results were obtained and presented in subsetion 4.3.3 to demonstrate its ability to track emulated building responses during load-based testing. A detailed description of the design and control of the apparatus is provided in subsection 4.3.1 with sufficient detail to allow future researchers to reproduce the device. In addition, a two-dimensional dynamic numerical model of the apparatus is presented in subsection 4.3.2 that was used to guide the overall design process and that could be useful to others in developing improvements to the apparatus in the future. It is believed that this apparatus could be the basis for a standardized solution for applying load-based testing to air

conditioning and heat pumping equipment that is reproducible across different facilities.

4.1 Impact of thermostat location on load-based testing

In this section, dry-coil cooling tests were carried out to investigate the impact of thermostat installation location. In order to provide a range of representative testing results, three different locations were chosen in the psychrometric chamber that represents the indoor room. In all three tests, the indoor unit return air temperature was controlled to the setpoints determined based on outputs from the virtual building model, while the test thermostat and the equipment controls would respond to the variations of the local air temperature that the thermostat sensed.

4.1.1 Thermostat locations in test chamber

The same test setup and test equipment were used here, as described in section 2.4. In figure 4.2, three thermostat locations were considered for this study that are indicated by colored dots. The figure shows the interior of the psychrometric chamber that mimics the indoor environment for the test unit. The red and yellow locations are on the indoor unit of the equipment that is studied. The red dot is location A with the thermostat mounted on the sidewall of the indoor unit cabinet at about 5 feet above the floor. The yellow dot is location B with the thermostat mounted across the air inlet where the indoor unit draws return air from the conditioned space. The return air temperature is also measured using a thermocouple grid at location B. The blue dot is location C, which is roughly 15 feet away from the indoor unit and roughly 5 feet above the chamber floor. In this psychrometric chamber, conditioned air is supplied from the floor in the left three-quarters of the chamber and return air is collected at the right upper corner of figure 4.2. The airflow pattern can be seen schematically from the blue arrows in figure 4.2. Location C is the closest to the chamber return air inlet among the three locations in this study.

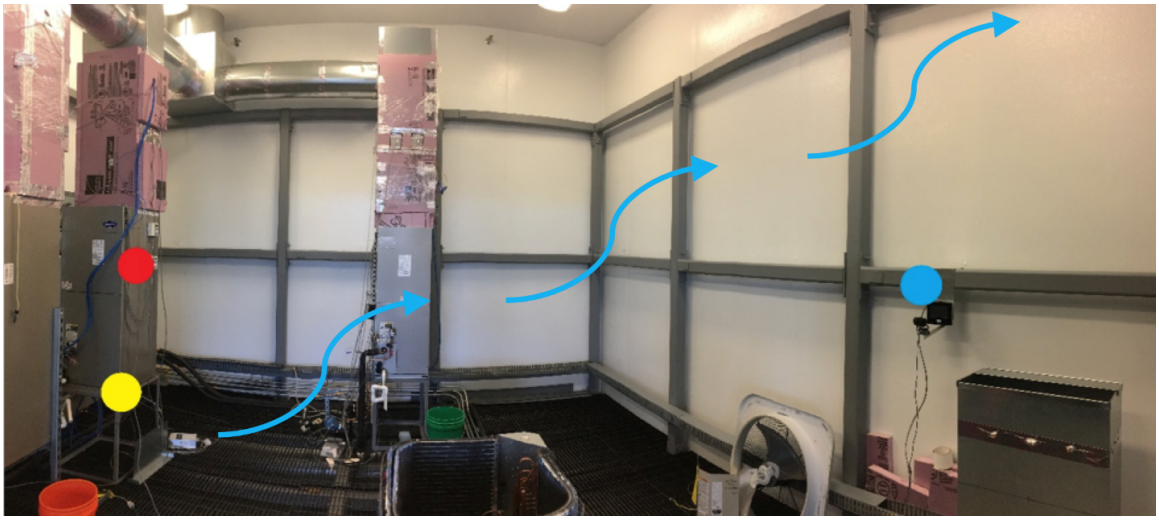

Fig. 4.2. Three thermostat locations in test chamber

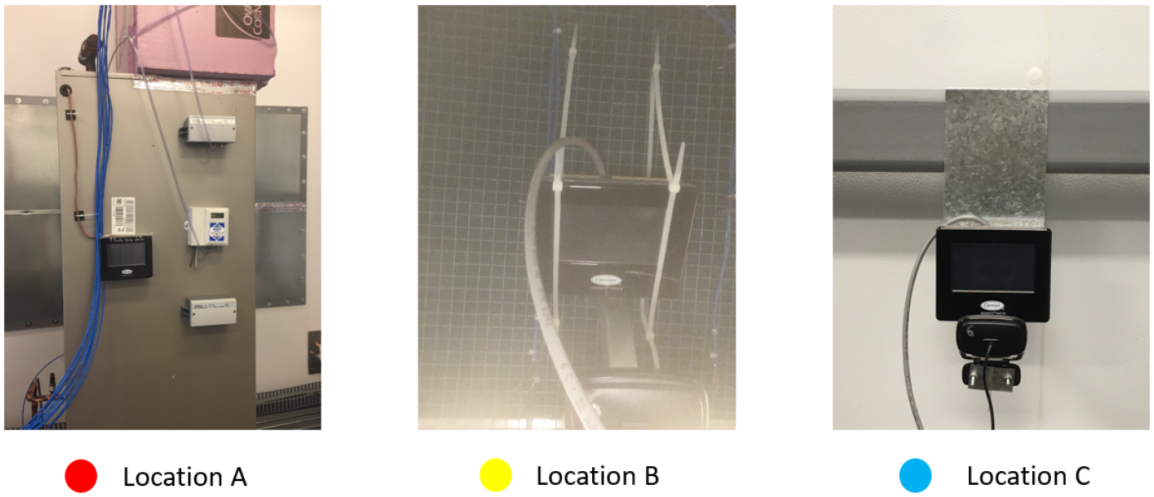

Fig. 4.3. Three thermostat locations in closer looks

Figure 4.3 shows the thermostat installations for the three locations. The black thermostat shown in figure 4.3 was mounted on a 0.5-inch-thick wooden layer to thermally isolate it from the metal panels. The thermostat temperature is primarily affected by convective heat transfer from the surrounding air and the air that flows

through the device. A Logitech HD Webcam C525 was installed facing the screen of the thermostat to record videos of thermostat readings throughout load-based tests. For location B, the thermostat was attached using cable ties to the grid that holds the return air filter at the bottom of the indoor unit. The thermostat at location C was suspended from a support structure. Characteristics of the three locations are summarized in table 4.1.

Table 4.1.
Characteristics of three locations

	Location A	Location B	Location C
Height from floor	5 ft	2 ft	5 ft
Distance from unit return air inlet	3 ft	0 ft	15 ft

Comments: 1.Location B has the largest air velocity.

2.Location C is far from chamber supply air outlet.

4.1.2 Dry-coil test results

Test results associated with the thermostat location A are shown in figure 4.4. The test unit cycled on and off for the $77°F$ and $86°F$ test intervals, but modulated its speed to match sensible cooling rates to the sensible building loads at the $95°F$ and $104°F$ test intervals. The unit ran out of capacity for the $113°F$ interval.

As is shown in figure 4.5 for location B, the test unit also cycled on and off for the $77°F$ and $86°F$ test intervals. The cycling patterns for the $86°F$ test interval were not perfectly identical to each other, which may result from the faster dynamics of the test thermostat when mounted in the return air stream at location B. However, the subsequent two test intervals with equipment variable-speed behaviors converged

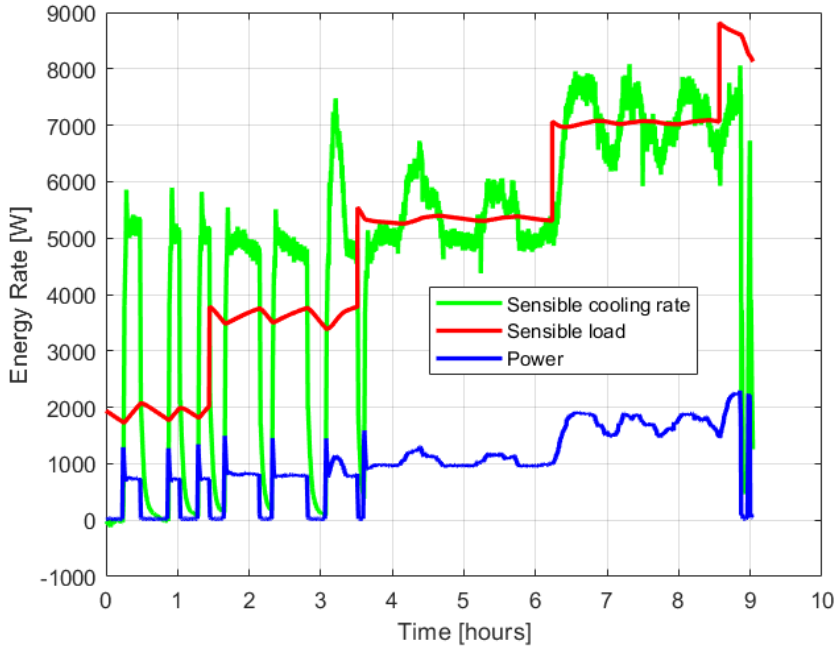

Fig. 4.4. Dry-coil test results with thermostat mounted at location A

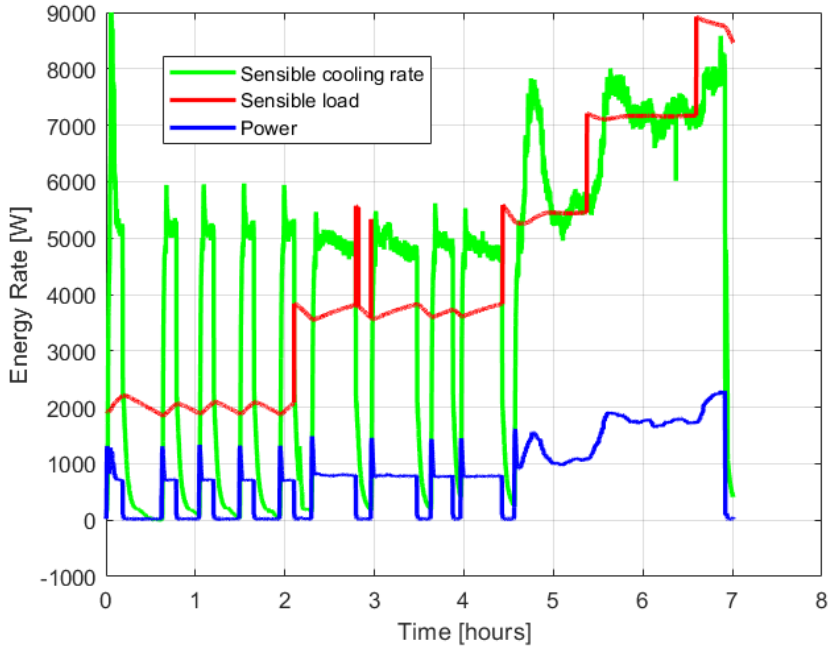

Fig. 4.5. Dry-coil test results with thermostat mounted at location B

relatively quickly. Thus, thermostat location B is somewhat advantageous in terms of testing time for reaching steady state under variable-speed operation.

For location C, the $77°F$ and $86°F$ test intervals did not converge in terms of COP, as can be seen in figure 4.6. This test took longer time than those at location A and B, since the air velocity is lower here leading to slower thermostat dynamics. Also, there were significantly larger temperature variations for the C location test. In addition, the test unit was not able to deliver cooling continuously without cycling on/off even for the $95°F$ test interval where the sensible building loads are relatively large.

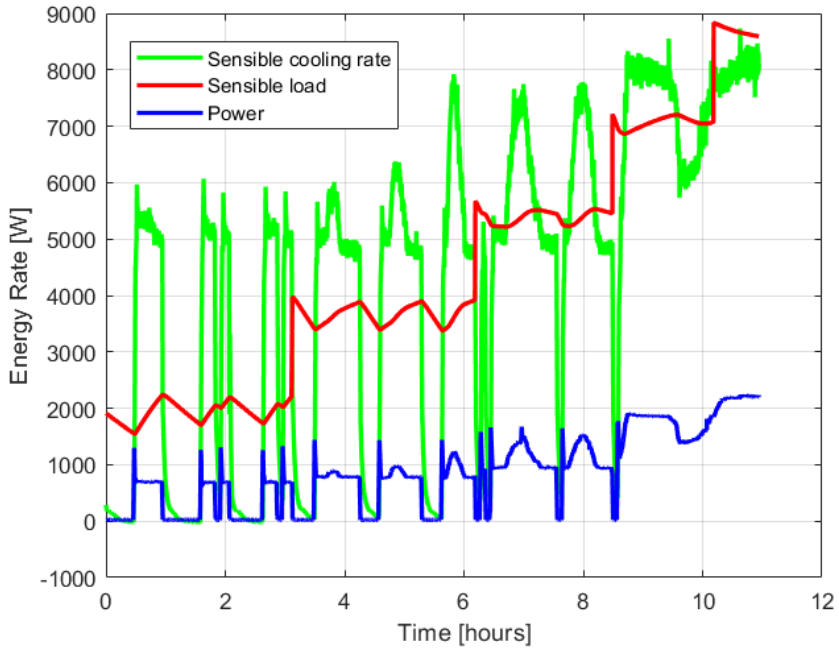

Fig. 4.6. Dry-coil test results with thermostat mounted at location C

Before launching the whole sweep of load-based cooling tests, the CSA EXP07 draft standard [10] requires that test operators offset/calibrate thermostat display temperature based on a comparison between the indoor unit return air temperature measurement and the pre-calibrated thermostat display temperature when the return

air temperature is controlled in steady state to the thermostat setpoint of the cooling test (i.e. $79^{\circ}F$ for these dry-coil tests).

This test thermostat displays temperatures in increments of $1^{\circ}F$ that is also the resolution of offset. An offset of $+1^{\circ}F$ means that the thermostat reading is lower compared to the test unit return air temperature and the thermostat reading should be calibrated upwards by $+1^{\circ}F$ using a bias adjustment. It is interesting to note that location A has no offset, location B has a $+1^{\circ}F$ offset and location C has a $-1^{\circ}F$ offset. These differences can be used to roughly estimate the steady-state air temperature maldistribution within the indoor test chamber.

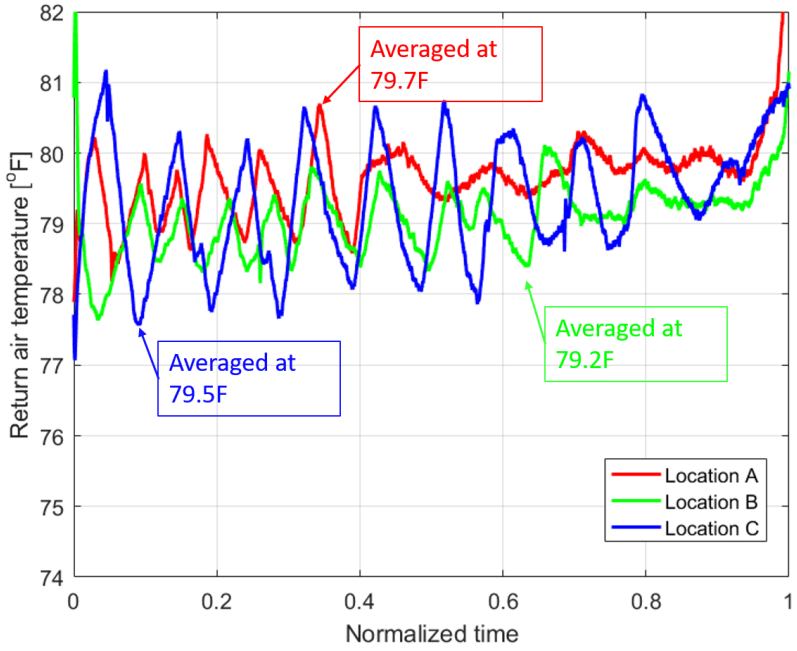

Fig. 4.7. Equipment Return air temperatures in three tests

The return air temperatures of the test unit in the three dry-coil tests are plotted against normalized test time in figure 4.7. The average temperature for each test is also marked on figure 4.7. Although all three return air temperatures were controlled close to $79^{\circ}F$ throughout the tests, it is obvious that the test with thermostat location

Table 4.2.
Results for three dry-coil tests

T_j		$77°F$	$86°F$	$95°F$	$104°F$	$113°F$
Location A	Behavior	Cycling	Cycling	Variable -speed	Variable -speed	Out of capacity
	Convergence	Yes	Yes	Yes	Yes	Yes
	COP	6.747	6.279	4.972	4.021	3.356
	Uncertainty	±0.656	±0.456	±0.335	±0.267	±0.249
	Test duration	1.4hrs	2.1hrs	2.7hrs	2.5hrs	1hr
	Cycle period	0.47hrs	0.70hrs	-	-	-
	Cycle duty	0.40	0.64	-	-	-
Location B	Behavior	Cycling	Cycling	Variable -speed	Variable -speed	Out of capacity
	Convergence	Yes	Yes	Yes	Yes	Yes
	COP	6.235	5.771	5.008	3.963	3.356
	Uncertainty	±0.707	±0.424	±0.335	±0.270	±0.249
	Test duration	2.2hrs	2.2hrs	0.9hrs	1.3hrs	1hr
	Cycle period	0.44hrs	0.55hrs	-	-	-
	Cycle duty	0.36	0.84	-	-	-
Location C	Behavior	Cycling	Cycling	Cycling	Variable -speed	Out of capacity
	Convergence	No	No	Yes	Yes	Yes
	COP	6.352	5.927	4.987	4.264	3.356
	Uncertainty	±0.709	±0.461	±0.335	±0.274	±0.249
	Test duration	3.1hrs	3.1hrs	3.3hrs	1.7hrs	1hr
	Cycle period	1.03hrs	1.03hrs	1.65hrs	-	-
	Cycle duty	0.39	0.69	0.91	-	-

B had the smallest temperature fluctuation, while the test with location C had the most significant fluctuation.

Details of the three dry-coil tests are provided in table 4.2. The cycling periods were shortest for location B and longest for location C. The test duration under variable-speed operation was also shortest for location B. There were significant differences in COPs for the different thermostat locations at test conditions where the unit cycled on and off. The results for the $113^{\circ}F$ test interval was identical for the three tests, since full-load dry-coil test results are not sensitive to thermostat location.

Table 4.3.
$SCOP_c$ for three dry-coil tests

Climate zone		Cold/dry	Marine	Hot/dry
Location A	$SCOP_c$	5.72	5.54	5.31
	Uncertainty	±0.23	±0.21	±0.19
Location B	$SCOP_c$	5.47	5.33	5.12
	Uncertainty	±0.23	±0.21	±0.19
Location C	$SCOP_c$	5.56	5.43	5.24
	Uncertainty	±0.24	±0.22	±0.19
$SCOP_c$ difference	$\frac{SCOP_{c,A}-SCOP_{c,B}}{SCOP_{c,A}}$	4.5%	3.9%	3.4%
	$\frac{SCOP_{c,A}-SCOP_{c,C}}{SCOP_{c,A}}$	2.8%	2.1%	1.2%

The impacts of thermostat location on seasonal performance are presented in table 4.3 for three dry climates in terms of $SCOP_c$. As can be seen, $SCOP_c$ for all three dry climates were the highest with the thermostat installed at location A and lowest for location B. Relative differences of $SCOP_c$ varied from 1% to 5%. The $SCOP_c$ differences are partly due to different thermostat and test unit dynamics that led to different cycling behaviors. The $SCOP_c$ differences also resulted from the differences in the average return air temperature, as can be seen from figure 4.7, because of the poor resolution ($1^{\circ}F$) in the thermostat temperature offset. The

average return air temperature was highest for tests at location A that led to better seasonal performance.

The results demonstrate that the seasonal performance is somewhat sensitive to thermostat location and dynamics. In terms of reasonable thermostat dynamics and test behaviors, location A seems to be a reasonable choice. However, it is likely that the same thermostat location (e.g. location A) would result in different test behavior and performance in a different psychrometric test chamber and test reproducibility is likely to be no better than 5% in terms of $SCOP_c$. Frankly speaking, there is no guarantee that the "location A" (thermostat mounted on the indoor unit sidewall 5 ft above floor) will be identical to each other across different test facilities.

Location B and C were meant to represent a range of dynamic behaviors for the thermostat. Location C had slow dynamics, whereas location B had relatively fast dynamics. One advantage of location B is that it is likely the most repeatable choice for different facilities since the thermostat is located in a flow stream with a known air flow and a temperature that is the test unit return air temperature. It also has the fastest dynamics, which could reduce the testing time. However, a drawback is that the thermostat dynamics are not representative of a field application. The seasonal performance at location B was the worst among the three locations, which could have resulted jointly from the most sensitive response of the thermostat and the lowest average return air temperatures maintained during the dry-coil test for location B.

Understanding the influence of thermostat location within the indoor test room on equipment performance is extremely important towards understanding the potential for reproducibility of load-based test results across different test facilities. This study demonstrated that the dynamics of the test thermostat can vary significantly with location due to non-uniform air velocity and temperature distribution within the room. Locations with higher air velocity and faster thermostat dynamics result in faster convergence of test intervals but more unsteady equipment cycling behaviors. Thus, it is important to define a strategy that provides a reproducible environment for the test thermostat across different laboratory facilities.

4.2 Air sampling apparatus

Since the study on a range of thermostat installation locations demonstrated that the dynamics of the test thermostat in load-based testing can vary significantly with location due to non-uniform air velocity and temperature within the indoor test room, it is challenging to directly define a realistic installation location that can be reproduced across different testing facilities.

As an alternative approach, a thermostat environment emulator could be employed that emulates inlet conditions to the thermostat that are representative of field conditions and that can be reproduced across different test facilities. This includes providing typical flow conditions and the appropriate virtual building dynamics associated with varying inlet temperatures to the test thermostat. Meanwhile, the indoor test room where the emulator is located emulates/provides the same virtual building dynamics to the test equipment associated with its varying return air temperatures, as is shown in figure 4.1. The environment emulator should include a plenum or a small chamber that encloses the test thermostat, air velocity controls that provide representative flow conditions and air temperature controls that emulate the virtual building dynamics to the test thermostat.

In terms of providing typical flow conditions to the test thermostat, the NEMA standard [13] specifies that air should flow across the thermostat vertically and uniformly with a nominal velocity of 30 ft/min. This is thought to be representative of a wall-mounted thermostat and is the basis for the air velocity specification in the current work.

In terms of the test thermostat inlet air temperature control, low-cost, small and fast-responding cooling/heating devices or alternative approaches are preferred for integration within the thermostat environment emulator. The approach considered in this section is to sample the indoor test equipment return air and draw it to the inlet of the test thermostat inside the emulator, with the goal of having consistent

inlet conditions for both the thermostat and the test equipment in load-based testing. The emulator developed using this approach is called an "air sampling apparatus."

The air sampling apparatus is composed of an air sampling tree, an air sampling plenum, a variable-speed fan, and controls. Figure 4.8 includes a diagram of the air sampling apparatus along with an assembled prototype. Airflow is drawn from the indoor test equipment return air inlet through the air sampling tree to the test thermostat inside the air sampling plenum using an axial fan. The test thermostat is mounted on a plywood board with thermocouples measuring the air temperature 1" upstream of (below) the thermostat. This measurement is used as the reference for feedback control of the indoor psychrometric chamber during load-based testing with the setpoints determined dynamically by the virtual building model outputs.

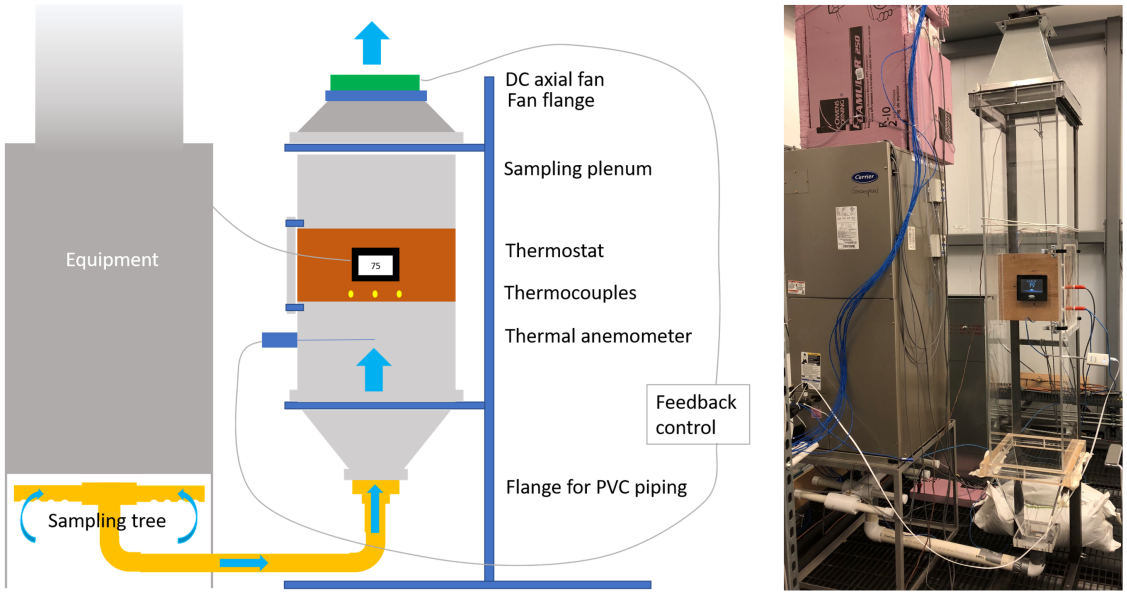

Fig. 4.8. Air sampling apparatus

The air sampling tree was designed and constructed according to AHRI 550/590 [14]. Air is drawn through the sampling holes on the branches of the tree to merge into the main trunk and then enters the downstream components of the apparatus.

The branches were constructed using 2"-diameter PVC pipes and connection parts. The main trunk that connects the sampling tree to the sampling plenum uses 4" PVC pipes.

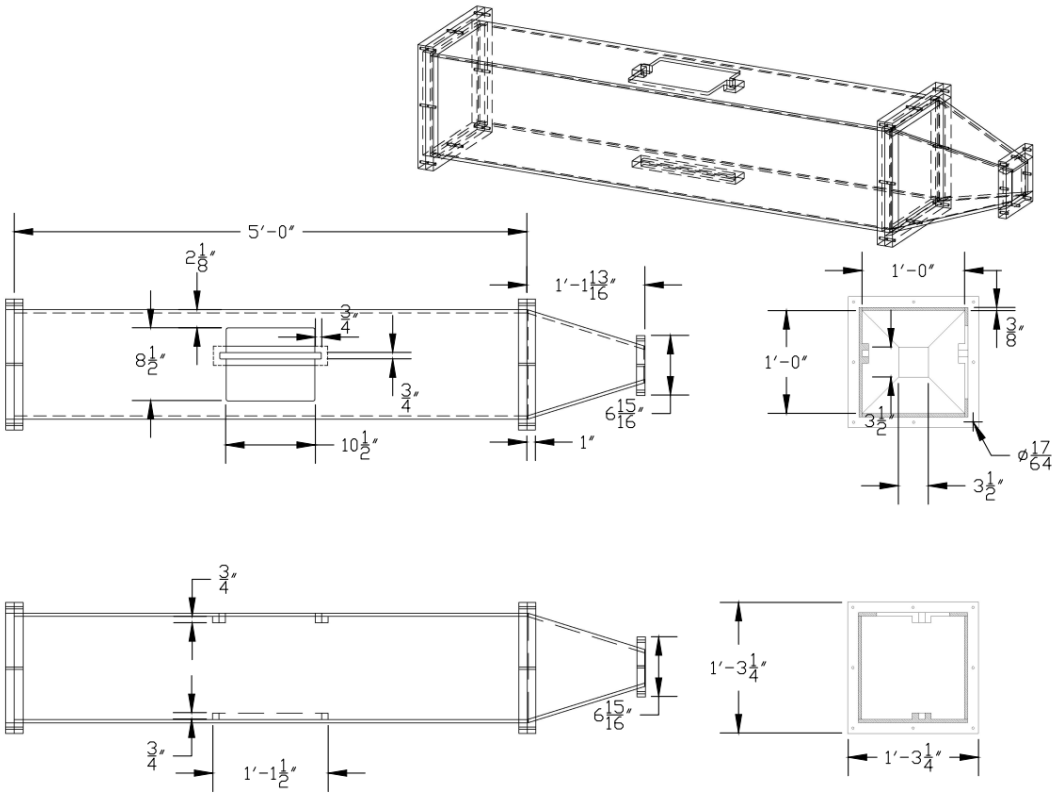

Fig. 4.9. Drawing of air sampling plenum

The air sampling plenum was designed to generate uniform airflow upstream of the test thermostat and fabricated using transparent material (acrylic) to be able to view the thermostat display. The plenum design is shown in figure 4.9. The square plenum is 5' long and has an internal dimension of 12" x 12", so that most common size thermostats can be accommodated inside the plenum. A smaller cross-sectional area could result in uneven distribution of internal airflow, while a larger cross-sectional area will be unnecessary and more expensive. The thickness of the acrylic enclosure is 3/8". The 1'-long pyramid shape piece at the inlet to the plenum

serves as a transition for air to flow inside and expand smoothly from the sampling tree. In the center of the plenum, where the airflow pattern is relatively stable and uniform, there is a slot for a thermostat mounting panel. Inside the slot, there are additional smaller pieces attached to help hold the panel. A plenum cap above the slot can seal the apparatus with 4 latches. In figure 4.8, the wires for instrumentation and the thermostat connection run through the plenum cap. With this design, it is convenient to insert or pull the thermostat panel into or out of the sampling plenum. Downstream of the sampling plenum there is a nozzle fabricated from sheet metal that acts as a transition to the axial fan.

The variable-speed axial fan is controlled to maintain 30 ft/min (0.15m/s) airflow across the test thermostat according to NEMA DC 3-2013 [13]. A Mechatronics G1338H DC axial fan was selected that allows its speed to be controlled using a variable DC drive. A DROK 200085 Boost DC voltage regulator and a 12VDC power supply (Harrison Laboratories 6206A, 64VDC (variable), 0.5A power supply, configured at 12 VDC) jointly serve as the variable DC drive. The 12 VDC output from the power supply is scaled linearly from 0 to 100% by the voltage regulator according to a 0 to 5 VDC control signal that the regulator receives. An air velocity measurement location can be seen in figure 4.8 where a thermal anemometer (SensoAnemo series 5100LSF transducer with omnidirectional sensor) was installed 1' upstream of the test thermostat. The tip of the probe is located at the center of the plenum (and the thermostat). The measurement was utilized to control the DC fan speed. For load-based tests, the plywood board where the thermostat was mounted was cut into a wood frame with an upstream opening and the thermostat was mounted on a thin sharp-edge plastic strip that doesn't disturb the airflow upstream of the thermostat as is shown in figure 4.12. This leads to a more uniform airflow distribution inside the plenum upstream of the thermostat. Feedback control of the fan speed based on measurement of the air velocity was implemented to ensure constant airflow across the thermostat. The proportional gain and integral time for the air sampling apparatus DC fan controller were tuned to be 0.05 VDCmin/ft and 50s.

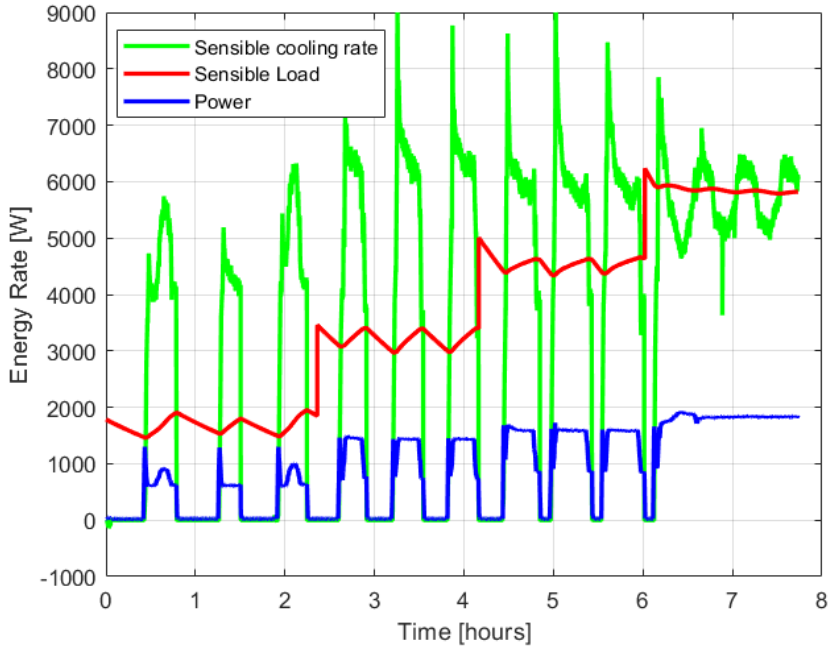

Fig. 4.10. Sensible cooling rate, sensible load, and power measured in dry-coil load-based testing using air sampling apparatus

To evaluate the air sampling apparatus, a dry-coil load-based test was conducted using the experimental setup and test procedures presented in chapter 2. Results for the variable-speed air conditioner test are shown in figure 4.10 and figure 4.11. In figure 4.10, the green line represents a real-time measurement of the test equipment sensible cooling rate, the red line represents the sensible virtual building load that the equipment responds to and the blue line represents a measurement of the equipment total power. The whole sweep of the dry-coil load-based test included four dynamic test intervals that utilized $77°F$, $86°F$, $95°F$, and $104°F$ outdoor temperatures and their associated sensible building loads. The dynamic responses of the test equipment and its integrated controls to the building loads is evident, which significantly distinguishes load-based testing from traditional steady-state testing. For example, the test equipment cycled on and off to satisfy the thermostat during the 1^{st}, 2^{nd} and 3^{rd} test intervals, while within the 4^{th} interval, the equipment continuously modulated its

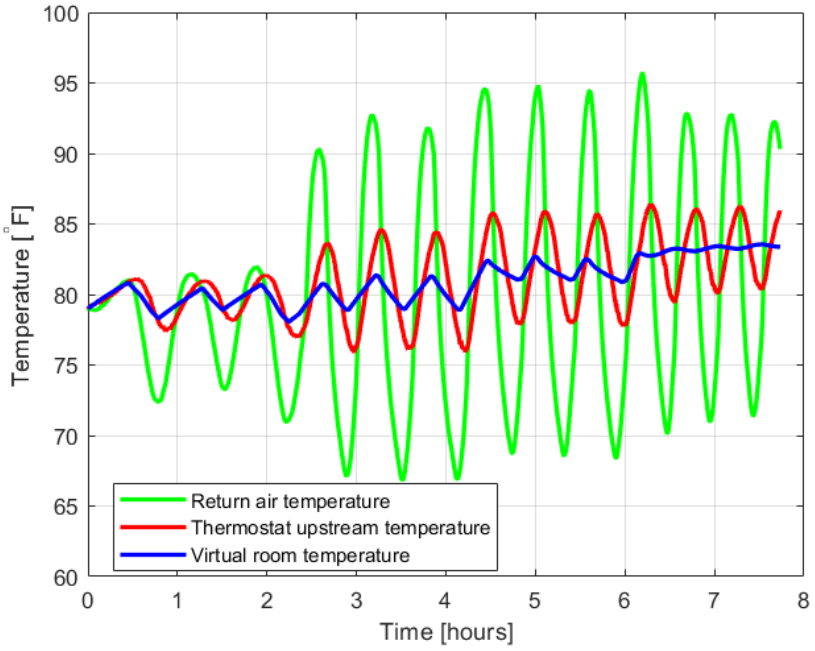

Fig. 4.11. Temperatures in dry-coil load-based test testing using air sampling apparatus

compressor and indoor fan speed in trying to maintain the thermostat setpoint and match its cooling rate to the building load. Speed modulations were also observed when the equipment cycled on during the first three test intervals.

In figure 4.11, the green line represents the indoor test equipment return air temperature measurement, the red line represents the thermostat upstream temperature measurement in the apparatus, and the blue line represents the virtual room temperature setpoints adjusted based on outputs from the virtual building model in real time. As can be seen in figure 4.11, the air sampling apparatus failed to achieve its goal of having consistent inlet temperatures for both the thermostat (red line) and the indoor test equipment (green line). There were fluctuations in the indoor equipment return air temperature that were much larger and out of phase compared with the variations of the thermostat upstream temperature. This occurred because the thermostat upstream temperature response was damped by a significant thermal

mass associated with the acrylic air sampling plenum that was thermally coupled to the airflow inside the plenum through convective heat transfer. Therefore, the return air temperature fluctuated in response to feedback control of the psychrometric chamber reconditioning system trying to maintain the thermostat upstream temperature to the time-varying virtual room temperature setpoints (blue line). The amplitude of the fluctuations increased with increasing load at conditions where the equipment was cycling on and off. In addition, the slow transient response of the thermostat upstream temperature to the variations in return air temperature led to poor feedback control tracking to the setpoints from the virtual building model. Sluggish response of the thermostat led to unrealistic behavior of the test equipment with frequent full-load (high speed) operation occurring in part-load test intervals where the equipment was also cycling on and off.

Additional modifications were investigated to improve the apparatus dynamic response that included adding internal insulation inside of the apparatus plenum and increasing the overall apparatus air flow while providing a flow restriction to maintain a target velocity upstream of the thermostat. However, the air sampling apparatus could not achieve the goal of providing thermostat inlet temperatures that closely match inlet temperatures to the test equipment with air flows representative of a wall mount within a building. A single degree of freedom in temperature control of the indoor room is not sufficient to ensure that both the equipment and thermostat inlet temperatures adequately track the desired response. Therefore, this approach was abandoned in favor of an independently controlled apparatus.

4.3 Independently conditioned apparatus

An independently conditioned/controlled apparatus is basically a smaller version of the NEMA testing apparatus [13] using fast-responding thermoelectric devices. The use of separate cooling/heating devices instead of the air sampling device requires that the thermostat inlet temperature “mirror” the response of the return air temperature

with both independently controlled to temperature setpoints dictated by the virtual building model. As the dedicated cooling/heating devices, TECs (thermoelectric coolers) can be readily scaled to a small thermostat emulator/apparatus, can provide a fast response, and can provide either heating or cooling when their power polarity is reversed. CP45H series TEC modules from CUI devices are used, whose dimensions can be found in figure 4.15 and whose performance specifications can be found in figure 4.17 and table 4.4.

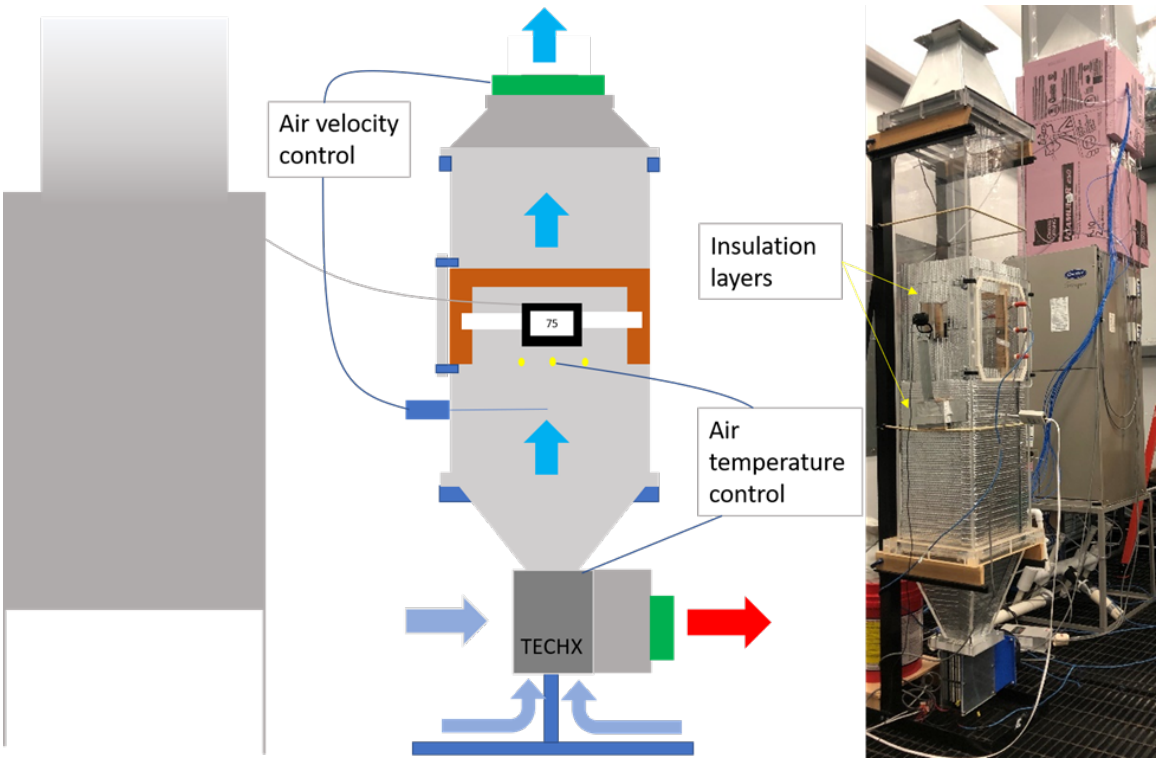

Fig. 4.12. Independently conditioned apparatus

The independently conditioned apparatus is composed of four parts: 1) thermostat plenum (enclosure), 2) thermostat inlet air velocity control, 3) TEC heat exchanger (TECHX), and 4) thermostat inlet air temperature control, as is illustrated by the left-hand-side schematic in figure 4.12. There is also a picture of the whole setup inside the indoor psychrometric chamber including the indoor test equipment, the

apparatus and insulation that was added to the plenum. During load-based testing, the plenum fan on the top constantly draws airflow into the plenum through the TECHX at the bottom, such that the air velocity across the test thermostat is maintained at 30 ft/min according to NEMA DC 3-2013 [13]. The measurements taken by thermocouples located 1 inch upstream of the test thermostat are used as a control input to regulate the TECHX to track virtual room temperature setpoints that are outputs from the virtual building model. The TECs assembled within the TECHX provide heat pumping between a crossflow air stream and the air that vertically enters the apparatus.

The thermostat plenum and the air velocity control were adapted from the air sampling apparatus introduced in section 4.2. Therefore, the independently conditioned apparatus is still a pass-through device that draws air from the indoor chamber and exhausts air to the chamber. As the indoor psychrometric chamber controls the indoor equipment return air temperature to the virtual room temperature setpoints during load-based testing, the inlet conditions of the apparatus at its inlet are close to the desired setpoints. Hence, the TECHX only needs to address the dynamics associated with the thermostat plenum in order to control the thermostat inlet temperature to the same setpoints. In addition to the plenum used in the air sampling apparatus, there are thermal insulation layers attached internally to the plenum upstream of the test thermostat to reduce convective heat transfer between the airflow and the acrylic plenum, as can be seen in figure 4.12. Also, a web camera is utilized to record the thermostat display temperature and to better monitor the test thermostat behaviors.

The design and controls of the TECHX are described in subsection 4.3.1 with sufficient detail to allow future researchers to reproduce the device. A two-dimensional dynamic numerical model of the TECHX is introduced in subsection 4.3.2 to predict its response that was used to guide the overall design process. This model could be useful to others in developing future improvements to the apparatus. Load-based test results acquired using the independently conditioned apparatus are presented in subsection 4.3.3 that validate its ability to meet the target objectives.

4.3.1 Design and controls of the TEC heat exchanger

3D drawings of the TEC heat exchanger assembly are shown in figure 4.13. The drawing on the left shows that the whole assembly is flanged to the bottom of the acrylic thermostat plenum. When the thermostat inlet temperature is above the target temperature setpoint established by the virtual building model (i.e. TECHX is in cooling mode), airflow that enters the thermostat plenum will be cooled as it flows upwards through the vertical conditioning channels (see figure 4.15) of the TECHX. In this mode, the crossflow air will be heated as it flows through the horizontal ambient air channels. When the TECHX is in heating mode, the air that flows through the conditioning channels will be heated while the ambient air through the horizontal channels will be cooled.

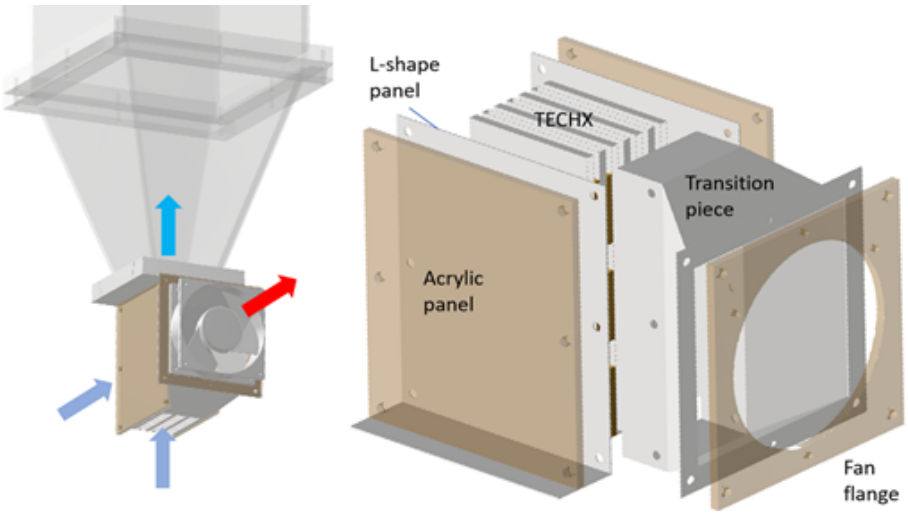

Fig. 4.13. 3D drawings of TECHX assembly

The right-hand-side drawing of figure 4.13 presents a closer look at the whole assembly of the TECHX. The heat exchanger is sandwiched by two L-shape panels and two acrylic panels with six bolts running through the assembly. The two L-shape sheet metal panels also jointly serve as a flange to connect to the thermostat plenum above. The transition piece connects the rectangular heat exchanger to the circular heat exchanger fan mounted on the flange in figure 4.13. The heat exchanger fan

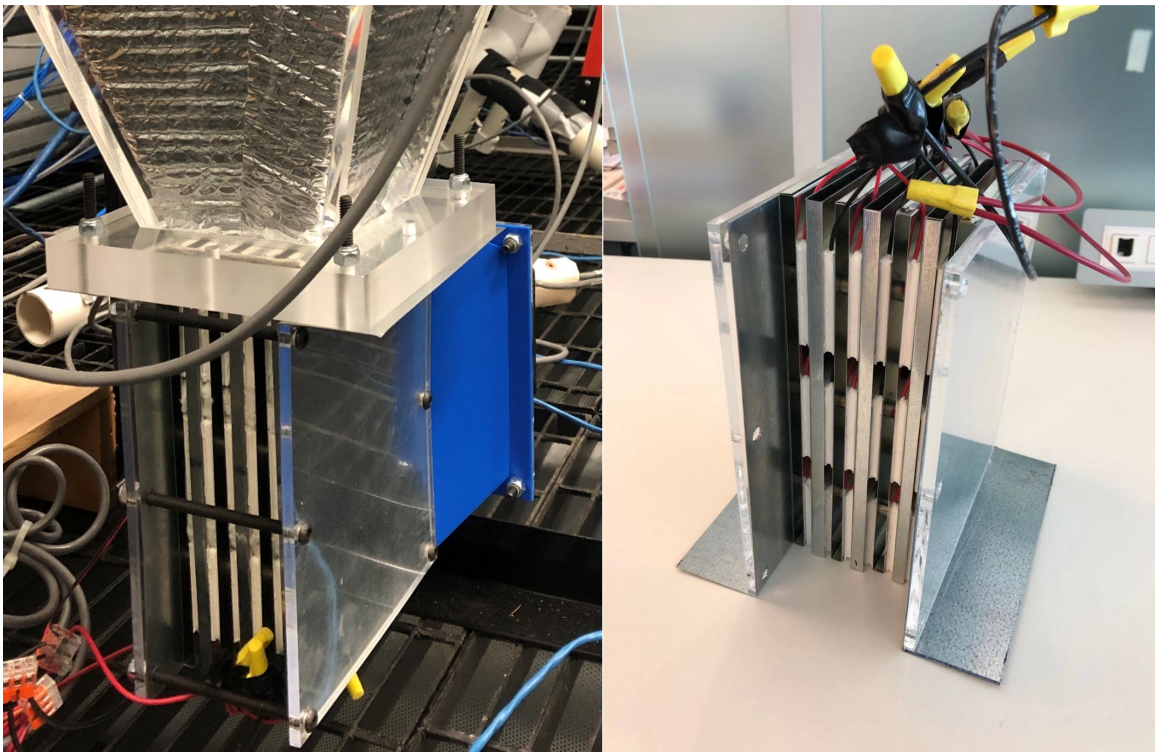

Fig. 4.14. TECHX assembly

needs to be distinguished from the plenum fan mentioned above. The plenum fan is installed on the top of the apparatus and is used to draw 30 cfm airflow vertically through the apparatus (assuming the internal airflow is 30 ft/min uniformly across the 1ft x1 ft plenum cross-section area), while the heat exchanger fan here draws 300 cfm crossflow ambient air to serve as a heat sink in the cooling mode and a heat source in the heating mode of the TECHX. There is no feedback control for the heat exchanger fan and it is directly powered to its maximum speed (approximately 300 cfm), since the higher the airflow, the better the performance of the TECHX. Figure 4.14 shows the manufactured TECHX where the white parts are TECs and the blue plastic is the 3D-printed transition piece according to the drawing above.

Figure 4.15 presents more details of the TECHX. One pair of the conditioning and ambient air channels is shown in subfigure (a) where a layer of six TECs is

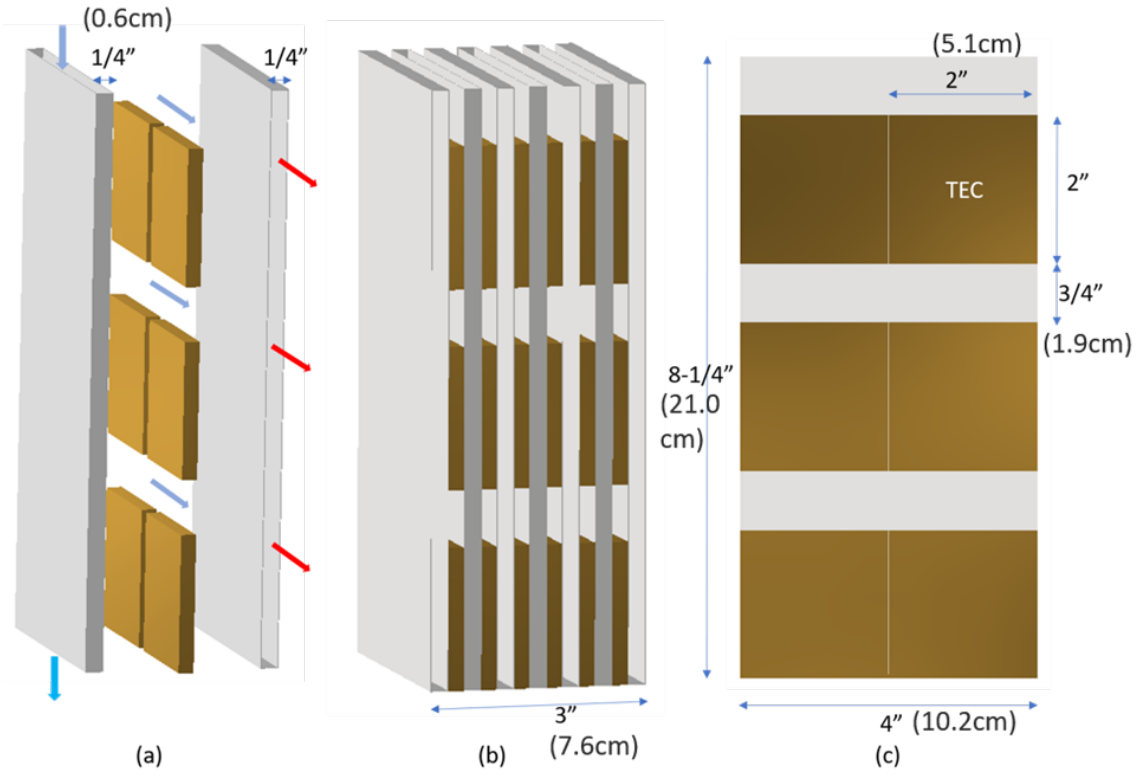

Fig. 4.15. (a) Schematic of airflow pattern (b) 3D drawing of TECHX (c) Arrangement of TEC layer

sandwiched between the two channels. Both the air channels are made of 30-gauge (1/80" thickness) sheet metal. The polarity of the six TECs is consistent within this layer. In cooling mode, the left-hand-side surfaces of the six TECs are cold to cool down the conditioning channel on the left. The vertical airflow will then be cooled within this 1/4"-gap conditioning channel. Heat will be pumped to the right-hand-side surfaces of the TECs and sink to the right-hand-side 1/4"-gap ambient air channel, and ultimately to the crossflow air within this channel. In heating mode, the heat transfer direction is reversed along with the polarity of the supplied voltage to the TECs. The whole TECHX is shown in subfigure (b), as 4 ambient air channels and 3 conditioning channels are sandwiched in a staggered pattern along with the 6 TEC layers. There is one more ambient air channel than the conditioning channels.

Therefore, each conditioning channel is sandwiched by two ambient air channels along with the TECs to ensure adequate uniformity of the discharge air temperature among the three conditioning channel discharge ports. The polarity of each TEC layer is reversed compared to its neighboring layer(s) in order to achieve a consistent heat pumping direction between the cooled and heated air streams. The overall thickness of the TECHX is approximately 3".

The TEC layout that includes 6 TECs per layer is shown in subfigure (c) of figure 4.15. There are 6 TECs/layer×6 layers=36 TECs used in the overall design. The height of each TECHX air channel is $8 - 1/4$" and its width is 4". Each TEC is 2" × 2" × 0.2". Each TEC layer has three rows of TECs and each row has two TECs placed side by side. There is a 3/4"-wide wiring spacing above each row of two TECs. The air gaps within these wiring spacings could become thermal bridges between the conditioning channels and ambient air channels when ventilated; therefore, the gaps were blocked using insulating materials once the wiring was complete. In addition, the TECs were adhered to the neighboring air channels using thermally conductive tape.

Since the air velocity across the test thermostat in the independently conditioned apparatus is constantly maintained at 30 ft/min by its feedback controller, the air-side capacity of the TECHX can only be modulated by modulating the power supplied to the TECs. In addition, switching between cooling mode and heating mode of the TECHX can be accomplished by switching the polarity of the supplied power. Ultimately, the inlet temperature of the test thermostat should be controlled to the virtual room temperature setpoints that are adjusted based on outputs from the virtual building model in load-based testing. Therefore, the feedback controller of the TECHX compares the measurement of the test thermostat inlet temperature to its setpoints and then outputs a bipolar control signal.

A schematic of the TECHX control is shown in figure 4.16. The feedback control signal has its polarity decoupled from its magnitude. The magnitude of the signal is used to scale the voltage of the DC power from 0 to 100% by voltage regulator 1.

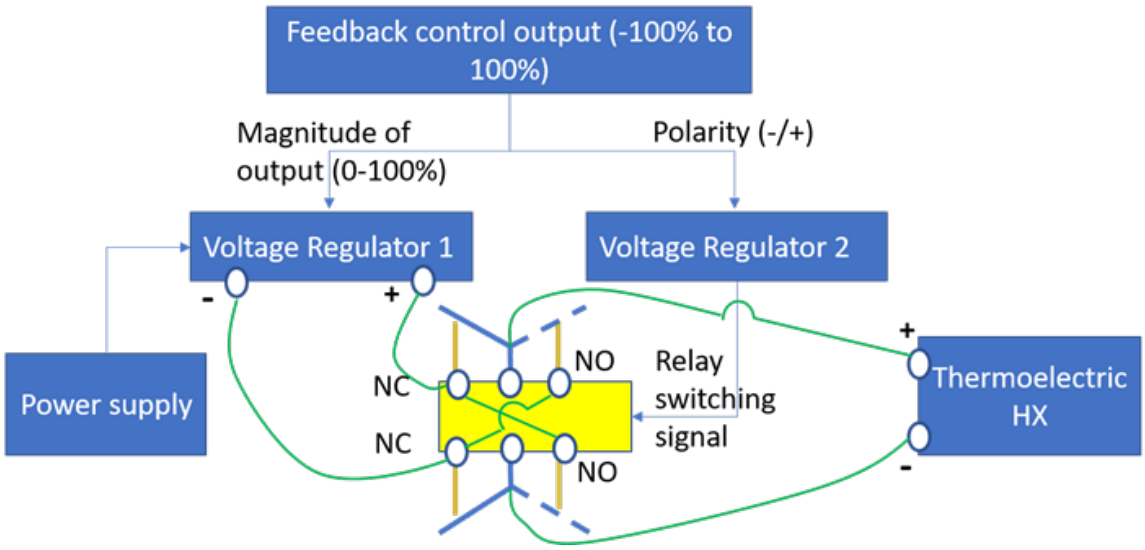

Fig. 4.16. Schematic of the TECHX control

Then, the scaled power is connected to a dual-pole-dual-throw (DPDT) relay (PRD Series power relay from TE connectivity), indicated by the yellow block in figure 4.16. Meanwhile, the polarity of the feedback control signal is interpreted by voltage regulator 2, and this regulator outputs a voltage signal to the coil of the DPDT relay to trigger the switch of its contacts. Therefore, the DPDT relay can output a bipolar and modulated power to the TECHX.

A 48V 15.7A power supply was selected to power all 6 TEC circuits that are in parallel. Each circuit has 6 TECs connected in series that belong to one TEC layer shown in figure 4.15. Therefore, the 6 TECs in each layer are thermally in parallel while electrically connected in series. Voltage supplied to the TECHX can range from -48V to 48V, echoing the -100% to 100% range indicated by figure 4.16. Negative voltage triggers cooling mode of the TECHX and positive voltage triggers its heating mode. A feedback PI controller for the TECHX was tuned to have a proportional gain of $38.4 V/^{\circ}F$ and an integral time of 4 min.

4.3.2 Dynamic model of a thermoelectric heat exchanger

A 2D dynamic model of the TECHX is introduced in this subsection to predict its thermal response to applied power. This dynamic model was useful in finalizing the design of the TECHX, including sizing the TEC modules and power supply. It was important to consider the dynamics because the TECHX needed to respond quickly to provide adequate control of the thermostat inlet temperature in response to changes in the apparatus inlet temperature. The primary dynamics are associated with the thermal characteristics of the heat exchanger metal materials, whereas the TEC modules are assumed to respond quickly and are modeled using quasi-steady relationships.

Lineykin et al. [37] introduced a model that characterizes TEC steady-state performance using only a small amount of manufacturer's rating data as the model parameters, which involve TEC electric resistance R, TEC maximum input voltage V_{max}, maximum input current I_{max} and maximum achievable temperature difference between hot and cold end of the TEC ΔT_{max}. Model inputs involve cold-side temperature T_{cold}, hot side temperature T_{hot} and voltage V (or current I, determined by how power is applied to the TEC) of the supplied power. The TEC steady-state model is utilized in the dynamic TECHX model of this work assuming that the TECs used in the heat exchanger have fast dynamics compared to the dynamics of the heat exchanger material.

The Seeback coefficient that characterizes the thermoelectric cooling effect is estimated using equation (4.1), which is the ratio of maximum input voltage to hot end temperature in Kelvin. A thermal resistance of the module θ is determined using equation (4.2). Then the current of the module is calculated using equation (4.3).

$$S = \frac{V_{max}}{T_{hot}} \tag{4.1}$$

$$\theta = \frac{\Delta T_{max}}{I_{max} V_{max}} \frac{2T_{hot}}{T_{hot} - \Delta T_{max}} \tag{4.2}$$

$$I = (V - S(T_{hot} - T_{cold}))/R \tag{4.3}$$

The cold-end cooling capacity of the TEC module is calculated using equation (4.4), whereas the heating rate on the other end of the TEC module is determined from an overall energy balance using equation (4.5). The COP of the TEC module in cooling mode is calculated using equation (4.6) as the ratio of the cooling rate over the supplied power.

$$\dot{Q}_c = ST_{cold}I - \frac{1}{2}I^2R - \frac{\Delta T}{\theta} \tag{4.4}$$

$$\dot{Q}_h = \dot{Q}_c + IV \tag{4.5}$$

$$COP = \frac{\dot{Q}_c}{IV} \tag{4.6}$$

Manufacturers data for the TECs used in the design of the independently conditioned apparatus is given in table 4.4. This data was utilized to generate a set of performance curves for the TEC module (figure 4.17) using the model above. In figure 4.17, the curves generated by this model are very consistent with the performance curves provided by the TEC manufacturer, particularly at low currents and with small temperature differences, which is the region where the TECs were designed to operate. It is fair to conclude that this TEC steady-state model can adequately characterize the performance of this TEC for the apparatus.

Table 4.4.
TEC manufacturer's data

T_{hot}	V_{max}	I_{max}	R	$\dot{Q}_{c,max}$	ΔT_{max}
$27°C$	15.7V	4.5A	2.5Ω	41W	70K
$50°C$	17.3V			45W	77K

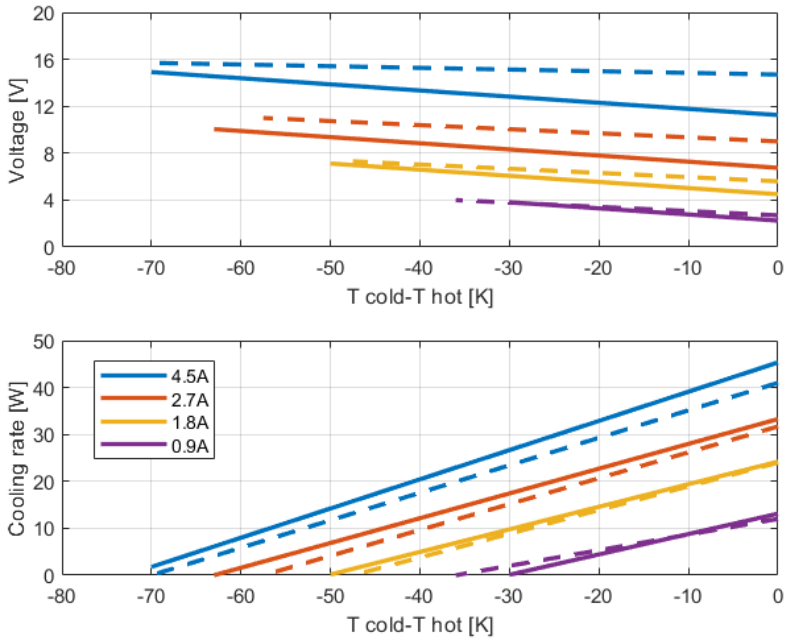

Fig. 4.17. Comparison of TEC predicted (solid lines) and manufacturer's (dashed lines) performance for cooling

A numerical dynamic heat transfer model was developed and applied for the cooling mode of the TECHX. In heating mode, the TECHX should have faster response and more capacity, since the TEC heating rate is always significantly higher than its cooling rate (equation (4.5)) under the same TEC temperature difference and supplied power.

The problem setup for the dynamic TECHX model is depicted in figure 4.18. In the right-hand-side schematic, only one pair of the conditioning and ambient air channels is modeled. For analysis purposes, the inlet condition for the cooled channel was assumed to be 10 cfm, as 30 cfm divided by 3 conditioning channels) and $79^{\circ}F$ (indoor design temperature for dry-coil load-based testing in the CSA EXP-07 draft standard [10]), whereas the inlet condition for the ambient channel was 75 cfm (300 cfm divided by 4 ambient air channels) at $79^{\circ}F$. In the left-hand-side schematic of figure 4.18, the conditioned airflow, conditioning channel sheet metal, ambient air

channel sheet metal and ambient airflow were meshed in the vertical direction into 84 cells with a differential cell height of 8.25”/84 ≈ 0.01”. Therefore, each airflow cell was a 4”×0.25”×0.01” air strip and each sheet metal cell was a 4”×0.0125”×0.01” steel bar. Heat that is transferred between neighboring cells involves convection from air to sheet metal, conduction in the sheet metal, heat pumping through the TECs and the thermal insulation filled within the TEC wiring spacings. The cooling rates and the heating rates of the TECs characterized by the TEC steady-state model above were treated as heat sinks/sources uniformly distributed on the surfaces of the air channel sheet metal cells that are contacting the TECs. Since the mesh grid extends in the vertical direction and the direction across different heat exchanger layers, there are two geometric dimensions (2D) in this TECHX model.

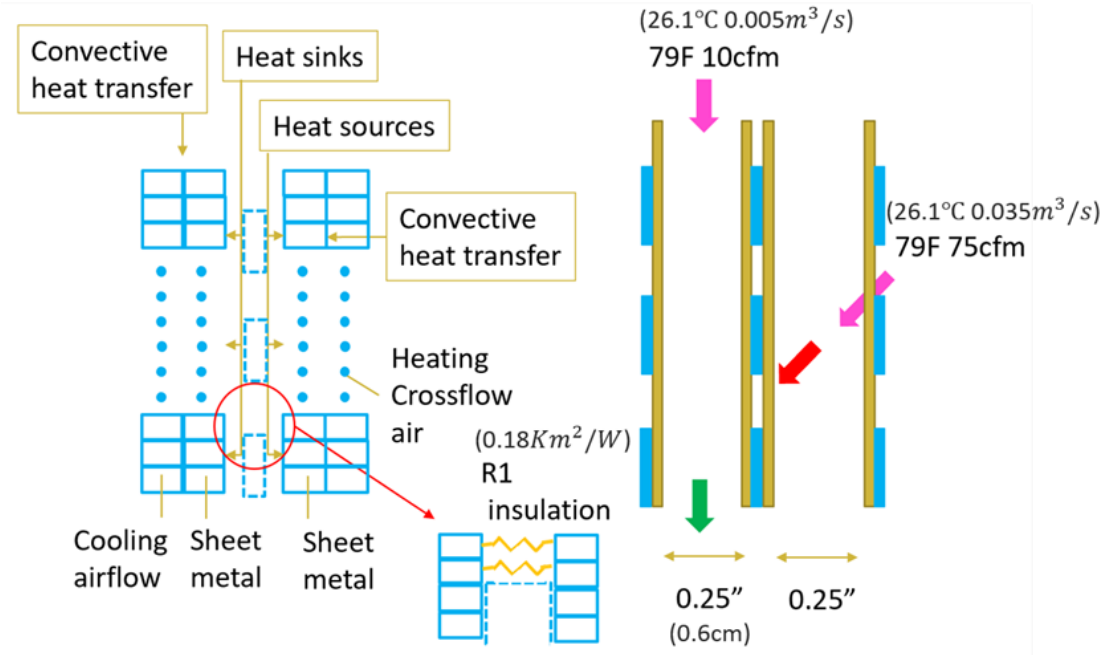

Fig. 4.18. Problem setup for dynamic TECHX model

A large number of discretized equations are involved in this model, but only two are listed below to illustrate the heat transfer mechanisms captured by the model.

Equation (4.7) describes a cell of the conditioning channel sheet metal that contacts the cold ends of the TECs. ρ_s, C_s, k_s are the sheet metal density, specific heat and thermal conductivity, respectively. ΔV_s is the sheet metal cell volume and Δt is the differential time step of the dynamic model. $T^t_{i,2}$ is the temperature of the cell at the current time step. Subscript i represents the row number of the cell in the vertical direction. Subscript 2 indicates that the cell belongs to the column of cells that represent the conditioning channel sheet metal. In this model, columns 1, 2, 3 and 4 represent the conditioned airflow, the conditioning channel sheet metal, the ambient air channel sheet metal and the ambient airflow separately. $T^{t+1}_{i,2}$ is the temperature of the cell for the next timestep. h_c is the convective heat transfer coefficient at the film of the conditioning channel, that is acquired using the correlations introduced by Gnielinski [38]. ΔA is the differential convective heat transfer area. A_s is the sheet metal cross-section area. δ is the differential height of each cell. Δq_c is the differential heat removal due to the TEC modules. The unsteady term is on the left side of the equation, while the right side of the equation is a summation of a convective heat transfer term, two conductive heat transfer terms and a heat sink term. Equation (4.8) describes a cell of the conditioned airflow. The convective heat transfer term is doubled here since the cell is cooled on both sides in this conditioning channel. The last term represents the heat transported in and out associated with the fluid flow. $\rho_a ir$ and Cp_{air} are the air density and specific heat. ΔV_{air} is the airflow cell volume and V_{air} is the 10 cfm conditioned air flowrate.

$$\rho_s C_s \Delta V_s \frac{T^{t+1}_{i,2} - T^t_{i,2}}{\Delta t} = h_c \Delta A (T^t_{i,1} - T^t_{i,2}) + A_s k_s \frac{T^t_{i-1,2} - T^t_{i,2}}{\delta} + A_s k_s \frac{T^t_{i+1,2} - T^t_{i,2}}{\delta} - \Delta q_c \tag{4.7}$$

$$\rho_{air} Cp_{air} \Delta V_{air} \frac{T^{t+1}_{i,1} - T^t_{i,1}}{\Delta T} = 2 h_c \Delta A (T^t_{i,2} - T^t_{i,1}) + \rho_{air} Cp_{air} \dot{V}_{air} (T^t_{i-1,1} - T^t_{i,1}) \tag{4.8}$$

Initially, the temperature profile was set to $79°F$ everywhere. During the simulation, the TECHX responds to a constant voltage across the six TECs that are

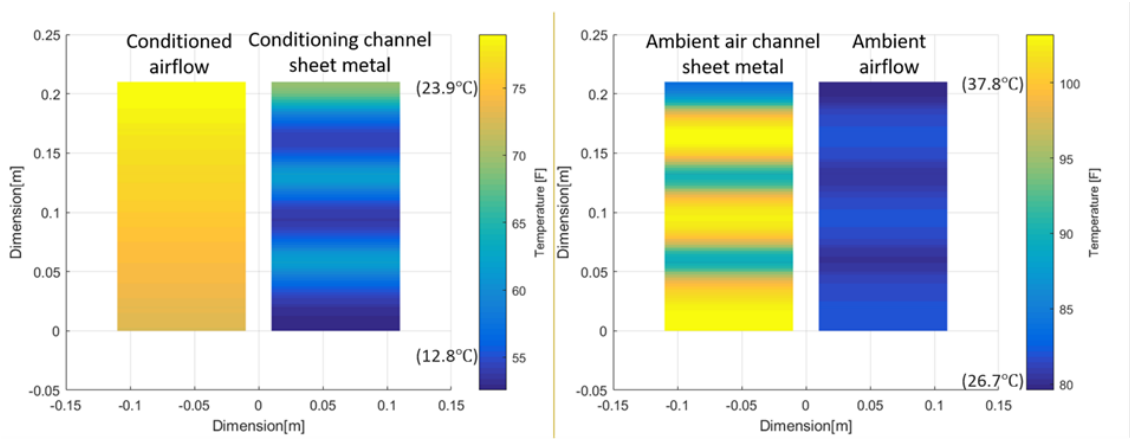

Fig. 4.19. TECHX temperature distribution responding to 20V power after 50 seconds

connected in series, and ultimately reach a steady state. Figure 4.19 shows the simulated temperature distribution of the TECHX after 50 seconds in response to a supplied voltage of 20V where the heat exchanger reached steady state. Each colored block has a size of $8 - 1/4$" $\times$ 4", which is the actual size of each layer of the TECHX. From left to right, the four blocks indicate temperature distribution of the conditioned airflow, the conditioning channel sheet metal, the ambient air channel sheet metal and the ambient airflow. The left-hand-side and right-hand-side graphs use different color scales. In the left-hand-side graph of figure 4.19, the TECHX is able to cool the $79°F$ air gradually down to approximately $73°F$. To cool the air, the conditioning channel sheet metal has the temperature of its coldest cell dropped to about $53°F$. The hottest sheet metal cell reaches a temperature of about $69°F$. The sheet metal temperature distribution is strongly affected by the airflow temperature gradient on one side and the arrangement of the six TECs on the other side. Similar results can be observed on the right-hand-side graph of figure 4.19. The ambient air channel sheet metal has its temperature distributed from about $84°F$ to $103°F$. However, ambient air temperature has a smaller range ($80°F$ to $82°F$) compared to

the conditioned air, as air is drawn through the ambient air channels at a much higher rate.

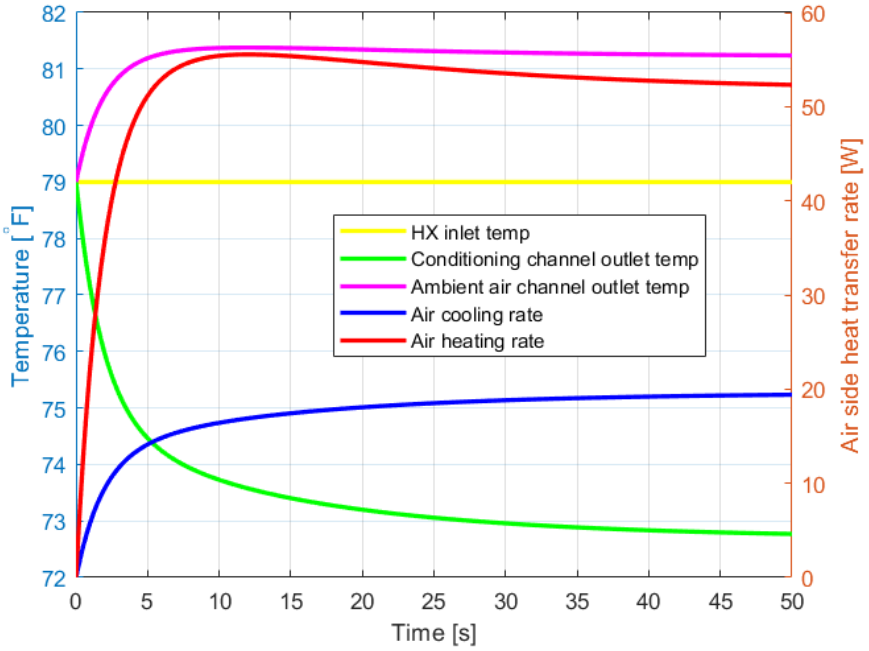

Fig. 4.20. Air-side response of TECHX to 20V power

Figure 4.20 shows the air-side dynamic response of the TECHX to the 20V signal. The left axis shows the air-side temperature, while the right axis indicates air-side heat transfer rate. The conditioning channel outlet temperature (green line) and the ambient air channel outlet temperature (magenta line) start to deviate from $79°F$ while the heat exchanger inlet temperature (yellow line) stays constant at $79°F$. The conditioning channel outlet temperature drops significantly in the first 10 seconds and reaches a steady state of about $72.8°F$ within 50 seconds. The ambient air channel outlet temperature, which is calculated as the average of all ambient airflow cells, reaches a steady state of about $80.7°F$. Air-side cooling rate (blue line) and heating rate (red line) were determined from the simulated temperature differences between the inlets and the outlets of the air channels. At steady state, the air-heating rate is significantly higher than the air-cooling rate, since the TECs dissipate more heat on

their hot ends than the heat they absorb on their cold ends. All the air-side responses are fast within the first 10 seconds and reach steady state within about 50 seconds. A slight overshoot is observed in the heating response, since the heat exchanger can dissipate more heat at the beginning when the temperature difference is much smaller than at steady state.

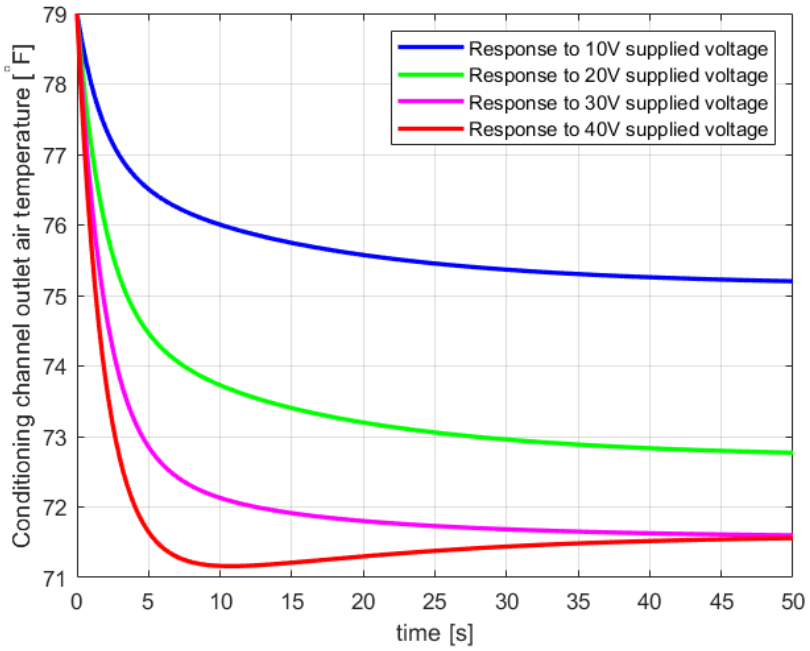

Fig. 4.21. TECHX responses to different supplied voltages

Figure 4.21 shows how the TECHX conditioning channel outlet air temperature responds to various supplied voltages ranging from 10V to 40V. The conditioning channel outlet air temperature is the most important response of the TECHX since this conditioned airflow is then discharged into the thermostat plenum to control the test thermostat inlet temperature. As can be seen from figure 4.21, the TECHX responds more quickly as the applied voltage increases. In addition, from 10V to 30V, the steady-state conditioning channel outlet temperature decreases with increasing voltage. However, with a 40V supplied voltage, an undershoot of the outlet temperature is observed and the steady-state temperature is roughly equal to the temperature

associated with the 30V supplied voltage. The reason is that there is a tradeoff between increasing cooling rate with increased current and decreasing cooling rate due to joule heating and conduction losses with increasing current and temperature difference across the TEC (see equation (4.4)). This sensitivity study was useful in terms of sizing the TECHX power supply and designing the TECHX control.

Table 4.5.
TEC steady-state results for different applied voltages

Supplied voltage	$(T_{hot} - T_{cold})_{average}$	TEC current	$\dot{Q}_{c,average}$	$COP_{average}$
10V	12.64K	0.40A	1.05W	1.57
20V	24.99K	0.80A	1.72W	0.64
30V	37.30K	1.20A	2.05W	0.34
40V	49.80K	1.59A	2.08W	0.20

Average steady-state performance measures were determined for the six TECs operating within the TECHX for the different supply voltages and are presented in table 4.5. With increasing supplied voltage, steady-state TEC temperature difference increases significantly and roughly linearly. A dramatic steady-state COP decrease can be observed as voltage changes from 10V to 20V. With further increased supplied voltage, the COP keeps dropping. The TEC cooling rate also increases in response to increasing voltage, but the capacity begins to saturate between 30 and 40 V. The maximum achievable steady-state cooling capacity for this design and configuration ($79°F$ ambient air, 30 cfm plenum airflow, 300 cfm crossing airflow, etc.) can be estimated as $2.08W \times 36 TEC modules \approx 75W$ associated with a $40V \times 1.59A/layer \times 6 TEC layers \approx 382W$ supplied power.

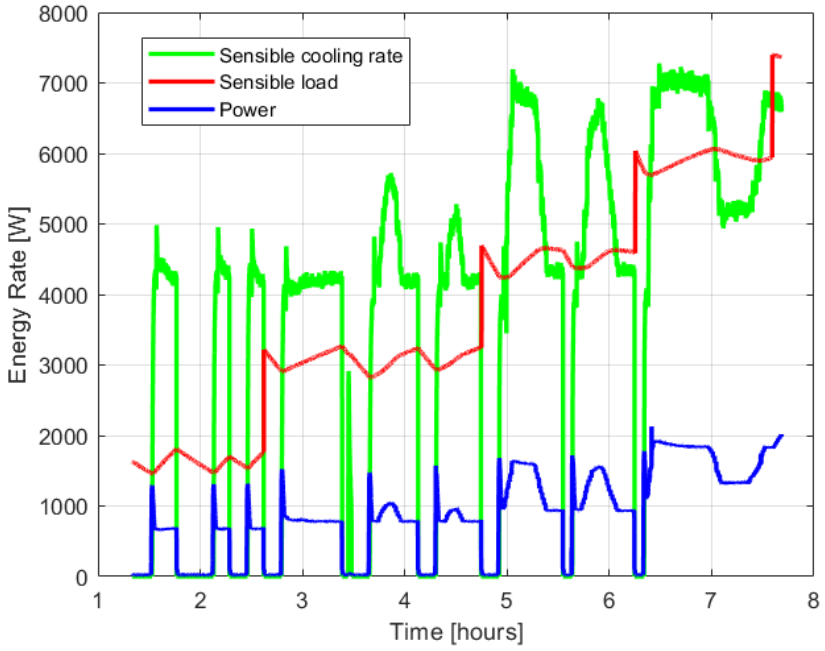

Fig. 4.22. Sensible cooling rate, sensible load, and power measured in dry-coil load-based testing using independently conditioned apparatus

4.3.3 Load-based testing results

To evaluate the thermostat environment emulator, dry-coil and wet-coil load-based cooling tests were conducted using the experimental setup and test procedures presented in chapter 2. The dry-coil test results can be seen in figure 4.22 and 4.23. In figure 4.22, the green line indicates measurement of the equipment sensible cooling rate, the red line indicates sensible virtual building load and the blue line is the measurement of the equipment total power consumption. Four load-based test intervals can be observed with the test equipment frequently cycling on/off at low loads, longer operation at moderate loads, and continuous operation at high loads (the 4^{th} test interval). After the 4^{th} interval, the equipment could not maintain the indoor temperature since its sensible capacity was unable to match the increased building load.

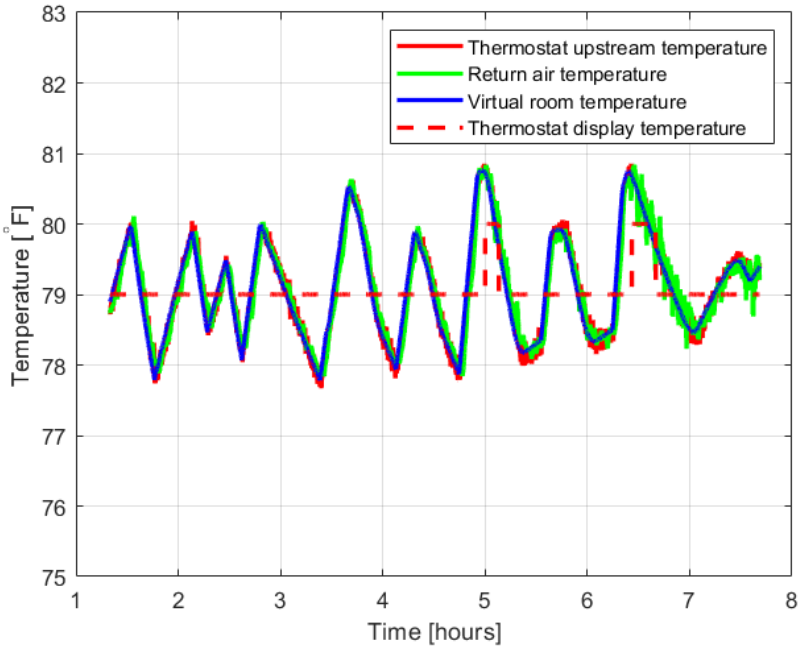

Fig. 4.23. Temperatures in dry-coil load-based testing using independently conditioned apparatus

Figure 4.23 shows the measured test thermostat inlet (red line) temperatures, the measured test equipment return air inlet temperatures (green line), the virtual room temperature setpoints (blue line) and the thermostat display temperatures (red dashed line). It is important to note that the return air and thermostat inlet temperatures were almost perfectly controlled to the virtual room temperature setpoints throughout this test. Specifically, red, green and blue lines overlap each other very well. The indoor temperature was maintained within a dead band between $78°F$ and $80°F$ for most of the time by the test unit thermostat that had a $79°F$ setpoint. The thermostat displayed a $79°F$ temperature for most of the time. It briefly shifted to $80°F$ twice due to the surges in sensible building load. One such event was seen after the test shifted from the 2^{nd} to the 3^{rd} interval and the other was seen after the test shifted from the 3^{rd} to the 4^{th} interval.

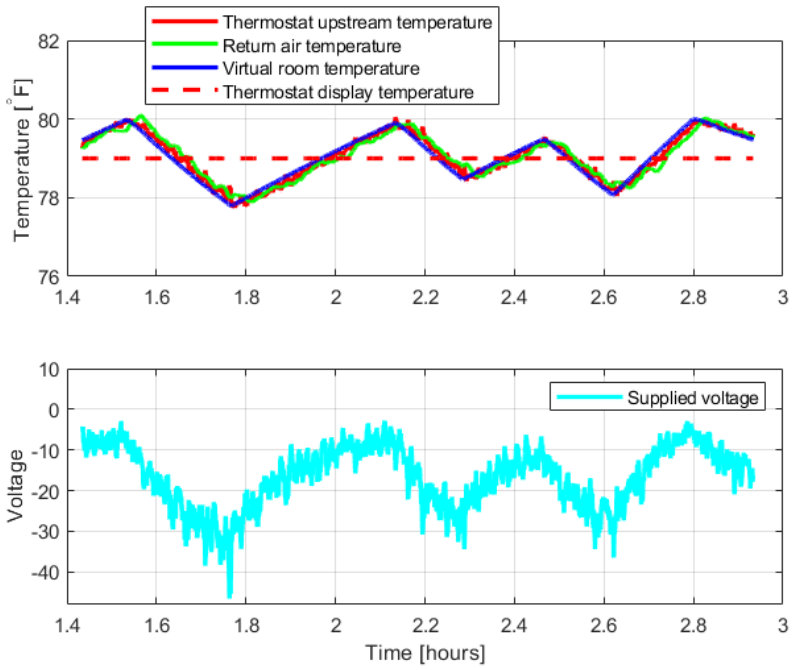

Fig. 4.24. Thermostat inlet temperature control

The upper subplot of figure 4.24 presents a closer look at these temperatures. Although both the thermostat inlet temperature and the indoor test equipment return air temperature tracked the virtual room temperature setpoints well, the thermostat inlet condition controlled by the TECHX generally followed the setpoints better than the return air temperature controlled by the indoor psychrometric chamber reconditioning system. For example, when the virtual room temperature changed direction, the temperature overshoot or undershoot of the thermostat inlet temperature was smaller than the return air temperature. The voltage supplied to the TECHX in the same duration is shown in the lower subplot of figure 4.24. To control the thermostat inlet temperature to the virtual room temperature setpoints, the TECHX ran in cooling mode (negative voltage) for most of the time. The magnitude of the supplied voltage ranged roughly from 0V to 40V. As the virtual room temperature decreased, a larger voltage was supplied to the TECHX to track the decreasing setpoints. High frequency noise can be observed in both the supply voltage and the thermostat inlet

temperature. The reason could be real-time thermal disturbances generated by the test thermostat which was actively self-heating. Thermal mass associated with the thermostat sensor undoubtedly damps this noise but thermocouple measurements upstream of the thermostat have a much faster response. If the airflow inside the thermostat plenum were designed to be downwards (opposite to the current design), the heat generated by the thermostat would lead to even larger disturbances in the temperature measurement upstream of the thermostat, since the heat gains in terms of upwards natural convection could work against the downward cooling airflow.

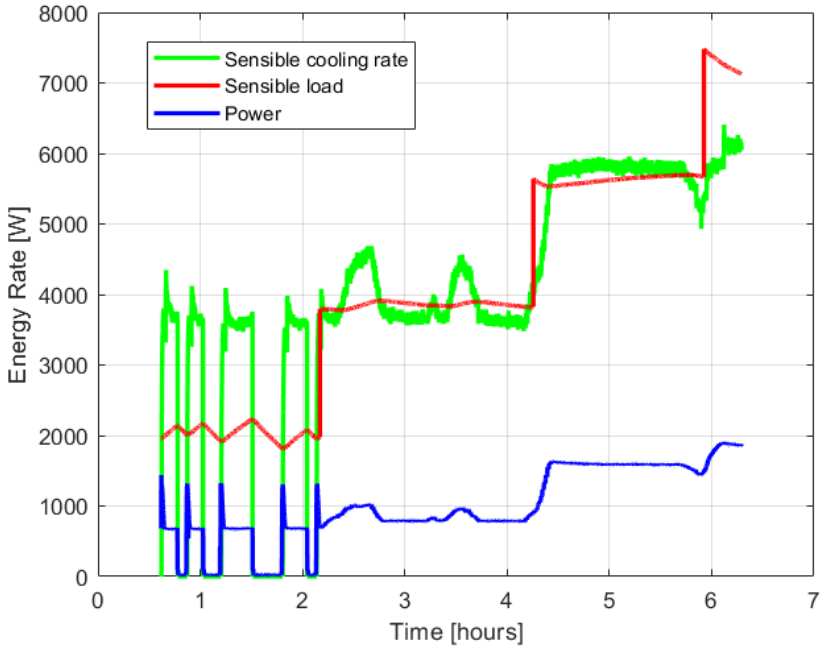

Fig. 4.25. Sensible cooling rate, sensible load, and power measured in wet-coil load-based testing using independently conditioned apparatus

The wet-coil test results can be seen from figure 4.25 to 4.27. Three test intervals with different sensible building loads can be observed in figure 4.25. In the 1^{st} interval, the test equipment cycled on/off, while in the 2^{nd} and $3rd$ intervals, the equipment was able to modulate its speed and match its sensible cooling rate to the load without cycling off. After the $3rd$ interval, the equipment could not maintain the indoor

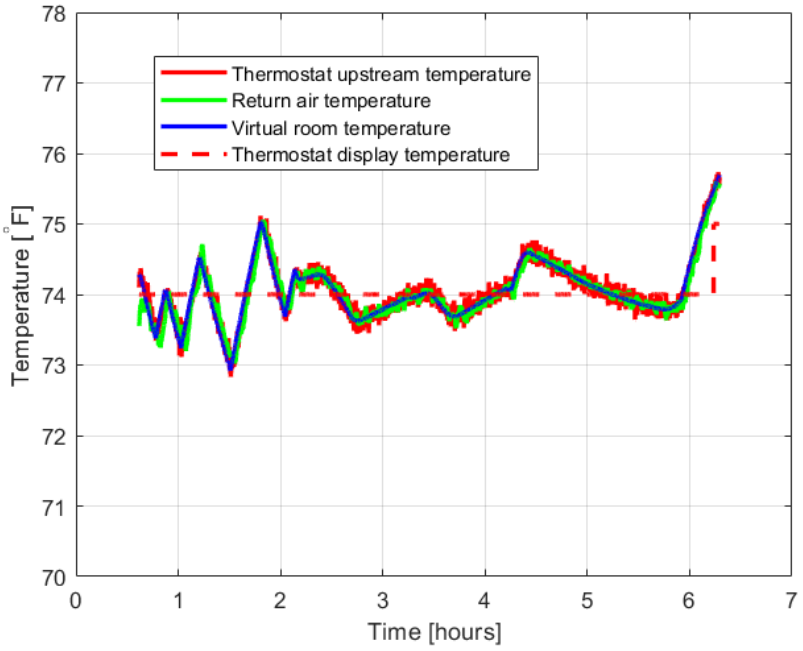

Fig. 4.26. Temperatures in wet-coil load-based testing using independently conditioned apparatus

temperature associated with the thermostat setpoint of $74°F$. Figure 4.26 shows both the indoor equipment return air temperature and the thermostat inlet temperature were almost perfectly controlled to the virtual room temperature setpoints throughout the test using the independently conditioned apparatus. During the first three test intervals, the thermostat displayed a temperature of $74°F$, as the indoor temperature was maintained by the test equipment within a dead band between $73°F$ and $75°F$, while the sensible building load ranged roughly from 2000W to 6000W. As a variable-speed air conditioner, the test equipment maintained the indoor temperature to its thermostat setpoint ($74°F$) better when it modulated its speed, since the indoor temperature variations during the 2^{nd} and $3rd$ test intervals were significantly smaller than the 1^{st} interval when it was cycling on/off. The temperatures rose above the setpoint in the 4^{th} test interval when the equipment cooling capacity was no longer sufficient to meet the load.

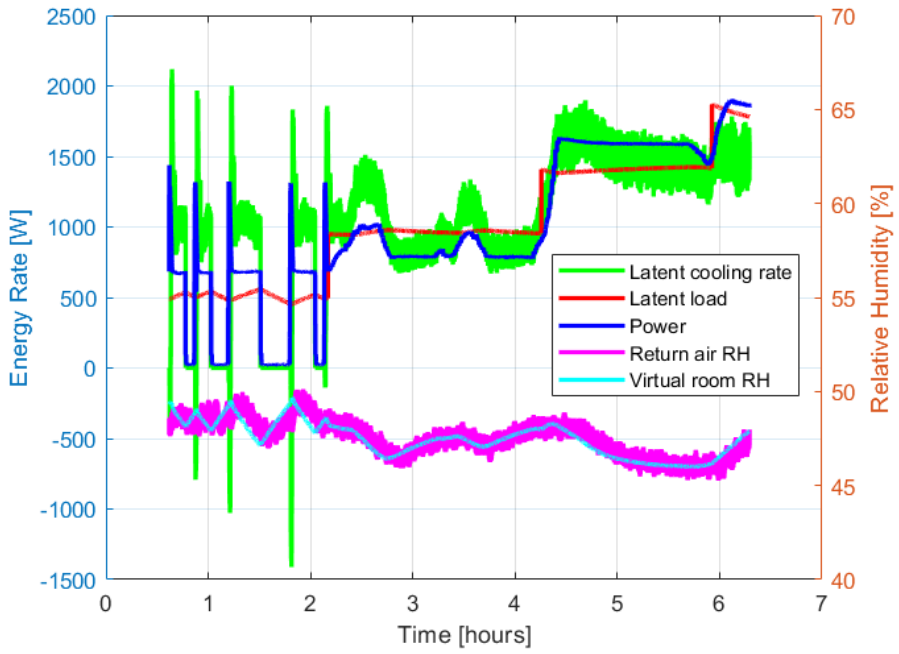

Fig. 4.27. Latent results in wet-coil load-based testing using independently conditioned apparatus

Figure 4.27 describes the latent results for this wet-coil test including real-time measurements of the test equipment latent cooling rate (green line), total power consumption (blue line), indoor return air relative humidity (magenta line), and virtual building model dynamic outputs such as latent building load (red line) and virtual room relative humidity setpoints (cyan line). The latent building load was calculated using the real-time sensible building load associated with a prescribed sensible heat ratio of 0.8 in the wet-coil test. In the 1^{st} test interval, as the equipment turned on its indoor fan in each cycle, negative latent cooling rate was observed, since the condensate on the indoor coil reevaporated to add moisture to the room. Indoor relative humidity was maintained between 45% and 50% during this test, and its return air relative humidity was well controlled to the virtual building relative humidity setpoints adjusted based on the virtual building model outputs.

In this test setup, although the test thermostat incorporates a humidity sensor with a default indoor relative humidity setpoint, it was observed that a dehumidifying mode was not triggered on during this wet-coil test and the equipment native controls responded merely according to the thermostat temperature setpoint, since the latent building load was not extremely high and the room humidity level was moderate. Nevertheless, the thermostat environment emulator cannot achieve humidity control using its cooling/heating device (TECHX), and it could be necessary to modify the emulator to incorporate humidifying/dehumidifying devices if there were significant differences in the humidity dynamic behavior between the inlet to the unit and the inlet to the thermostat. This should be the subject of future work.

4.4 Interim conclusion

A thermostat environment emulator was developed for use in load-based testing as a means of emulating inlet conditions to a test thermostat that are representative of field conditions and that can be reproduced across different test facilities. This device provides typical flow conditions and appropriate virtual building dynamics associated with varying inlet temperatures to a thermostat connected to its test equipment. The environment emulator includes a plenum that encloses the test thermostat, air velocity controls that maintain representative internal airflow and air temperature controls that emulate the virtual building dynamics to the test thermostat that are needed in load-based testing. The chapter provided a detailed description of the design and operation of this thermostat environment emulator that can be used as a basis for providing a standardized solution for applying load-based testing to air conditioning equipment that is reproducible across different facilities. A model of the emulator was also developed and described in detail and could be used to investigate future improvements.

In developing the thermostat environment emulator, two different approaches were investigated: air sampling and independently conditioned methods. The air sampling

approach draws from the return air inlet to the test equipment with the goal of having consistent inlet temperature variations for both the thermostat and the indoor test equipment. However, significant transients associated with the apparatus led to poor performance of this approach and it was abandoned. The independently conditioned device is designed to be located in the indoor environmental chamber and draws air that is similar in temperature and humidity to the test equipment return air at an airflow that is typical of that encountered for a wall-mounted thermostat in a building. The air is cooled or heated, as needed, using thermoelectric coolers (TECs) that are controlled to maintain the thermostat inlet temperature in response to setpoints established by the virtual building model used for load-based testing. A two-dimensional dynamic numerical model of the TEC heat exchanger was developed to predict its response, size different types of TEC modules and choose the associated power supply. The apparatus was integrated into load-based cooling tests for dry-coil and wet-coil climate conditions as specified in chapter 2. The device was able to control the thermostat inlet temperature almost perfectly to the virtual room temperature setpoints for both tests.

Future work is needed to eliminate the high frequency noise that was observed in both the supply voltage and the thermostat inlet temperature in figure 4.24. The reason for the noise could be real-time thermal disturbances generated by the test thermostat which was actively self-heating. It should be possible to eliminate this noise through more advanced or better tuned control of the TECHX. It also may be necessary to consider TECHX devices with more cooling capacity to accommodate potential environmental chambers and situations with inlet temperatures that are significantly warmer than the desired setpoints.

5. EXTENDING LOAD-BASED TESTING FOR EQUIPMENT PERFORMANCE MAPPING

The seasonal performance of unitary residential air-conditioning equipment for various climate zones can be rated by a traditional temperature-bin-based approach, as is introduced in chapter 2. However, a "holy grail" for load-based testing and performance rating is to be able to map equipment performance from automated testing results measured over a relatively short period of time. This performance map can then be implemented as a "model" in a building simulation to generate seasonal performance ratings that are specific to various building types and climates.

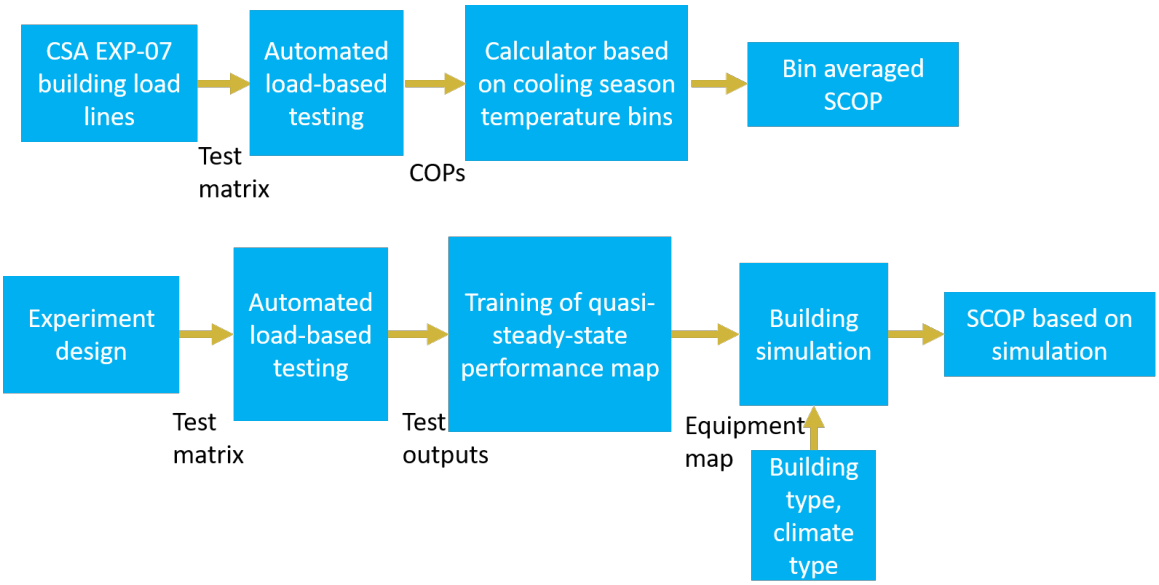

Fig. 5.1. Conceptual comparison between temperature-bin-based and simulation-based performance rating approaches

Figure 5.1 presents a conceptual comparison between the temperature-bin-based and simulation-based seasonal performance rating ($SCOP_c$) approaches. The tra-

ditional approach starts with carrying out load-based tests according to the test matrix/intervals determined by the CSA EXP-07 [2] building load lines. The bin-averaged $SCOP_c$ for each climate zone can then be obtained as the test COPs are effectively averaged according to specific ambient temperature bin hour fractions and EXP-07 building load for each bin. A potential disadvantage of this rating approach is that the $SCOP_c$ values are merely associated with EXP-07 building load lines instead of characterizing different residential building load responses.

A next-generation performance rating approach is developed to determine a rating based on an equipment performance map that is an output from automated load-based testing. As a result of experimental design, a test matrix is defined for load-based testing that generates desired test outputs to be used in training a map of the test equipment that can represent equipment performance across its operating envelope with acceptable accuracy. Based on prescribed building and climate types, test equipment $SCOP_c$ can be obtained using building simulation that incorporates the equipment performance map.

In section 5.2, the investigation of extending load-based testing for performance mapping started with identification of an appropriate model form for residential cooling equipment. A steady-state model form is needed for the intended purposes, since the automated load-based testing results are harvested after the equipment reaches a quasi-steady or steady-periodic condition. In addition, this model form should have the ability to map both the equipment performance and its integrated controllers, as both are captured by load-based testing. Moreover, the development of model form should focus on mapping of variable-speed equipment, since it is the more general case and the load-based testing methodology is particularly important for the next-generation equipment with variable-speed drives and advanced on-board controls.

After the identification of a mapping model form, it is important to optimally search/design an acceptably small number of load-based tests required to train the model. Alternatively, a more general experimental design approach can be obtained that focuses more on sampling test points that provide uniform, complete and unbi-

ased coverage of the operating envelope of equipment, instead of depending on the mapping model form. In order to finalize a test matrix, section 5.4 presents both an optimal/heuristic experimental design approach and an unbiased sampling approach using a clustering algorithm. Compared to the EXP-07 test intervals, the test inputs determined by these approaches are not constrained by specific building load lines.

As load-based tests were carried out according to the experimental design approaches, an optimal set of 12 datapoints from the test results was obtained to train the mapping model, while the test results outside the range of the optimal set were used to validate the trained model. As presented in section 5.5, this optimal performance map is able to well represent the test equipment in terms of cooling rates and COPs in various working conditions and could be incorporated into a building simulation.

Section 5.6 demonstrates a co-simulation approach that couples the obtained mapping model to building dynamics under the framework of EnergyPlus [36]. The simulation-based $SCOP_c$ was calculated as a sum of annual equipment total cooling rate over a sum of annual consumed power of the test equipment that was mapped, which marks the last step of a next-generation seasonal performance rating approach. The rating result was then compared against the rating obtained using the traditional temperature-bin-based approach, followed by a discussion of pros and cons between the two approaches.

5.1 Input and output variables in performance mapping

The identification of a mapping model form should begin with establishing its input and output variables. Since the performance mapping will be an extension of load-based testing, its inputs and outputs can be imported from the test inputs and outputs but modified according to the mapping purposes. Per chapter 2, the outdoor dry bulb temperature, sensible building load, thermostat setpoint and building sensible heat ratio are the test inputs.

Outdoor dry bulb temperature, T_{OD}, is selected as an input to the performance mapping model because it influences the equipment condensing temperature and efficiency. The test unit return air indoor dry bulb temperature, T_{ID}, is also important because it influences the equipment evaporating temperature and efficiency for dry indoor coil operations. Sensible building load, $BL_{c,s}$, is another important input to the performance mapping since the air-conditioning equipment is controlled to match the load using its sensible cooling rate and maintain the temperature of the space to its setpoint. This input is particularly important in ensuring that the equipment performance mapping is able to capture equipment part-load performance and the associated control decisions, which are very important in determining seasonal performance. Latent effects are captured by including the indoor wet bulb temperature, B_{ID} in the mapping inputs, since combined heat and mass transfer to the coil is largely dependent on wet bulb temperature for conditions where moisture condensation is occurring.

Indoor air flowrate is not employed as a performance mapping input variable, since it is modulated at part-load conditions according to decisions made by the embedded controllers of some variable-speed equipment. It could be used as an intermediate variable, if this were preferred by a particular mapping model form. In the mapping model proposed in section 5.2, the rated or maximum air flowrate is used as a model parameter but not an input variable once the model for an air conditioner is established.

A load-based cooling test interval outputs a converged COP that is used directly in the rating approach based on temperature bins. However, more output variables are needed for the purposes of performance mapping with a rating approach based on simulation. For example, equipment total cooling rate $\dot{Q}_t$ is another primary output beside equipment COP. Equipment latent cooling rate $\dot{Q}_l$ and equipment sensible heat ratio SHR can be derived using equipment total cooling rate and equipment sensible cooling rate (equal to the sensible building load for quasi-steady equipment behavior). Equipment power consumption $\dot{W}$ can be derived as a ratio of $\dot{Q}_t$ over

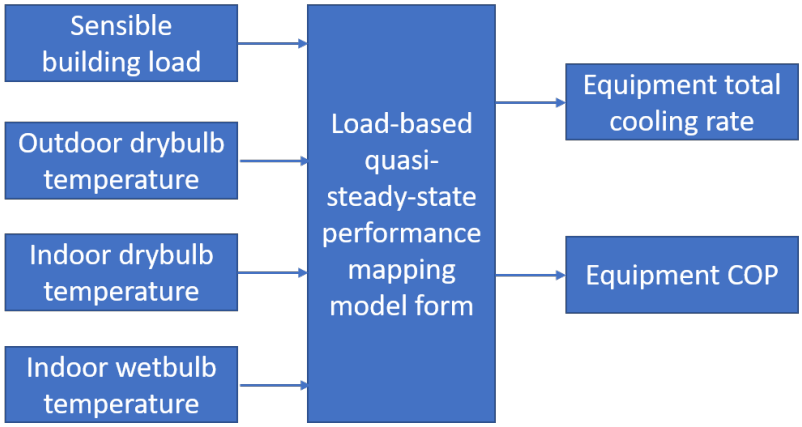

Fig. 5.2. Input and output variables in performance mapping of this study

COP. The primary input and output variables that will be used in a performance mapping model are illustrated in figure 5.2.

5.2 A load-based quasi-steady-state model for a variable-speed air conditioner

In this section, an approach for mapping the quasi-steady-state performance of a variable-speed air conditioner is described that utilizes inputs and outputs introduced above. The model is semi-empirical ("graybox") and utilizes some physical understandings of the processes with the hope that they will reduce the amount of training data required for the mapping compared to a purely "blackbox" modeling approach.

Utilization of the model starts with prediction of the maximum cooling capacity of the equipment. Equation (5.1) provides an empirical correlation of equipment cooling capacity based on rated capacity, indoor wet bulb temperature, and outdoor dry bulb temperature. This cooling capacity is evaluated as an intermediate variable here, since it may be revisited and updated through multiple iterations. Indoor wet bulb and outdoor dry bulb temperatures are normalized by the rating conditions ($B_{ID,rat} = 67°F$, $T_{OD,rat} = 95°F$) resulting in dimensionless coefficients in the polynomial relationship. At rating conditions ($B_{ID} = B_{ID,rat}, T_{OD} = T_{OD,rat}$), evaluation of

equation (5.1) is supposed to return $\dot{Q}_{t,max} = \dot{Q}_{rat}$, i.e. $\alpha \times \sum_{j=0}^{5} a_j = 1$. Therefore, $\dot{Q}_{t,max}$ is forced to physically represent the cooling capacity. It is important to guarantee that the predicted $\dot{Q}_{t,max}$ physically and numerically makes sense, such that the model will be able to distinguish the equipment part-load operation from its full-load operation. Without this constraint, model training could numerically return α and a_i that do not guarantee that the equipment cooling capacity is physically represented by equation (5.1).

$$\dot{Q}_{t,max} = \dot{Q}_{rat} \times \alpha \times (a_0 + a_1 \frac{B_{ID}}{B_{ID,rat}} + a_2 \frac{T_{OD}}{T_{OD,rat}} + a_3 (\frac{B_{ID}}{B_{ID,rat}})^2 + a_4 (\frac{T_{OD}}{T_{OD,rat}})^2 + a_5 \frac{B_{ID}}{B_{ID,rat}} \frac{T_{OD}}{T_{OD,rat}}) \tag{5.1}$$

The second step is to evaluate equipment sensible capacity at specific indoor and outdoor temperatures. A bypass factor approach from the ASHRAE toolkit model [21] is utilized here. This approach is like the NTU-effectiveness calculation procedure used in air-to-refrigerant heat exchanger analysis when $C_{min}/C_{max} = 0$. The bypass factor, BF, is defined in equation (5.2) where the NTU is the maximum number of transfer unit when the indoor fan draws the maximum amount of indoor air flowrate $\dot{V}_{ID,max}$, with its full speed.

$$BF = 1 - \varepsilon = exp(-NTU) \tag{5.2}$$

Since both the return air dry bulb temperature and wet bulb temperature are known, the return air enthalpy can be calculated using psychrometric relations. The supply air enthalpy is then calculated using an energy balance in equation (5.3), where the supply and return air enthalpy difference is determined using equipment total capacity divided by maximum indoor air mass flowrate.

$$h_{SA} = h_{ID} - \frac{\dot{Q}_{t,max}}{\rho_{ID} \dot{V}_{ID,max}} \tag{5.3}$$

The bypass factor is the ratio of the airflow that bypasses the cooling coil over the total airflow that is drawn through the coil by indoor fan. The bypassed air is

assumed to have the same psychrometric conditions as the return air, while the airflow that is not able to bypass the coil is assumed to be effectively conditioned to the dewpoint of the moist air at an effective cooling coil surface temperature. These two streams of airflow are assumed to be evenly mixed in proportion to the bypass factor. The air enthalpy at the apparatus dewpoint enthalpy, h_{ADP}, can be solved using an energy balance for the mixing process (equation (5.4)). The apparatus dewpoint temperature can then be calculated according to psychrometrics using h_{ADP} and an assumed air pressure of 1 bar. The supply air temperature, T_{SA}, can be solved using a sensible energy balance equation (equation (5.5)) for the mixing process. Then the equipment sensible capacity can be calculated using equation (5.6) as a product of the maximum indoor air mass flowrate, the specific heat and the temperature difference between return and supply air.

As a model parameter, bypass factor BF distinguishes itself from model coefficients such as a_i, b_i, etc., since it has significant physical meaning that characterizes evaporator heat and mass transfer at equipment full-load scenarios. Although BF can be obtained in model training along with a_i, b_i using quasi-steady-state datapoints, it was found that BF sometimes could be trained to be a negative value that makes no physical sense. Therefore, it was decided to obtain BF merely using equipment performance at rating conditions ($T_{ID,rat} = 80°F$, $B_{ID,rat} = 67°F$, $T_{OD,rat} = 95°F$). In this way, BF will be obtained before optimization associated with the training introduced in section 5.3, where the other model coefficients will be accommodated with respect to the pre-determined BF value.

$$(1 - BF)h_{ADP} + BF \times h_{ID} = h_{SA} \tag{5.4}$$

$$(1 - BF)T_{ADP} + BF \times T_{ID} = T_{SA} \tag{5.5}$$

$$\dot{Q}_{s,max} = \rho_{ID}\dot{V}_{ID,max}Cp(T_{ID} - T_{SA}) \tag{5.6}$$

$$SHR_{fl} = \frac{\dot{Q}_{s,max}}{\dot{Q}_{t,max}} \tag{5.7}$$

$$\dot{Q}_{l,max} = \dot{Q}_{t,max} - \dot{Q}_{s,max} \tag{5.8}$$

The sensible heat ratio at equipment full-load scenarios SHR_{fl}, can be calculated using equation (5.7) as a ratio of equipment sensible capacity over equipment total capacity. A value of SHR_{fl} that is determined to be larger than one means that the indoor coil is dry and the indoor wet bulb temperature should not be directly used to characterize equipment total capacity in equation (5.1). For a dry coil, the heat transfer across a dry evaporator coil is driven by the indoor dry bulb temperature instead of the indoor wet bulb temperature. However, an effective indoor wet bulb temperature, $B_{ID,eff}$, at this full-load scenario can still be used here, if it is located at the boundary between the dry-coil condition and wet-coil condition. This effective value is higher than the actual wet bulb temperature, and it can be solved iteratively using equations (5.1) to (5.7), in order to achieve $SHR_{fl} = 1$. If the calculated SHR_{fl} is smaller than one, no iterations are needed and the predicted $\dot{Q}_{s,max}$ can directly be used. After the determination of the equipment sensible capacity, its latent capacity can be calculated using equation (5.8).

The third step is to evaluate the sensible part-load ratio of this equipment using equation (5.9). If the sensible building load, $BL_{c,s}$, is larger than the equipment sensible capacity, $\dot{Q}_{s,max}$, the equipment will run full out and a part-load ratio of one is forced. When the building load is smaller than the sensible capacity, the equipment sensible cooling rate at part load, $\dot{Q}_s$, is set equal to the sensible building load $BL_{c,s}$.

$$PLR = min(\frac{BL_{c,s}}{\dot{Q}_{s,max}}, 1) \tag{5.9}$$

$$\dot{Q}_s = PLR \times \dot{Q}_{s,max} \tag{5.10}$$

The fourth step is to relate the equipment latent capacity (calculated in equation (5.8)) to the equipment latent cooling rate in terms of the specific sensible part-load ratio using (5.11). Therefore, the equipment total cooling rate can be calculated using equation (5.12) as a sum of equipment sensible cooling rate (5.10) and latent cooling rate (5.11). Subsequently, the sensible heat ratio at equipment part-load scenarios is evaluated using equation (5.13).

$$\dot{Q}_l = \dot{Q}_{l,max}(b_1 PLR + b_2 PLR^2 + b_3 PLR^3 + b_4 PLR^4) \tag{5.11}$$

$$\dot{Q}_t = \dot{Q}_s + \dot{Q}_l \tag{5.12}$$

$$SHR = \frac{\dot{Q}_s}{\dot{Q}_t} \tag{5.13}$$

The last step in applying the mapping model is to calculate equipment coefficient of performance. Equation (5.14) corrects equipment rated COP (obtained as $\dot{Q}_{rat}/\dot{W}_{rat}$) to equipment COP at specific operating conditions and part-load ratio using two correction factors. Equation (5.15), presents the correction factor for operating conditions, $f_{COP,T}$, as a bi-quadratic polynomial in terms of normalized outdoor dry bulb temperature and effective indoor wet bulb temperature, $B_{ID,eff}$, that was obtained in the second step above. Equation (5.16) presents the correction factor for part-load effects, $f_{COP,PLR}$, as a cubic polynomial in terms of sensible part-load ratio. Equipment power consumption can be obtained using equation (5.17) as a ratio of $\dot{Q}_t$ over COP.

$$COP = f_{COP,T} f_{COP,PLR} \times COP_{rat} \tag{5.14}$$

$$\begin{aligned} f_{COP,T} = c_0(1 + c_1\frac{B_{ID,eff}}{B_{ID,rat}} + c_2\frac{T_{OD}}{T_{OD,rat}} + \\ c_3(\frac{B_{ID,eff}}{B_{ID,rat}})^2 + c_4(\frac{T_{OD}}{T_{OD,rat}})^2 + c_5\frac{B_{ID,eff}}{B_{ID,rat}}\frac{T_{OD}}{T_{OD,rat}}) \end{aligned} \tag{5.15}$$

$$f_{COP,PLR} = d_0 + d_1 PLR + d_2 PLR^2 + d_3 PLR^3 \tag{5.16}$$

$$\dot{W} = \frac{\dot{Q}_t}{COP} \tag{5.17}$$

The overall procedure to implement this load-based quasi-steady-state model is illustrated schematically using figure 5.3. The steps are to evaluate: 1) equipment total cooling capacity; 2) equipment sensible capacity using the bypass factor approach; 3) equipment sensible part-load ratio and sensible cooling rate by comparing the sensible building load to the equipment sensible capacity; 4) equipment latent cooling rate at part-load conditions and the associated total cooling rate and SHR; 5) equipment COP at specific outdoor drybulb temperature, effective indoor wetbulb temperature and part-load ratio.

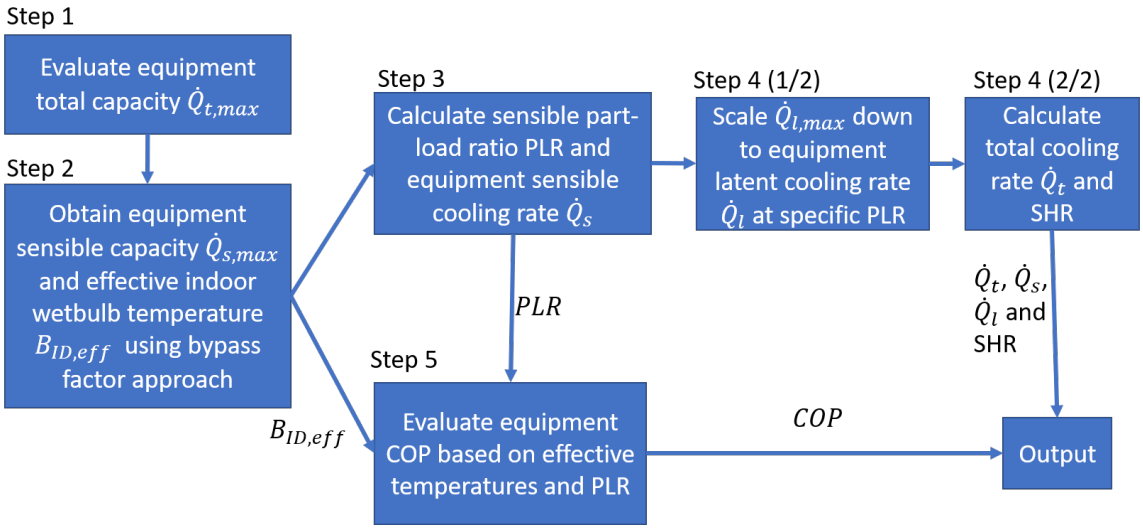

Fig. 5.3. Implementation procedure for the load-based quasi-steady-state model

This model can distinguish between equipment full-load and part-load operations by comparing sensible building load to equipment sensible capacity that is evaluated using a bypass factor approach. This model can also handle both equipment dry-

coil and wet-coil scenarios at part-load by employing an effective indoor wet bulb temperature that is solved iteratively as the sensible heat ratio is enforced to one.

5.3 Model training and validation based on a simulation database

In order to evaluate the performance mapping model form presented above, a significant amount of equipment performance data is required that reflects the operation of the equipment associated with its integrated controls. It is challenging to acquire a large amount of data through load-based testing because of the significant time and cost required. As a result, for the initial development of the mapping approach, data were acquired by simulation using another semi-empirical performance model with a prescribed algebraic control logic that is described in this section.

Nyika et al. [27] developed a semi-empirical generalized model for variable-speed ducted residential equipment. This model represents equipment sensible cooling rate and power consumption at steady states using equipment total cooling rate, indoor air flowrate, outdoor dry bulb temperature, indoor dry bulb and wet bulb temperatures as model inputs. The inputs and outputs are slightly different than the variables for our purposes. In particular, Nyika's model utilizes indoor air flowrate as an input variable and therefore the model does not incorporate an integrated equipment controller that dictates air flowrate. However, Nyika additionally presented an empirical algebraic controller model to be coupled with the equipment model that correlated equipment part-load ratio to indoor air flowrate linearly. In this formulation, indoor air flowrate was an intermediate variable, and therefore the combined model was able to map both the equipment performance and its controls. Nyika's model was used in this chapter to generate a simulation database. Although the details of Nyika's model won't be covered in this section, the process of generating simulated data using the model is described.

Nyika's model was developed for a four-ton variable-speed air conditioner. The equipment rated performance is tabulated in table 5.1 below. Its rated capacity and

power are based on operating conditions of $T_{ID} = 80°F$, $B_{ID} = 67°F$ and $T_{OD} = 95°F$, consistent with AHRI210/240 [2].

Table 5.1.
Rated information for a four-ton variable-speed air conditioner

$\dot{Q}_{rat}$	$\dot{W}_{OD,rat}$	$\dot{W}_{ID,rat}$	$\dot{V}_{ID,max}$
14241 W	3160 W	394 W	1500 cfm

In order to acquire realistic and representative simulation data, the applicable range of this model should be limited to the range of regression data used by Nyika et al., and is summarized in table 5.2. Therefore, an input matrix for our simulation was sampled using the ranges shown in table 5.2. For example, T_{OD} was sampled from $70°F$ to $115°F$ using a sampling step of $5°F$. T_{ID} was sampled from $65°F$ to $85°F$ using a step of $4°F$. B_{ID} was sampled using a step of $3°F$ from $50°F$ to $77°F$ or T_{ID}, whichever was lower. The applicable range for equipment total cooling rate, $\dot{Q}_t$, is not explicitly tabulated in table 5.2, but out-of-range total cooling rates were filtered out by comparing calculated equipment part-load ratios to their applicable range tabulated in table 5.2. Prior to filtering, $\dot{Q}_t$ was initially sampled from $2kW$ to $20kW$ using a step of $1kW$.

Table 5.2.
Applicable range of Nyika's model

	T_{OD}	B_{ID}	T_{ID}	$\frac{\dot{Q}_t}{\dot{Q}_{t,max}}$	$\frac{\dot{V}_{ID}}{\dot{V}_{ID,max}}$
Lower bound	$67°F$	$49.4°F$	$65°F$	0.31	0.5
Upper bound	$115°F$	$77°F$	$85°F$	1	1

The simulated data were filtered using the applicable ranges specified for both $\frac{\dot{Q}_t}{\dot{Q}_{t,max}}$ and $\frac{\dot{V}_{ID}}{\dot{V}_{ID,max}}$. In addition, some datapoints were dropped when the equipment sensible heat ratio was lower than 0.5, since this SHR is already associated with an un-

realistically high latent cooling. Overall, 2960 datapoints were acquired that covered the complete operating envelope of this four-ton variable-speed air conditioner.

The database of 2960 datapoints is too large to be represented/predicted using the proposed mapping model form that incorporates psychrometric functions and numerical iterations. Therefore, 197 datapoints as a subset from this database were evenly sampled to cover the operating envelop of the four-ton variable-speed air conditioner. These 197 datapoints were used as a validation dataset, $S_{validation}$, in order to validate prediction accuracy of the performance mapping model trained using a separate training dataset $S_{training}$.

Heuristically, a few rules of thumb are preferred for the training set. 1) Fewer datapoints than the validation set should be included since ultimately the training dataset will be obtained by load-based testing which is expensive and time-consuming. 2) Training datapoints as potential test points should have their inputs consistent with load-based testing (i.e. the outdoor drybulb temperature, sensible building load, indoor drybulb temperature and building sensible heat ratio are inputs, as is mentioned in section 5.1). 3) As an input for each datapoint, sensible building load should be decoupled from outdoor drybulb temperature since it is not preferred that the performance map is trained using datapoints constrained by a specific building load line. 4) At least for the load-based quasi-steady-state model presented in section 5.2, wet-coil data are preferred as training data, since no iterations are required for wet-coil performance determination during the training process such that model training will be faster and more stable. 5) The training dataset should originate from the same source (Nyika's model) as the validation dataset.

In order to obtain $S_{training}$, a candidate dataset $S_{candidate}$ was generated from which a smaller training dataset could be selected. For $S_{candidate}$, T_{OD} was sampled from $77°F$ to $104°F$ using a sampling step of $9°F$; T_{ID} had two values: $73°F$ and $77°F$; sensible heat ratio had three values: 0.65, 0.8 and 0.95; sensible building load had three values: $1/4\dot{Q}_{rat}$, $1/2\dot{Q}_{rat}$ and $3/4\dot{Q}_{rat}$. 56 datapoints were left after datapoints were filtered according to the ranges specified in table 5.2. Currently, it was decided

to select 12 datapoints as a training subset from the candidate dataset to train the load-based quasi-steady-state model and obtain its coefficients.

5.3.1 Model training

Before the model training process, the bypass factor BF as a model parameter is obtained using equations (5.2) to (5.7) and equipment rated performances for sensible capacity, total capacity, full-speed indoor airflow rate that are measured at $T_{ID,rat} = 80°F$, $B_{ID,rat} = 67°F$, $T_{OD,rat} = 95°F$. Other model parameters/coefficients are trained subsequently using datapoints from the training dataset.

For each training dataset, the process to train the model is briefly introduced below. The model coefficients are grouped as two coefficient vectors that are trained separately since they serve two different cost functions. As is shown in equation (5.19), θ_Q represents the coefficient vector that is used for equipment cooling rate prediction. The coefficient vector includes the polynomial coefficients in equation (5.1) and (5.11). In equation (5.18), $X_{Q,i}$ represents an input data vector for each training datapoint. The optimization cost function for this non-linear regression of the sub-model of equipment cooling rate prediction is a root mean of square errors between the original equipment latent cooling rate $\dot{Q}_l$ and the predicted equipment latent cooling rate $\dot{Q}_l(X_Q|\theta_Q)$. In order to force $\dot{Q}_{t,max}$ in equation (5.1) to represent the equipment cooling capacity, α is constrained by the selections of a_j, as is shown in equation (5.21). In addition, the correction factor in equation (5.11) should be equal to one, when $PLR = 1$, since equipment latent cooling rate prediction at part-load should be equal to its latent capacity prediction with $PLR = 1$. This can be formulated as equation (5.22). Both equation (5.21) and (5.22) are constraints to the optimization process in equation (5.20). When the cost function is minimized, the optimal $\hat{\theta}_Q$ represents the best estimate.

$$X_{Q,i} = [T_{OD,i}, B_{ID,i}, T_{ID,i}, BL_{c,s,i}], \qquad 1 \leq i \leq N_{train} \tag{5.18}$$

$$\theta_Q = [\alpha, a_o, a_1, a_2, a_3, a_4, a_5, b_1, b_2, b_3, b_4] \tag{5.19}$$

$$\hat{\theta}_Q = \underset{\theta_Q}{argmin} \sqrt{\frac{1}{N_{train}} \sum_{i=1}^{N_{train}} (\dot{Q}_{l,i} - \dot{Q}_l(X_{Q,i}|\theta_Q))^2} \tag{5.20}$$

$$\alpha \times \sum_{i=0}^{5} a_j = 1 \tag{5.21}$$

$$\sum_{j=1}^{4} b_j = 1 \tag{5.22}$$

The parameter estimation for the sub-model of equipment COP prediction is conducted similarly. Before the estimation process, $\hat{\theta}_Q$ and the associated cooling rate prediction sub-model should be employed to determine sensible part-load ratio, PLR_i, and effective indoor wet bulb temperature, $B_{ID,eff,i}$, for each training datapoint. Therefore, the input data vector of each training datapoint includes outdoor dry bulb temperature, effective indoor wet bulb temperature, and sensible part-load ratio, as is shown in equation (5.23). In equation (5.24), θ_{COP} represents the coefficient vector that is used for equipment power prediction, which includes the polynomial coefficients in equation (5.15) and (5.16). The optimization cost function for the regression of the sub-model of equipment COP prediction is a root mean of square errors between the original COP and the predicted $COP(X_{COP,i}|\theta_{COP})$. The correction factor in equation (5.16) should be equal to one, when $PLR = 1$, since equipment COP prediction at part-load should be equal to full-load COP prediction with $PLR = 1$. This can be formulated as equation (5.26), which is a constraint to the optimization process in equation (5.24). The optimal $\hat{\theta}_{COP}$ represents the best estimate.

$$X_{COP,i} = [T_{OD,i}, B_{ID,eff,i}, PLR_i], \qquad 1 \leq i \leq N_{train} \tag{5.23}$$

$$\theta_{COP} = [c_o, c_1, c_2, c_3, c_4, c_5, d_0, d_1, d_2, d_3] \tag{5.24}$$

$$\hat{\theta}_{COP} = \underset{\theta_{COP}}{argmin} \sqrt{\frac{1}{N_{train}} \sum_{i=1}^{N_{train}} (COP_i - COP(X_{COP,i}|\theta_{COP}))} \tag{5.25}$$

$$\sum_{j=0}^{3} d_j = 1 \tag{5.26}$$

This overall training process is utilized in an optimal search of the training dataset based on the simulation database and future manipulation with load-based test results. In this training process, both of the coefficient vectors were estimated using a trust region nonlinear optimization approach developed by Byrd et al. [39].

5.3.2 Acquisition of the optimal training dataset

A successive optimization approach was used to search for the best training subset $\hat{S}_{training}$ that includes 12 datapoints sampled from the candidate dataset $S_{candidate}$ that has 56 datapoints, such that $\hat{S}_{training}$ can be utilized to train the proposed model form (introduced in section 5.2) that best predicts the 197 datapoints from the validation dataset $S_{validation}$. The beginning of section 5.3 introduced how $S_{candidate}$ and $S_{validation}$ were generated.

The successive optimization process is composed of an inner-loop optimization and an outer-loop optimization. Given a specific training subset $S_{training}$ selected from $S_{candidate}$, the inner-loop optimization is to search for the best estimate of the coefficient vector $\hat{\theta}_Q(S_{training})$ for equipment cooling rate prediction sub-model, following the training procedure indicated by equations from (5.18) to (5.22). For the purpose of conciseness, the procedure is represented by equation (5.27), where $RMSE_{\dot{Q}_l}(S_{training}, \theta_Q)$ indicates the root mean square error obtained given a specific coefficient vector and a specific training dataset.

$$\hat{\theta}_Q(S_{training}) = \underset{\theta_Q}{argmin} RMSE_{\dot{Q}_l}(S_{training}, \theta_Q) \tag{5.27}$$

Given the validation dataset, $S_{validation}$, the outer-loop optimization is to search for the best estimate of the training subset, $\hat{S}_{training}$, from $S_{candidate}$, in terms of comparing how models associated with their equipment cooling rate prediction coefficient vectors trained using different $S_{training}$ can predict the $S_{validation}$. How the $S_{validation}$ is predicted in terms of COP is not considered here, since at least with respect to the simulation database, it is observed that COP is easier to be captured by the model trained using good selection of $S_{training}$, while equipment cooling rates are more difficult. This outer-loop optimization is shown in equation (5.28), where $RMSE_{\dot{Q}_l}[S_{validation}, \hat{\theta}_Q(S_{training})]$ indicates the root mean square error obtained given the $S_{validation}$ and the $\hat{\theta}_Q(S_{training})$ estimated by the inner-loop optimization for a specific $S_{training}$. A genetic algorithm [40] was used here for the outer-loop optimization.

$$\hat{S}_{training} = arg\min_{S_{training}} RMSE_{\dot{Q}_l}[S_{validation}, \hat{\theta}_Q(S_{training})], \forall S_{training} \subset S_{candidate} \quad (5.28)$$

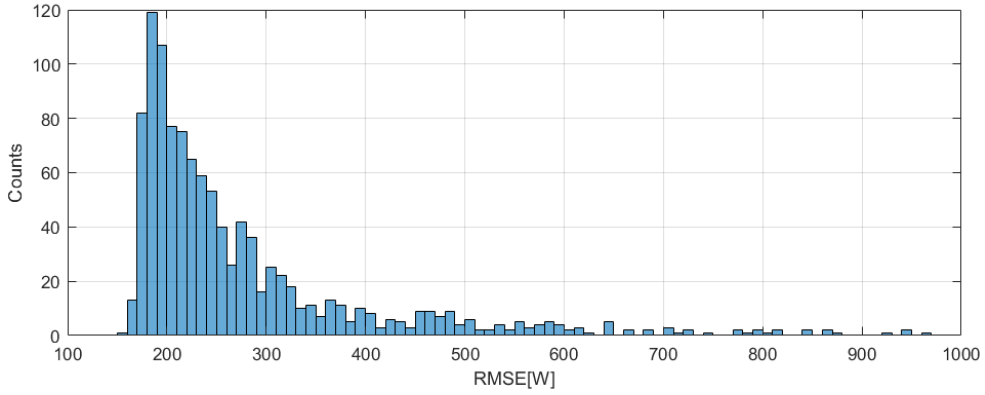

Fig. 5.4. Histogram of unique training datasets

Since the computation cost was high during the overall successive optimization, 1096 unique training datasets were evaluated without reaching convergence of the genetic algorithm. Most of the evaluation results are shown in the histogram in figure 5.4. 80% of the training datasets led to models with equipment latent cooling rate

prediction of $S_{validation}$ having an RMSE less than 350W. 30% of the training datasets led to RMSE values less than 200W.

Table 5.3.
Optimal training dataset with respect to the simulation database

Datapoint	$T_{OD}[^\circ F]$	$T_{ID}[^\circ F]$	$\frac{BL_{c,s}}{\dot{Q}_{rat}}$	SHR
1	77	77	0.75	0.8
2	86	77	0.5	0.65
3	86	77	0.5	0.95
4	95	73	0.25	0.65
5	95	73	0.75	0.95
6	95	77	0.5	0.65
7	95	77	0.25	0.8
8	95	77	0.75	0.8
9	95	77	0.5	0.95
10	104	73	0.5	0.65
11	104	73	0.75	0.95
12	104	77	0.5	0.8

Among the 1096 datasets that were evaluated, the best/optimal 12-point training dataset (with respect to the simulation database) is shown in table 5.3. These 12 datapoints are distributed through the equipment wet-coil operating envelope but with preferences for $95^\circ F$ outdoor drybulb temperature and $0.5\dot{Q}_{rat}$ sensible building load (both seen with 6 datapoints). It was hoped that this optimal training dataset would inform heuristic rules for performing load-based tests on any variable-speed equipment that can lead to a performance map with similar accuracy.

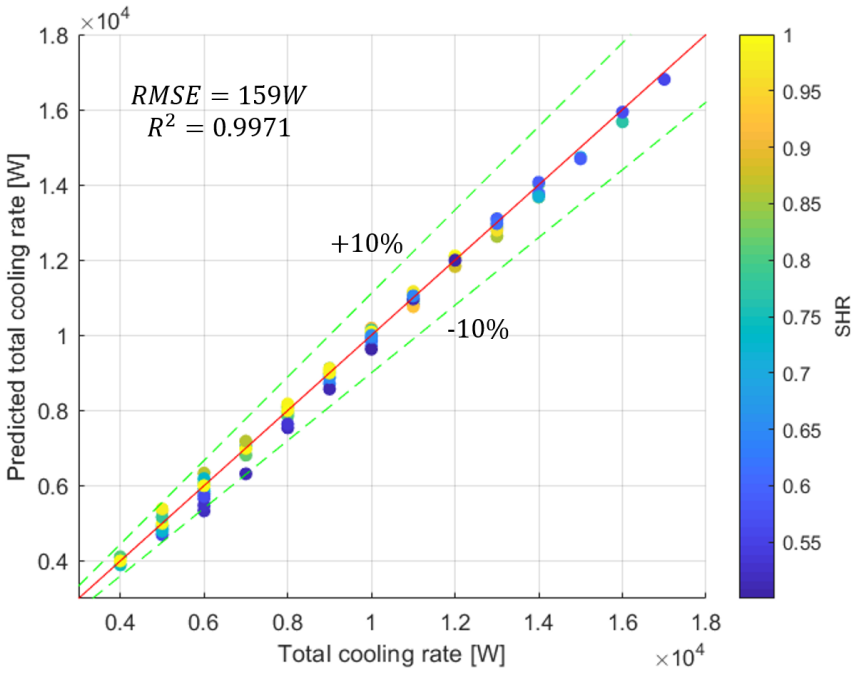

Fig. 5.5. Parity plot for equipment total cooling rate prediction

5.3.3 Prediction results obtained using the optimal training dataset

The load-based quasi-steady-state model was first identified using the 12-point optimal training dataset from the simulation database. Then, the prediction accuracy of the model was assessed, as the model was used to predict the validation dataset with 197 datapoints that cover the complete operation envelope of the four-ton variable speed air conditioner.

Prediction results are shown from figure 5.5 to 5.9 that compare predictions of equipment total cooling rate, latent cooling rate, sensible heat ratio, COP and power consumption with the original simulation data. Root mean square error and R^2 are shown at the left-upper corner of each figure. The parity plots for equipment latent cooling rate, SHR, COP have color representing the sensible building load of each datapoint. The parity plots for equipment total cooling rate and power consumption have color representing the equipment sensible heat ratio of each datapoint.

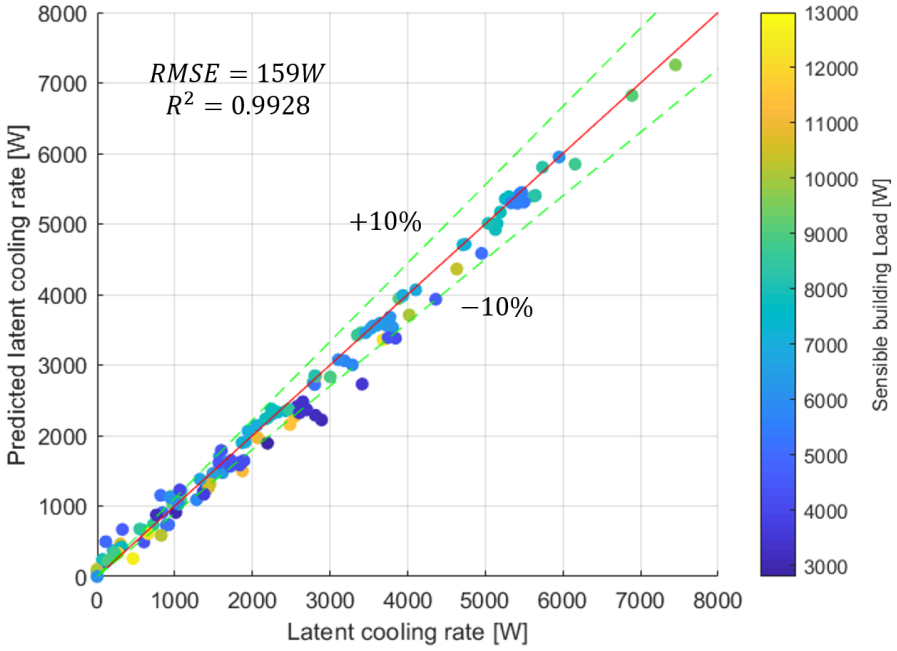

Fig. 5.6. Parity plot for equipment latent cooling rate prediction

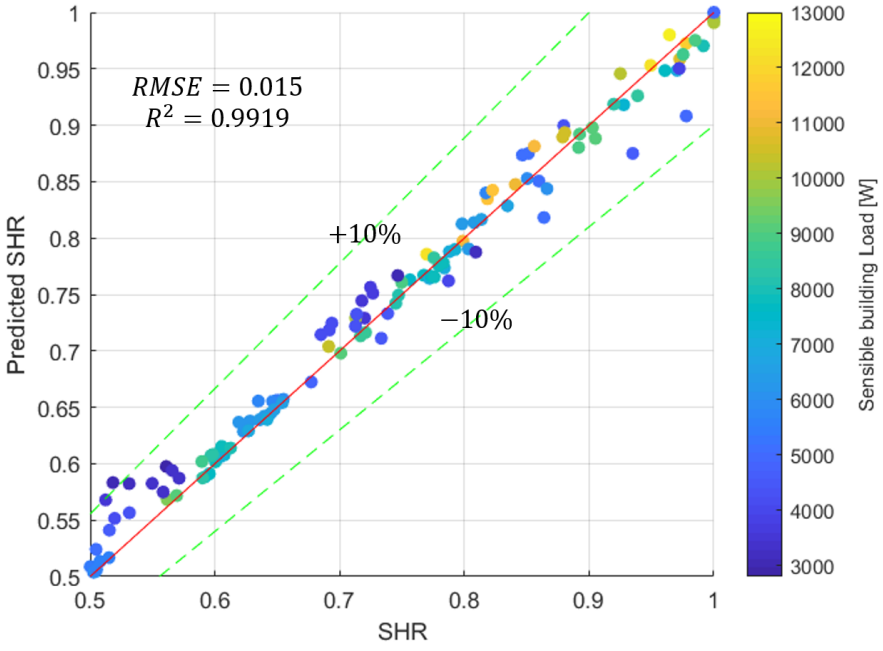

Fig. 5.7. Parity plot for equipment sensible heat ratio prediction

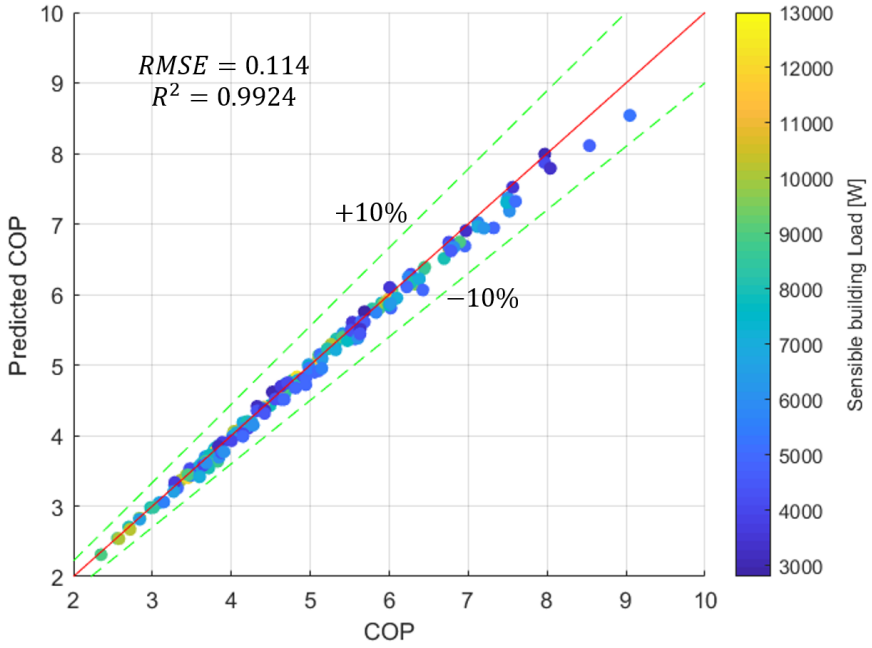

Fig. 5.8. Parity plot for equipment COP prediction

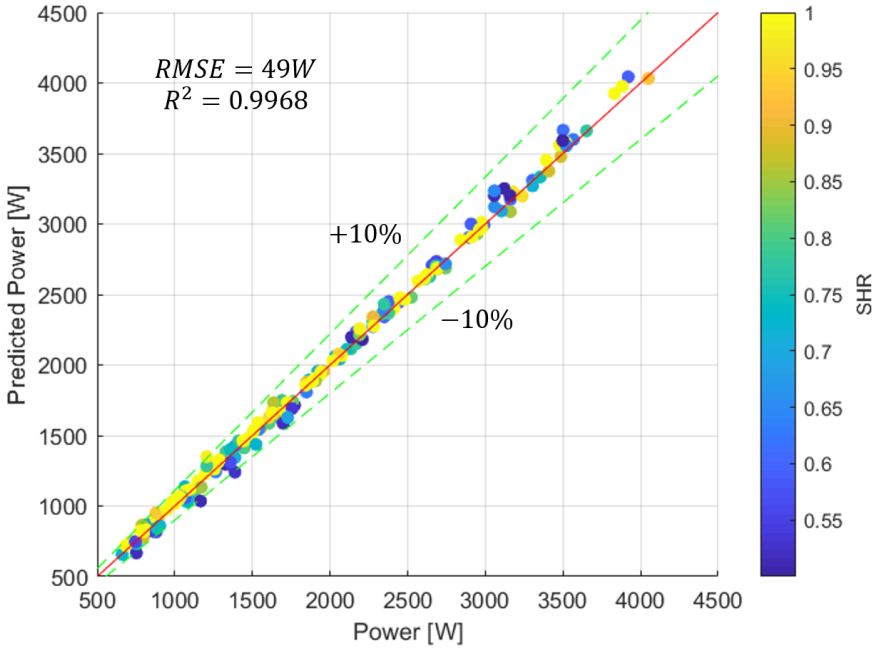

Fig. 5.9. Parity plot for equipment power prediction

As can be seen from these plots, the equipment total cooling rate, COP and power are well predicted by the model and the R^2 values are very close to 1. However, figure 5.7 shows some points with overprediction in sensible heat ratio at low sensible building loads and low SHRs. This overprediction of SHR echoes the underprediction of equipment latent cooling rate at low loads indicated by some dark blue points in figure 5.6. In general, the model does better at higher part-load ratios. This could be due to inadequate treatment of the effect of the modulated airflow on heat and mass transfer of the evaporator using the bypass factor approach in lower part-load scenarios. Nevertheless, the prediction results for COP and power consumption are very good, such that, at least for this equipment represented by the simulation database, this mapping model form shows promise for use in representing quasi-steady-state variable-speed cooling equipment performance throughout its operating envelope. Moreover, the trained model with acceptable accuracy can be obtained using only 12 training datapoints that are optimally found.

5.4 Performance mapping experimental design

An optimal training dataset of 12 datapoints was obtained in the section above that can be used to train the proposed mapping model form that is able to represent the simulation database with acceptable prediction accuracy. It was hoped that this optimal training dataset with respect to the 4-ton equipment simulation database would inform heuristic rules for performing load-based tests on any equipment type that can lead to a performance map with similar accuracy. A heuristic experimental design is proposed that inherits the datapoints determined from the section above with some additional test points to form a test matrix of 15 test points that are tabulated in table 5.4, where the first 12 points are identical to table 5.3. The last three points were added as a supplement because they are at low loads that could possibly trigger the test equipment cycling on/off behaviors.

Table 5.4.
Test matrix obtained using heuristic experimental design

Test point	$T_{OD}[^\circ F]$	$T_{ID}[^\circ F]$	$\frac{BL_{c,s}}{\dot{Q}_{rat}}$	SHR
1	77	77	0.75	0.8
2	86	77	0.5	0.65
3	86	77	0.5	0.95
4	95	73	0.25	0.65
5	95	73	0.75	0.95
6	95	77	0.5	0.65
7	95	77	0.25	0.8
8	95	77	0.75	0.8
9	95	77	0.5	0.95
10	104	73	0.5	0.65
11	104	73	0.75	0.95
12	104	77	0.5	0.8
13	77	71	0.25	0.65
14	77	79	0.25	0.95
15	86	71	0.25	0.8

Although the datapoints in table 5.4 work well for model training applied to the four-ton air conditioner simulation data, it is not known how well this would work for other equipment. Therefore, a more general clustering experimental design approach was developed that generates a uniform, complete and unbiased coverage of the operating envelope for any variable-speed air conditioner.

Hierarchical clustering is an algorithm that groups objects over a variety of scales by creating a hierarchical clustering tree. The tree is not a single set of clusters, but rather a multilevel hierarchy, where clusters at a lower level are joined as clusters at a higher level of the hierarchical tree. Objects in a cluster are similar to each other, while

objects from different clusters are dissimilar. Therefore, the similarities/dissimilarities of objects in each level is the criteria of partitioning/grouping. There are various choices of similarity metrics, and the Euclidean distance between two objectives in their vector space is a popular measurement that was used in this section. Every objective at the lowest level of the hierarchical tree is a cluster itself. In an upper level, two clusters from the lower level that are in the closest proximity to each other are grouped into a new cluster. In this way, the complete set of all the objectives form the last and final cluster at the very top level of the hierarchical tree. A user of the algorithm can decide which level of clustering/partitioning is needed in different applications. Chopping off the hierarchical tree at a lower level results in more clusters while a higher-level cut-off results in less clusters.

The goal of applying hierarchical clustering in experimental design is to group similar test points in a cluster and partition the experiment design space into dissimilar clusters. Therefore, the test points sampled from these clusters (e.g. cluster centroids) can represent the entire experimental design space well. Compared to random sampling from the design space, test points sampled after clustering should better span across the space. Another benefit is that the sampled test points are repeatable using the clustering approach, while the results from random sampling are not. This will contribute to the repeatability of the experimental results.

When utilizing the algorithm for the current application (sampling/designing representative test points from the complete operating envelope of any variable-speed air conditioner), points were compared to each other in terms of their proximity in a hyperspace of four dimensions: outdoor dry bulb temperature, indoor dry bulb temperature, sensible building load and building sensible heat ratio (test inputs to load-based testing). In this section, clustering involving two dimensions will be presented first as an example followed by the final results of clustering in the hyperspace, since two-dimensional clustering and sampling are easier to explain and visualize.

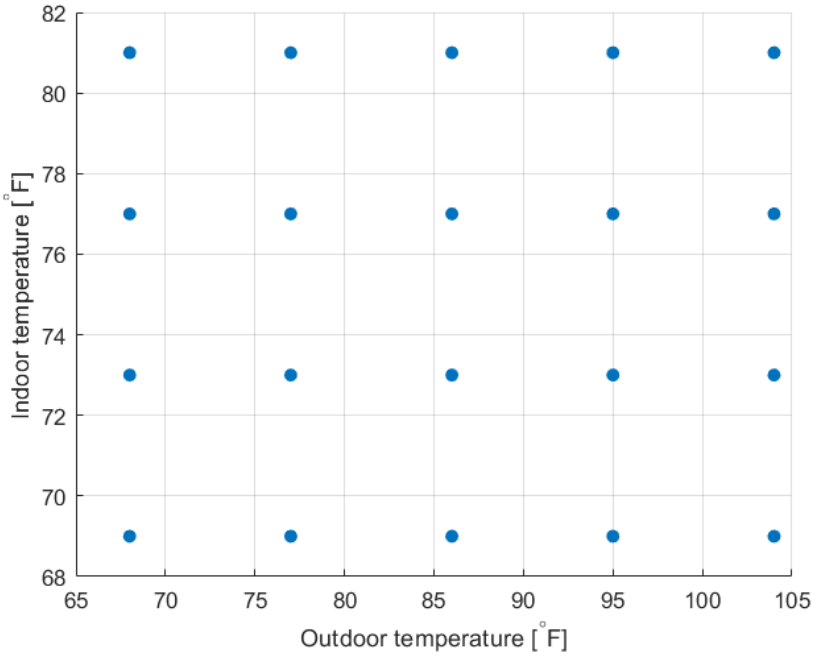

Fig. 5.10. Uniform sampling of candidate test points

5.4.1 Clustering of test points in a 2-dimensional experimental design space

This subsection will explain how to group 20 test points into 6 clusters within a 2-dimensional experiment design space (outdoor temperature and indoor temperature for an experimental study of an single-speed air conditioner in dry climates, for example). The outdoor temperature ranges from $68°F$ to $104°F$, and the indoor temperature ranges from $69°F$to $81°F$. The first step is to uniformly sample 20 candidate test points covering the complete design space, as can be seen in figure 5.10. Five alterations of outdoor temperature are introduced in the candidate set, along with four alterations of indoor temperature. More candidate test points can be sampled, but this will require more computational effort and may also possibly end up with different clustering results.

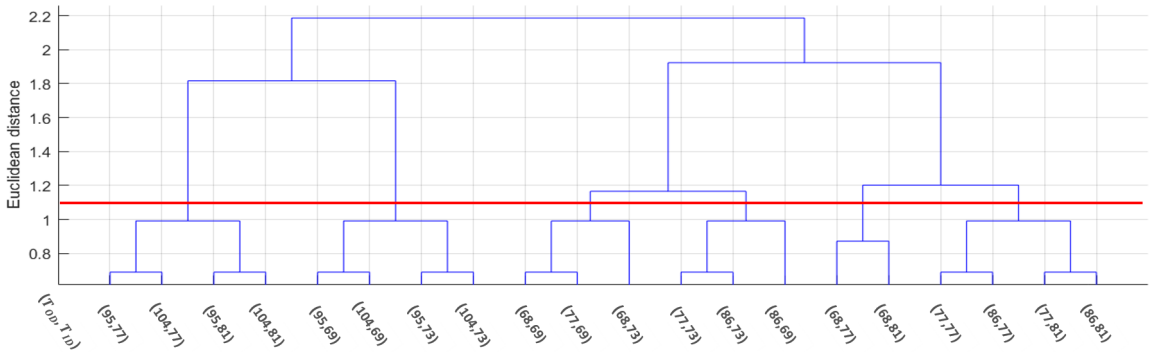

Fig. 5.11. Hierarchical clustering tree

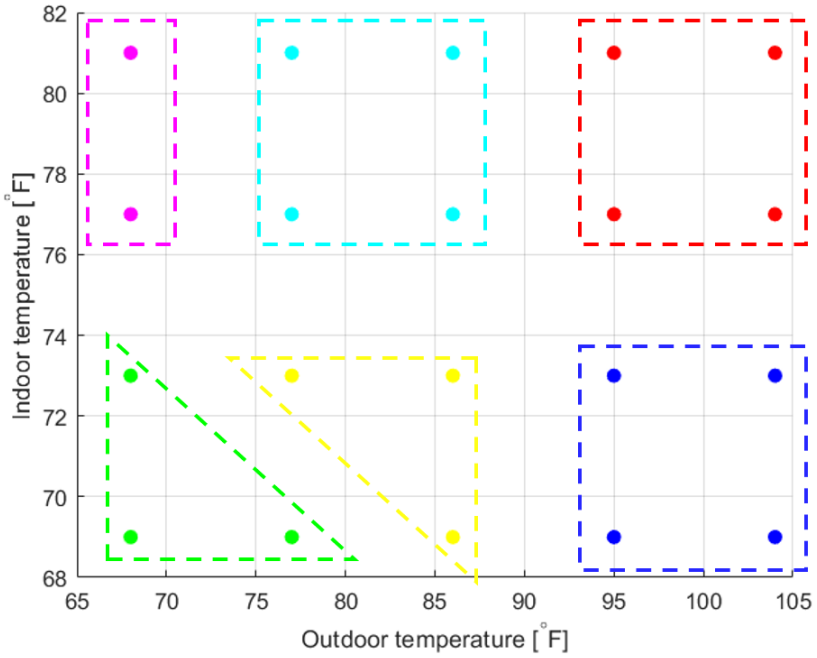

Fig. 5.12. 6 clusters of 20 candidate test points

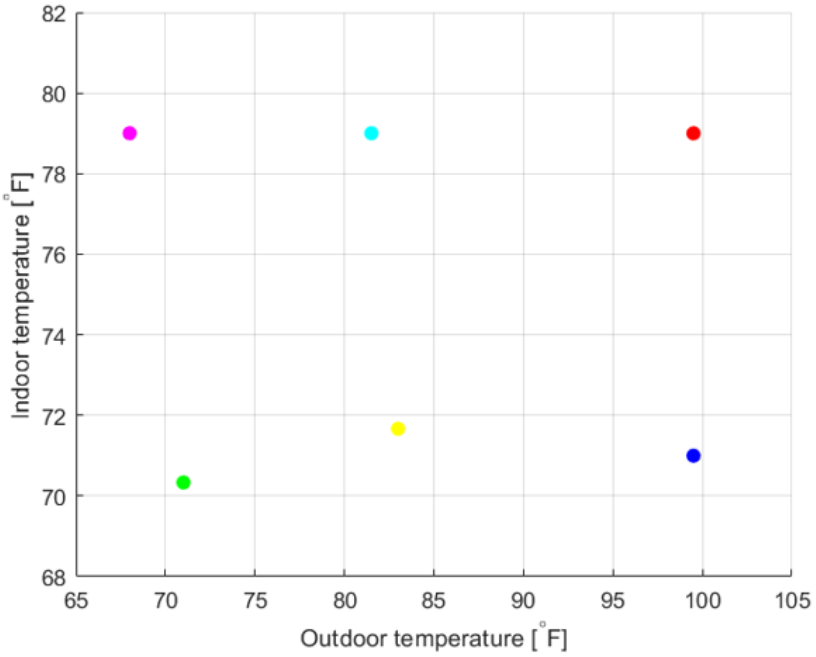

Fig. 5.13. 6 cluster centroids

The second step is to normalize the 20 values in each dimension before calculating the distance information such that they are centered and have a mean of zero, and are scaled to have a standard deviation of one. Therefore, the discrepancies in scales of the two dimensions won't distort the proximity calculations. This is particularly important when Euclidean distance is extended to a four-dimensional design space in next subsection.

The third step is to calculate the Euclidean distances between every two candidate test points among the 20 points. The fourth step is to link two test points that are the closest to each other together into clusters. If one test point is equally close to more than one point, it will be paired to its first neighbor. Therefore, the sequence of test points provided to the algorithm does affect the clustering results. Afterwards, these newly formed clusters should be linked to each other to create bigger clusters at higher levels until all the test points are grouped together in a hierarchical tree. For this example, the hierarchical tree is shown in figure 5.11. When calculating distance

between two clusters that have more than one test point, the average distance of test points between clusters should be considered.

The fifth step is to chop off the hierarchical tree in order to obtain a desired number of clusters. For this example, the 20 test points are grouped into 6 clusters, and therefore the hierarchical clustering tree should be chopped off at the Euclidean distance of roughly 1.1 , which is illustrated using a red cut-off line in figure 5.11. The 6 clusters of points can be seen in figure 5.12 that are represented by different colors. The very last step is to find the centroid of each cluster, in order to represent these clusters, as can be seen in figure 5.13. In this way, 6 representative test points are sampled from the 2-dimensional experimental design space.

5.4.2 Clustering of test points in a 4-dimensional experimental design space

In this subsection, following the steps illustrated in the previous subsection, representative test points were clustered and sampled from the operating envelope of a variable-speed air conditioner, in terms of a hyperspace of four dimensions: outdoor dry bulb temperature, indoor dry bulb temperature, sensible building load and building sensible heat ratio.

Candidate test points that uniformly span the hyperspace were initially sampled. In this case, T_{OD} was sampled from $68°F$ to $104°F$ using a sampling step of $9°F$. T_{ID} was sampled from $69°F$ to $81°F$ using a step of $4°F$. Sensible building load $BL_{c,s}$ was sampled as a fraction of air conditioner rated capacity $\dot{Q}_{rat}$ using a step of $0.2\dot{Q}_{rat}$ from $0.2\dot{Q}_{rat}$ to $\dot{Q}_{rat}$. Sensible heat ratio SHR was sampled from 0.6 to 1 using a step of 0.1. Totally, there were 500 combinations with these alterations in the four dimensions. However, 331 candidate test points were left after the rest were filtered out according to the full-load curve of the model by Nyika et al. [27]. It is not useful to incorporate candidate test points that will over load an air conditioner using significantly high sensible building load or low sensible heat ratio, since these points

Table 5.5.
Test matrix obtained using clustering experimental design

Test point	$T_{OD}[^{\circ}F]$	$T_{ID}[^{\circ}F]$	$\frac{BL_{c,s}}{\dot{Q}_{rat}}$	SHR
1	74	78	0.81	0.93
2	76	71	0.49	0.7
3	76	79	0.64	0.72
4	77	71	0.2	0.65
5	77	71	0.2	0.89
6	77	79	0.3	0.7
7	77	79	0.4	0.95
8	78	71	0.59	0.96
9	95	69	0.6	0.75
10	97	79	0.8	0.95
11	98	78	0.6	0.72
12	100	71	0.3	0.65
13	100	71	0.38	0.91
14	100	79	0.3	0.65
15	100	79	0.38	0.91

are outliers with respect to an air conditioner's operating envelope. Different full-load curves can be used, such as the default capacity curves from EnergyPlus [36], as long as these curves are able to determine a reasonable air conditioner full-load envelope.

The clustering procedure included the normalization of values in each dimension, calculation of Euclidean distances and linkages in order to build a hierarchical clustering tree. It was decided to chop off the tree in order to have 15 clusters and ultimately 15 representative test points (same number of test points as the heuristic experimental design). It is believed that a number of load-based tests ranging from 12 to 15 is appropriate in terms of having a reasonable testing burden and mapping

accuracy for the purpose of air conditioner performance mapping. The centroids of the 15 clusters that are listed in table 5.5 are the representative test points obtained using the clustering experimental design approach.

Table 5.4 and table 5.5 were combined into an overall test matrix for load-based testing in order to provide data for both training and validation. In the following section, these tests will be carried out in order to evaluate how actual test results can be used to train and validate the proposed mapping model form.

5.5 Load-based test results and an optimal performance map

Using the experimental setup introduced in chapter 2, load-based tests were carried out with respect to the virtual building model, automated testing procedures, convergence criteria described in chapter 2 and the thermostat environment emulator described in chapter 4, except for the following modifications:

1. Throughout each test interval, the psychrometric chamber that simulates the outdoor environment used temperature setpoints according to the T_{OD} column in table 5.4 and 5.5.

2. The sensible building load model used in load-based testing, equation (2.12) in chapter 2, was not used and a fixed sensible building load $BL_{c,s}$ for each test point specified in table 5.4 and 5.5 was used instead. Similarly, the fixed SHR values in these two tables were used in equation (2.14) that characterizes virtual building latent dynamics.

3. After the test unit was turned on, the test thermostat inside its environment emulator had its setpoint adjusted according to the T_{ID} column in table 5.4 and 5.5 throughout each test interval except for full-load test scenarios.

4. When initializing the virtual building models, the initial values for the virtual room humidity ratios $w_{ID,sp}(0)$ were configured using the following rules of thumb.

When the SHR value (see table 5.4 and 5.5) was below 0.75, a humidity ratio corresponding to 60% relative humidity at the thermostat setpoint temperature was used for $w_{ID,sp}(0)$. When the SHR value was above 0.85, a humidity ratio corresponding to 30% relative humidity was used. When the SHR value was in-between, a humidity ratio corresponding to 45% relative humidity was used. These are reasonable initial guesses for the floating virtual room humidity levels that differ from test to test, and the humidity ultimately converged according to the test inputs in table 5.4 and 5.5.

Using the modifications above, load-based tests were performed according to the test inputs specified in table 5.4 and 5.5, while still following the majority of the procedures established in chapter 2. Since the sensible load line and its dependency on ambient temperature, indoor, outdoor design temperatures and balance point temperature were not used anymore, the building loads and the temperatures were decoupled from each other as separate test inputs, and therefore these tests could explore the complete operating envelope of the test equipment.

5.5.1 Dehumidifying mode test results

Detailed test results for the whole 30 tests are documented in the appendix of the thesis. Most of them are similar to the wet-coil test results shown in chapter 2 and 4 in terms of the test equipment behaviors and the variation patterns for indoor temperature and humidity, except for the following five tests that are shown below in table 5.6.

It was observed that the five tests in table 5.6 had the test equipment running in a dehumidifying mode instead of a regular cooling mode. Specifically, the indoor room temperature was overcooled by the equipment to be lower than its thermostat setpoint, as can be seen by comparing column 3 to 4 in table 5.6. Sensible building loads for these five tests were small while latent building loads were significant. In order to match the loads with equipment cooling rates and maintain a comfortable indoor humidity level, the test equipment controller overrode its thermostat setpoint

Table 5.6.
Test results for five dehumidifying mode tests

Test	$T_{OD}[^\circ F]$	Thermostat setpoint $[^\circ F]$	$T_{ID}[^\circ F]$	$B_{ID}[^\circ F]$	$\dot{Q}_s[W]$	SHR	COP
1	77	71	70.8	62.6	2385	0.64	7.37
2	77	71	69.4	61.5	1888	0.65	6.94
3	95	73	69.5	61.2	2492	0.66	5.03
4	100	79	77.2	66.7	2898	0.65	4.93
5	100	71	69.6	61.3	2895	0.65	4.63

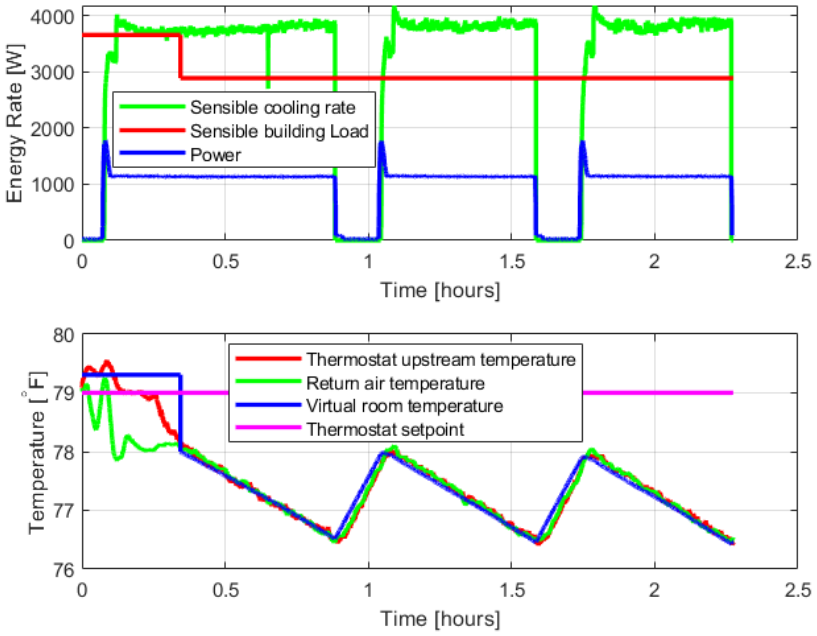

Fig. 5.14. Sensible results of dehumidifying mode test 4 in table 5.6

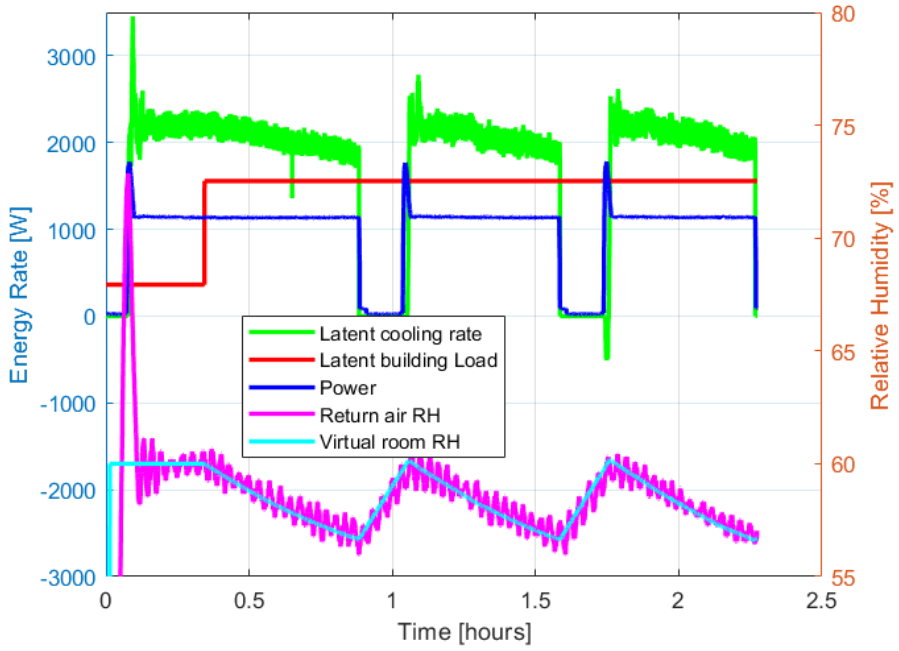

Fig. 5.15. Latent results of dehumidifying mode test 4 in table 5.6

in dehumidifying mode, leading to a lower indoor cooling coil sensible heat ratio than would have occurred in normal cooling mode.

Test results for the dehumidifying mode test 4 in table 5.6 are shown in figure 5.14 and figure 5.15. Similar legends were used as the corresponding result plots in chapter 2 and 4. As can be seen in figure 5.14, the virtual building dynamics were not initiated until the thermostat upstream temperature and the return air temperature were controlled to 78 $^{\circ}F$, although the equipment was functioning before that point. At that moment, even though the thermostat environment was 1$^{\circ}F$ lower than the thermostat setpoint, the test equipment kept cooling the virtual room in dehumidifying mode for more than half an hour before it cycled off. This was due to the indoor relative humidity that was quite high (close to 60%) and due to the significant latent building load that kept adding moisture to the virtual room, as can be seen in figure 5.15. Since the sensible building load was not significant, the indoor room temperature was always below the thermostat setpoint throughout the

test as the equipment was cycling on and off. As a result, indoor room RH was effectively maintained below 60% by the equipment under the dehumidifying mode. This dehumidifying mode test is strong evidence for the fact that the laboratory load-based testing methodology is able to reflect test equipment field behaviors guided by its native controls with various operating modes.

Besides the 30 performance mapping load-based tests, results of additional 9 cooling load-based test intervals introduced in subsection 2.4.2 are also included in the following evaluation. For conciseness, these 9 points will be referred to as EXP-07 datapoints since they were obtained according to the test matrix in chapter 2 that echoes the CSA EXP-07 draft standard [10]. These 39 test points were obtained within a month, and therefore uncertainties due to refrigerant leakage/discharge, environmental chamber/ductwork reconfiguration are thought to be negligible. It is important to include these EXP-07 datapoints in order to ultimately compare the next-generation performance rating approach against the traditional temperature-bin-based rating approach (introduced in EXP-07 and chapter 2).

An important question that arises is whether the mapping model form proposed in section 5.2 is able to map the test equipment performance in both regular cooling mode and the dehumidifying mode, since different control strategies could be utilized by the equipment controller in different modes. A preliminary way to answer this question is to train the mapping model form with/without the 5 dehumidifying mode test points. Comparative results from these approaches are shown below as figure 5.16 and figure 5.17. Since the RMSE of the model representation was not significantly inflated (RMSE increases from 0.1274 to 0.1580 only) when the 5 dehumidifying mode test points were introduced, it seems to be reasonable to utilize the model form to also cover the dehumidifying mode performance at least for this test equipment. Otherwise, there would need to be a separate mapping model form for equipment dehumidifying mode and the mapping methodology would be significantly more complicated since issues are difficult to address such as defining boundaries for two maps and how to train maps separately.

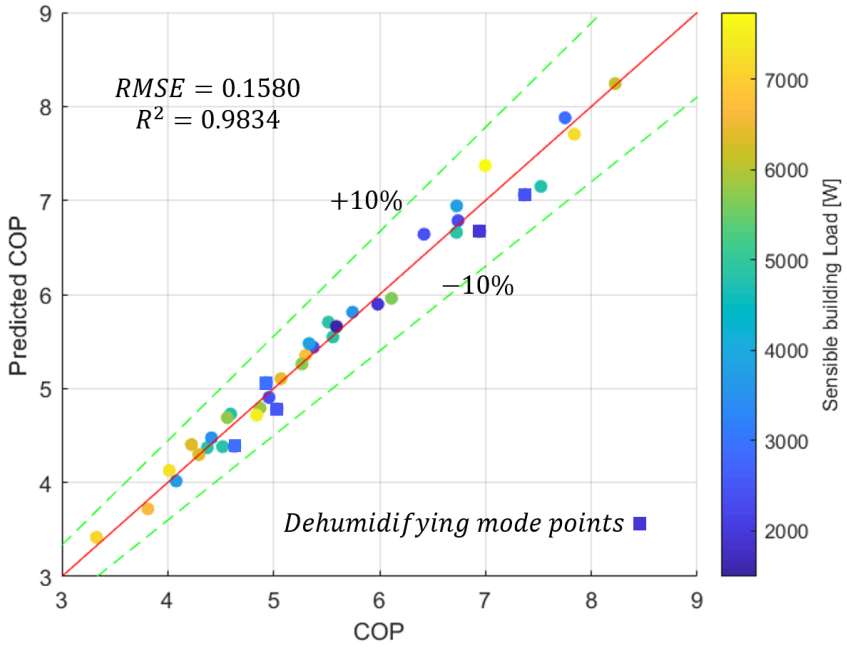

Fig. 5.16. Representation of 39 points including 5 dehumidifying mode points

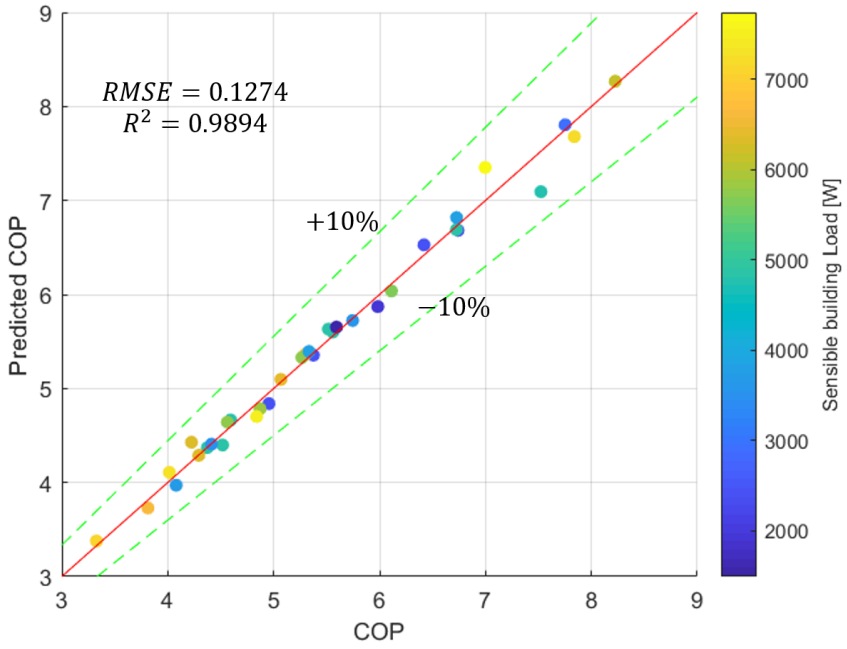

Fig. 5.17. Representation of 34 points excluding 5 dehumidifying mode points

5.5.2 Acquisition of the optimal training dataset

Although the prediction results of figure 5.16 and 5.17 seem promising, it is not realistic to train the mapping model form using up to 34 or 39 datapoints that are obtained by load-based testing, which is expensive and time-consuming. Similar to the approach used in section 5.3, a training dataset $S_{training}$ with 12 datapoints can be optimally searched that best predict the whole 39 datapoints.

In this problem setup, the candidate dataset $S_{candidate}$ includes the 30 performance mapping load-based test points. The 9 EXP-07 datapoints were not considered in $S_{candidate}$ since they did not originate from the performance mapping experimental design methods. However, the validation dataset $S_{validation}$ is composed of the whole 39 datapoints that includes the EXP-07 datapoints.

Similar to the approach presented in section 5.3, a successive optimization approach was utilized. Given a specific training subset $S_{training}$ selected from $S_{candidate}$, the inner-loop optimization searches for the best estimates of two coefficient vectors: $\hat{\theta}_Q(S_{training})$ for the equipment cooling rate prediction sub-model, and $\hat{\theta}_{COP}(S_{training})$ for the equipment COP prediction sub-model. The inner-loop optimization basically follows the training procedures presented in subsection 5.3.1. Specifically, $\hat{\theta}_Q(S_{training})$ is obtained according to equation (5.29), and $\hat{\theta}_{COP}(S_{training})$ is obtained according to equation (5.30).

$$\hat{\theta}_Q(S_{training}) = \underset{\theta_Q}{argmin} RMSE_{\dot{Q}_l}(S_{training}, \theta_Q) \tag{5.29}$$

$$\hat{\theta}_{COP}(S_{training}) = \underset{\theta_{COP}}{argmin} RMSE_{COP}(S_{training}, \theta_{COP}) \tag{5.30}$$

$$\hat{S}_{training} = arg \underset{S_{training}}{min} \{MAPE_{\dot{Q}_t}[S_{validation}, \hat{\theta}_Q(S_{training})] + MAPE_{COP}[S_{validation}, \hat{\theta}_{COP}(S_{training})]\}, \forall S_{training} \subset S_{candidate} \tag{5.31}$$

Given the validation dataset $S_{validation}$, the outer-loop optimization searches for the best estimate of the training subset $\hat{S}_{training}$ from $S_{candidate}$, in terms of comparing how models associated with their coefficient vectors trained using different $S_{training}$ can predict equipment total cooling rates and COPs in $S_{validation}$. This outer-loop optimization is shown in equation(5.31), where $MAPE_{\dot{Q}_t}[S_{validation}, \hat{\theta}_Q(S_{training})]$ indicates the mean absolute percentage error (MAPE) of equipment total cooling rate prediction for $S_{validation}$ using $\hat{\theta}_Q(S_{training})$ that is estimated by the inner-loop optimization for a specific $S_{training}$. $MAPE_{COP}[S_{validation}, \hat{\theta}_{COP}(S_{training})]$ indicates the MAPE of COP prediction for $S_{validation}$ using $\hat{\theta}_{COP}(S_{training})$ that is also estimated by the inner-loop optimization.

MAPEs are used here for the outer-loop optimization instead of RMSE, because MAPE is non-dimensional, and therefore the cost function in equation (5.31) won't have a biased weight on total cooling rate prediction over COP prediction. MAPE of total cooling rates is used here instead of latent cooling rates, since mean absolute percentage error of latent cooling rates could overemphasize the prediction errors when latent cooling rates are close to zero and the cooling coil is dry. A non-dimensional $(1 - R^2)$ could also be used here.

A genetic algorithm [40] was chosen for the outer-loop optimization, with 25 evolutionary generations. Each generation has 75 individuals. Each individual is actually a $S_{training}$ set with 12 datapoints sampled by the genetic algorithm and the fitness of each individual is the sum of two MAPEs calculated according to equation (5.31). For each generation, there is an elite individual that is guaranteed to survive and get into the next generation. The genetic optimization process can be visualized using figure 5.18.

The optimization took about 70 hours to finish, but the genetic algorithm still did not converge as the average of a generation (blue line with dot) did not converge to the minimum of a generation (green line with dots). However, the minimum values were already very close to the red line, which is the minimized sum of MAPEs predicted by a mapping model that was trained using the whole 39 points in $S_{validation}$ and is

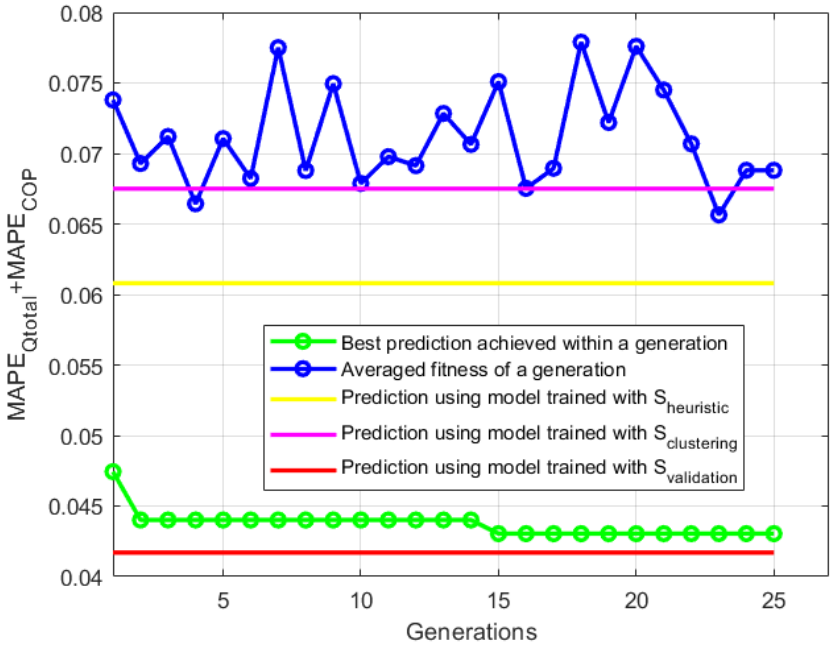

Fig. 5.18. Cost function evaluated over generations

also the searching limit for the overall optimization process. The elite individual over generations changed twice as the green line dropped twice in figure 5.18. The sum of MAPEs can also be predicted by a mapping model that was trained using $S_{heuristic}$ that includes the 15 test points obtained according to the heuristic experimental design approach. Indicated by the yellow line, this sum of MAPEs is better (smaller) than any average values of a generation (blue line), and it is actually better than 61.4% of all the evaluations during the overall optimization. The sum of MAPEs predicted by a mapping model trained using $S_{clustering}$ (magenta line) is not as good as the prediction using $S_{heuristic}$. $S_{clustering}$ includes the 15 test points obtained according to the clustering experimental design approach.

Test results of the 12 optimal datapoints are tabulated in table 5.7. The corresponding test input matrix is shown in table 5.8. Comparing table 5.7 against table 5.8, it is observed that the test results deviated slightly from the test inputs in terms of T_{ID}, $\frac{\dot{Q}_s}{\dot{Q}_{rat}}$ and SHR. These deviations were strongly characterized by the test

equipment behaviors such as cycling on/off, speed modulation, full-load operation and cooling/dehumidifying modes.

Table 5.7.
Test results of the optimal training dataset

$T_{OD}[^{\circ}F]$	$T_{ID}[^{\circ}F]$	$B_{ID}[^{\circ}F]$	$\frac{\dot{Q}_s}{\dot{Q}_{rat}}$	SHR	COP
74	78.6	60.3	0.8	0.93	7.00
76	71.3	61.4	0.49	0.70	7.52
77	77.3	63.3	0.75	0.80	7.84
77	78.1	66.7	0.3	0.69	7.75
77	79.3	61.7	0.39	0.94	6.73
95	69.5	61.2	0.26	0.66	5.03
95	69.9	59.5	0.61	0.76	4.87
95	76.0	63.0	0.25	0.80	4.96
95	77.2	66.0	0.5	0.65	5.56
95	77.3	60.1	0.5	0.94	4.59
104	77.4	64.0	0.5	0.79	4.37
104	73.0	56.6	0.69	0.95	3.81

Table 5.8.
Test input matrix of the optimal training dataset

$T_{OD}[^{\circ}F]$	$T_{ID}[^{\circ}F]$	$\frac{BL_{c,s}}{\dot{Q}_{rat}}$	SHR
74	78	0.81	0.93
76	71	0.49	0.7
77	77	0.75	0.8
77	79	0.3	0.7
77	79	0.4	0.95
95	73	0.25	0.65
95	69	0.6	0.75
95	77	0.25	0.8
95	77	0.5	0.65
95	77	0.5	0.95
104	77	0.5	0.8
104	73	0.75	0.95

5.5.3 The optimal performance map

Trained using the optimal training dataset $\hat{S}_{training}$, model coefficients for the optimal performance map were obtained and are tabulated in table 5.9. Coefficient c_0 is relatively small compared to the others, since the constant term in equation (5.15) could be negligible. Prior to the training of these model coefficients, the indoor coil bypass factor BF was determined as 0.07169 using the equipment rated performance for sensible capacity, total capacity and full-speed indoor airflow rate that were measured at $T_{ID,rat} = 80°F$, $B_{ID,rat} = 67°F$, $T_{OD,rat} = 95°F$. Based on table 5.9 and the BF value, this mapping model can be reproduced outside this thesis.

Table 5.9.
Model coefficients of the optimal performance mapping model for the test equipment

	z_0	z_1	z_2	z_3	z_4	z_5
z=a	1.8181e2	1.5065e1	1.0758e2	1.2889e2	1.9334e1	-2.0607e2
z=b	-	-9.7014e-1	9.1578	-1.2912e1	5.7239	-
z=c	1.2476e-3	1.3826e3	4.5505e2	1.6661e3	6.0301e2	-3.2987e3
z=d	6.7166e-1	1.0476	-1.5545	8.3525e-1	-	-

Representation of the whole 39 load-based test datapoints by the performance map are shown from figure 5.19 to 5.23 that compare predictions of equipment total cooling rate, latent cooling rate, sensible heat ratio, COP and power consumption with the measured data. Root mean square error and R squared are shown at the left-upper corner of each figure. Green scatter points on these figures represent the 12 optimal training datapoints that were used to obtain the performance map. Red scatter points represent the other 18 performance mapping load-based tests that are used to validate the prediction results here. Blue scatter points represent the 9 EXP-07 datapoints.

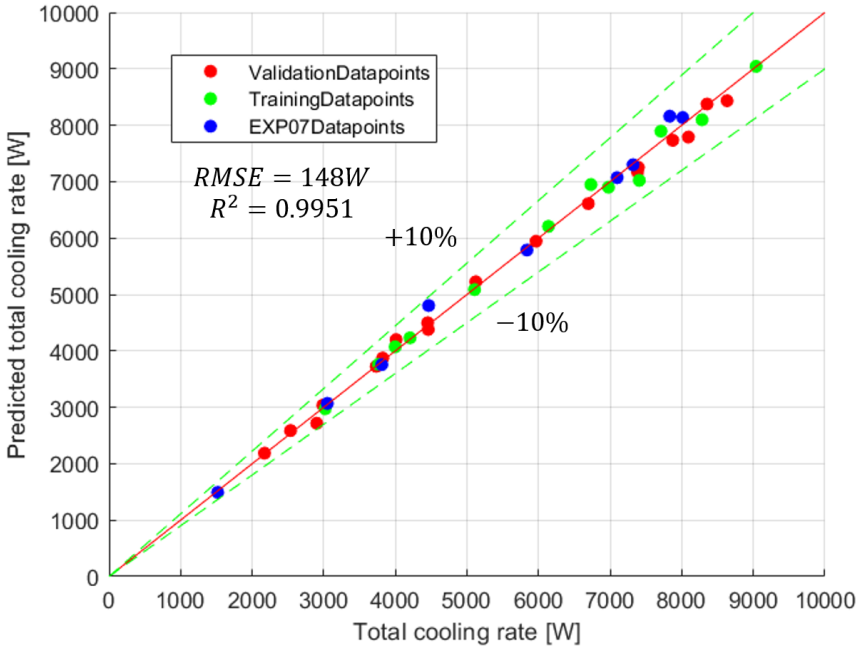

Fig. 5.19. Parity plot for equipment total cooling rate prediction

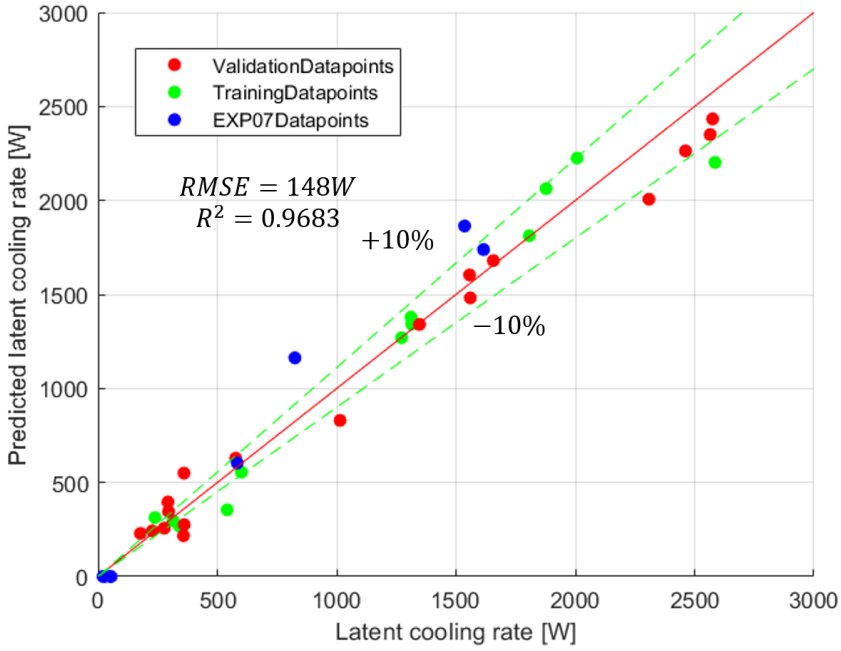

Fig. 5.20. Parity plot for equipment latent cooling rate prediction

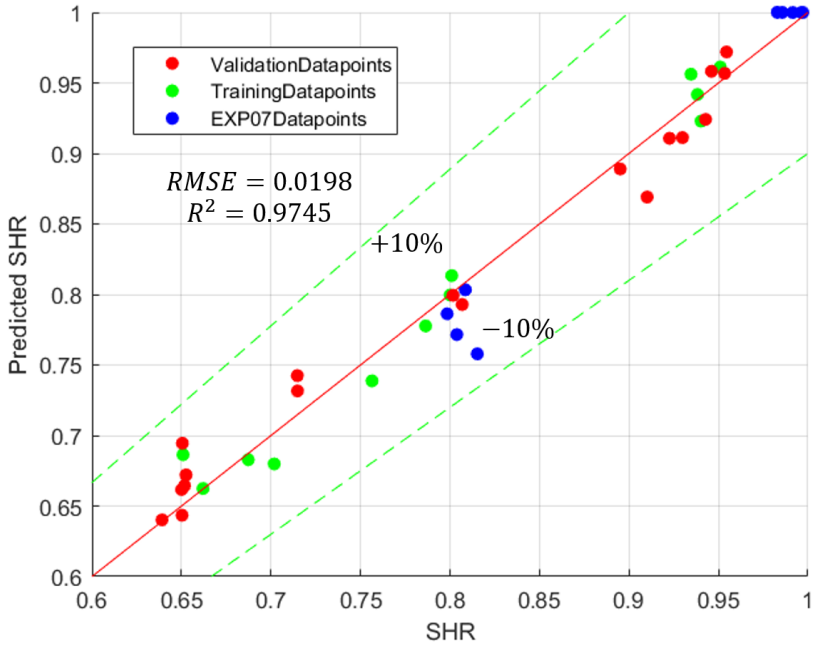

Fig. 5.21. Parity plot for equipment sensible heat ratio prediction

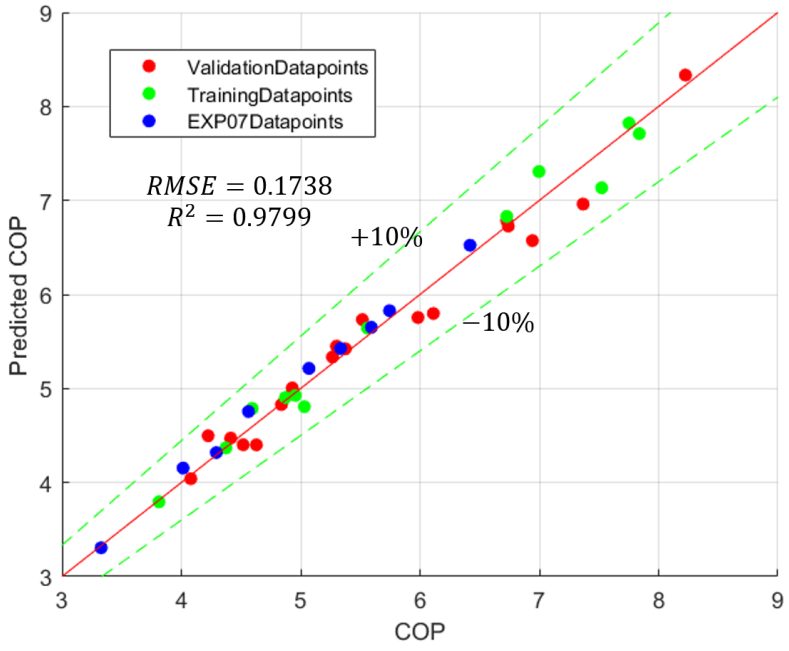

Fig. 5.22. Parity plot for equipment COP prediction

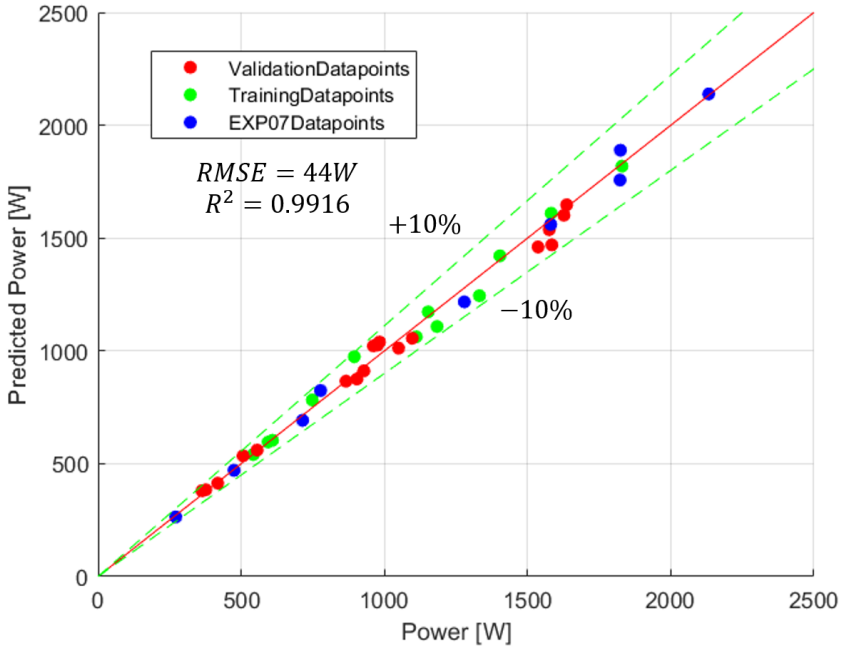

Fig. 5.23. Parity plot for equipment power prediction

As can be seen from these plots, although a few latent cooling rate prediction points (for example, two blue EXP-07 datapoints) lie outside of the ±10% dashed error lines, the equipment total cooling rate, COP and power were well predicted by the model and the R^2 values are very close to 1. These representation results are promising, considering that there are uncertainties for these test results originating from both instrumentation and test equipment control in particular. Since the proposed quasi-steady-state load-based performance mapping model form can well represent both the 4-ton variable-speed air conditioner simulation database and the test equipment that was used throughout this work, it is believed that the accuracy of this mapping model is adequate when used in estimating seasonal performance ratings for variable-speed air conditioners.

Once a performance map for the test equipment is identified with acceptable prediction accuracy, it is interesting to see whether the model prediction makes physical sense or not by conducting a parametric study using the performance map. Figures

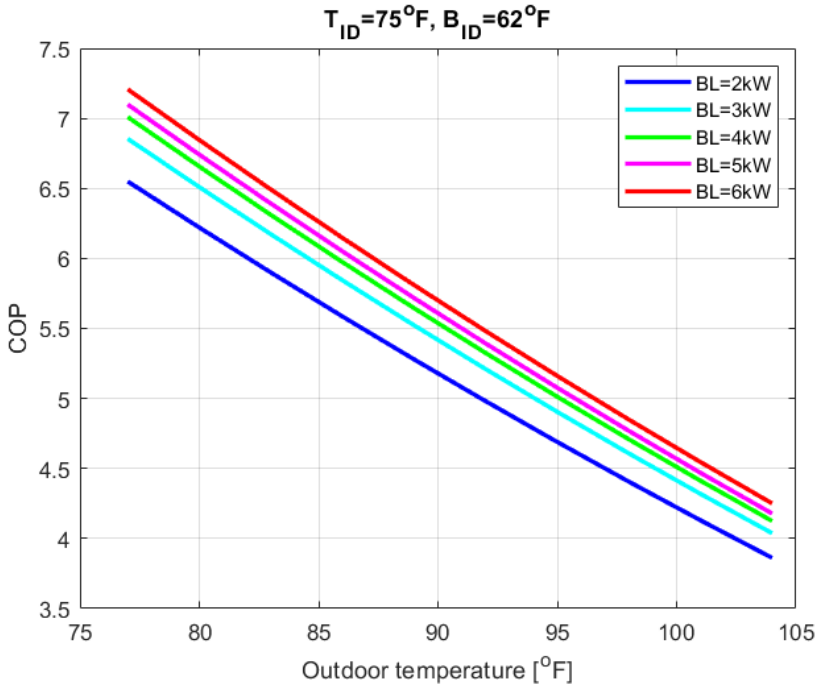

Fig. 5.24. Parametric study of the optimal performance map: Impact of T_{OD} and BL on COP

5.24 to 5.26 show results for three parametric studies. A set of mapping data were generated for figure 5.24 where indoor dry bulb temperature was held constant at $75°F$ and indoor wet bulb temperature was held at $62°F$. As the outdoor temperature increases, the test equipment COP is predicted to drop significantly. In addition, as the sensible building load increases while the outdoor temperature is held at a constant value, the test equipment COP increases. It makes sense that COP at very low part-load is smaller due to significant cycling degradation. However, whether a specific variable-speed air conditioner has optimal performance at an intermediate part-load or not, depends strongly on how the vapor compression cycle components are sized and optimized in the design phase of the equipment. Nevertheless, the performance map does not show an optimal COP with respect to the part-load variation, as was evident from the test results (training datapoints).

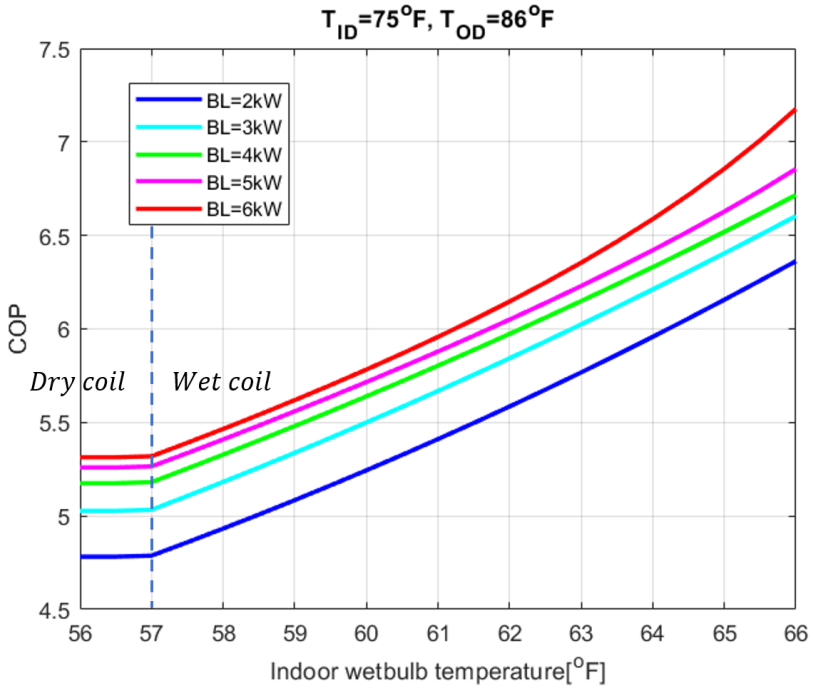

Fig. 5.25. Parametric study of the optimal performance map: Impact of B_{ID} and BL on COP

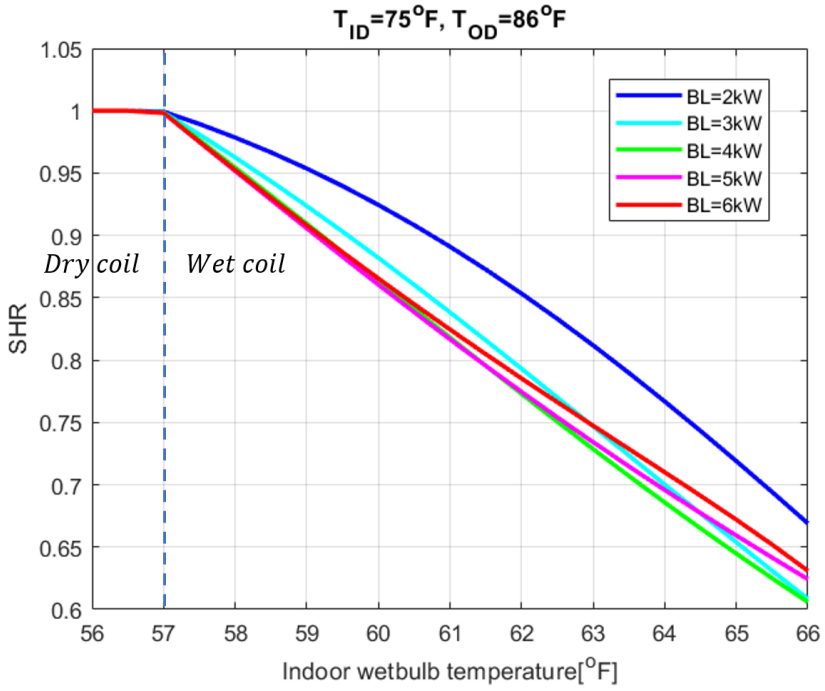

Fig. 5.26. Parametric study of the optimal performance map: Impact of B_{ID} and BL on SHR

Another set of mapping data were generated for figure 5.25 where indoor dry bulb temperature was held constant at $75°F$ and outdoor temperature was held at $86°F$. As the indoor wet bulb temperature increases, the test equipment COP is predicted to increase significantly due to the increased latent cooling rate and the associated moisture condensation on the indoor coil. When the indoor wet bulb temperature is below $57°F$, the indoor coil is dry, and the equipment COP shows no dependency on the wet bulb temperature.

Figures 5.26 and 5.25 share the same set of mapping data. In figure 5.26, as the indoor wet bulb temperature increases, the indoor coil sensible heat ratio drops significantly due to the increased latent cooling rate compared to the sensible cooling rate that is constant for each curve. The vertical dashed lines in figures 5.25 and 5.26 mark the separation of wet-coil and dry-coil scenarios. In the model form introduced in section 5.2, the effective wetbulb temperature ($B_{ID,eff} = 57°F$ here) is the critical wet bulb temperature that separates dry-coil and wet-coil cooling. It is obtained using iterations associated with the bypass factor approach at equipment full-load scenarios. Since the bypass factor iterations cannot be employed during part-load where the airflow rate is unknown, the critical wet bulb temperature is assumed unchanged at part-load conditions. Therefore, the performance map here predicts the same effective wet bulb temperature regardless of the sensible building load variations. In reality, there should be some dependency of $B_{ID,eff}$ on load. However, in the wet-coil scenarios, the SHR curves show some dependency on the sensible building loads, as the blue curve with respect to $BL_{c,s} = 2kW$ has larger SHR compared to the curves associated with larger loads. A few SHR curves are mixed together when the SHR is lower than 0.8. This could be a numerical issue resulting from the training process.

EXP-07 datapoints can be reproduced/predicted in terms of COP using the performance map. The reproduced values can be further plugged into $SCOP_c$ calculation in equation (2.15), in order to evaluate the impact of COP reproduction/prediction on temperature-bin-based $SCOP_c$. The comparison results can be seen in table 5.10. After the COP reproduction, the $SCOP_c$ values across 7 climates zones increase by

small percentages ranging from 0.9% to 1.3%, since each COP was slightly overpredicted by the performance map, as can be seen in figure 5.22. These percentage differences are as small as differences due to repeating CSA EXP-07 tests that were presented in table 2.12.

Table 5.10.
Impact of reproduction of COPs on temperature-bin-based $SCOP_c$

Climate zone	Very cold	Cold/dry	Cold/humid	Marine
Temperature-bin-based $SCOP_c$	5.83	5.02	5.81	4.92
$SCOP_c$ with COPs reproduced by mapping	5.94	5.15	5.92	5.05
Percentage difference	0.9%	1.2%	0.9%	1.3%
Climate zone	Mixed	Hot/humid	Hot/dry	
Temperature-bin-based $SCOP_c$	5.77	5.86	4.78	
$SCOP_c$ with COPs reproduced by mapping	5.88	5.96	4.91	
Percentage difference	0.9%	0.9%	1.3%	

5.6 Next-generation performance rating using equipment performance map

The most important application of a performance map involves integration of the mapping model into a building simulation, in order to enable simulation-based seasonal performance ratings that are both building-specific and climate-specific. Ideally, the equipment performance map would be directly integrated within the framework of a specific building simulation software that has typical and realistic building mod-

els. For implementation within EnergyPlus [36], this would require cooperation of the software developers, which was outside the scope of this study.

However, a framework or toolbox of co-simulation developed by Dostal [41] could be used to allow the performance map to be programmed in a different platform and coupled to an EnergyPlus simulation that is running in parallel.

Table 5.11.
Building geometry information

Zones:	3 zones: living zone crawlspace and attic zone	Floor area:	40ft x 30ft for each floor
Floors:	2 floors in living zone and an attic	Location:	Albuquerque international airport

A DOE prototype single-family building [35] was utilized here to interact with the equipment performance map under co-simulation. The building was simulated in Albuquerque, NM, and its information is tabulated in table 5.11. The building geometry is very similar to the building shown in figure 3.3 from chapter 3. Only the living spaces were conditioned that have two floors, and the conditioned area was roughly 2377 ft^2. A single thermostat with dual setpoints was used to maintain a $79°F$ cooling setpoint and a $72°F$ heating setpoint. EnergyPlus sized a 2-ton heat pump for this building that only ran out of capacity for 3 hours in peak summer throughout an annual simulation. Hence, the equipment performance map obtained in the section above is very suitable to be co-simulated with the building in terms of replacing the original heat pump, since the mapped equipment also has a 2-ton rated cooling capacity.

During the EnergyPlus simulation, the conditioned zone air temperature is always controlled within a deadband between the heating and cooling setpoints unless the equipment has insufficient capacity. In order to achieve this, an approach of energy rate control is utilized by EnergyPlus that can calculate the exact amount of required

equipment heating/cooling rates/loads (i.e. ideal loads) with respect to the dual setpoints based on a zone air energy balance for each simulation timestep.

This default EnergyPlus thermostat control approach is very suitable to be coupled to the performance map, since the ideal sensible load can be directly used as an input to the mapping model form ($BL_{c,s}$). Typically, this energy rate control is used along with an equipment model that is programmed within EnergyPlus. However, there is an approach to indirectly utilize the default energy rate control to guide an equipment model outside of EnergyPlus under the framework of co-simulation. Procedures for running the co-simulation are illustrated using the flowchart in figure 5.27 and summarized in following steps.

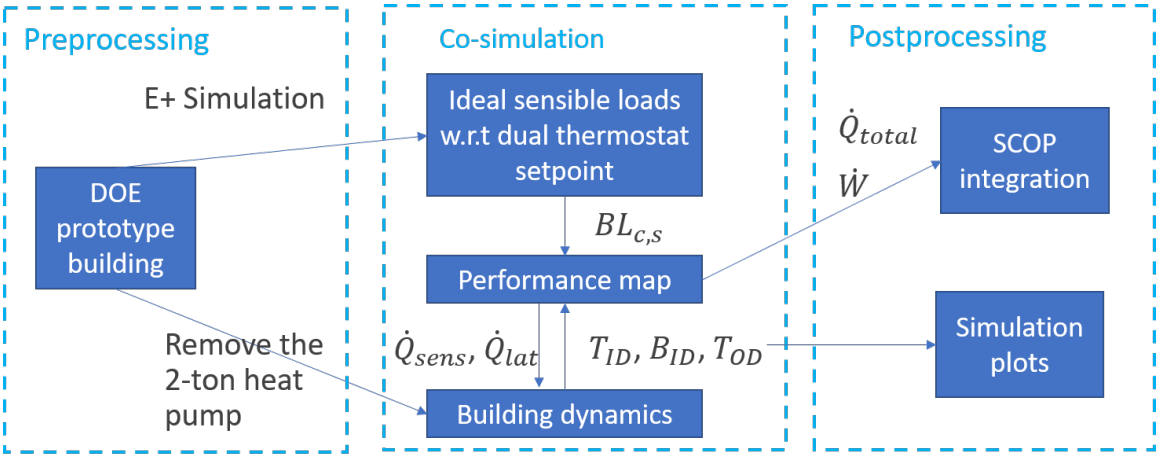

Fig. 5.27. Flowchart of EnergyPlus and performance map co-simulation

1. To prepare for the co-simulation, the original EnergyPlus building model needed to be pre-processed by carrying out an annual simulation in order to obtain a sequence and associated timestamp of the ideal sensible loads with respect to the dual thermostat setpoints using a simulation timestep of 1 hour.

2. In order to replace the original 2-ton heat pump in the EnergyPlus building model by the equipment performance map proposed in this work, all associated com-

ponents of the heat pump needed to be removed. Therefore, only the sensible and latent building dynamics were left.

3. During the co-simulation, for each timestep, the pre-calculated ideal sensible load is sent to the performance map as the sensible building load $BL_{c,s}$. Meanwhile, the building dynamics obtained in step 2 return real-time values of indoor dry bulb and wet bulb temperatures, along with outdoor temperature to the map. The performance map then calculates the corresponding equipment sensible/latent cooling rates and input power. The cooling rates are then fed back to the building dynamics as negative sensible/latent heat gains in real-time. When the ideal sensible load calls for heating, the cooling performance map is not utilized and the ideal heating rate is directly fed back to the building dynamics as sensible heat gain to maintain the conditioned zone air temperature in heating season.

4. During the co-simulation, inputs and outputs of the performance map are logged for post-processing associated with building responses and ambient conditions such as indoor/outdoor temperature/humidity. After the co-simulation, a simulation-based seasonal performance rating can be obtained as a sum of annual equipment total cooling rate over a sum of annual consumed power for the mapped equipment. Meanwhile, it is strongly suggested that plots be generated that illustrate part of or the entire sweep of the co-simulation. For example, it is very interesting to see whether the indoor temperature and humidity responded reasonably or not, to the predicted equipment cooling rates.

5.6.1 Co-simulation results

Following the procedures above, co-simulation results were obtained and the annual building responses are plotted in figure 5.28. In the upper subplot, outdoor temperature is represented by the red line that varies dynamically on both a seasonal and diurnal bases, according to the weather file for Albuquerque international airport.

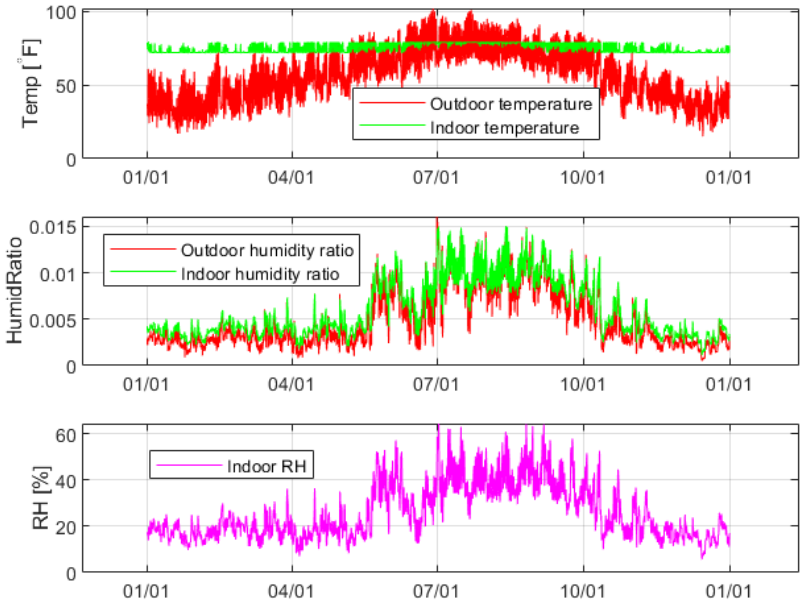

Fig. 5.28. Co-simulation results: annual building responses

The indoor dry bulb temperature is represented by the blue line that is perfectly controlled within a deadband between $72°F$ and $79°F$, since ideal sensible cooling and heating rates were delivered to the living zone with respect to the dual-setpoint thermostat. In the middle subplot, the outdoor humidity ratio (red line) and the indoor humidity ratio (green line) follow a similar pattern due to infiltration. However, in heating season, the indoor humidity ratio is slightly higher than the outdoor humidity due to the indoor moisture gain, and in cooling season, the indoor humidity has peaks that are lower than the outdoor humidity due to the simulated equipment's moisture removal. The latent cooling of the equipment is not very significant, since this a dry climate. Rather than indoor humidity ratio, indoor comfort depends more on indoor relative humidity that is shown in the lower subplot of figure 5.28. In heating season, the indoor RH floats at about 20%, while in cooling season, the indoor RH floats at about 40%. The maximum values of the RH are well controlled below 65% by the simulated equipment that was mapped.

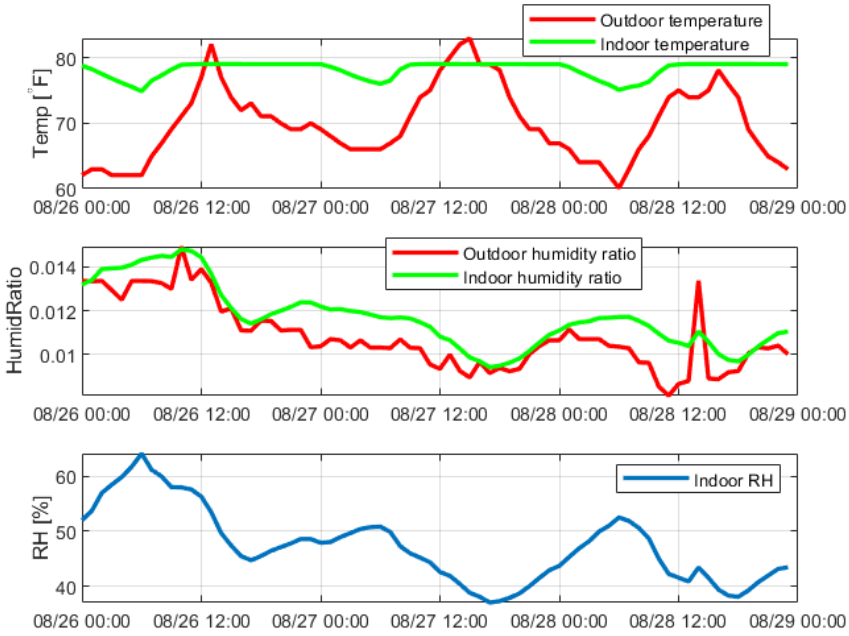

Fig. 5.29. Co-simulation results: building responses for three days in August

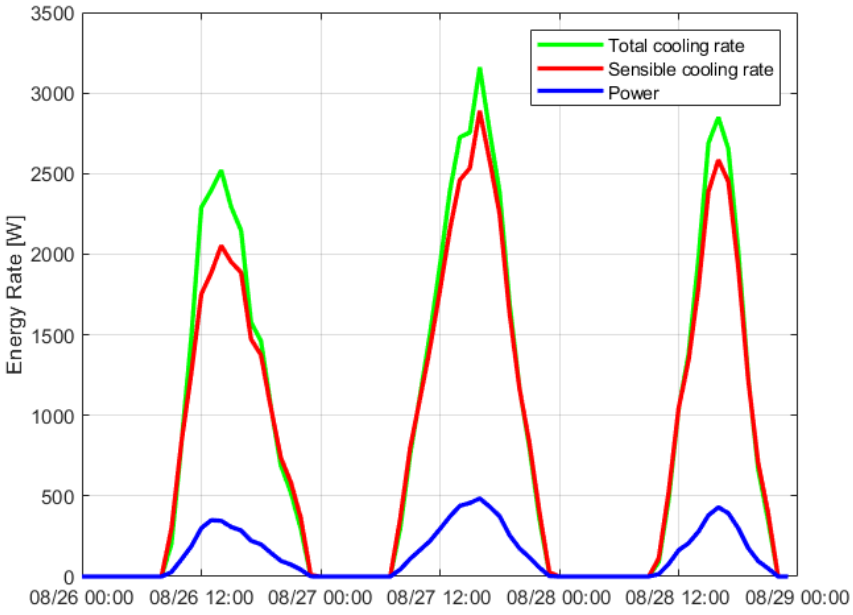

Fig. 5.30. Co-simulation results: equipment responses for three days in August

In order to show more co-simulation details, results for three days (August 26, 27 and 28) are shown in figure 5.29 and 5.30. Since this was the beginning of fall, the ambient temperature ranged roughly from $60°F$ to $83°F$. The indoor temperature was maintained at or below the cooling setpoint of $79°F$. In the early mornings, due to the relatively low ambient temperature and internal sensible gain, the indoor temperature gradually dropped to roughly $75°F$. Therefore, neither heating nor cooling was needed, as can be seen in figure 5.30 that shows the equipment quasi-steady-state responses for the three days in August. Sensible cooling rate in red line spiked up to more than 2kW in the afternoons along with the power (in blue line), in response to the increased ambient temperature. From about 14:00 to 15:00 in every afternoon, roughly 500W latent cooling rate can be observed, as the equipment ran at higher speed and the indoor environment was not very dry.

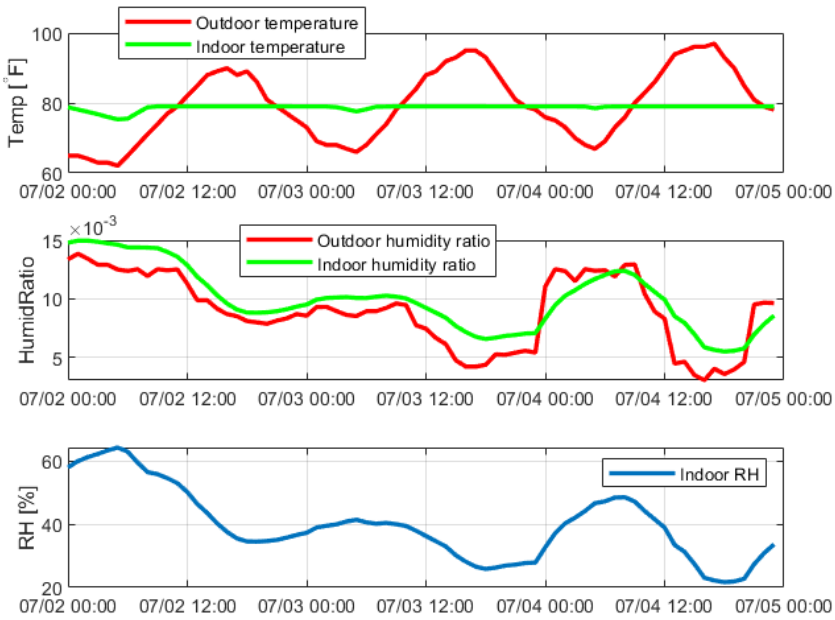

Fig. 5.31. Co-simulation results: building responses for three days in July

Figure 5.31 and 5.32 show co-simulation results for another three days (July 02, 03 and 04). Similar legends are used here. Since this was the middle of summer, the

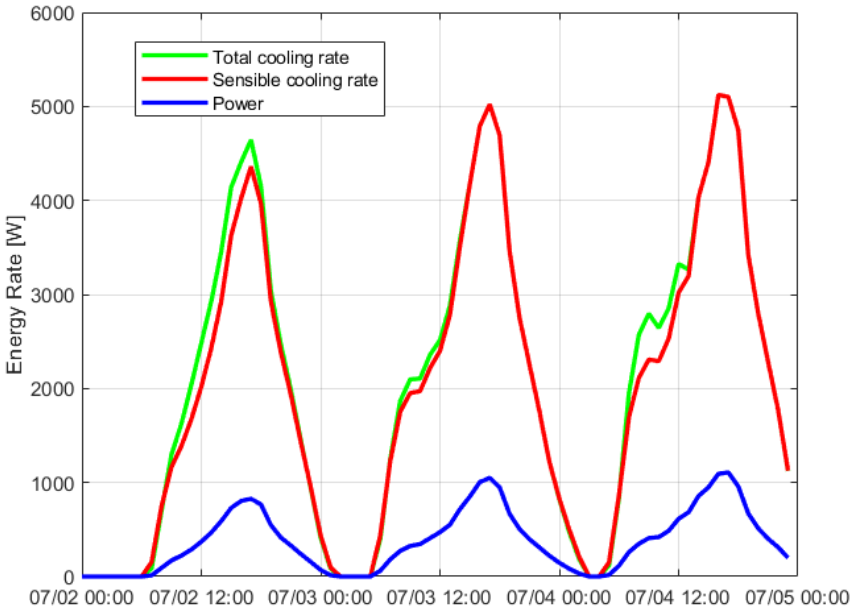

Fig. 5.32. Co-simulation results: equipment responses for three days in July

ambient temperature rose to more than $90°F$ in the afternoon, and therefore about 5kW sensible cooling was delivered by the equipment to the living zone for a few peak hours. In the mornings, after the equipment ramped up its speed, moisture removal was observed. However, at about 2:00 or 3:00 in the morning of July 02, the indoor RH rose as high as 60% without latent cooling from the equipment. This can also be observed in the early morning of August 26 in figure 5.29. Since the indoor temperature was low during the early mornings and the simulated equipment was controlled according to the thermostat temperature setpoint, the equipment delivered neither sensible cooling nor moisture removal to the living zone. Therefore, indoor RH could rise uncontrollably. If the actual equipment that is studied in this work were installed and turned on in the field, it would respond using its dehumidifying mode (seen in subsection 5.5.1) to provide moisture removal while slightly overcooling the space. Implementation of this mode should be addressed in future work, as a humidistat or a thermostat with an RH setpoint should be programmed under the framework of

co-simulation that calls for latent cooling associated with additional sensible cooling to maintain an RH setpoint and slightly overcool the space. However, in the current work using the co-simulation toolbox [41], this was difficult to achieve since the determination of the amount of temperature overcool, that exactly maintains the RH setpoint, requires iterations using building dynamics and the equipment performance map jointly within a simulation timestep. This manipulation of the joint iterations is beyond the scope of the EnergyPlus co-simulation toolbox [41]. However, the lack of a humidistat for this co-simulation in the dry climate zone doesn't significantly influence the results, since the hours when RH is higher than 60% were very limited.

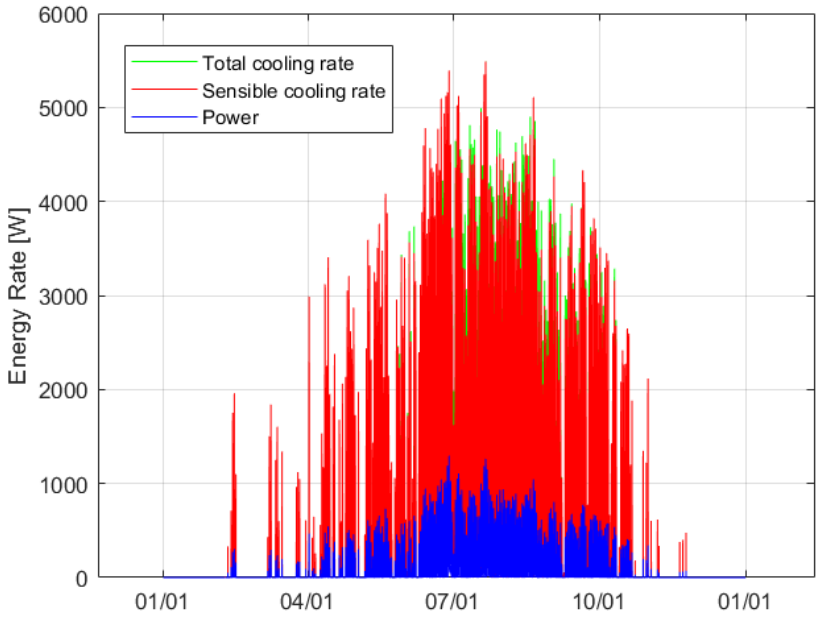

Fig. 5.33. Co-simulation results: annual equipment responses

Figure 5.33 shows the annual equipment responses. The blue line represents the power consumption, red line represents the sensible cooling rate and green line represents the total cooling rate. The air conditioner ramped up during cooling season, and the maximum total cooling rate was roughly 5.5kW, which is quite lower than the rated capacity of the equipment. Although not significant for this dry climate,

latent cooling can be frequently observed in the third quarter of the year. Finally, the simulation-based seasonal performance rating $SCOP_c$ was obtained as a sum of annual equipment total cooling rate over a sum of annual consumed power of the simulated air conditioner, and was found to be 5.79.

5.6.2 Comparison of simulation-based $SCOP_c$ against temperature-bin-based $SCOP_c$

Before presenting comparison results, it is necessary to dig deeper into the determination of temperature-bin-based $SCOP_c$ than the concise introduction in section 2.3, in order to understand nuances that contribute to differences in $SCOP_c$. According to CSA EXP-07 [10], temperature-bin-based $SCOP_c$ is determined using equation (5.32).

$$SCOP_c = \frac{\sum_{k=1}^{m}(DCR(T_k) \times n_k)}{\sum_{k=1}^{m}(\frac{DCR(T_k)}{COP(T_k)} \times n_k)} \tag{5.32}$$

where m is the number of temperature bins for the cooling climate zone, $DCR(T_k)$ is a sensible building load for the k^{th} temperature bin, n_k is the number of hours in the k^{th} temperature bin during the cooling season and $COP(T_k)$ is the COP for the k^{th} temperature bin estimated by interpolation using EXP-07 test outputs ($COP(T_{OD,j})$). Thus, the seasonal cooling coefficient of performance ($SCOP_c$) is the ratio of a total cooling load to a total electrical usage over the cooling season. The sensible load line of equation (2.12) evaluated at the design indoor temperature is used along with bin data for outdoor temperature to determine $DCR(T_k)$. Temperature bin data for each climate zone can be found in CSA EXP-07. According to the draft standard, Albuquerque, NM, belongs to hot/dry climate zone, of which the temperature bin hour fractions can be found in the fourth column (2^{nd} major column) of table 5.12.

The draft standard utilized an approach of cooling degree days to determine the bin hour fractions for the hot/dry climate based on the most current Typical Meteorological Year (TMY) data of a few typical cities in Arizona, New Mexico, California

Table 5.12.
Temperature bin hour fractions

Climate zone/location			EXP-07 hot/dry	Albuquerque	Albuquerque
Approach to determine bin hours			Cooling degree days	Cooling degree days	Utilizing Co -simulation results
k	$T_k[^\circ F]$	Range $[^\circ F]$	Bin hour fractions		
1	72	<74.5	0.213	0.439	0.443
2	77	74.5-79.5	0.143	0.174	0.208
3	82	79.5-84.5	0.154	0.145	0.152
4	87	84.5-89.5	0.131	0.125	0.105
5	92	89.5-94.5	0.163	0.091	0.072
6	97	94.5-99.5	0.109	0.021	0.016
7	102	99.5-104.5	0.058	0.005	0.004
8	107	104.5-109.5	0.025	—	—
9	112	>109.5	0.004	—	—

and Texas. In this thesis, cooling degree days (CDD_{Daily}) were evaluated for the Albuquerque TMY data using equation (5.33) that compares daily averaged temperature T_{DA} to a prescribed balance point temperature ($67^\circ F$) and makes sure that CDD_{Daily} is positive. Moreover, weekly moving averaged cooling degree days were calculated for each day associated with previous 6 days using equation (5.34). A day was determined as a cooling day, if its CDD_{Daily} was larger than $8^\circ F$ or if its CDD_{Weekly} was larger than $2^\circ F$. All 24 hours of the day were binned according to the 9 bins in table 5.12, if a day was deemed as a cooling day.

$$CDD_{Daily} = max(T_{DA} - 67, 0) \tag{5.33}$$

$$CDD_{Weekly} = \frac{\sum_{n-6}^{n} CDD_{Daily}}{7} \tag{5.34}$$

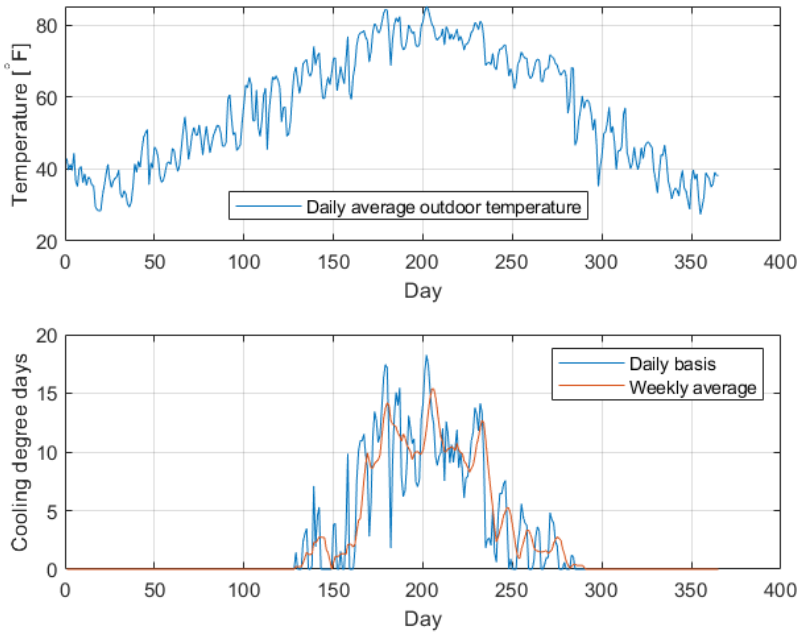

Fig. 5.34. Daily averaged outdoor temperature and cooling degree days for Albuquerque

Following this approach and utilizing the TMY3 weather data that were used for the co-simulation, temperature bin hour fractions were determined specifically for Albuquerque in this work and are shown in the fifth column of table 5.12. The upper plot of figure 5.34 shows the daily averaged outdoor temperature and the lower plot shows the cooling degree days on both daily and weekly averaged bases.

The last column of table 5.12 presents the temperature bin hour fractions determined from the co-simulation results using the Albuquerque TMY3 weather data. In this case, whether an hour is deemed as an effective cooling hour depends on the simulated ideal cooling sensible load for this hour obtained through co-simulation, instead of using the approach of cooling degree days. If the simulated ideal cooling sensible load for the hour was positive, the corresponding outdoor temperature was binned, as the hour was deemed as a cooling hour.

As can be seen in table 5.12, bin hour fractions determined for Albuquerque in the fifth and sixth columns are very similar, although they were obtained using two different approaches in terms of how to identify cooling days/hours. However, the EXP-07 hot/dry climate bin hour fractions are significantly different from the two columns on its right. The reason could be that climates of the typical cities that were used by EXP-07 to determine hot/dry climate bin hour fractions doesn't represent the weather of the single location of Albuquerque, NM.

In addition to the temperature bins, two important factors that impact $SCOP_c$ determination are the sensible building load (or demand cooling rate) $DCR(T_k)$ and the $COP(T_k)$ for the k^{th} temperature bin. Both of these are significantly influenced by the sensible load line used in EXP-07 load-based testing shown in equation (2.12). A different load line will result in different sensible building loads used in EXP-07 test intervals as test inputs and ultimately affect the test outputs (i.e. $COP(T_{OD,j})$) that dictate $COP(T_k)$.

In order to evaluate sensitivity of $SCOP_c$ to the load line, it is possible to obtain a specific sensible building load line for the single-family residential building in Albuquerque that was used in the co-simulation above. It would be very interesting to see how the $SCOP_c$ will change when the EXP-07 load line is substituted with the building-specific load line shown in figure 5.35.

The green line in figure 5.35 is a sensible load line that was identified using the ideal sensible cooling loads obtained in the co-simulation in the section above, while the red line is the EXP-07 sensible load line sized according to the rated capacity of the mapped equipment that was used in the co-simulation. It's obvious that the equipment is oversized for the single-family building in Albuquerque and therefore the EXP-07 load line prescribes a higher sensible load for the test equipment than the building-specific load line when the outdoor temperature is larger than $82°F$. However, the Albuquerque building has a lower balance point temperature ($63°F$) than the EXP-07 virtual building ($72°F$) for the same indoor temperature setpoint of 79 $°F$, possibly due to higher solar and internal gains.

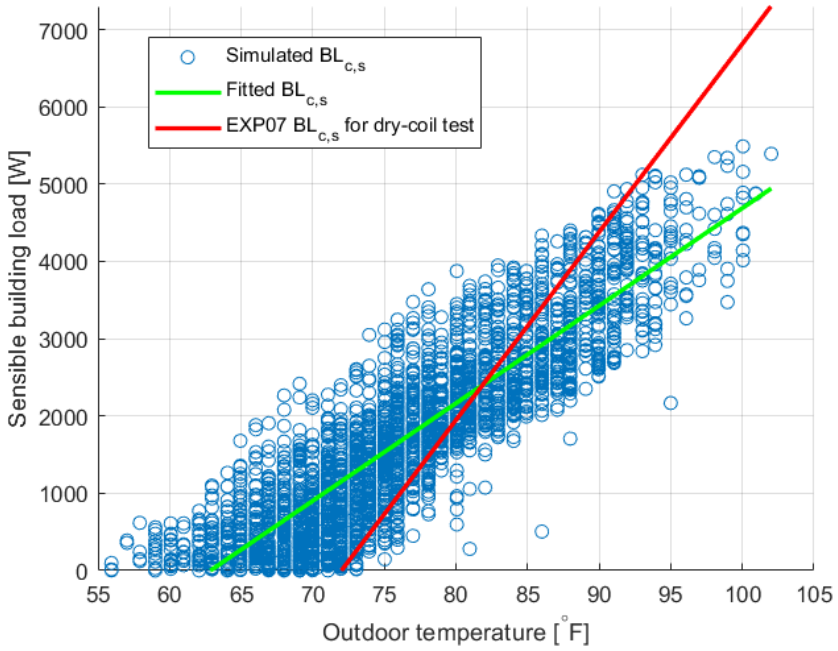

Fig. 5.35. Sensible building load line for the simulated single-family building in Albuquerque

The performance map, different load lines and various temperature bin hour fractions were used to compare different approaches for the temperature-bin-based $SCOP_c$ with the simulation-based $SCOP_c$. Comparison results are tabulated in table 5.13. $SCOP_c$ 1 is the EXP-07 $SCOP_c$ determined for the hot/dry climate. $SCOP_c$ 2 differs from $SCOP_c$ 1 only due to the performance mapping uncertainty as the COPs utilized in $SCOP_c$ 2 were determined from the map using the EXP-07 load line. $SCOP_c$ 3 and $SCOP_c$ 4 can be compared against $SCOP_c$ 2, since different temperature bin hour fractions were used among the three according to table 5.12. Both $SCOP_c$ 3 and $SCOP_c$ 4 are significantly larger than $SCOP_c$ 2, since they have larger bin hour fractions at lower ambient temperatures where COPs are higher. $SCOP_c$ 3 and $SCOP_c$ 4 are close since their bin hour fractions are similar, although the fractions were determined using different approaches. Instead of the EXP-07 load line, the building-specific load line was used for the determination of $SCOP_c$ 5. Compared

to $SCOP_c$ 4, $SCOP_c$ 5 is slightly larger although they were obtained using the same bin hour fractions, since the sensible load line used for $SCOP_c$ 5 specifies higher loads with low ambient, as can be seen in figure 5.35. On one hand, the COP from the performance map at the $77°F$ test interval with a load from the building-specific load line was higher compared to the COP at $77°F$ for the EXP-07 load line, since a higher part-load contributes to less cycling degradation loss. On the other hand, the higher COP for $77°F$ was weighted more heavily when averaging the COPs to obtain the temperature-bin-based $SCOP_c$, as the $77°F$ COP was used for both $72°F$ and $77°F$ bins where the summed fraction is larger than 60% according to table 5.12.

The results obtained using the simulation-based approach ($SCOP_c$ 6) yielded the highest $SCOP_c$ compared to the temperature-bin-based approach. $SCOP_c$ 5 is the closet to $SCOP_c$ 6, since $SCOP_c$ 5 was obtained using the same performance map, the same TMY3 weather data (to generate its temperature bins), and the same residential building (to generate its sensible load line) as for the determination of $SCOP_c$ 6. Possible reasons for a slightly higher value for $SCOP_c$ 6 than $SCOP_c$ 5 can be that building simulation is able to reflect higher COPs when the indoor coil is wet (for a few hours that can be found in the co-simulation) and when the ambient is slightly lower than $77°F$. For the temperature-bin-based $SCOP_c$, COP extrapolation below $77°F$ is not considered. Since the determination of the temperature-bin-based $SCOP_c$ 1 followed the procedures introduced in chapter 2 and the CSA EXP-07 draft standard, $SCOP_c$ 1 is inherently different than the simulation-based $SCOP_c$ 6 due to different weather data used, a different load line used, not being able to capture very low ambient performance and not considering wet-coil hours even for the dry climate. An advantage for $SCOP_c$ 1 is that COPs were obtained directly as test outputs that won't be compromised by potential mapping prediction uncertainty. However, advantages for the simulation-based $SCOP_c$ are significant, since $SCOP_c$ 6 is literally both climate-specific and building-specific that comprehensively captures the annual performance of the test equipment as if it were installed in a single-family building in Albuquerque.

Table 5.13.
Simulation-based $SCOP_c$ compared against a range of temperature-bin-based $SCOP_c$

	$SCOP_c$ 1	$SCOP_c$ 2	$SCOP_c$ 3
Approach for $SCOP_c$ determination	Temperature-bin -based $SCOP_c$	Temperature-bin -based $SCOP_c$	Temperature-bin -based $SCOP_c$
COPs used for five test intervals	COPs tested using EXP-07 load line	COPs reproduced by the map using EXP-07 load line	COPs reproduced by the map using EXP-07 load line
DCR used for each bin	EXP-07 load line	EXP-07 load line	EXP-07 load line
Bin hour fractions used	EXP-07 hot/dry climate bin hours	EXP-07 hot/dry climate bin hours	Albuquerque bins determined using cooling degree days
$SCOP_c$ value	4.78	4.91	5.33
	$SCOP_c$ 4	$SCOP_c$ 5	$SCOP_c$ 6
Approach for $SCOP_c$ determination	Temperature-bin -based $SCOP_c$	Temperature-bin -based $SCOP_c$	Simulation-based $SCOP_c$
COPs used for five test intervals	COPs reproduced from mapping using EXP-07 load line	COPs predicted by the map using the building-specific load line	—
DCR used for each bin	EXP-07 load line	The building-specific load line	—
Bin hour fractions used	Albuquerque bins determined using building simulation	Albuquerque bins determined using building simulation	—
$SCOP_c$ value	5.38	5.50	5.79

5.7 Interim conclusion

A next-generation approach for seasonal performance ratings was developed that uses load-based testing for performance mapping. With this approach, equipment seasonal performance can be rated using building simulations that incorporate specific building types, climate zones and the identified equipment performance map.

In order to achieve this goal, a model form was identified that is able to map both the equipment performance and its integrated controllers under quasi-steady-state operation and that can be obtained using a small amount of training data. A load-based quasi-steady-state model for variable-speed air conditioners was proposed and demonstrated in this chapter. The inputs to the performance mapping model were selected to include outdoor dry bulb temperature, indoor dry bulb and wet bulb temperatures, and sensible building load. The outputs from the model include equipment cooling rates and coefficient of performance. The demonstration involved training and validation using datapoints sampled from an equipment performance database that was acquired using simulation. Although some errors for equipment sensible heat ratio and latent cooling rate prediction occurred at low load scenarios, the model was able to accurately map the equipment total cooling rate, COP and power consumption across its operating envelope.

A critical step was to define an optimal test matrix that specifies an acceptably small number of testing requirements for mapping equipment performance using the proposed model form. Starting from a simulation database and utilizing an approach of optimal successive searching, it was shown that 12 datapoints can be used to train a mapping model such that it is able to well represent equipment performance. It was hoped that this optimal training dataset with respect to the simulation database would inform general heuristic rules for performing load-based tests on any equipment type that can lead to a performance map with similar accuracy. A heuristic experimental design was proposed that incorporates the 12 datapoints with some supplementary test points. In addition to the heuristic approach, a more general ex-

perimental design approach was developed using hierarchical clustering analysis that focused more on a uniform, complete and unbiased coverage of the operating envelope for any variable-speed air conditioner. In order to accommodate both training and validation analysis, an overall test matrix that incorporated 30 test points/intervals was obtained using both the heuristic experimental design approach and the clustering experimental design approach.

Load-based tests were then carried out using designed test matrix and utilizing the experimental setup associated with the test equipment used throughout this thesis work. Although five dehumidifying mode test intervals were obtained instead of regular cooling mode when two test inputs (sensible heat ratio and sensible building load) were both low, the proposed performance mapping model form was able to well represent all 30 performance mapping test intervals along with 9 previously determined EXP-07 test intervals. Using the test data, the successive optimal searching approach was utilized to obtain 12 optimal training datapoints from the test results that were used to train the mapping model such that all test results were best predicted. Therefore, the optimal performance map with respect to the test equipment was obtained. Since this mapping model form can be trained using acceptably small number of datapoints and can well represent both the 4-ton variable-speed air conditioner simulation database and the test equipment, it is believed that the performance mapping approach can be utilized in further estimation of seasonal performance ratings for variable-speed air conditioners.

Experimental design for performance mapping needs to be further validated and finalized in future work such that it can be applied to any residential cooling equipment type. Although two optimal training datasets were obtained using a successive optimal searching approach for a simulation database and a variable-speed air conditioner in current work, it is premature to propose one of them as an universal test matrix. However, it will be possible to obtain a near-optimal finalized experiment design and associated test matrix, after additional pieces of equipment are tested and mapped.

The last step to obtain a next-generation seasonal performance rating was to couple the performance map to a building simulation for a specific climate type and a specific building type. A framework of co-simulation with an EnergyPlus building model was utilized to virtually install and operate the mapped equipment in a single-family building in Albuquerque, NM, as a demonstration. A significant amount of detailed building and equipment quasi-steady-state responses were observed during the annual co-simulation and a $SCOP_c = 5.79$ was obtained as a simulation-based seasonal performance rating for the test equipment. The simulation-based $SCOP_c$ is significantly higher than the temperature-bin-based $SCOP_c$ for the equipment, due to the use of more appropriate weather data, building-specific load lines and because the annual simulation was able to better capture very low ambient performance and wet-coil hours even for dry climates. Therefore, it is believed that this next-generation performance rating approach is able to comprehensively and appropriately reflect annual field performance for cooling equipment that is specific to a climate and residential building and that only requires a small number of data points to generate a performance map from automated laboratory load-based testing.

6. CONCLUSIONS AND FUTURE WORK

6.1 Conclusions

Currently, performance ratings for unitary residential air conditioners and heat pumps in the U.S. marketplace are based on results of steady-state laboratory tests according to the procedures and methodology established by standard AHRI 210/240 [2]. However, this current methodology is inadequate to credit equipment that has improved part-load performance due to the employment of variable-speed components and advanced controls. The automated load-based testing and rating methodology presented in this work better reflects the field performance of test equipment with its native controls. This methodology is already implemented within the Canadian Standards Association (CSA) EXP-07 draft standard [10] and is likely to be a basis for future testing and rating standards within the United States and elsewhere. The key element of the approach is that the dynamic response of a virtual building is emulated using the psychrometric chamber controls to interact with the test equipment in real-time, such that the equipment behaves as if it were installed in the field.

Starting from the CSA EXP-07 standard, an updated, more complete, and archival description of the laboratory load-based testing methodology was introduced in chapter 2 that includes the basis for development, necessary steps for automation and convergence criteria. Specifically, background of the virtual building modeling approach and its parameters were introduced and example dynamic testing results for a state-of-the-art high efficiency, variable-speed heat pump operating in cooling mode were presented. Standardized procedures were also presented that can be used to automatically test different dynamic load-based test intervals as a whole sweep using convergence criteria applied to individual test intervals. In demonstrating the approach for the variable-speed heat pump, typical dynamic behaviors of the equipment

were observed such as on/off cycling, continuous capacity modulation due to feedback control of compressor speed, indoor humidity variation with operating conditions and controller fluctuations, and capacity limits that lead to loss of indoor temperature conditions. The type of information obtained during these dynamic tests can be extremely useful in evaluating advanced controllers during the development process and provide appropriate incentives for improving performance within rating procedures.

In load-based testing, the test equipment thermostat senses the floating air temperature and communicates with the test equipment as if it were installed in the field. Therefore, it is important to properly emulate a test environment for the thermostat that is representative of field conditions and that can be reproduced across different test facilities. To address this, in chapter 4, a thermostat environment emulator was developed for use in load-based testing as a means of emulating inlet conditions to a test thermostat that are representative and reproducible. This device provides typical flow conditions and appropriate virtual building dynamics associated with varying inlet temperatures to a thermostat connected to its test equipment. The environment emulator includes a plenum that encloses the test thermostat, air velocity controls that maintain representative internal airflow and air temperature controls that emulate the virtual building dynamics to the test thermostat that are needed in load-based testing. This part of work also provided a detailed description of the design and operation of this thermostat environment emulator that can be used as a basis for providing a standardized solution for applying load-based testing to air conditioning equipment that is reproducible across different facilities. A model of the emulator was also developed and described in detail and could be used to investigate future improvements. The emulator was integrated into load-based cooling tests for dry-coil and wet-coil climate conditions and was able to control the thermostat inlet temperature almost perfectly to the virtual room temperature setpoints for both tests.

In terms of obtaining performance ratings from load-based testing, a temperature-bin-based method was presented and demonstrated in chapter 2, that echos the ap-

proach used in CSA EXP-07. The temperature-bin-based climate-specific ratings are estimations of seaonal coefficient of performance ($SCOP_c$) for the test equipment, determined by effectively averaging the load-based test results (COPs) according to specific ambient temperature bin hour fractions for each climate and the EXP-07 sensible building load for each bin. It was found that seasonal ratings were significantly higher in humid climates for the equipment considered in this study because of better test performance for wet-coil than dry-coil conditions. The highest rating occurred for a hot/humid climate, whereas the worst performance was for a hot/dry climate. The effect of building parameters on performance ratings was also investigated and illustrated the ability of load-based testing to capture the impacts of different building-load interactions. This capability for load-based testing could be very useful in the development process for improved equipment and controller technology.

As an alternative to the temperature-bin-based traditional seasonal performance rating approach, a next-generation approach was developed that uses load-based testing for performance mapping that is combined with building simulations to determine seasonal performance ratings that are both building-specific and climate-specific. A load-based quasi-steady-state model for a variable-speed air conditioner was proposed and demonstrated in chapter 5 as the mapping model form. The initial development involved training and validation using datapoints sampled from an equipment performance database that was acquired using simulation. Trained using acceptably small number of datapoints, the model was able to accurately map the equipment total cooling rate, COP and power consumption across its operating envelope. Based on the proposed mapping model form and the simulation database, a heuristic experimental design approach and a clustering experimental design approach were presented that specified a test matrix for load-based tests that were carried out using the experimental setup associated with the test equipment used throughout this thesis work. Trained using only 12 optimal test points, the performance map was able to predict the validation load-based test points within $\pm 10\%$ errors and with R^2 values close

to 1. Since the mapping model form can well represent both the variable-speed air conditioner simulation database and the test equipment throughout their operating envelopes, it is believed that the performance mapping approach can be utilized in the future for estimation of seasonal performance ratings for variable-speed air conditioners.

The next-generation seasonal performance rating approach was presented and demonstrated in chapter 5 that coupled the identified performance map to a building simulation with respect to a specific climate type and building type. A framework of co-simulation with an EnergyPlus [36] building model was utilized to virtually install and operate the mapped equipment in a single-family building in Albuquerque, NM, as a demonstration. The simulation-based $SCOP_c$ is a more appropriate performance rating for cooling equipment than the temperature-bin-based $SCOP_c$, due to the use of more specific weather data, consideration of building dynamics and because the associated annual simulation is able to better capture a few subtle but non-negligible building-equipment interactions. Therefore, it is believed that this is a next-generation performance rating approach and will be able to comprehensively and appropriately reflect annual field performance for a cooling equipment within a specific climate and a residential building.

To summarize, this thesis work successfully presented: 1) an updated, more complete, and archival description of the laboratory load-based testing methodology that includes the basis for development, necessary steps for automation and convergence criteria; 2) design and demonstration of a thermostat environment emulator that can provide realistic and reproducible inlet conditions to a test thermostat for the purpose of load-based equipment testing; 3) evaluation and validation of the complete load-based testing methodology using residential equipment within a laboratory setup; 4) a methodology to extend load-based testing for performance mapping that captures both the equipment performance and its integrated controllers under quasi-steady-state operation; 5) a next-generation approach for obtaining seasonal coefficient of performance for rating of residential unitary cooling equipment that is based on sim-

ulation that includes an equipment-specific performance map, specific building and climate types.

6.2 Future work

Since this work focused on development and investigation of a standardized next-generation testing and rating methodology for residential cooling equipment, the most important and straightforward future work is to repeat and reproduce the proposed approaches. In addition, seven potential future steps are proposed here in terms of improvements to the current methodology.

1. The thermostat environment emulator should be reproduced across different test facilities and be used to test different types of unitary cooling equipment. Specifically, it is important to observe whether the reproduced emulator can always track the virtual room temperature setpoints that are adjusted according to outputs from the virtual building model. It may be necessary to consider thermoelectric devices with more cooling capacity to accommodate potential environmental chambers and situations with inlet temperatures that are significantly warmer than the desired setpoints. In addition, when a single-speed test equipment turns on its compressor and fans in the $77°F$ low-load dry-coil test interval, the virtual room temperature setpoints will drop with a slope in time domain that could be too large to be tracked by both the environmental chamber and the thermostat environment emulator controls. This is another reason that the emulator might need to be redesigned to have a larger cooling capacity in order to become a universal solution for any thermostat in load-based testing.

2. Methods for addressing load-based testing with thermostats that include precise humidity control in dehumidifying mode should be considered in future development and investigation of the thermostat environment emulator. The emulator proposed in this work cannot achieve humidity control using its cooling/heating thermoelectric

devices. Therefore, if there were significant differences in the humidity dynamics between the inlet to test unit and the inlet to test thermostat, it could be necessary to modify the emulator to incorporate humidifying/dehumidifying devices or alternative approaches. It could be a good idea to integrate the air sampling approach explored in this work into the current design of the emulator, such that the thermostat inlet humidity will mirror the test unit inlet humidity, as long as there is no moisture condensation or addition during the sampling process.

3. The performance mapping model form could be improved in terms of determination of dry-coil scenarios. The model form proposed in the current work uses a bypass factor approach [21] that requires iterations to determine the transition to a dry coil when the indoor humidity level is low. Although the approach is effective and accurate when evaporator airflow is known, it requires significant computational effort during model training and during co-simulation due to the iterations. Moreover, the approach cannot be used when the part-load airflow is unknown, such that some errors for equipment latent cooling rate prediction were observed in low-load scenarios.

4. A significant future work is to investigate uncertainties that propagate through load-based testing, performance mapping to seasonal performance ratings, although current work has already covered error propagation from instrumentation to temperature-bin-based $SCOP_c$. On one hand, it is tricky to investigate error propagation through the proposed mapping model form that incorporates iterations along with psychrometric relations. On the other hand, it is challenging to quantify equipment control uncertainties.

5. Experimental design for performance mapping needs to be further validated and finalized such that it can be applied to any residential cooling equipment type, in order to obtain an acceptably accurate map trained using a small number of experimental results. Although two optimal training datasets were obtained using a

successive optimal searching approach for a simulation database and a variable-speed air conditioner in current work, it is premature to propose one of them as an universal test matrix. However, it will be possible to obtain a near-optimal finalized experiment design and associated test matrix, after additional pieces of equipment are tested and mapped.

6. During determination of the next-generation simulation-based $SCOP_c$, a humidistat or a thermostat with a RH setpoint should be programmed under the framework of co-simulation that calls for a dehumidifying mode to maintain RH setpoint and override the temperature setpoint. This is important for a few hours within an annual simulation in humid climate zones when latent load is high and sensible load is low, such as early summer mornings. In order to achieve this in the future, the performance map needs to be embedded and programmed deeper into the framework of the building simulation (software).

7. The co-simulation of the equipment performance map obtained in the current work can be carried out throughout the U.S. to couple to various residential building types and climate zones, in order to fully evaluate the proposed approach of the next-generation performance rating that is extended from automated laboratory load-based testing and performance mapping.

8. The approaches proposed in this work for cooling equipment can be further extended and applied to laboratory load-based testing, performance mapping and rating of unitary heat pumps operated in heating mode. The future investigation could start from the CSA EXP-07 draft standard [10] that presents a detailed description of load-based heating test procedures and associated temperature-bin-based seasonal performance ratings.

REFERENCES

REFERENCES

[1] J. Mitchell and J. Braun, *Principles of Heating, Ventilation, and Air Conditioning in Buildings*. Wiley, 2012. [Online]. Available: https://books.google.com/books?id=nXekZwEACAAJ

[2] A. Standard, "210/240.(2017). performance rating of unitary air-conditioning & airsource heat pump equipment. arlington, va, usa: Air-conditioning, heating & refrigeration institute," 2017.

[3] J. Proctor and P. G. Cohn, "Two-stage high efficiency air conditioners: Laboratory ratings vs. residential installation performance," *Transactions of the 2006 ACEEE Summer Study on Energy Efficiency in Buildings*, 2006.

[4] R. Hart, W. Price, J. Taylor, H. Reichmuth, and M. Cherniack, "Up on the roof: From the past to the future," *ACEEE Summer Study on Energy Efficiency in Buildings, American Council for an Energy-Efficient Economy (ACEEE), Pacific Grove, CA*, p. 3, 2008.

[5] P. Fairey, D. S. Parker, B. Wilcox, and M. Lombardi, "Climatic impacts on heating seasonal performance factor (hspf) and seasonal energy efficiency ratio (seer) for air-source heat pumps," *ASHRAE Transactions*, vol. 110, p. 178, 2004.

[6] L. Cremaschi and P. Perez Paez, "Experimental feasibility study of a new load-based method of testing for light commercial unitary heating, ventilation, and air conditioning (ashrae rp-1608)," *Science and Technology for the Built Environment*, vol. 23, no. 7, pp. 1178–1188, 2017.

[7] A. L. Hjortland and J. E. Braun, "Load-based testing methodology for fixed-speed and variable-speed unitary air conditioning equipment," *Science and Technology for the Built Environment*, pp. 1–12, 2018.

[8] A. Patil, A. L. Hjortland, L. Cheng, P. Dhillon, J. E. Braun, and W. T. Horton, "Load-based testing to characterize the performance of variable-speed equipment," 2018.

[9] D. Parveen, A. Patil, L. Cheng, J. E. Braun, and W. T. Horton, "Performance evaluation of heat pump systems based on a load-based testing methodology," 2018.

[10] C. Standard, "Exp07:19 load-based and climate-specific testing and rating procedures for heat pumps and air conditioners," 2019.

[11] L. Cheng, A. Patil, and P. Dhillon, "Impact of virtual building model and thermostat installation on performance and dynamics of variable-speed equipment during load-based tests," 2018.

[12] N. A. Boldt, "A new nema standard for room thermostat test equipment," *IEEE Transactions on Industry Applications*, no. 6, pp. 703–709, 1974.

[13] National Electrical Manufacturers Association, "NEMA DC 3 Residential Controls – Electrical Wall-Mounted Room Thermostats," 2014.

[14] A. Standard, "550/590 (ip), 2011: 2011 standard for performance rating of water-chilling and heat pump water-heating packages using the vapor compression cycle," *Air-Conditioning, Heating, Refrigeration Institute, Arlington, VA, USA*.

[15] S. Bustamante, P. Castro, A. Laso, M. Manana, and A. Arroyo, "Smart thermostats: an experimental facility to test their capabilities and savings potential," *Sustainability*, vol. 9, no. 8, p. 1462, 2017.

[16] B. Shen, "Improvement and validation of unitary air conditioner and heat pump simulation models at off-design conditions," 2006.

[17] "Achp." [Online]. Available: https://achp.readthedocs.io/en/latest/index.html

[18] H. Cheung, "Inverse modeling of vapor compression equipment to enable simulation of fault impacts," Ph.D. dissertation, Purdue University, 2014.

[19] J. Cai and J. E. Braun, "A generalized control heuristic and simplified model predictive control strategy for direct-expansion air-conditioning systems," *Science and Technology for the Built Environment*, vol. 21, no. 6, pp. 773–788, 2015.

[20] H. Yang and H. Li, "A generic rating-data-based (grdb) dx coils modeling method," *HVAC&R Research*, vol. 16, no. 3, pp. 331–353, 2010.

[21] M. J. Brandemuehl, *HVAC 2 toolkit: A toolkit for secondary HVAC system energy calculations*. American Society of Heating, Refrigerating and Air-Conditioning Engineers, 1993.

[22] F. Winkelmann, B. Birdsall, W. Buhl, K. Ellington, A. Erdem, J. Hirsch, and S. Gates, "Doe-2 supplement: version 2.1 e," Lawrence Berkeley Lab., CA (United States); Hirsch (James J.) and Associates ..., Tech. Rep., 1993.

[23] H. Henderson, "Residential equipment part load curves for use in doe-2," 1999.

[24] J. Cai *et al.*, "Gray-box modeling of multistage direct-expansion units to enable control system optimization," *ASHRAE Transactions*, vol. 121, p. 203, 2015.

[25] A. L. Hjortland, "Automated fault detection, diagnostics, impact evaluation, and service decision-making for direct expansion air conditioners," Ph.D. dissertation, Purdue University, 2018.

[26] "Energyplus input and output reference." [Online]. Available: https://energyplus.net/sites/all/modules/custom/nrel_custom/pdfs/pdfs_v8.9.0/InputOutputReference.pdf

[27] S. Nyika, S. O. Holloway *et al.*, "Generalized performance maps for variable-speed, ducted, residential heat pumps," *ASHRAE Transactions*, vol. 120, p. 80, 2014.

[28] V. Aute, C. Martin, and R. Radermacher, "A study of methods to represent compressor performance data over an operating envelope based on a finite set of test data (no. 8013)," *College Park, MD: Air-Conditioning, Heating, and Refrigeration Institute*, 2015.

[29] I. Henderson and E. Member, "SiMULATiNG COMBINED THERMOSTAT , AiR CONDiTiONER , AND BUILDING PERFORMANCE IN A HOUSE," pp. 370–380, 1989.

[30] H. Henderson, R. Raustad, K. Rengarajan, O. Publication, and P. Number, "Measuring Thermostat and Air Conditioner Performance in Florida Homes Authors," 1991.

[31] National Electrical Manufacturers Association, "NEMA DC 3 Residential Controls – Electrical Wall-Mounted Room Thermostats," 1990.

[32] J. Cai and J. E. Braun, "Efficient and robust training methodology for inverse building modeling," *Proceedings of SimBuild*, vol. 5, no. 1, pp. 456–461, 2012.

[33] P. Bacher and H. Madsen, "Identifying suitable models for the heat dynamics of buildings," *Energy and Buildings*, vol. 43, no. 7, pp. 1511–1522, 2011.

[34] C. R. Touretzky and M. Baldea, "Nonlinear model reduction and model predictive control of residential buildings with energy recovery," *Journal of Process Control*, vol. 24, no. 6, pp. 723–739, 2014.

[35] "Residential prototype building models." [Online]. Available: https://www.energycodes.gov/development/residential/iecc_models

[36] "Energyplus." [Online]. Available: https://energyplus.net/

[37] S. Lineykin and S. Ben-Yaakov, "Analysis of thermoelectric coolers by a spice-compatible equivalent-circuit model," *IEEE Power Electronics Letters*, vol. 3, no. 2, pp. 63–66, 2005.

[38] V. Gnielinski, "New equations for heat and mass transfer in turbulent pipe and channel flow," *Int. Chem. Eng.*, vol. 16, no. 2, pp. 359–368, 1976.

[39] R. H. Byrd, J. C. Gilbert, and J. Nocedal, "A trust region method based on interior point techniques for nonlinear programming," *Mathematical programming*, vol. 89, no. 1, pp. 149–185, 2000.

[40] D. E. Goldberg and J. H. Holland, "Genetic algorithms and machine learning," 1988.

[41] J. Dostal, "Energyplus co-simulation toolbox." [Online]. Available: https://www.mathworks.com/matlabcentral/fileexchange/69074-energyplus-co-simulation-toolbox

APPENDICES

Results of 39 load-based test intervals are appended as follow in table 1, table 2 and table 3. Future researchers will then be able to revisit the data for further investigation of performance mapping approach. These datapoints were utilized in chapter 5 to train and validate a mapping model form. As can be seen in table 1, performance mapping tests 1 to 15 were obtained according to the heuristic experimental design test matrix that was shown in table 5.4. In table 2, performance mapping tests 16 to 30 were obtained according to the clustering experimental design test matrix that was shown in table 5.5. Table 3 presents the results of the 9 EXP-07 cooling test intervals that were used to validate the performance map. These three tables present ratios of the test equipment sensible cooling rates over the rated capacity of the equipment. Therefore, the associated sensible cooling rates can be easily calculated, given the 9639W rated capacity.

In order to illustrate the associated dynamic testing process and the test equipment behaviors, test plots are also appended as follow from figure 1 to 60. Associated test number can be found in caption of each figure for tests 1 to 30. Test plots for the 9 EXP-07 test intervals can be seen in figures 2.7 to 2.11 in chapter 2, and therefore are not represented here.

Table 1.
Performance mapping load-based test results obtained according to heuristic experimental design test matrix

Test	$T_{OD}[^{\circ}F]$	$T_{ID}[^{\circ}F]$	$B_{ID}[^{\circ}F]$	$\frac{\dot{Q}_s}{\dot{Q}_{rat}}$	SHR	COP	Behavior
1	77	77.3	63.3	0.75	0.80	7.84	Variable-speed
2	86	77.1	66.1	0.50	0.65	6.73	Variable-speed
3	86	77.4	60.3	0.50	0.94	5.52	Cycling
4	95	69.5	61.2	0.26	0.66	5.03	Cycling
5	95	73.0	56.6	0.66	0.95	4.22	Full-load
6	95	77.2	66.0	0.50	0.65	5.56	Variable-speed
7	95	76.0	63.0	0.25	0.80	4.96	Cycling
8	95	77.0	63.5	0.69	0.80	5.30	Full-load
9	95	77.3	60.1	0.50	0.94	4.59	Cycling
10	104	73.3	63.8	0.50	0.65	4.52	Variable-speed
11	104	73.0	56.6	0.69	0.95	3.81	Full-load
12	104	77.4	64.0	0.50	0.79	4.37	Cycling
13	77	70.8	62.6	0.25	0.64	7.37	Cycling
14	77	79.2	62.8	0.24	0.93	6.74	Cycling
15	86	71.2	59.8	0.25	0.81	5.38	Cycling

Table 2.
Performance mapping load-based test results obtained according to clustering experimental design test matrix

Test	$T_{OD}[^{\circ}F]$	$T_{ID}[^{\circ}F]$	$B_{ID}[^{\circ}F]$	$\frac{\dot{Q}_s}{\dot{Q}_{rat}}$	SHR	COP	Behavior
16	74	78.6	60.3	0.80	0.93	7.00	Variable-speed
17	76	71.3	61.4	0.49	0.70	7.52	Variable-speed
18	76	79.4	66.4	0.64	0.71	8.22	Variable-speed
19	77	69.4	61.5	0.20	0.65	6.94	Cycling
20	77	70.0	57.4	0.20	0.90	5.98	Cycling
21	77	78.1	66.7	0.30	0.69	7.75	Cycling
22	77	79.3	61.7	0.39	0.94	6.73	Cycling
23	78	71.3	55.1	0.59	0.95	6.11	Variable-speed
24	95	69.9	59.5	0.61	0.76	4.87	Variable-speed
25	97	79.0	60.8	0.78	0.95	4.84	Full-load
26	98	78.3	65.7	0.60	0.71	5.27	Variable-speed
27	100	69.6	61.3	0.30	0.65	4.63	Cycling
28	100	71.3	57.4	0.38	0.91	4.08	Cycling
29	100	77.2	66.7	0.30	0.65	4.93	Cycling
30	100	79.2	62.5	0.37	0.92	4.41	Cycling

Table 3.
EXP-07 cooling load-based test results

$T_{OD}[^\circ F]$	$T_{ID}[^\circ F]$	$B_{ID}[^\circ F]$	$\frac{\dot{Q}_s}{\dot{Q}_{rat}}$	SHR	COP	Behavior
77	78.0	56.7	0.15	0.98	5.59	Cycling
86	78.0	56.2	0.39	0.99	5.33	Cycling
95	78.2	56.0	0.60	0.99	4.56	Variable-speed
104	80.2	57.0	0.76	1.00	4.02	Variable-speed
113	79.0	56.2	0.73	1.00	3.33	Full-load
77	73.1	60.8	0.26	0.81	6.42	Cycling
86	73.4	61.2	0.38	0.82	5.75	Variable-speed
95	74.5	61.9	0.66	0.80	5.07	Variable-speed
104	74.0	62.0	0.65	0.80	4.29	Full-load

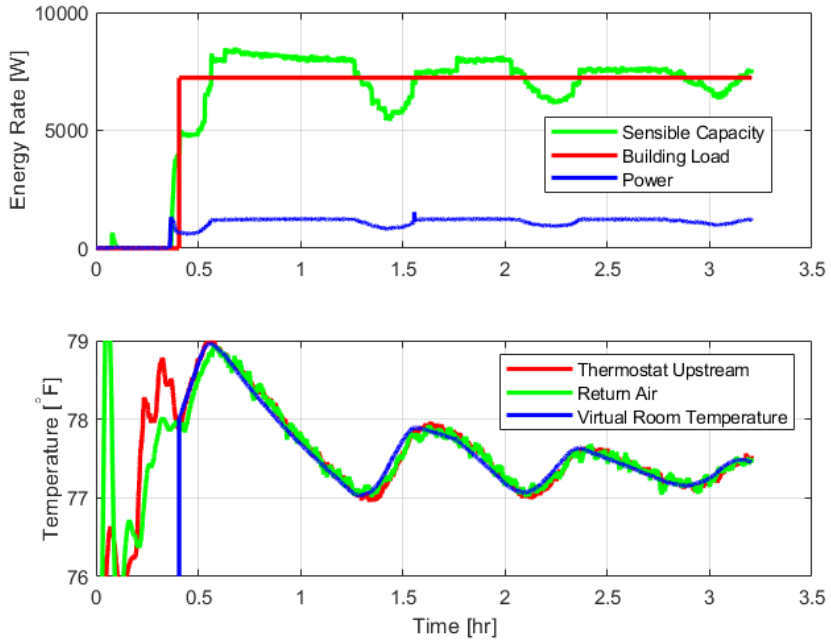

Fig. 1. Sensible results of performance mapping test 1

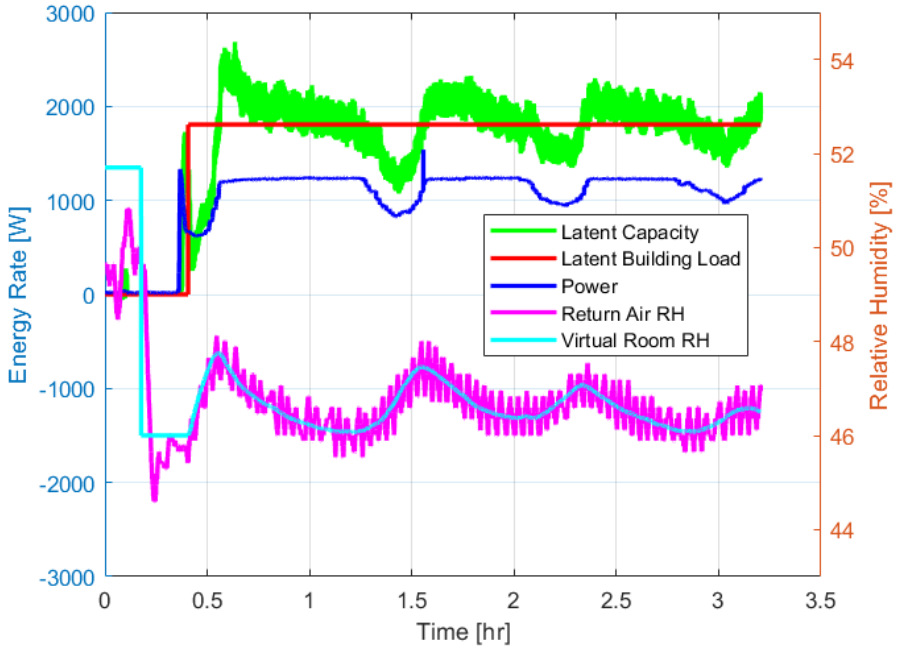

Fig. 2. Latent results of performance mapping test 1

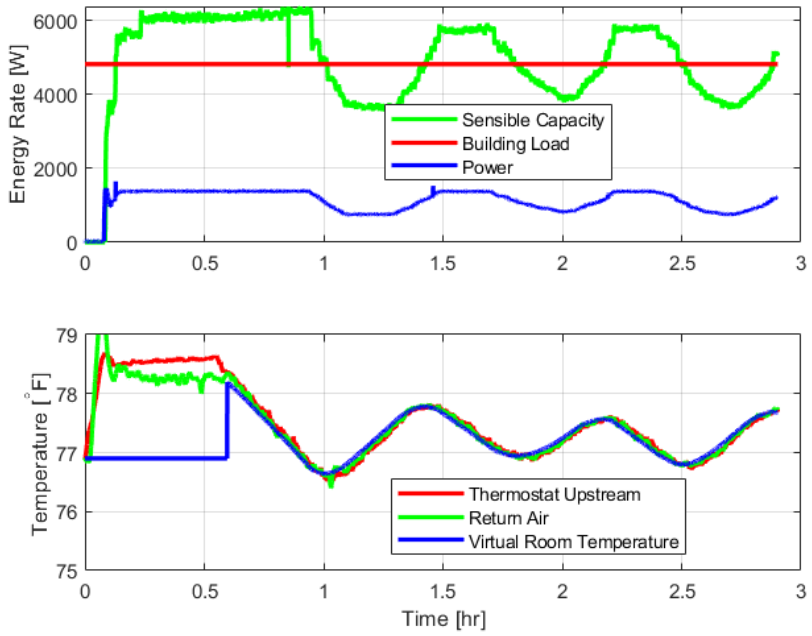

Fig. 3. Sensible results of performance mapping test 2

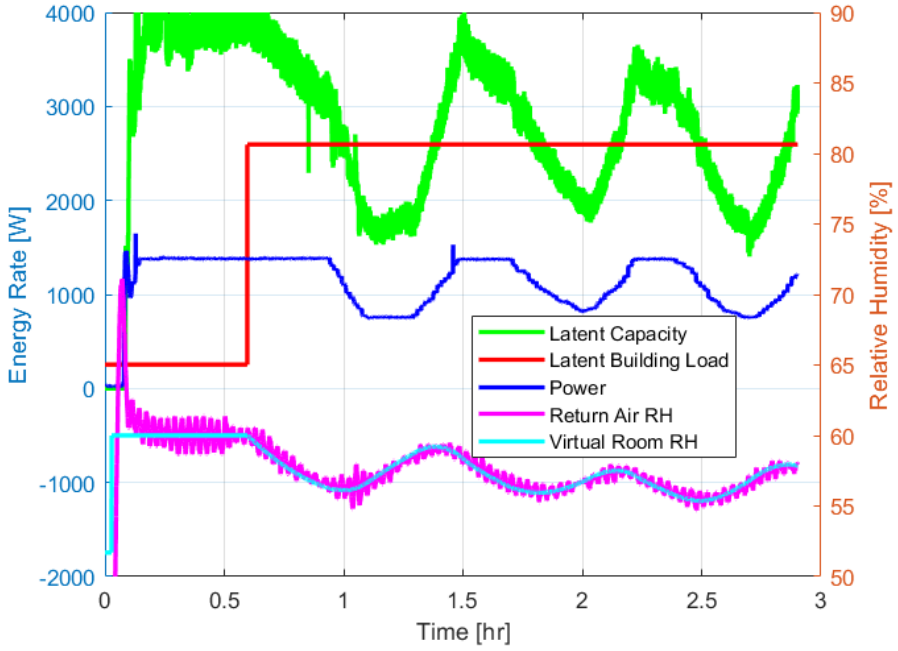

Fig. 4. Latent results of performance mapping test 2

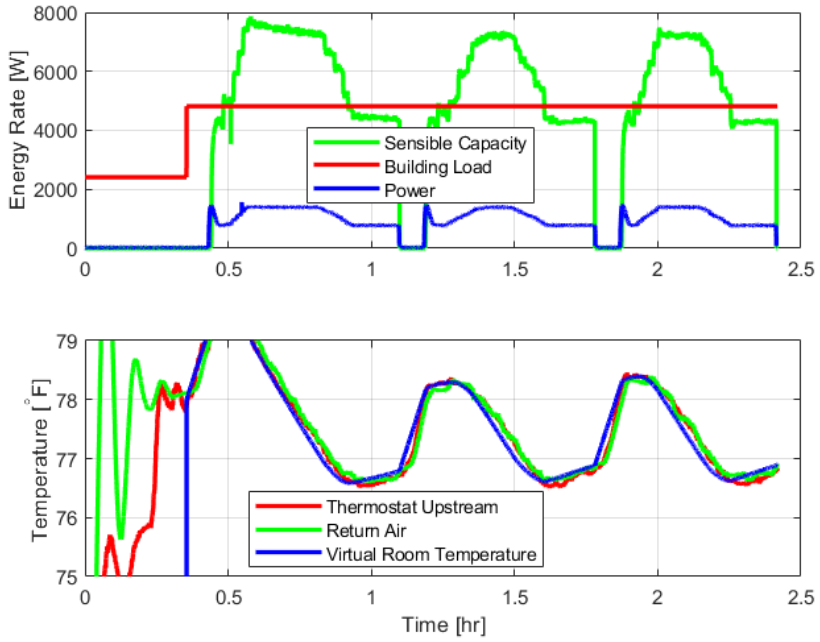

Fig. 5. Sensible results of performance mapping test 3

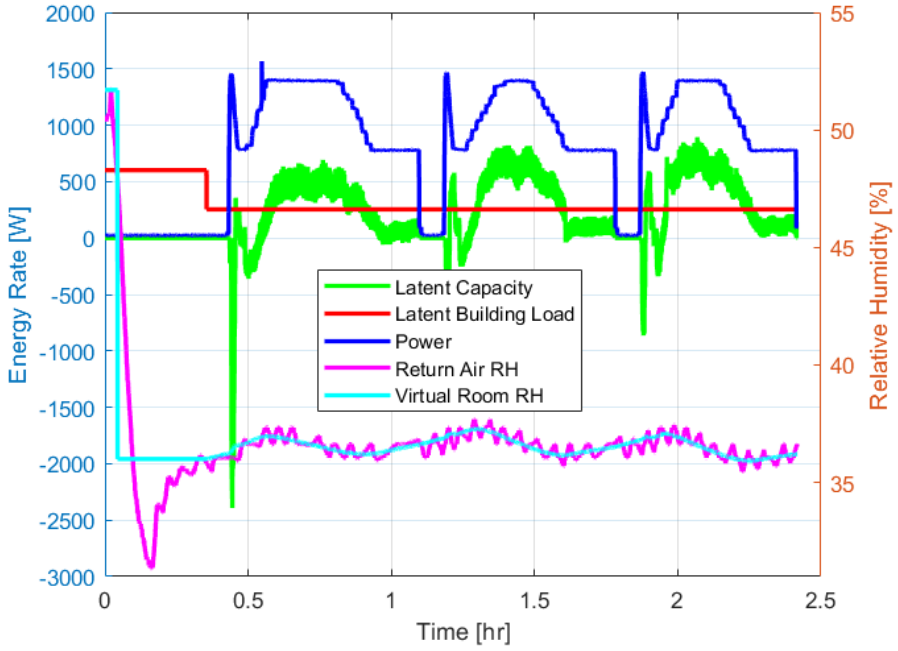

Fig. 6. Latent results of performance mapping test 3

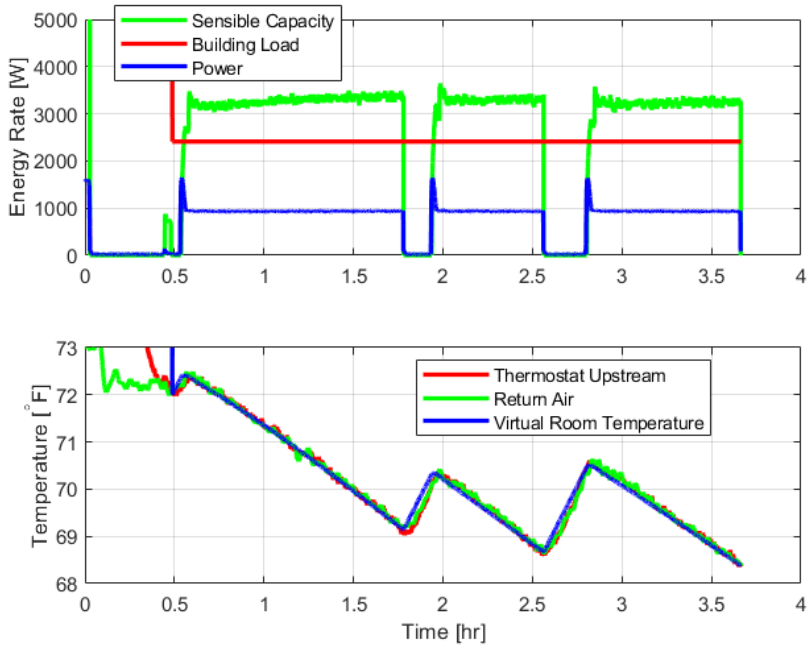

Fig. 7. Sensible results of performance mapping test 4

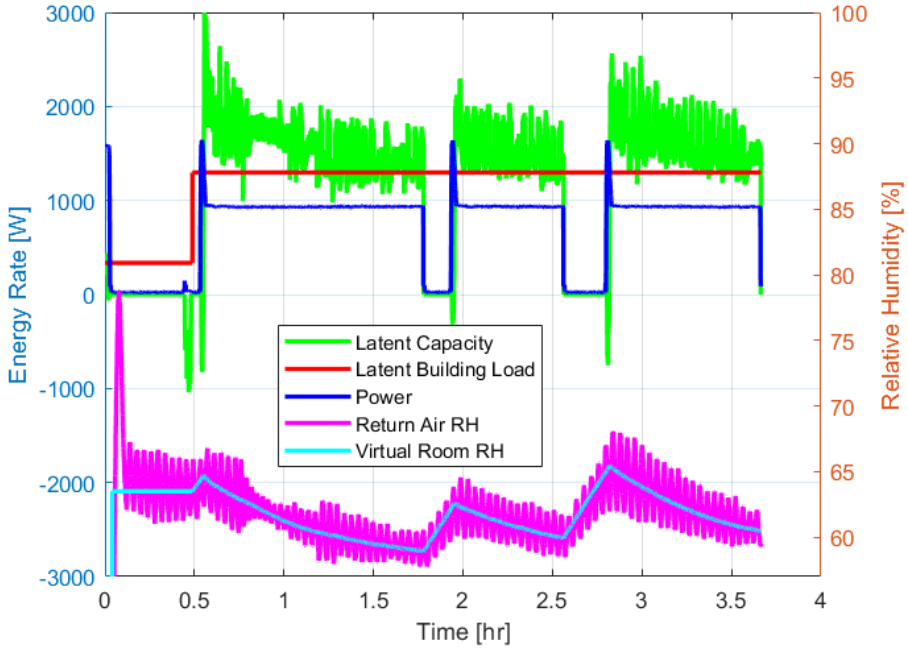

Fig. 8. Latent results of performance mapping test 4

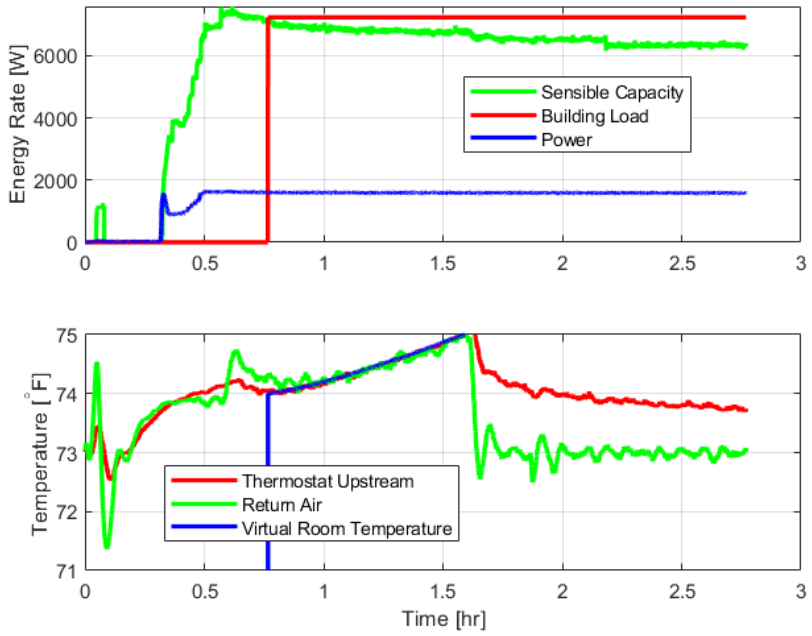

Fig. 9. Sensible results of performance mapping test 5

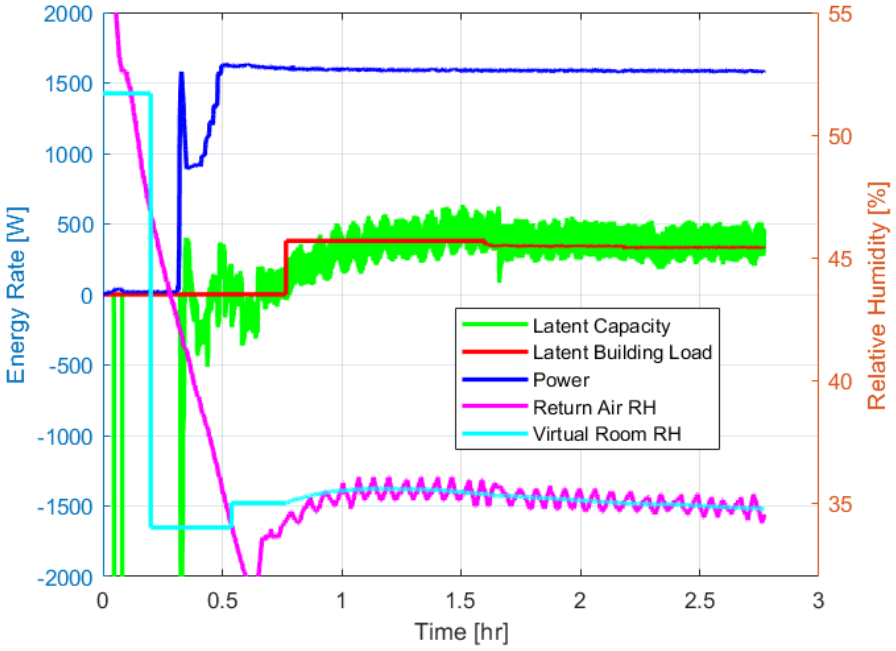

Fig. 10. Latent results of performance mapping test 5

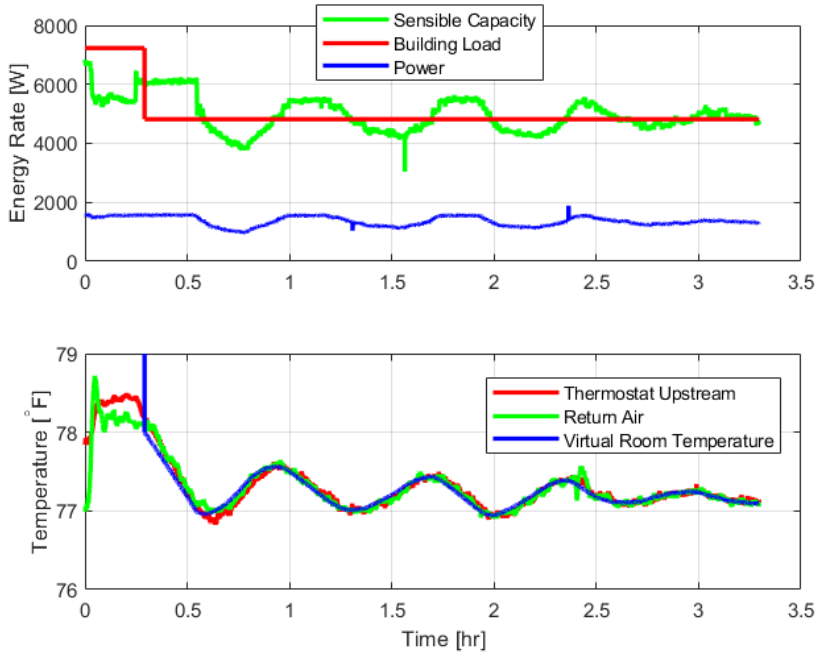

Fig. 11. Sensible results of performance mapping test 6

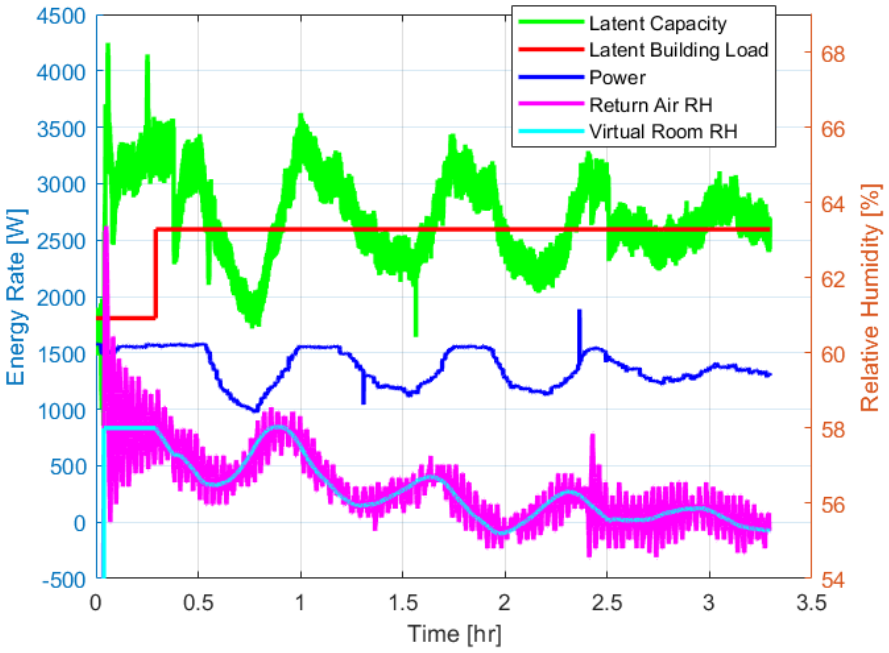

Fig. 12. Latent results of performance mapping test 6

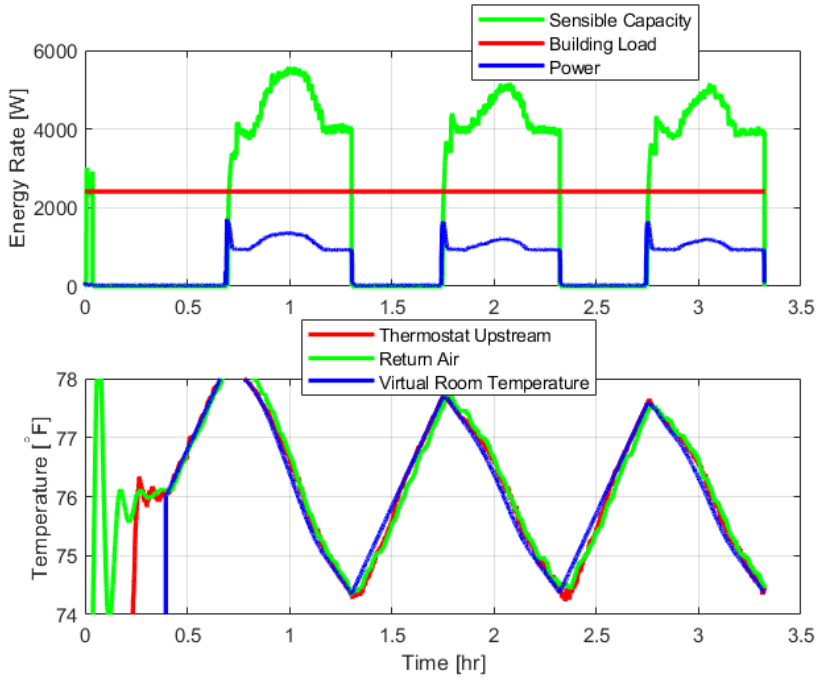

Fig. 13. Sensible results of performance mapping test 7

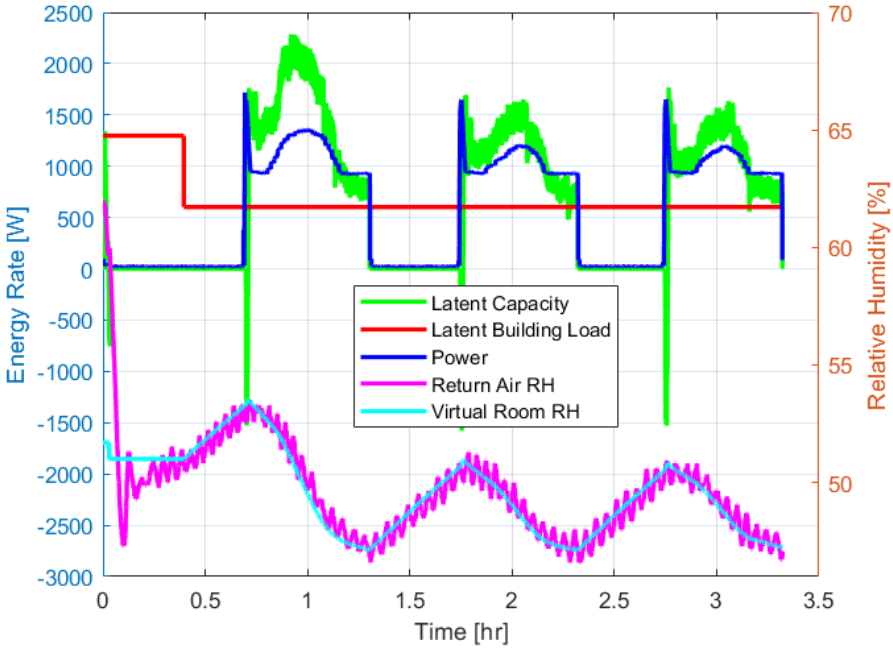

Fig. 14. Latent results of performance mapping test 7

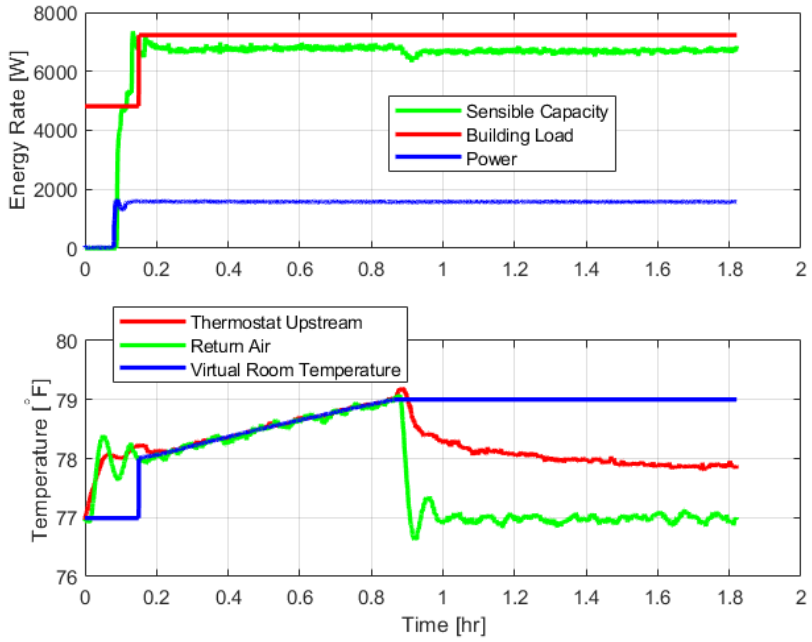

Fig. 15. Sensible results of performance mapping test 8

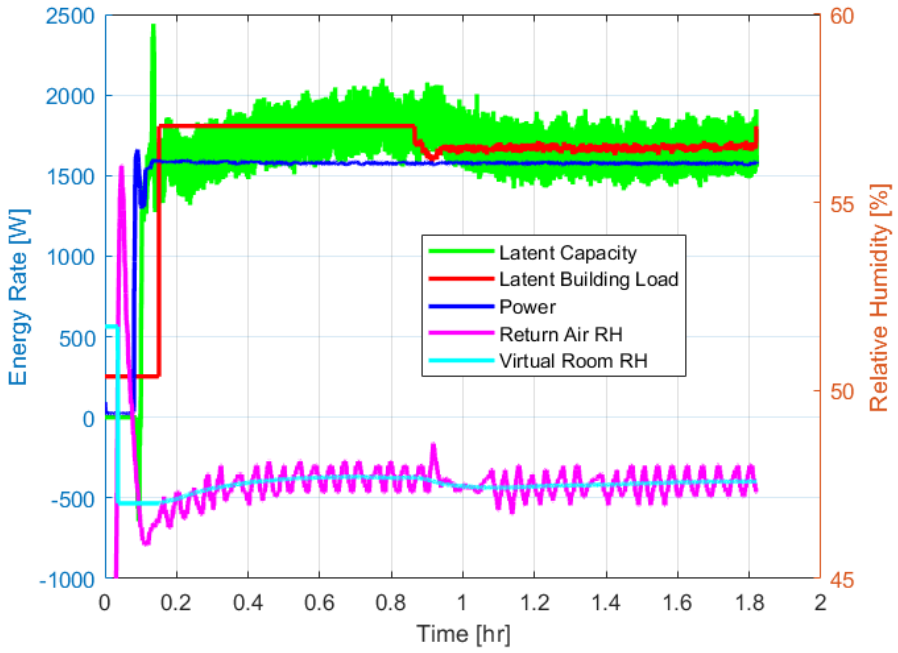

Fig. 16. Latent results of performance mapping test 8

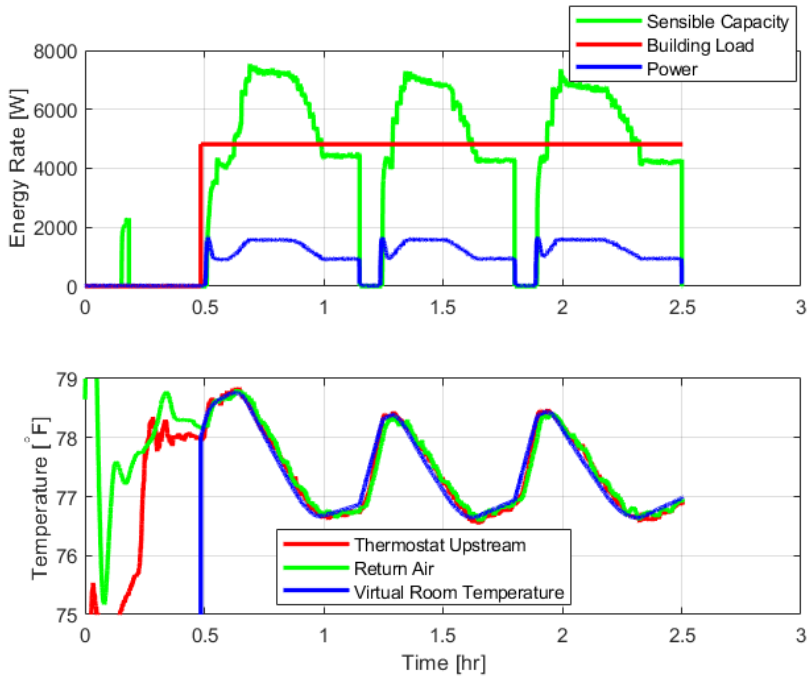

Fig. 17. Sensible results of performance mapping test 9

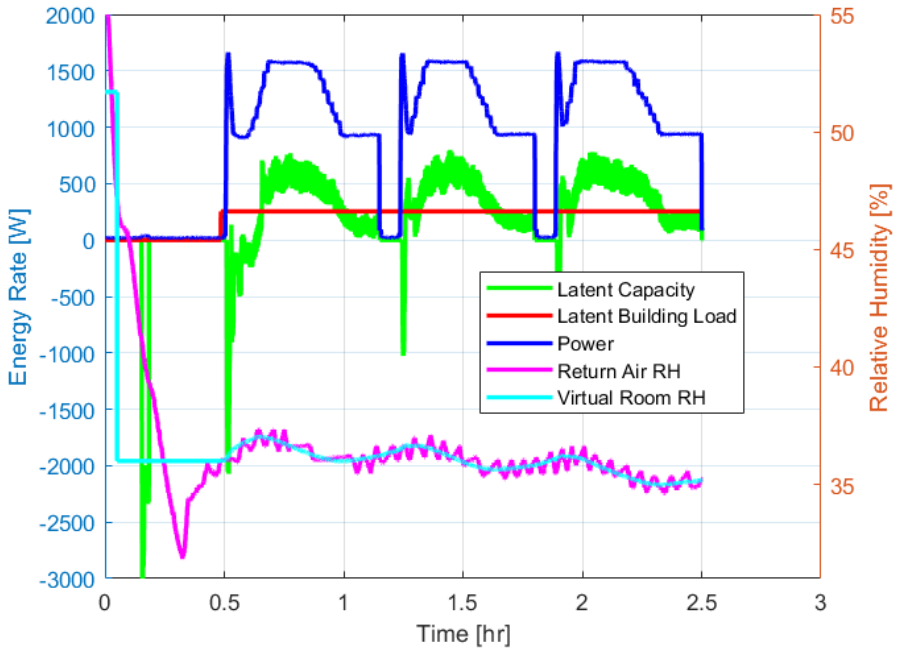

Fig. 18. Latent results of performance mapping test 9

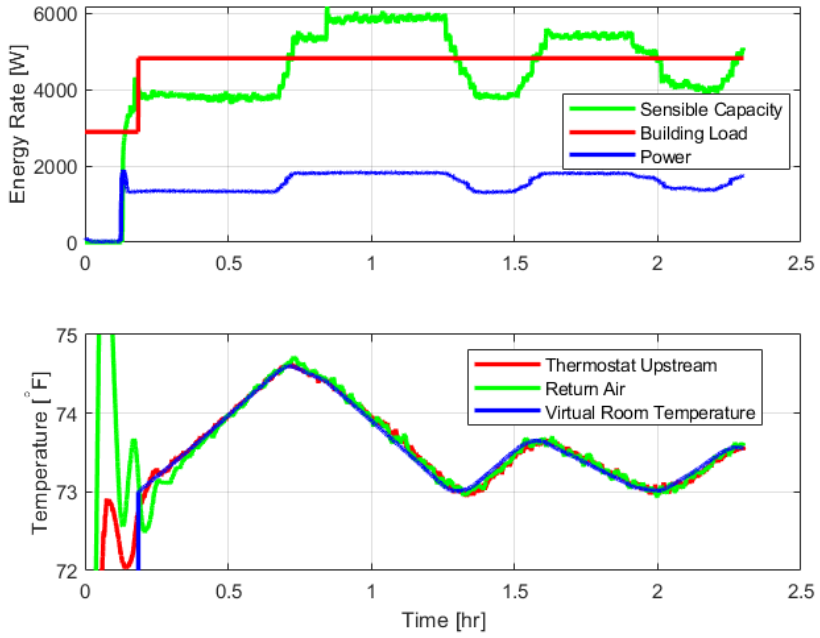

Fig. 19. Sensible results of performance mapping test 10

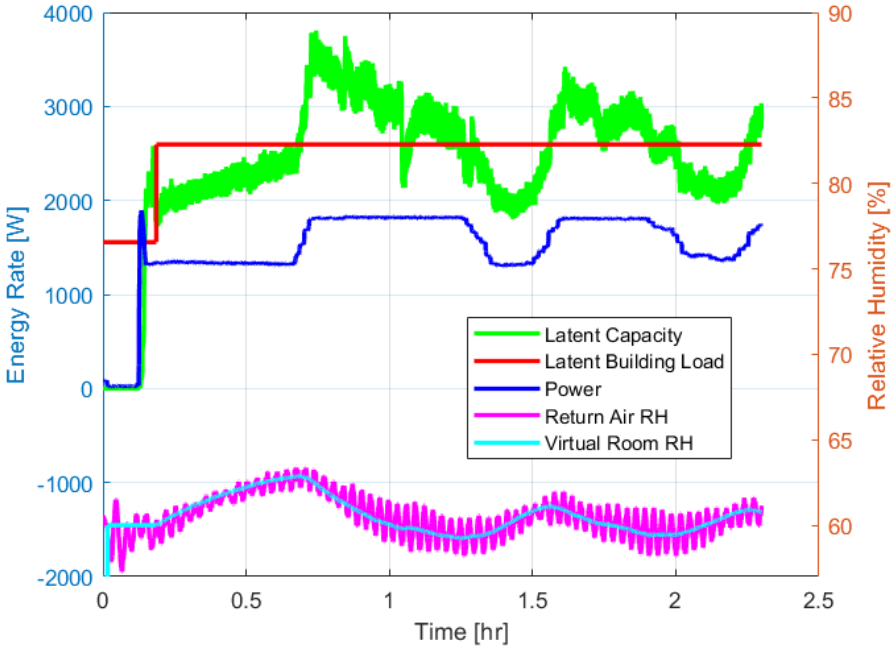

Fig. 20. Latent results of performance mapping test 10

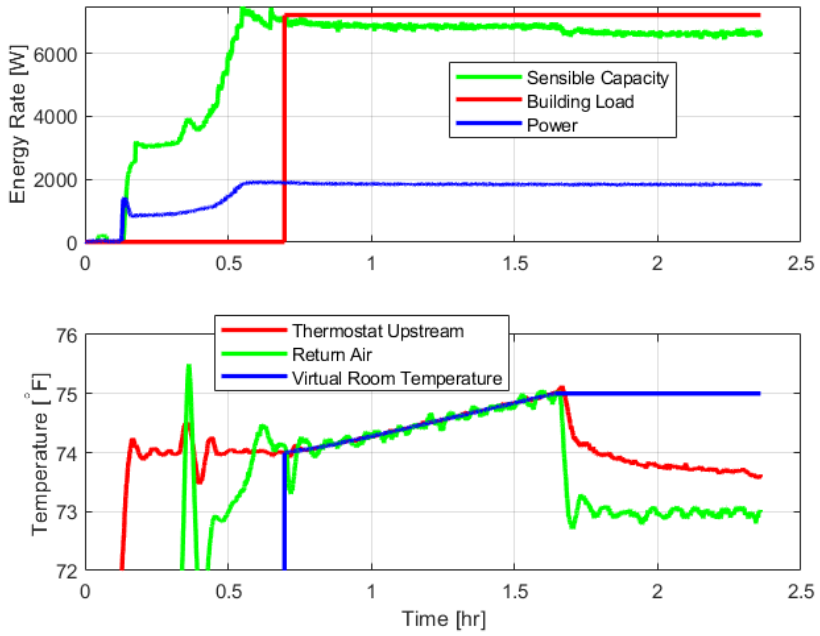

Fig. 21. Sensible results of performance mapping test 11

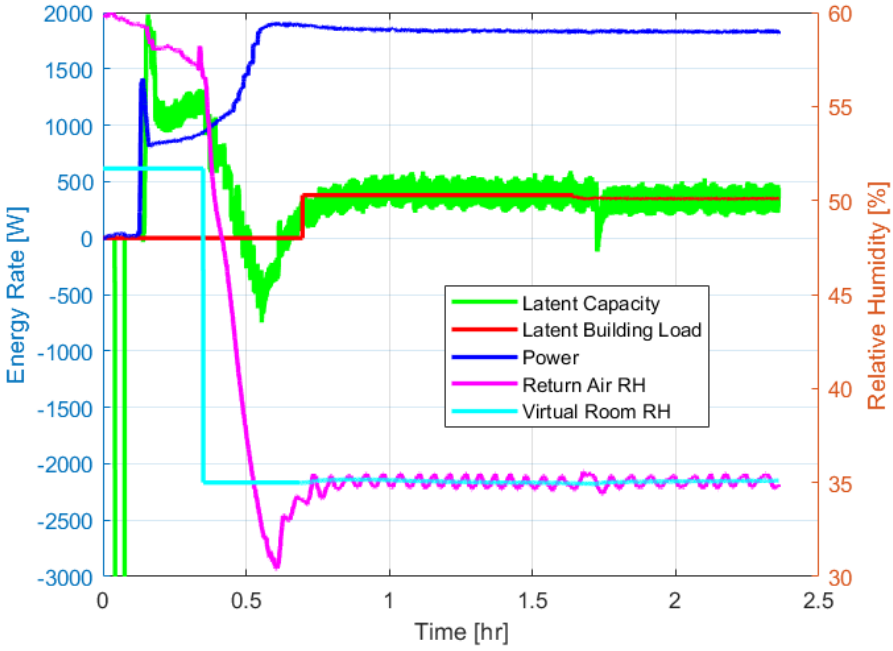

Fig. 22. Latent results of performance mapping test 11

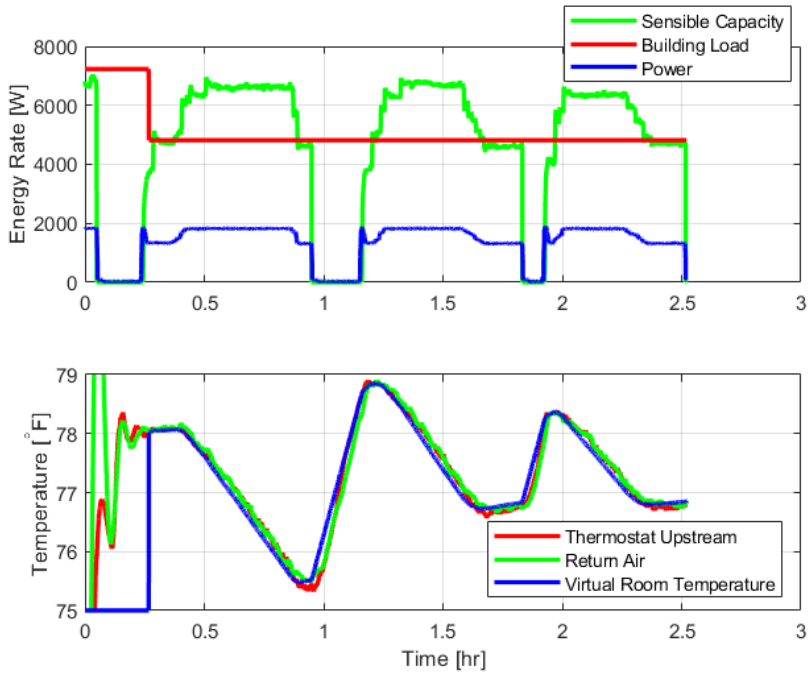

Fig. 23. Sensible results of performance mapping test 12

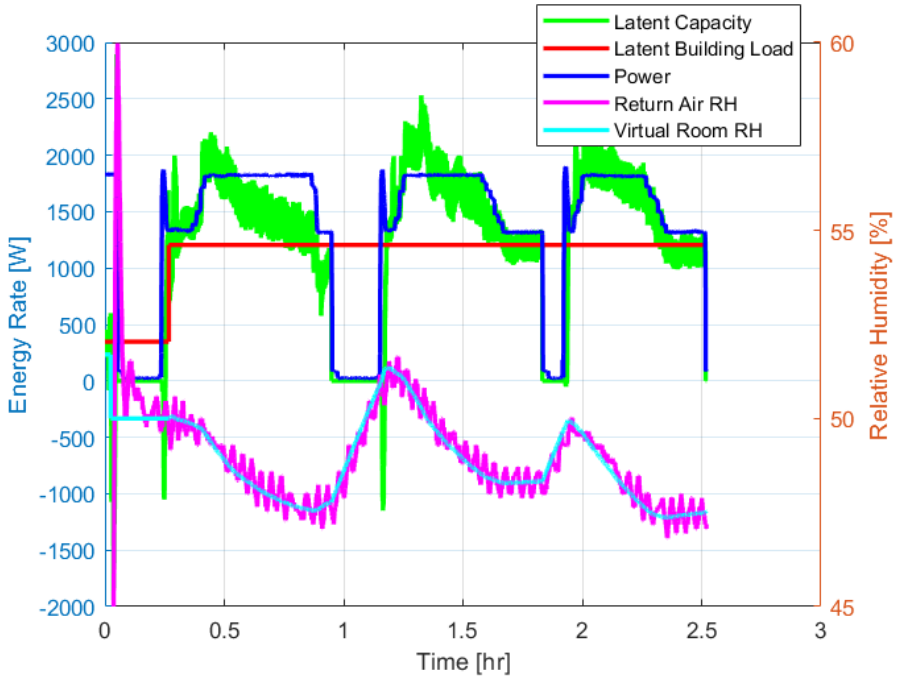

Fig. 24. Latent results of performance mapping test 12

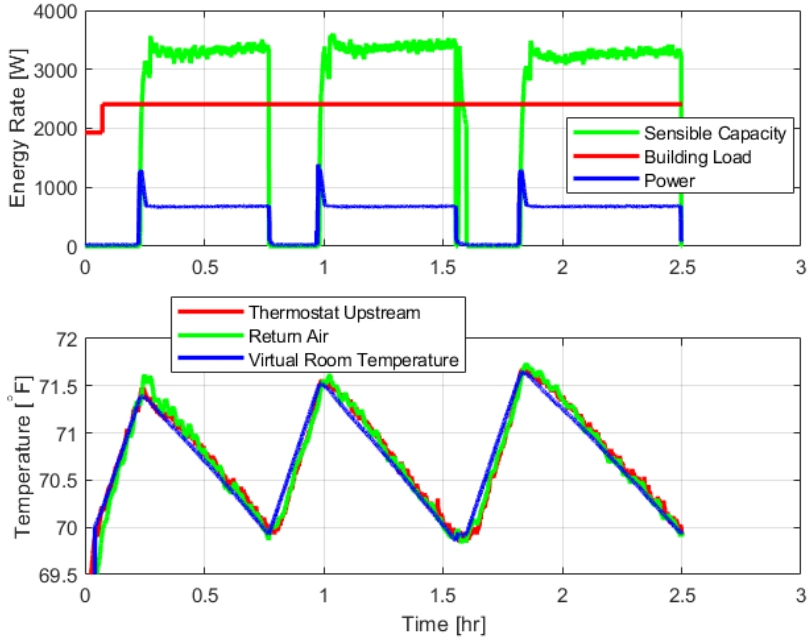

Fig. 25. Sensible results of performance mapping test 13

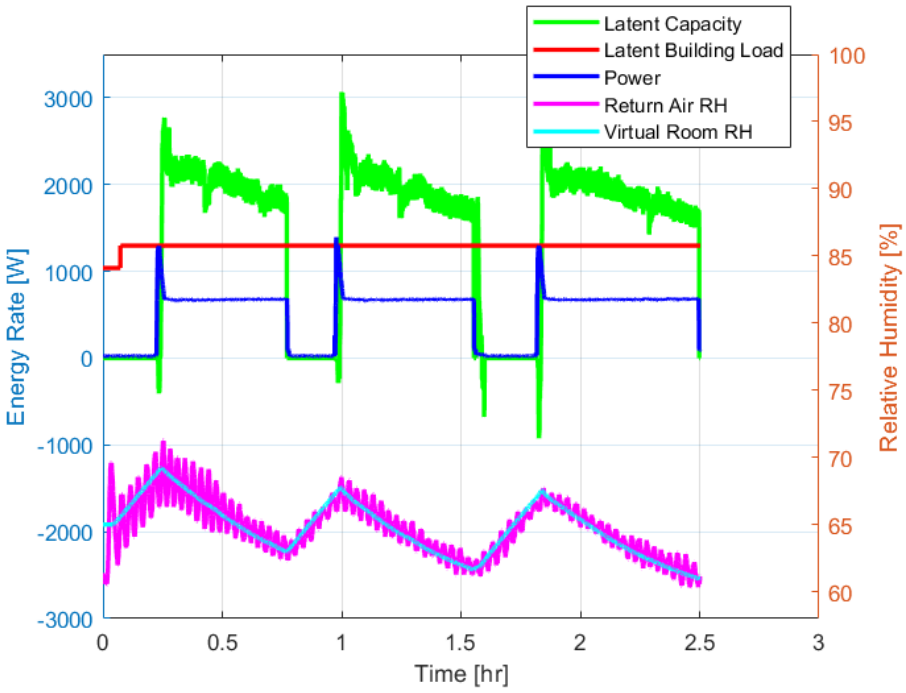

Fig. 26. Latent results of performance mapping test 13

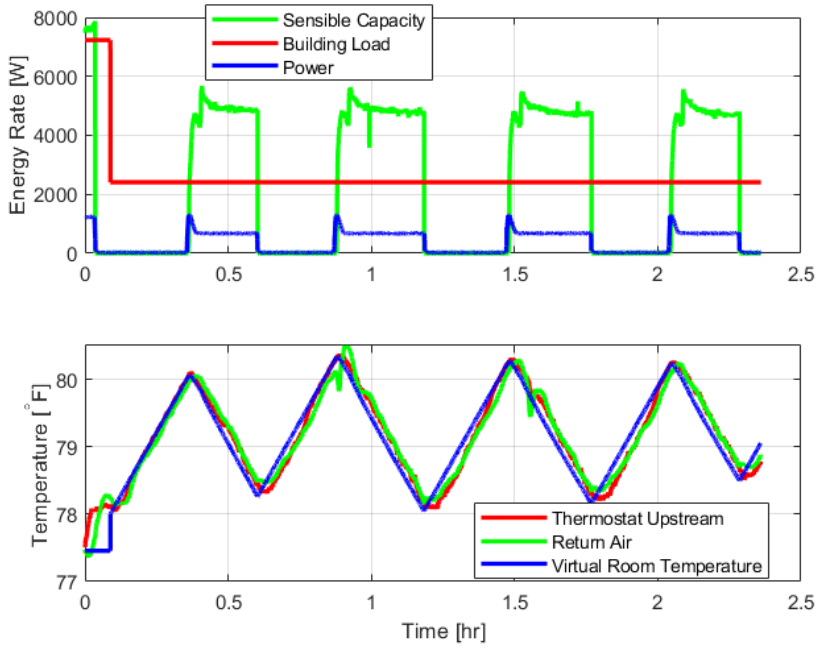

Fig. 27. Sensible results of performance mapping test 14

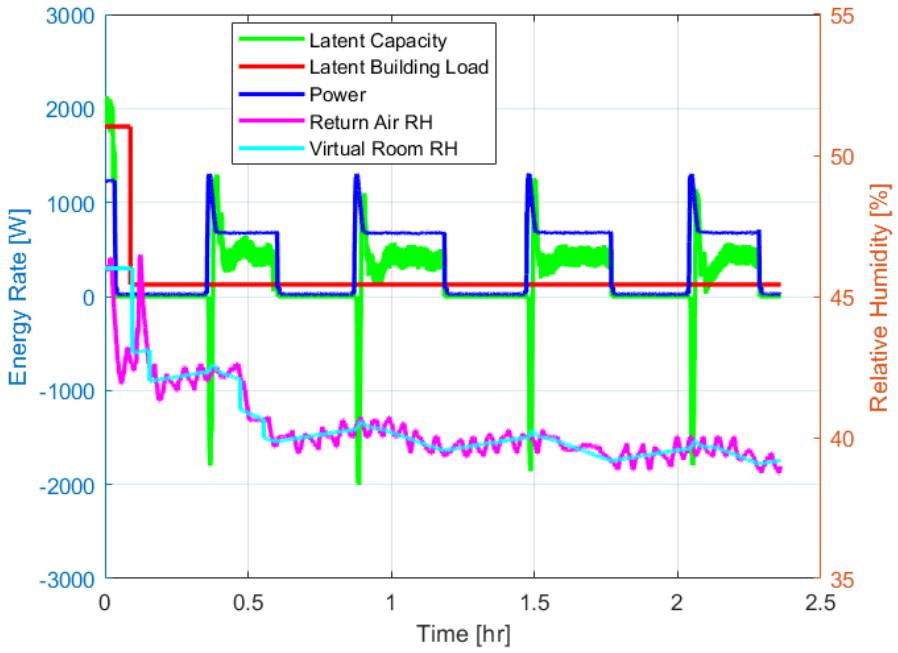

Fig. 28. Latent results of performance mapping test 14

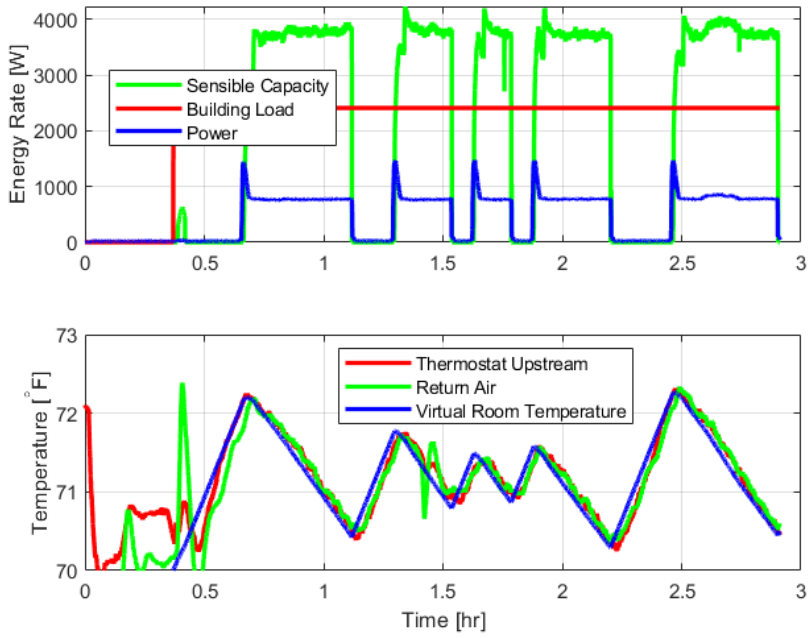

Fig. 29. Sensible results of performance mapping test 15

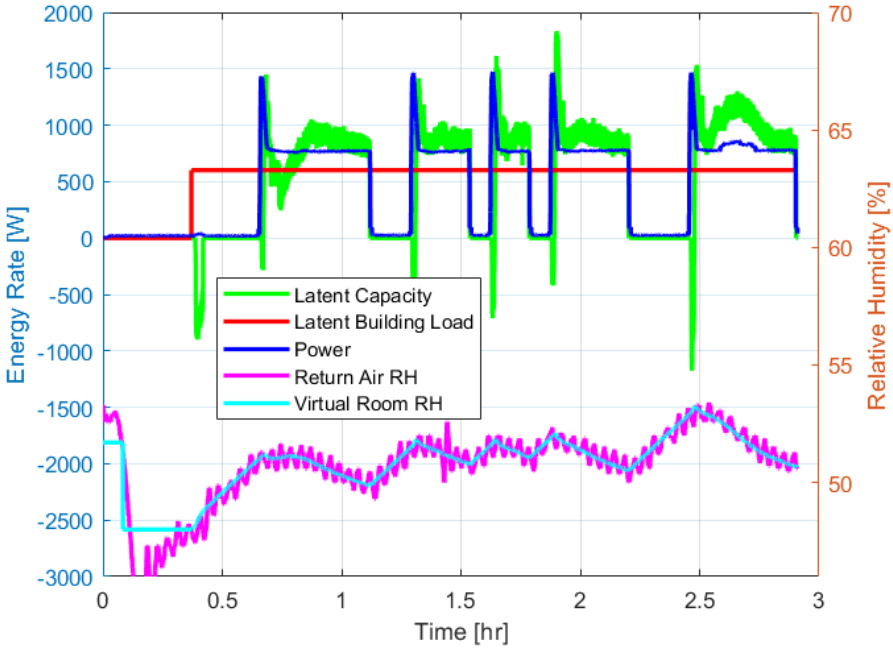

Fig. 30. Latent results of performance mapping test 15

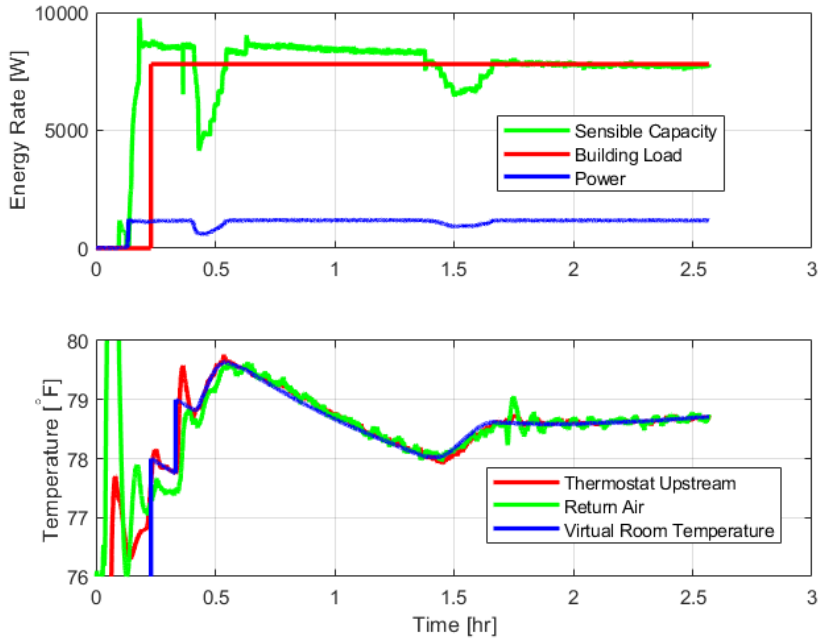

Fig. 31. Sensible results of performance mapping test 16

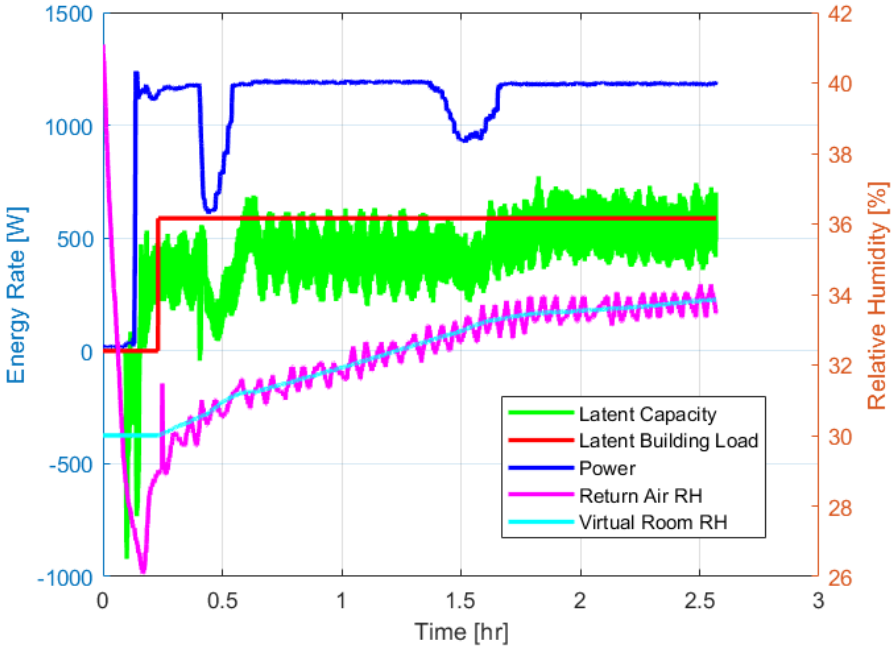

Fig. 32. Latent results of performance mapping test 16

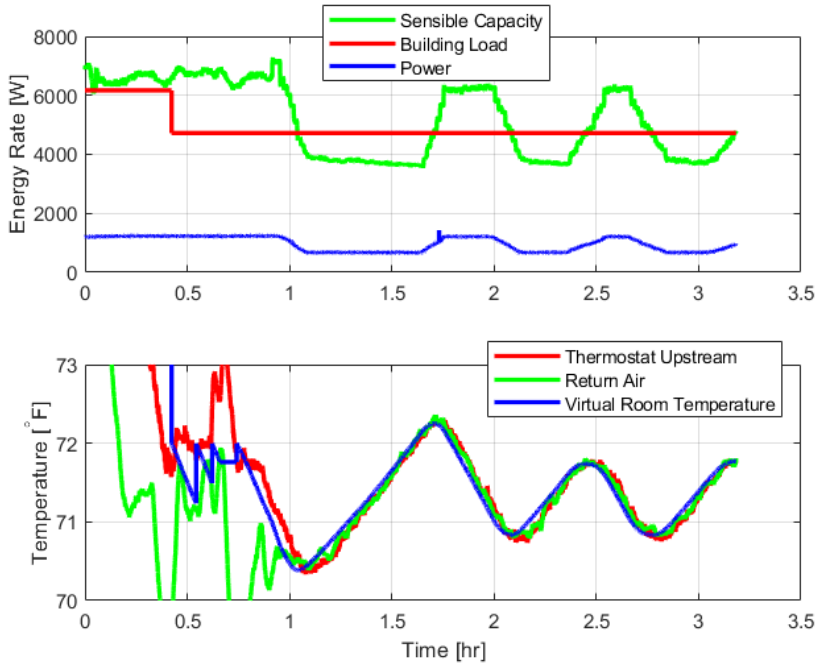

Fig. 33. Sensible results of performance mapping test 17

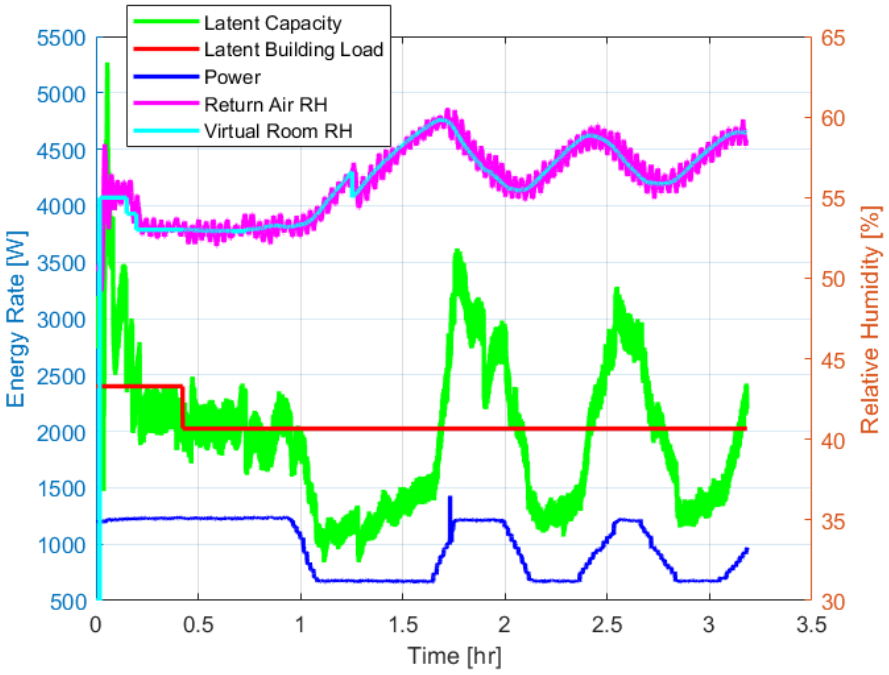

Fig. 34. Latent results of performance mapping test 17

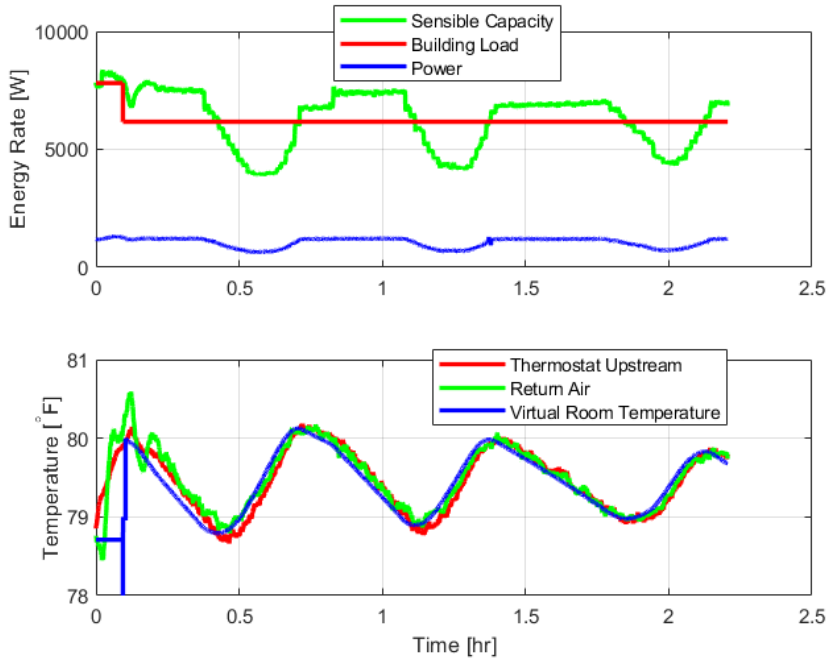

Fig. 35. Sensible results of performance mapping test 18

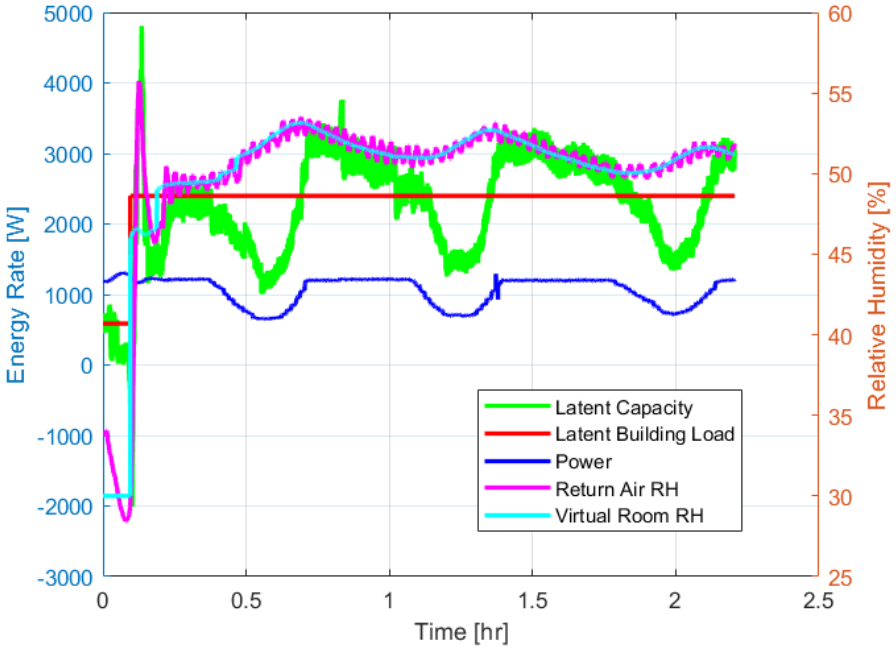

Fig. 36. Latent results of performance mapping test 18

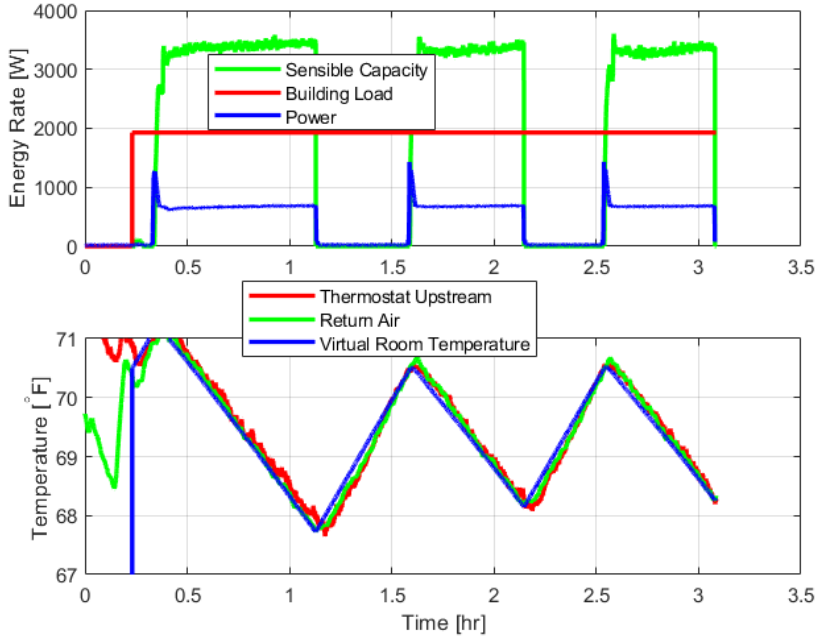

Fig. 37. Sensible results of performance mapping test 19

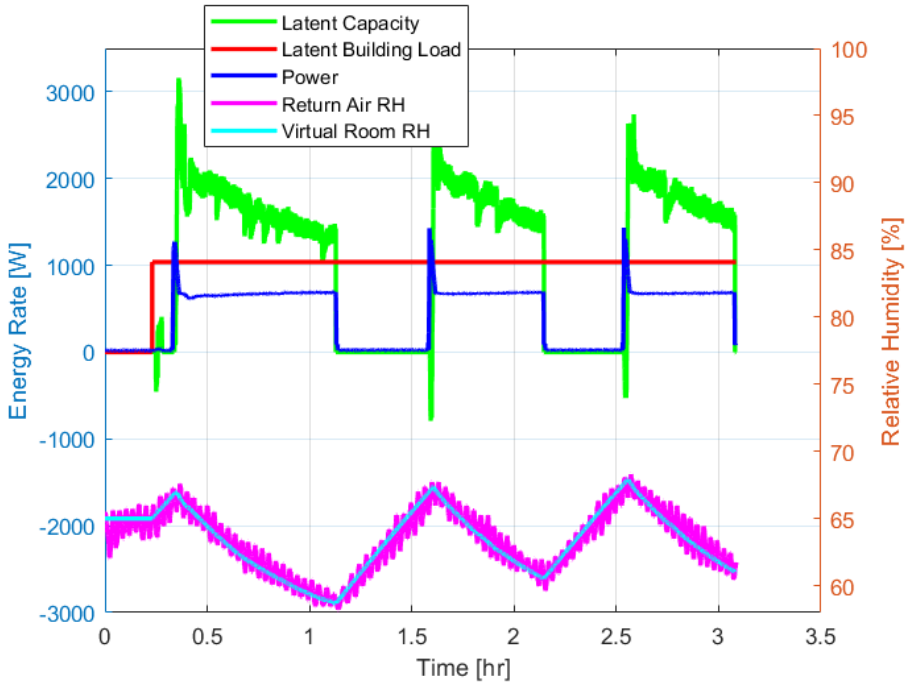

Fig. 38. Latent results of performance mapping test 19

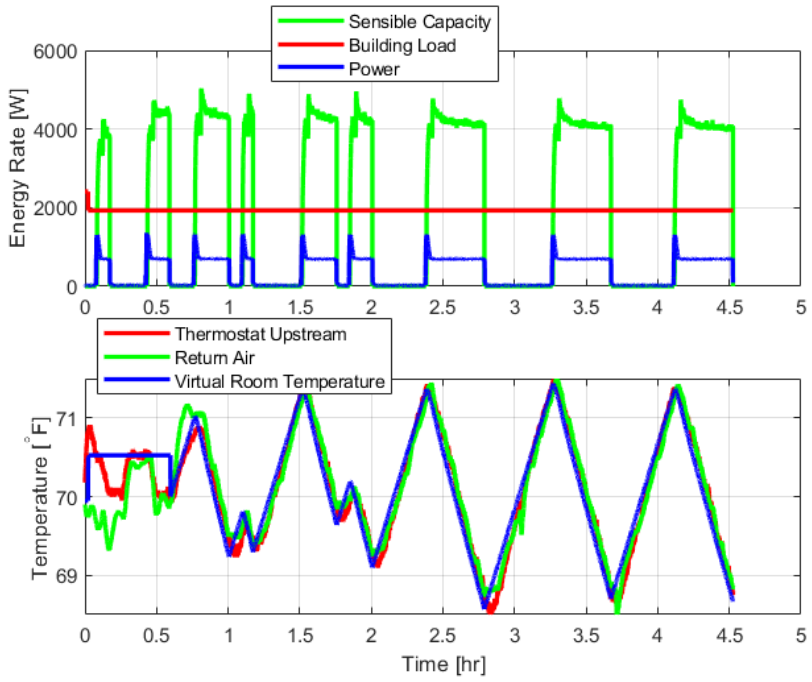

Fig. 39. Sensible results of performance mapping test 20

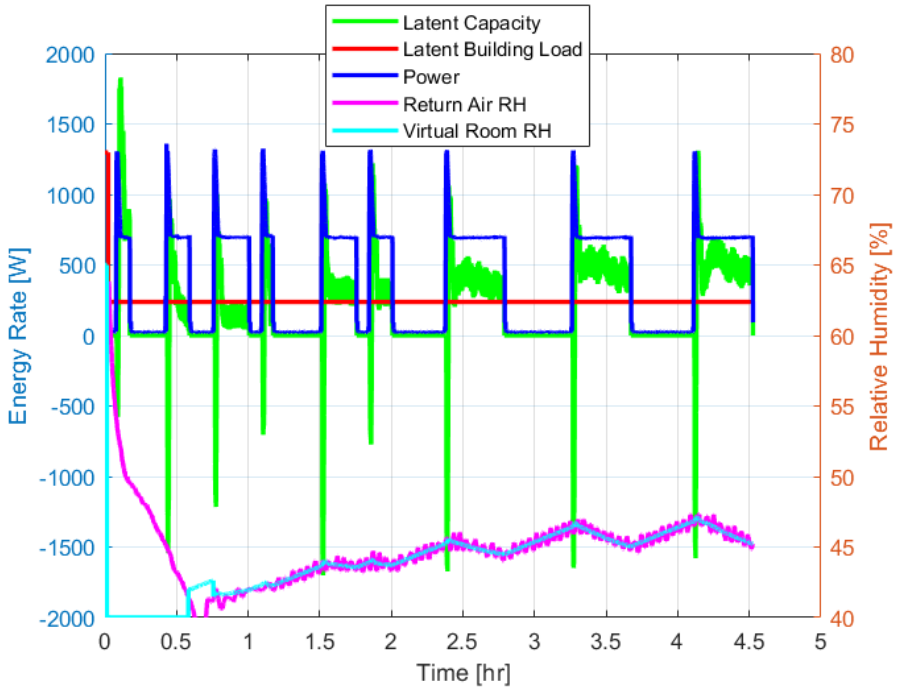

Fig. 40. Latent results of performance mapping test 20

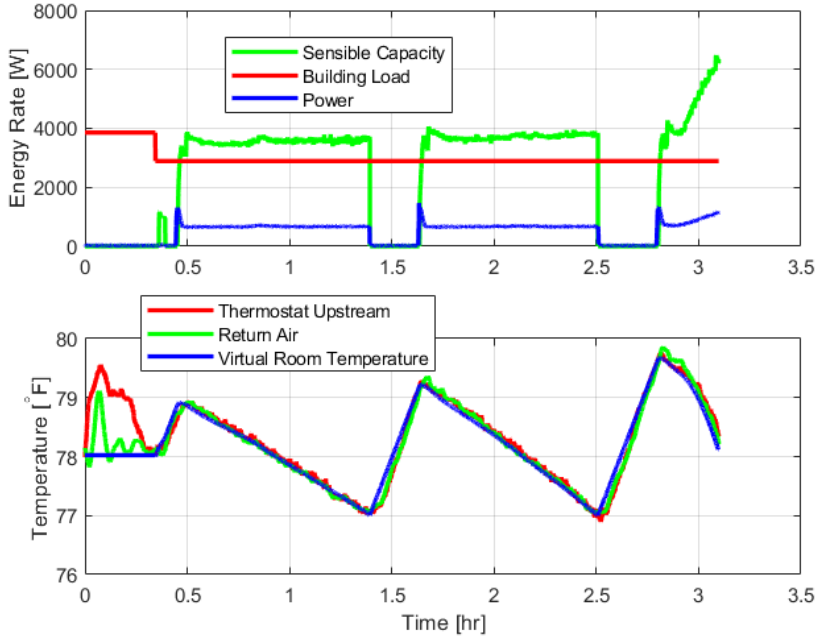

Fig. 41. Sensible results of performance mapping test 21

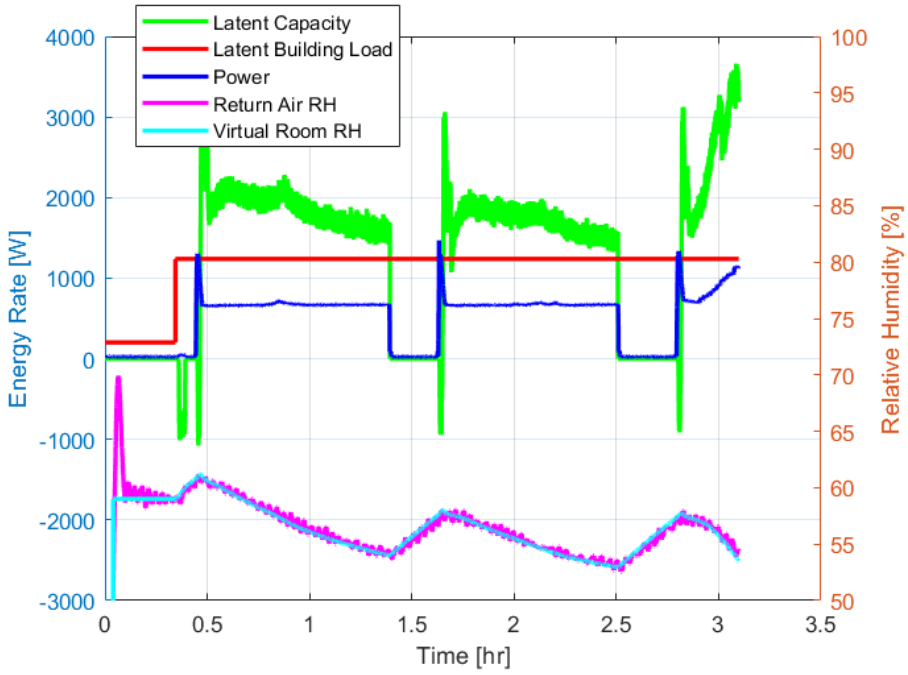

Fig. 42. Latent results of performance mapping test 21

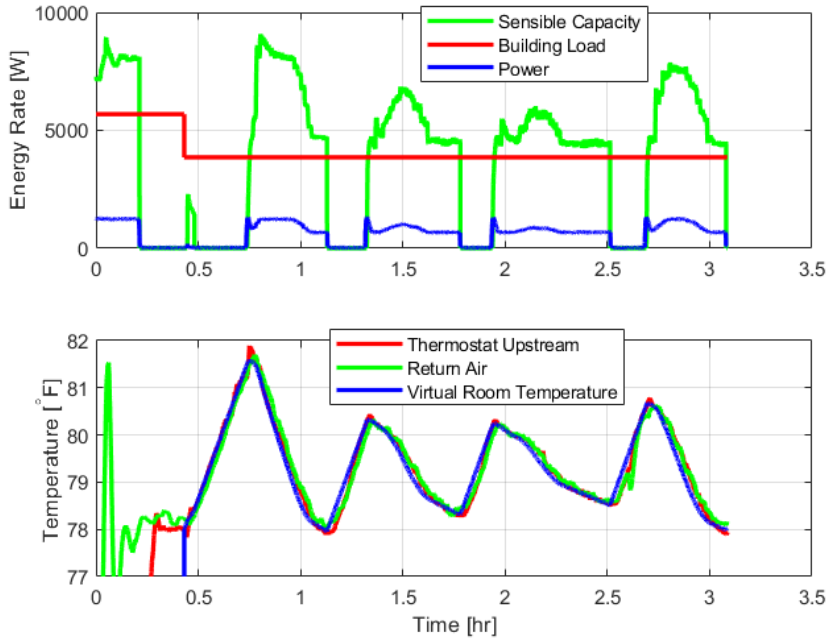

Fig. 43. Sensible results of performance mapping test 22

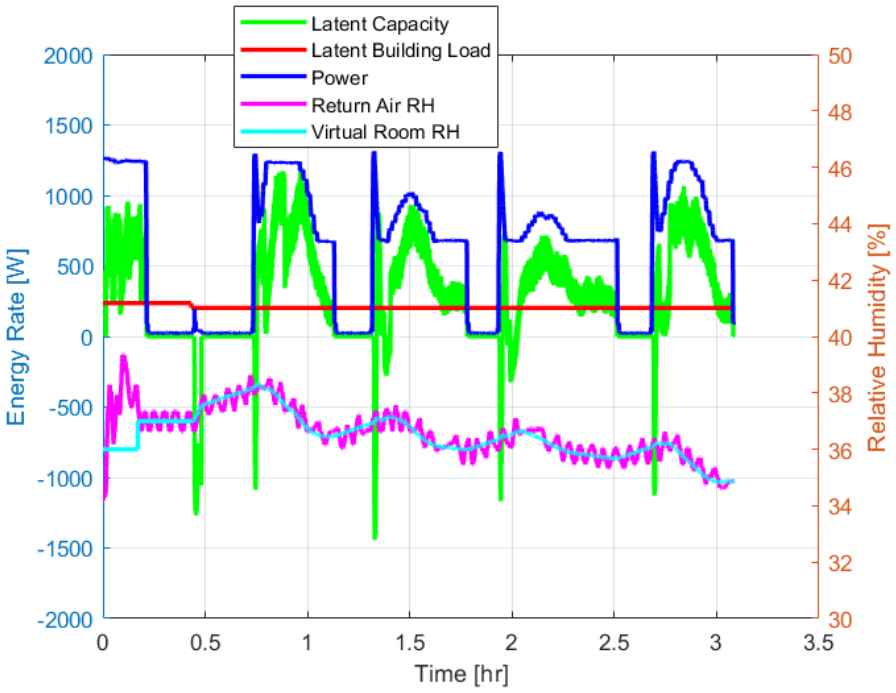

Fig. 44. Latent results of performance mapping test 22

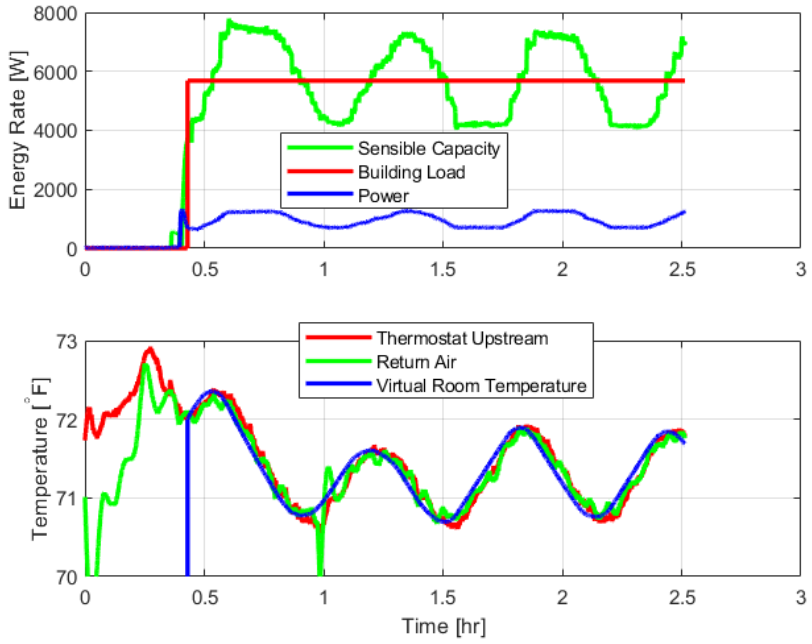

Fig. 45. Sensible results of performance mapping test 23

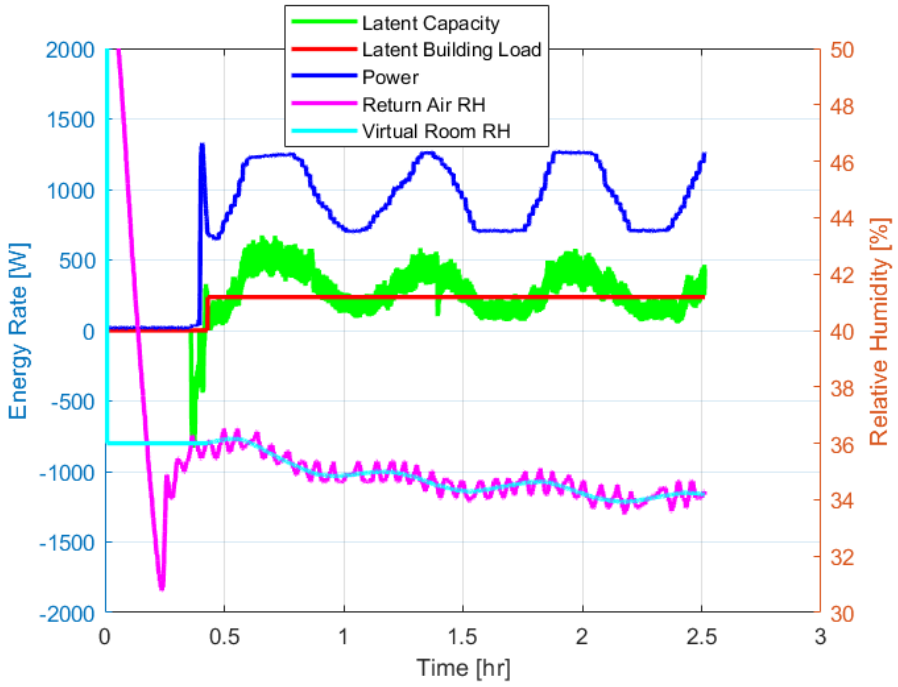

Fig. 46. Latent results of performance mapping test 23

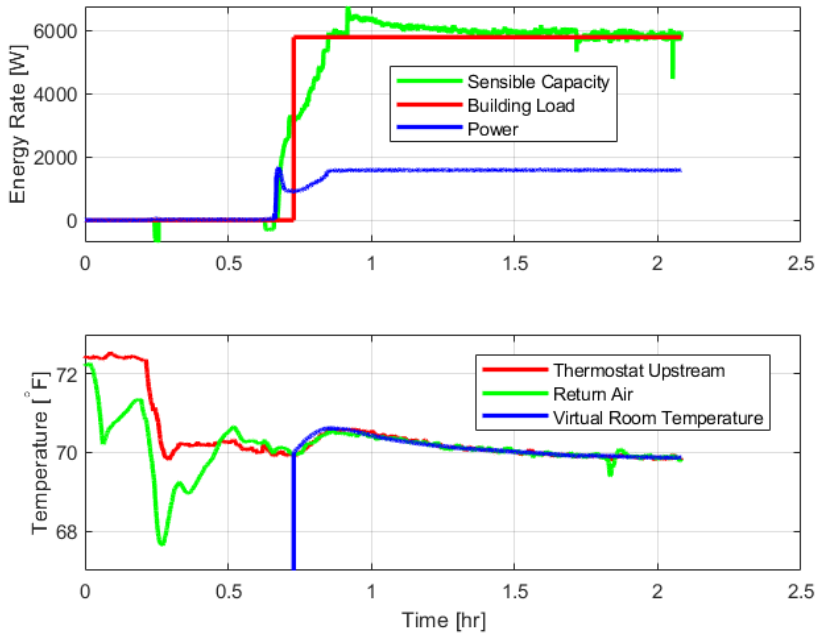

Fig. 47. Sensible results of performance mapping test 24

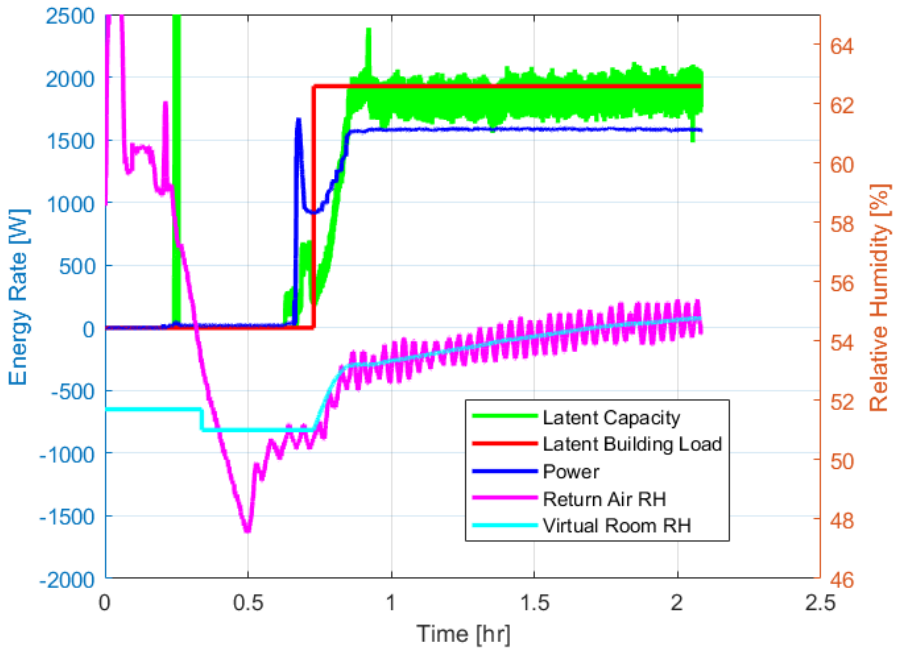

Fig. 48. Latent results of performance mapping test 24

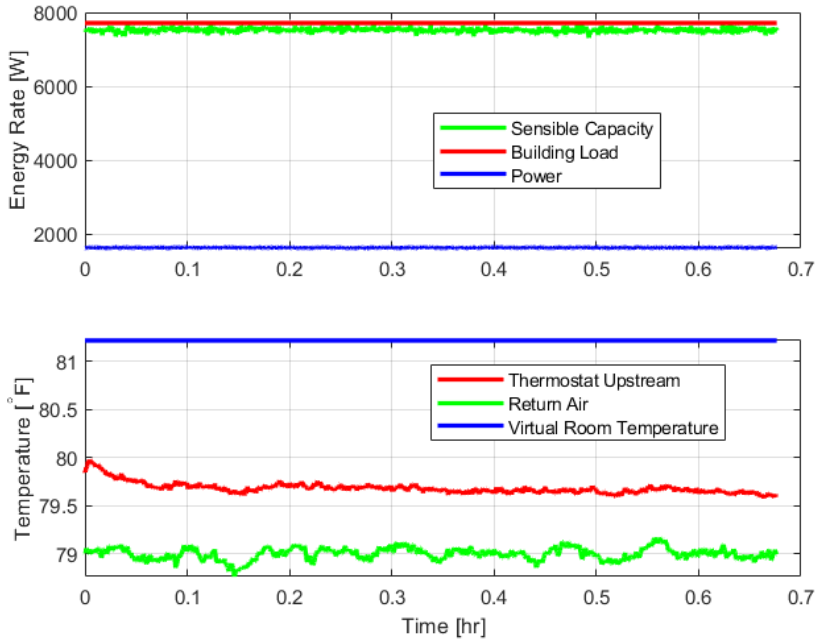

Fig. 49. Sensible results of performance mapping test 25

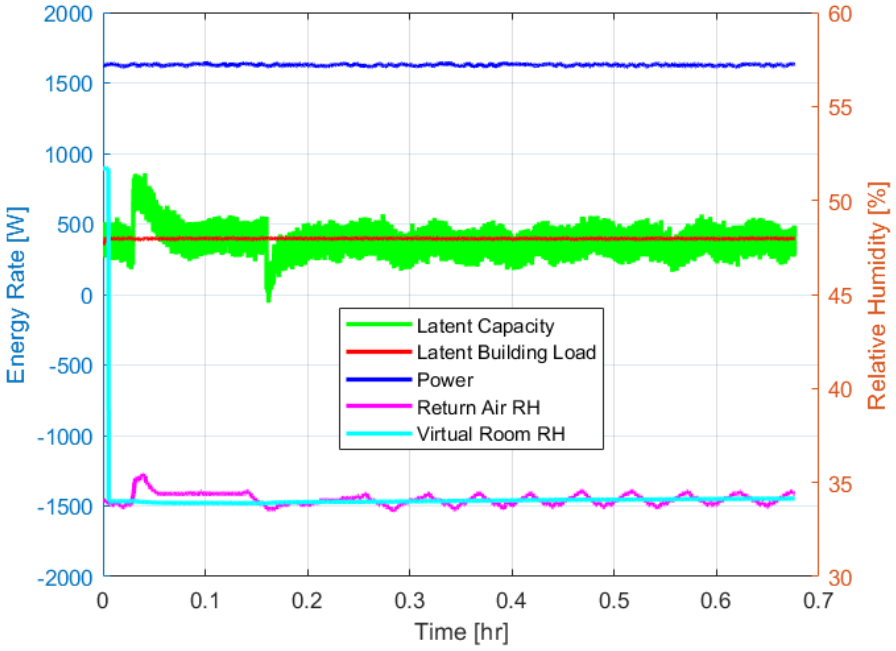

Fig. 50. Latent results of performance mapping test 25

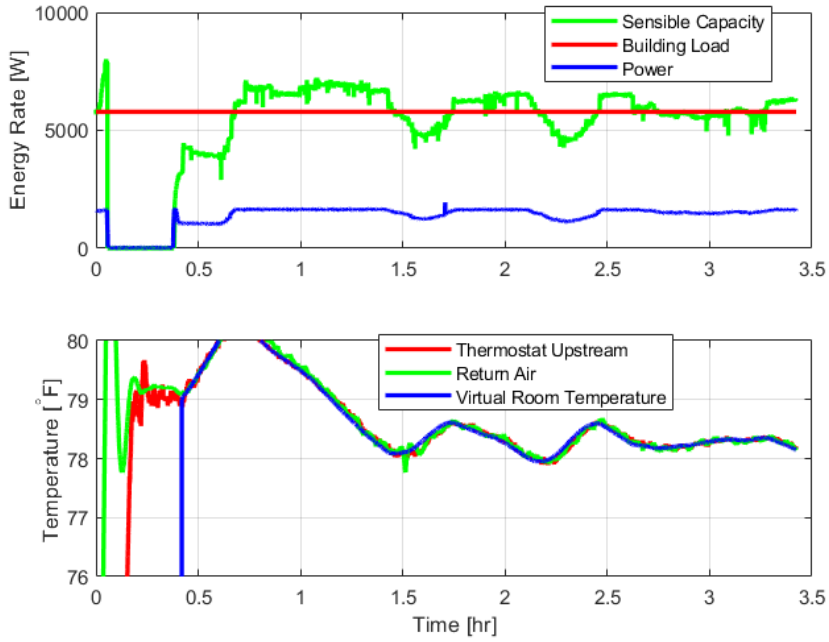

Fig. 51. Sensible results of performance mapping test 26

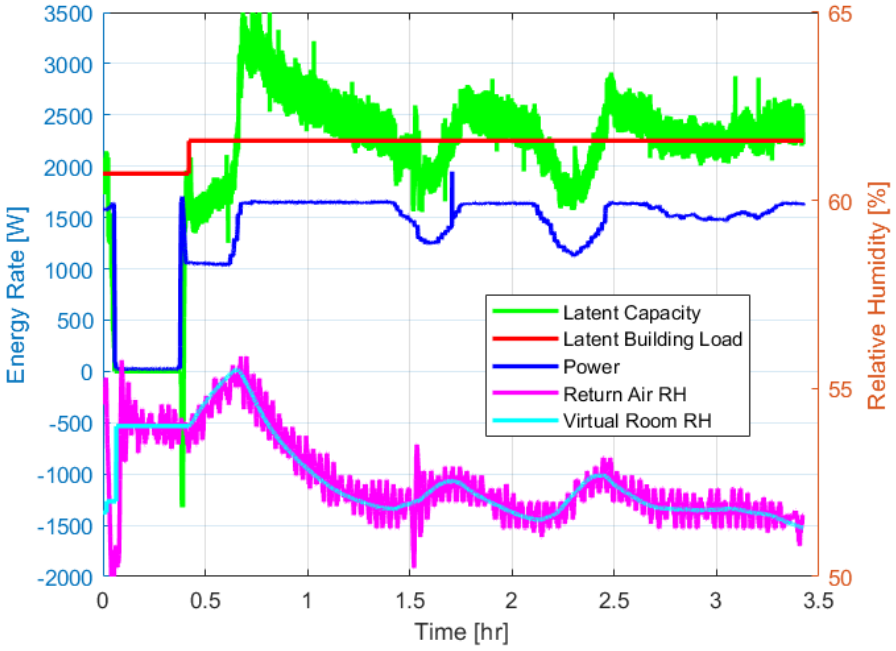

Fig. 52. Latent results of performance mapping test 26

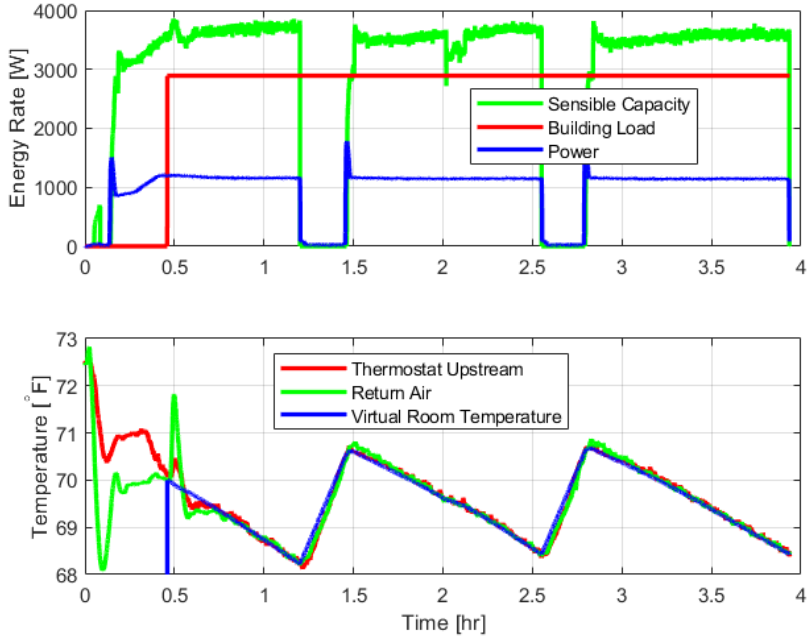

Fig. 53. Sensible results of performance mapping test 27

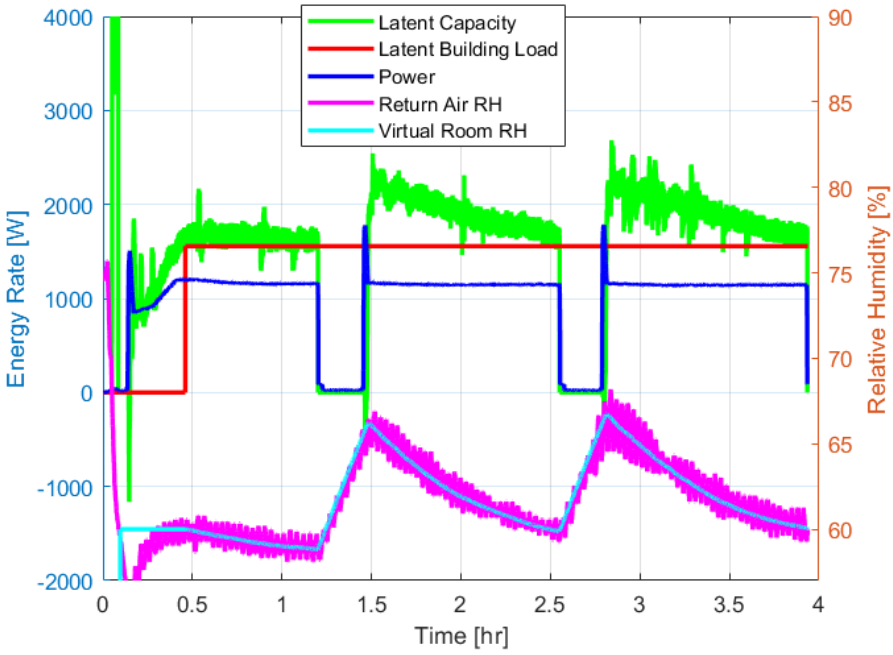

Fig. 54. Latent results of performance mapping test 27

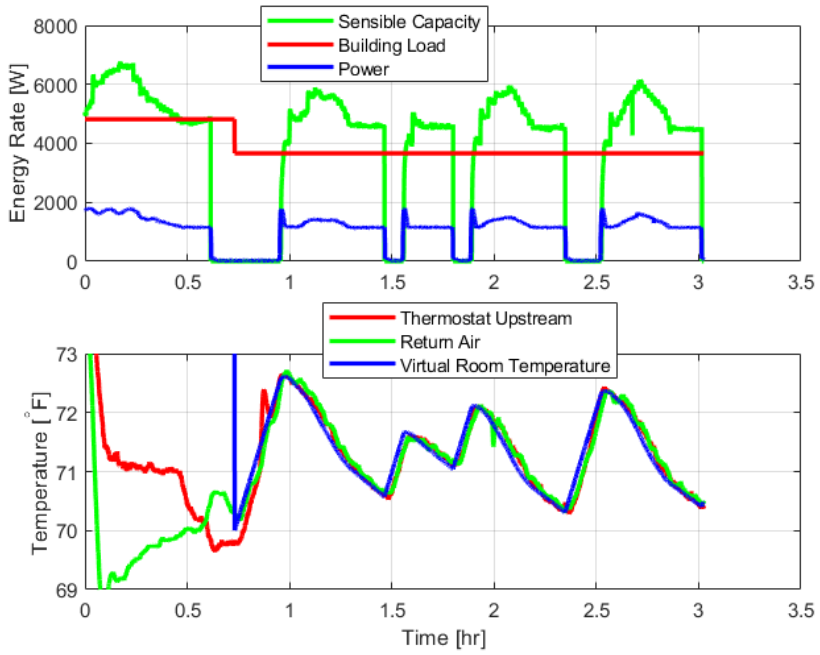

Fig. 55. Sensible results of performance mapping test 28

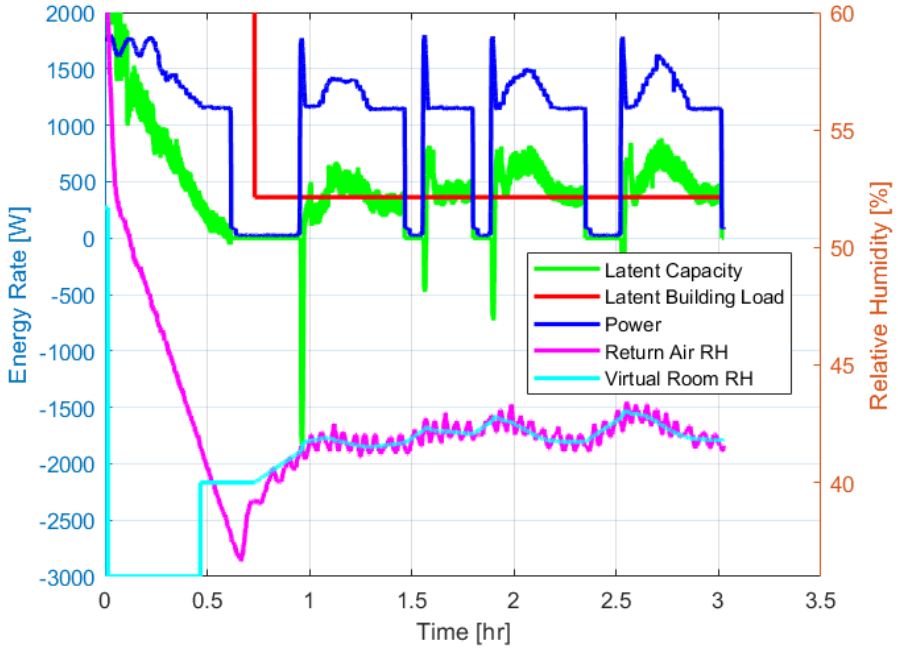

Fig. 56. Latent results of performance mapping test 28

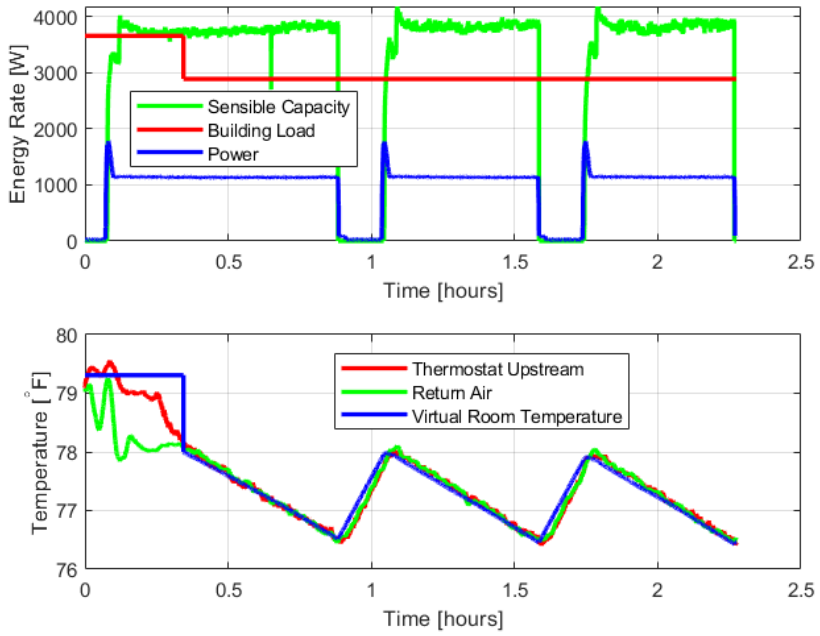

Fig. 57. Sensible results of performance mapping test 29

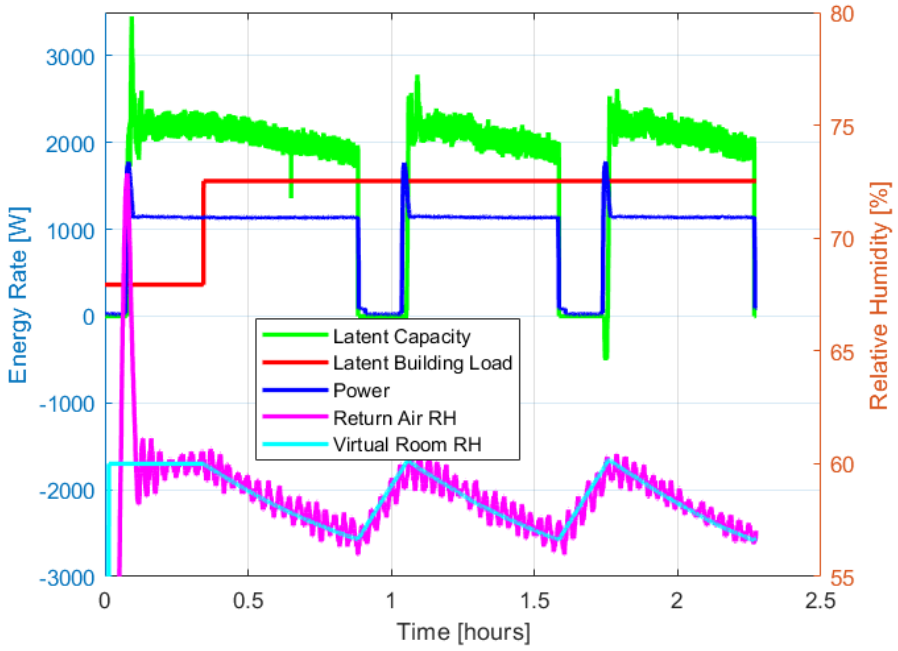

Fig. 58. Latent results of performance mapping test 29

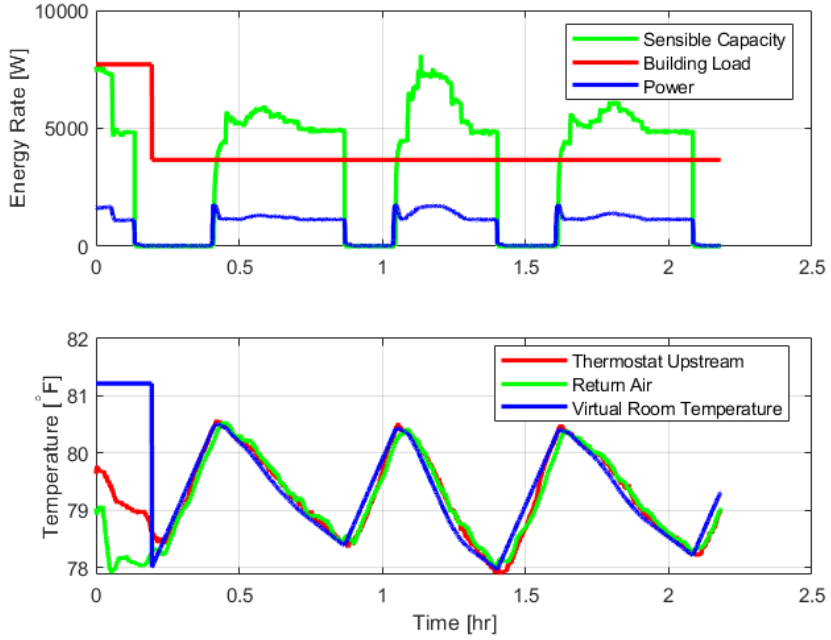

Fig. 59. Sensible results of performance mapping test 30

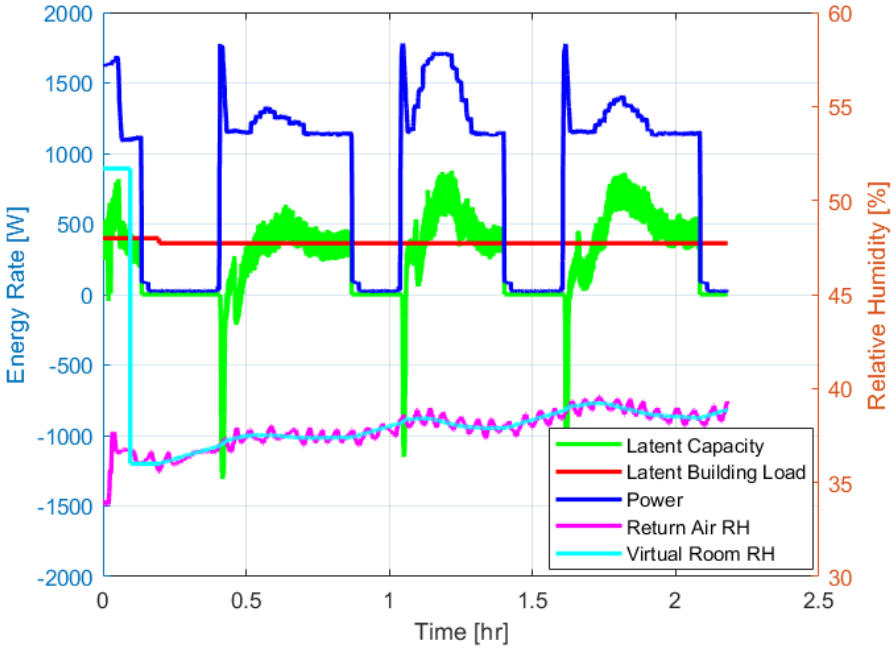

Fig. 60. Latent results of performance mapping test 30